MODELING AND REHABILITATION OF NON-DUCTILE SPATIAL RC COLUMNS

BY

KHALED ELMANDOOH MOHAMED IBRAHIM GALAL,
B.Sc., M.Sc.

SEPTEMBER 2002

A THESIS
SUBMITTED TO THE SCHOOL OF GRADUATE STUDIES
IN PARTIAL FULFILLMENT OF THE REQUIREMENTS
FOR THE DEGREE
DOCTOR OF PHILOSOPHY

MCMASTER UNIVERSITY

DOCTOR OF PHILOSOPHY (2002)
(Department of Civil Engineering)
(Earthquake Engineering Research Group)

McMaster University
Hamilton, Ontario, Canada

TITLE: Modeling and rehabilitation of non-ductile spatial RC columns

AUTHOR: Khaled ElMandooh Mohamed Ibrahim Galal,
B.Sc. (Ain Shams University), M.Sc. (Ain Shams University)

SUPERVISOR: Dr. A. Ghobarah, Professor and Joe NG/JNE Consulting Chair in Design, Construction and Management in Infrastructure Renewal, Department of Civil Engineering

NUMBER OF PAGES: xxii, 289

ABSTRACT

In frame structures, the multi-directional motion of an earthquake has a significant effect on the structure response. The columns, especially those at the building corners, are subjected to biaxial bending from combined longitudinal, transverse, and torsional motion of the structure, with added axial loads due to overturning. Moreover, the variation of the axial forces may be independent of the variation of the other lateral forces.

The non-ductile response of structural elements, particularly columns, has been the cause of numerous failures during earthquakes. The non-ductile behaviour of reinforced concrete columns arises from different causes such as insufficient anchorage length and bond for the longitudinal steel bars with concrete, insufficient confinement, or inadequate shear strength.

The objective of this research program is to analytically and experimentally evaluate the non-linear behaviour of non-ductile reinforced concrete columns under lateral cyclic deformations. The experimental data was used to verify the analytical predictions.

The analytical phase of this study included the development of an upgraded 3D beam-column element based on lumped plasticity modelling. The model accommodates flexural response by quadrilinear force-deformation relationship, and shear response by strength and stiffness degrading relationship. The model takes into account the effect of axial load variation on lateral deformation and its interaction with biaxial moments and shear, which is an important contribution.

The 3D model was validated using experimental data available in the literature by several independent researchers for reinforced concrete columns. The calculated and experimental results were encouragingly close, especially considering the complexity of the response. The effect of different axial load variation paths on the response of cyclically loaded columns was studied.

A new analytical procedure to obtain the moment-rotation and force-deflection relationships for reinforced concrete columns was developed. These relationships were used as input data for the 3D element. This procedure uses the basic mechanical and geometrical properties of the element. It takes into consideration the effect of bond-slip of tensile bars, buckling of compression bars as well as flexure and shear deformations. This procedure was verified using available experimental data. The comparison showed good agreement. A parametric study to evaluate the effect of variation in section and material properties was also conducted.

The experimental phase of this study included testing three reinforced concrete short columns under cyclic lateral loads and constant axial load. The first specimen, which represents columns designed according to current code (CSA A23.3-94), failed in a non-ductile shear manner. The second specimen was identical to the first one but rehabilitated using anchored carbon fibre reinforced polymers (CFRP). A significant increase in the displacement ductility of the column was achieved. The third specimen represents a non-ductile short column designed according to pre-1970 codes and rehabilitated using anchored CFRP wraps. Increased ductility was achieved. Two different techniques to reduce concrete bulging at column sides were evaluated in the two rehabilitated specimens; namely, by using through steel rods and fibre anchors. Both techniques proved to be effective.

ACKNOWLEDGEMENTS

The author would like to express his sincere gratitude to his research supervisor Professor A. Ghobarah for his guidance, support, encouragement, and helpful advice throughout the course of this research. Sincere appreciation is also expressed to the members of the supervisory committee Dr. D. Stolle and Dr. S. Ziada for their helpful discussions.

Special thanks and appreciation goes to all the faculty members, staff and colleagues at the department of civil engineering for their help at various occasions.

Dedicated to my parents, sister and brothers.

To my wife and sons.

TABLE OF CONTENTS

LIST OF FIGURES

LIST OF TABLES

LIST OF SYMBOLS

$\underline{a_f}$	displacement transformation matrix
A_b	area of steel bar
A_{c1} *to* A_{c5}	five effective concrete spring elements
A_e	effective sectional area = $0.8A_g$
A_g	gross area of the reinforced concrete section
A_s, A_s'	steel area in tension and compression
A_s, *to* A_{s4}	four effective steel spring elements
A_{sp}	area of transverse reinforcement for circular column
A_v	area of transverse reinforcement for rectangular column
b, t, d	width, total depth and the depth to tensile reinforcement of the R.C. section
c	the depth of the compression zone
C_c	compressive force in the compression zone of the section
C_s	compressive force in the compression steel bars
d_b	steel bar diameter
$d\underline{q}$	elastic beam deformation increments
$\underline{d_r}$	global displacement increment
$d\underline{S}$	forces or moment increments
$\underline{d_v}$	local element deformation increment
$d\underline{\widetilde{w}}_p$	plastic hinge deformation increments
D	overall section depth or diameter
D'	the distance between the centerlines of the hoop reinforcement on opposite sides of the section
E_c	elastic modulus of concrete
E_s	elastic modulus of steel
EA	effective axial rigidity
EI_y, EI_z	effective flexural rigidities
f	cracking surface function
$\underline{F_t}$	total flexibility matrix of the element

f_c' concrete cylinder compressive strength

f_{el} elastic beam flexibility matrix

f_p plastic hinge flexibility matrix

f_{sps} shear subhinge flexibility matrix

f_{spmi} flexure subhinges flexibility matrices

f_{ult} ultimate steel strength

f_y steel yield strength

f_{yh} yield strength of steel ties

FACMi and FACMj event factor for flexure subhinges at end I and J

FACS event factor for shear subhinge failure

g yielding surface function

GA' effective shear rigidity

GJ effective torsional rigidity

H_L the clear height of bar lugs

I, J, and K 3D element nodes

k_c coefficient of curvature

K_1, K_2, K_3 and K_4 original stiffnesses

K_{ii}, K_{ij}, K_{jj} flexural stiffness factors

$\underline{K}_{spm}$ diagonal plastic stiffness matrix

$\underline{K}_t$ element tangent stiffness

K_v shear stiffness per unit length of the element

l_{bar} embedded length of tensile bar in concrete

l_d development length

l_e length of the tensile bar elastically stressed

l_e' $l_e - l_{pl}$

l_{pl} length of the tensile bar plastically stressed

L length of the reinforced concrete column (from base to point of contraflexure)

L_p equivalent length of plastic hinge

M bending moment

M_1, M_2, *and* M_3 cracking, yield and ultimate moments

M_x, M_y, M_z current bending moments about X, Y and Z axes

M_{Cx}, M_{Cy} cracking moments about X and Y axes

M_{Yx}, M_{Yy} yield moments about X and Y axes

n modular ratio

P applied axial load on the column (=P_x)

P_o axial load capacity of the column (= $A_g f_c'$)

P_1, P_2, *and* P_3 cracking, yield and ultimate axial forces

q bond stress at elastic region

q_f frictional bond stress at plastic region

s spacing between ties or pitch of spiral ties

S_L the clear spacing of bar lugs

T tensile force in the tension steel bars

T_{ult} axial load tensile capacity

V_a shear strength carried by arch mechanism

V_c shear strength from concrete mechanism

V_{ci} initial shear strength from concrete mechanism

V_{cf} final shear strength from concrete mechanism

V_i initial (nominal) shear strength

V_f final (residual) shear strength

V_{fac} contraction factor for shear subhinge shear forces capacity

V_{FRP} shear strength from FRP mechanism

V_n nominal shear strength

V_p shear strength from axial force mechanism

V_s shear strength from steel mechanism

V_t shear strength carried by truss mechanism

V_{si} initial shear strength from steel mechanism

V_{sf} final shear strength from steel mechanism

YS1, YS2, and YS3 yield surfaces representing cracking, yield, and ultimate stage

q_1, q_2, q_3, δ_1, δ_2, δ_3 local bond stresses and corresponding slip

α 2/(M/VD) ≥ 1, M= moment, V= shear force, D= column diameter

β angle between column vertical axis and compression strut (≈30°)

δ_{ext}	bar displacement due to extension
δ_{slip}	bar displacement due to slip
δ_s	bar total displacement due to extension and slip
Δ_f	lateral deflection due to flexure
Δ_s	lateral deflection due to tensile bar bond-slip
Δ_{tot}	tip displacement corresponding to the total rotation
Δ_v	lateral deflection due to shear
ε_{cmax}	maximum compressive concrete strain
ε_{cr}	maximum tensile concrete strain
ε_{sh}	steel strain hardening
ε_u	ultimate steel strain
ε_y	steel yield strain
ϕ	section curvature
$\Phi(\underline{S}_m)$	yield function in the force-moment space
γ_v	rotation of the column due to shear
$\underline{\lambda}$	matrix of directional cosines for the local element coordinate system
μ	displacement ductility
μ_f	displacement ductility capacity if shear failure can be avoided
θ	rotation
θ_{strut}	the inclination of diagonal strut
θ_f	rotation of the column due to flexure
θ_{tot}	total rotation of the column
θ_s	rotation of the column due to bond-slip
ρ_v	vertical steel ratio
ρ_s	ratio of transverse steel volume to volume of concrete core

CHAPTER 1

INTRODUCTION AND LITERATURE SURVEY

1.1 INTRODUCTION

Reinforced concrete (RC) buildings designed to pre-1970's code provisions were found to be vulnerable to damage during earthquakes. Where current code regulations have reinforcement detailing requirements to ensure ductile behaviour, previous regulations were primarily strength based. It is not uncommon to find poor detailing, from a ductility point of view, in existing pre-1970's construction. The longitudinal and transverse reinforcement distribution and splicing details in beams, columns and beam-column joints, govern the ductility and control the failure mode in existing structures.

When ductile reinforced concrete frame structures are subjected to severe earthquake ground motion they are expected to deform well into the inelastic range and dissipate the seismic energy through large, but controllable, inelastic deformations at the critical regions. In frame structures, the multi-directional motion of an earthquake has a significant effect on the structural response. The columns, especially those at the building corners, are subjected to biaxial bending from combined longitudinal, transverse, and torsional motion of the structure. In addition, the columns are subjected to variable axial loads due to the structural response to lateral inertia forces as well as the vertical component of the ground motion. In order to predict the distribution of forces and

deformations in these structures under an earthquake ground motion, accurate models for the hysteretic behaviour of the different critical regions of the structure are necessary.

Planar models and analysis may oversimplify the complex multi-directional behaviour of the structure. In two-dimensional analysis it is assumed that it is sufficient to analyze the structure along its principal axes of resistance with horizontal ground motion acting in each direction at a time. In the analysis of irregular structures, there is a strong need for simple yet powerful spatial analytical models.

1.2 LITERATURE SURVEY

1.2.1 Theoretical models

Several analytical models for the non-linear analysis of reinforced concrete structural components have been proposed. These range from very refined and complex finite element models (Ngo and Scordelis, 1967) to simplified global models (Chen and Powell, 1982; Lai et al., 1984; Powell and Campbell, 1994; Petrangeli et al., 1999). Refined analytical models are typically used in predicting the response of small structures or structural subassemblies. Simplified global models have been typically used in the dynamic response analysis of large structures. Simple component global models may be unreliable and incapable of simulating the local behaviour of critical inelastic regions in the structure and may not yield accurate estimates of strain or curvature ductilities. On the other hand, the use of refined finite element models in non-linear static, cyclic and dynamic response of reinforced concrete frames is complex, time consuming and may not be practical.

The refined and detailed analysis of critical regions in the structure is impractical without the use of global models that predict the loading history of the particular region. Similarly, the global analysis of structures is unreliable without the use of more refined local models to estimate the parameters of the simple component models. A hybrid approach that uses the results of refined local (finite element) models suitable for detailed analysis of small regions and more simplified component (global) models suitable for global response analysis of multi-storey structures provides a powerful tool in the study of seismic response of reinforced concrete structures.

The major causes of deformation in reinforced concrete frame structures are axial/biaxial flexural deformations, shear deformations including shear sliding and bond-slip. The hysteretic load-deformation behaviour of frame members is a combination of these deformation mechanisms. A rational analysis of the hysteretic behaviour of reinforced concrete members needs to be based on the representation of all deformation components and on the interactions between the different mechanisms. This approach permits the determination of the relative contribution of each source of inelastic behaviour to the local and global response of reinforced concrete frames.

Global inelastic models for beams and columns can be categorized into three main categories, namely: Fibre (Filament) models, Multi-Spring models and Yield Surface (Section) models. In the following sections, each modeling approach will be discussed separately.

1.2.1.1 Fibre (Filament) models:

In the "fibre" type model (Powell and Campbell, 1994), the member cross section is divided into a number of small areas (fibres). Each area is assumed to be uniaxially stressed and to have behaviour governed by the hysteretic stress-strain characteristics of the material it simulates (steel or concrete). Figure 1.1 shows the discretization of a cross section incorporating two different fibre elements. In a fibre filament reinforced concrete element, the element has six degrees of freedom at each end. The element can have arbitrary cross section defined by special cross section shape matrix consisting of individual concrete and reinforcement fibres. Each concrete and steel fibre is considered to be subjected to a uniaxial state of stress. It is assumed that the displacements are small and plane section remains plane. Perfect bond between concrete and steel is assumed. Material constitutive models provide the resistance and tangent stiffness of the individual fibres. The non-linear nature of the element is derived from the fibre non-linear force-deformation relationship. Strength deterioration and stiffness degradation can be generated from the combination of concrete and steel longitudinal fibres whose behaviour is described by the uniaxial stress-strain characteristics of the steel and concrete materials.

Petrangeli at al. (1999) proposed a modification to a fibre model beam element to account for the shear behaviour. The element, which is based on the fibre section discretization, shares many features with the traditional fibre beam element. When the shear forces are negligible the element reduces to the traditional fibre element. The element basic concept was to model the shear mechanism for each concrete fibre,

assuming the strain field of the section as given by the superposition of the classical plane section hypothesis for the longitudinal strain field with an assigned distribution over the cross section for the shear strain field. Transverse strains are determined by imposing the equilibrium between the concrete and transverse steel reinforcement. The resulting model, although computationally more demanding than the traditional fibre element, was able to model shear sensitive RC elements with good efficiency (Petrangeli, 1999).

Although it was primarily intended to create an element which could capture the overall inelastic behaviour in addition to the localized plastic hinge deformation (bar pull-out and concrete crushing), the fibre model element is very sensitive to input data. The number of fibres in the cross section, and the number and location of the segments along the member length, in addition to the need to estimate the exact length and location of the expected plastic hinges, makes it difficult to predict the structure response without the need for tuning the different parameters. Another major disadvantage is that the required computational effort, which although may be less than that required for finite elements model, is still more than that for global models (Fischniger et al., 1999).

1.2.1.2 Multi-Spring models:

Lai et al. (1984) considered two inelastic elements at the two ends of an elastic member (figure 1.2.a). The region undergoing inelastic yielding is modeled by a set of springs representing concrete and reinforcing steel (figure 1.2.b). A yield surface is not required since the inelastic behaviour is controlled by the stress-strain properties of steel and concrete springs. The model is called a nine-spring model, and each element

comprises four effective steel spring elements (A_{s1}, A_{s2}, A_{s3}, and A_{s4}) and five effective concrete spring elements (A_{c1}, A_{c2}, A_{c3}, A_{c4}, and A_{c5}). The hysteretic behaviour of the springs is determined from concrete and steel hysteretic loops. Good correlation with biaxial cyclic loading experimental results has been reported by Li et al. (1988) using this model.

A refinement of Lai's model was provided by Saiidi et al. (1986) by considering four corner composite springs 1 to 4 as shown in figure 1.2c, instead of separating them into steel and concrete and one concrete spring 5 at the center of the member. Thus, the nine-spring model was reduced to a five-spring model. When the composite springs are subjected to tension, a steel member representing the longitudinal reinforcement will resist the force. A compression force on these springs, however, is resisted by the composite action of concrete and steel. Due to the difference between the tensile and compressive behaviour, the stress-strain curve for the composite springs is unsymmetrical.

Jiang and Saiidi (1990) further improved the model by using only four corner spring elements 1 to 4 as shown in figure 1.2d, and compared the results with biaxially loaded columns with constant or variable axial force. Compared with the five-spring model, the major advantage of this model is that only one type of spring is used, namely the composite spring. Even though the number of springs has been reduced, the comparison between analytical results and experimental data is still good and the computation is more efficient. It was shown that this model could simulate the stiffness degradation behaviour. Compared with the fibre model discussed above, the multispring

model is a simplified fibre model with more efficient computation. Shear effects in this model were ignored.

1.2.1.3 Yield Surface (Section) models:

In the "Section" type models, it is assumed that inelastic behaviour is defined for the cross section as a whole. The force-deformation relationship for the cross section is specified as a function of the cross section dimensions and the hysteretic force-deformation characteristics of the member material. An important advantage of this type of element is that it is controlled by only a few parameters (yield force, yield displacement, hardening parameter, unloading parameter) with clear physical meaning.

There are two basic approaches used in modeling the inelastic behaviour of a structural element using a "Section" model:

(a) Distributed Plasticity Approach

In this approach, it is assumed that yielding is distributed over the element length. The structural characteristics of the element are calculated by assuming a displaced shape for the element axis. From the resulting curvatures and axial strains, the internal forces are calculated at various sections. The element stiffness is then determined by integrating the curvature along the element. Mutli-dimensional action-deformation relationships must be specified for the cross sections, so that the effects of interaction between the various actions such as the bending moment, axial force, and shear force can be taken into account. These relationships will be in terms of action quantities, such as moment and axial force, and deformation quantities, such as curvature and axial strain.

The distributed plasticity approach tends to be preferable for structures in which the plastic zone locations are not known in advance.

(b) Lumped Plasticity (Plastic Hinge) Approach

Yield is assumed to take place only at generalized plastic hinges of zero length, and the structural member between hinges is assumed to remain linearly elastic. In this approach, multi-dimensional action-deformation relationships must be specified for the hinges, in terms of moment and axial force, as before, but related to deformations such as hinge rotations and axial extensions. Lumped plasticity models are particularly suitable for the analysis of building frames under seismic loads, since plastic behaviour in such structures is usually confined to small regions at the beam and column ends.

Several studies of the inelastic behaviour of frames under earthquake forces were conducted in the early seventies. Kannan and Powell (1973) and Otani and Sozen (1972) provided comprehensive surveys of early investigations of plane frames. The force-deformation or moment-rotation relationships assigned to a member can have a significant influence on the calculated response. As a result, non-linear analysis has concentrated on modeling stiffness changes in the members and the establishment of realistic hysteretic behaviour rules.

Hidalgo and Clough (1974) investigated a number of analytical models for the response prediction of a two-storey, single-bay frame, which they also tested on a shake table. Starting with a two-component elasto-plastic element, they attempted to improve the correlation between analysis results and experimental data by adding degradation effects to the model. One method of including degradation effects was to impose

empirical changes on the value of the elastic modulus at specified times during the excitation. A second technique was based on degradation of the generalized stiffness of the first mode of vibration of the structure. Although these techniques can provide accurate results for specific frames, they are not convenient for general purpose application.

Takeda et al. (1970) examined the experimental results from cyclic loading of a series of reinforced concrete connections, and proposed a hysteresis model that was in agreement with these results. Several investigators (Takizawa and Aoyama, 1976; and Otani et al., 1979) used this model, in both its original and modified forms.

Litton (1975) adopted a modified Takeda model for a reinforced concrete beam element for the DRAIN-2D computer program. This element consisted of an elastic beam element with inelastic rotational springs at each end. A similar type of element was suggested earlier by Otani and Sozen (1972). This element consisted of a bilinear beam element with an inelastic rotational spring and a rigid link at each end. Neither of these models considered biaxial interaction effects.

In 1976, Takizawa and Aoyama first introduced a biaxial trilinear degrading model, using plasticity theory. The model was developed based on a trilinear relationship between member end-moment M, and end-rotation θ. The M-θ relationship was derived from sectional analysis and characterized by crack and yield points. The crack and yield conditions were postulated to be ellipses in the moment space. In the biaxial moment space, there were two yield surfaces, one inner cracking surface and one outer yield surface. Fig 1.3 shows the yield surfaces in the stress space and the related trilinear

curves for uniaxial flexure in the principal directions X and Y. Two yield functions were established to check the state of generalized stress:

For the cracking surface,

$$f = \begin{bmatrix} M_x \\ M_y \end{bmatrix}^T \begin{bmatrix} \frac{1}{M_{Cx}^2} & 0 \\ 0 & \frac{1}{M_{Cy}^2} \end{bmatrix} \begin{bmatrix} M_x \\ M_y \end{bmatrix} \tag{1.1}$$

For the yield surface,

$$g = \begin{bmatrix} M_x \\ M_y \end{bmatrix}^T \begin{bmatrix} \frac{1}{M_{Yx}^2} & 0 \\ 0 & \frac{1}{M_{Yy}^2} \end{bmatrix} \begin{bmatrix} M_x \\ M_y \end{bmatrix} \tag{1.2}$$

where M_x, M_y = current bending moments about X and Y axes;
M_{Cx}, M_{Cy} = cracking moments about X and Y axes; and
M_{Yx}, M_{Yy} = yield moments about X and Y axes.

The following criteria of three-part plasticity were used for loading under biaxial flexure:

$f < 1$ elastic range

$f \geq 1$ and $g < 1$ cracked and unyielded range

$f \geq 1$ and $g \geq 1$ yielded range

Here, the elastic stiffness is modified once the cracking surface is reached, beyond which the cracking surface translates without changing shape. Upon reaching the yield surface, both cracking and yielding surfaces are allowed to expand along the direction of yielding. Ziegler's hardening rule was used for the translation of the crack surface and expansion for the crack and yield surfaces. Degradation was achieved by factoring the unloading stiffness using a degradation factor.

Riahi et al. (1979) described a 3-dimentional beam-column element and incorporated it into the ANSR computer program. The element was assumed to be made up of three parallel components, two elasto-plastic components to represent yielding and one elastic component to model strain hardening. Interaction for biaxial bending and axial force was considered, but the element did not have stiffness degrading characteristics.

Using experimental data, Takizawa and Aoyama (1976) as well as Chen and Powell (1982) verified the lumped plasticity analysis. The tests included uniaxial and biaxial bending. It was shown that the lumped plasticity model was able to capture the three-dimensional flexural behaviour of reinforced concrete columns. In addition to the lumped plasticity model, Chen and Powell checked the model of distributed plasticity against experimental results conducted by Zayas et al. (1980). Even though the overall response was similar, it was found that the analysis predicted substantially less stiffness and strength degradation.

In a recent study, Ricles et al. (1998) developed a new shear-flexural element for modeling the response of non-ductile reinforced concrete bridge columns subjected to biaxial seismic loading. The effect of column behaviour on the seismic response of bridges and the reliability of retrofitting were examined. In the element development, a conceptual model was adopted to accommodate the non-linear reinforced concrete behaviour. The biaxial flexural behaviour was simulated using member end moment-rotation relationships. A biaxial failure surface model was proposed for non-ductile shear

failure behaviour. The model was implemented in the ANSR-1 general-purpose program and verified using experimental data.

Abou-Elfath et al. (1998) developed a planar beam-column lumped plasticity model to represent the seismic response of non-ductile structures. The developed model accounted for the strength softening behaviour of non-ductile RC members. It also included the interaction between the axial force and the moment capacity of the RC members. The model was verified using the available experimental data as shown in figure 1.4. The analytical approach provided a practical and reliable tool to represent the behaviour of non-ductile RC buildings beyond their ultimate strength and up to failure.

1.2.2 EXPERIMENTAL STUDIES

1.2.2.1 Flexural behaviour

Numerous research projects were conducted to study the flexural characteristics of hysteresis loops of reinforced concrete members (Takizawa and Aoyama, 1976; Lai et al., 1984; and Wong et al., 1990). The flexural mechanism is a well-understood phenomenon, and current reinforced concrete design codes provide a satisfactory approach for design to ensure a ductile response under seismic loads.

1.2.2.2 Shear behaviour

The study of shear behaviour was traditionally concerned only with uniaxial loading. Experimental assessment of shear dominated behaviour of biaxially cyclically loaded short square reinforced concrete columns were conducted by Umehara and Jirsa

(1984), Maruyama et al. (1984), and Woodward and Jirsa (1984). The parameters studied in this project included loading history, axial load, and reinforcement content. The results showed that previous loading in either direction did not significantly affect the ultimate shear strength of the columns unless the maximum deflection of any previous loading exceeded the deflection corresponding to the ultimate shear strength of columns under monotonic loading. It was also shown that the diagonal unidirectional loading could be estimated using an interaction ellipse connecting the maximum capacities of the column under unidirectional loading along the principal axis.

More recent experimental work (Ghee et al., 1989) involved the seismic shear strength of 25 cantilever squat circular reinforced concrete columns. The main parameters studied were the aspect ratio (1.5, 1.75, 2 and 2.5), axial load ratio (0,0.1, 0.175, and 0.2), and transverse reinforcement amount. The response of columns were classified into four categories, 1) ductile flexural, 2) moderately ductile with shear failure, 3) limited ductility with shear failure, and 4) brittle shear failure. The tests showed that the shear strength was a function of displacement (flexural ductility), which was not accounted for by most design codes. A design model for shear strength degradation with increasing flexural ductility was suggested (figure 1.5). The initial shear strength V_i is assumed to apply for displacement ductility $\mu \leq 2$. At higher ductility, the shear strength degrades to a final value V_f at flexural displacement ductility capacity μ_f, which is defined as the displacement ductility capacity if the shear failure can be avoided.

$$V_i(kN) = V_{ci} + V_{si} = 0.37\alpha(1+\frac{3P}{f_c'})\sqrt{f_c'}(A_g) + \pi A_v f_{yh}\frac{D'}{2s} \tag{1.3}$$

where V_{ci} = Initial shear strength from concrete mechanism;

V_{si} = Initial shear strength from steel mechanism;

α = 2/(M/VD) ≥ 1, M= moment, V= shear force, D= column diameter;

P = axial load (kN);

f_c' = compressive strength of concrete (kPa);

A_g = gross sectional area (mm^2);

A_v = area of transverse reinforcement (mm^2);

f_{yh} = yield strength of transverse reinforcement (kPa);

s = spacing of spiral or hoop reinforcement (mm); and

D' = diameter of confined core (mm).

$$V_f(kN) = V_{cf} + V_{sf} = 18.5\rho_s\sqrt{f_c'}(0.8A_g) + \pi A_v f_{yh} D' \cot\theta_{strut} / 2s \quad (1.4)$$

where V_{cf} = Final shear strength from concrete mechanism;

V_{sf} = Final shear strength from steel mechanism;

ρ_s = Volumetric ratio of transverse reinforcement; and

θ_{strut} = The inclination of diagonal strut.

The value of θ_{strut} has a lower design limit of 25-degrees, which was the value suggested based on lower bound plasticity theory. If the shear force corresponding to development of the real flexural strength is less than V_f, as shown in figure 1.5 by line 1, then full flexural response is assured. Line 2 corresponds to the case when the shear corresponding to real flexural strength exceeds V_f but is less than V_i. The ductility μ_c achieved is defined by the intersection of line 2 with the shear strength degradation curve. Line 3 represents the case when shear force corresponding to real flexural strength exceeds V_i. In this case, a brittle failure will occur at $\mu < 2$. Tests were conducted on 8 single columns and 2 twin-column units subjected to shake-table testing under sinusoidal or simulated earthquake ground motion. It was reported that the single column response

was compatible with static test, while two twin-column units gave a more realistic simulation for the varying column axial load during an earthquake.

Saatcioglu and Ozcebec (1989) studied 14 square columns under bi-directional loading. The main parameters studied were axial load, transverse reinforcement, and bi-directional loading on column ductility. It was found that the ductility of columns was improved significantly with the use of proper confinement configuration. The level of damage in one direction adversely affected the column in the other direction.

Wong et al. (1990) tested 16 squat circular bridge columns with aspect ratio of 2 under multi-directional seismic loading. This study was a continuation of the testing program of Ghee et al. (1989). The parameters studied were axial compression load, spiral reinforcement content, and displacement patterns. The sensitivity of the strength and stiffness of shear resisting mechanisms to various displacement pattern and axial loads were investigated. It was concluded that compared with uniaxial loading, biaxial displacement led to more severe degradation of stiffness and strength. Wong et al. (1990) suggested a new design procedure for squat circular columns under multi-directional seismic demands. The new approach enabled the strength and the associated dependable displacement ductility to be determined, while also taking horizontal displacement history into account. Other observations confirmed the conclusions and recommendations of Ghee et al. (1989).

Watanabe and Ichinose (1991) proposed a design method for rectangular sections based on superposition of arch and truss actions using a lower bound plasticity approach. The method is based on limiting the diagonal compression stress resulting from the

combined arch and truss action. For ductile members, the permissible diagonal compressive stress is progressively reduced as the plastic rotation increases, thus indicating behaviour similar to that of figure 1.5. In this approach, the shear strength V_n is considered to be the sum of contributions from arch and truss mechanisms, illustrated in figure 1.6:

$$V_n = V_t + V_a \tag{1.6}$$

where the truss contribution V_t is given as

$$V_t = \frac{A_v f_y (jt)}{s} \cot\phi \tag{1.7}$$

and the arch contribution V_a is given by

$$V_a = b\frac{D}{2}(1-\beta)\nu_0 f_c' \tan\theta \tag{1.8}$$

where jt = the distance between upper and lower chords of the analogous truss, ϕ = the inclination of diagonal compression stress with member axis in truss mechanism ($\cot\phi$ decreases with the increase of inelastic plastic hinge rotation), θ = the inclination of diagonal compressive struts to column axis, and $\nu_0 f_c'$ = effective compressive strength of concrete (degrades with the increase of inelastic plastic hinge rotation).

The shear force V_a carried by arch action is based on an assumed compressive zone depth of half the member depth, as shown in figure 1.6. This approach has been adopted in the recommendation of the Architectural Institute of Japan (AIJ, 1988).

Priestley et al. (1994) studied shear retrofit of rectangular and circular reinforced concrete bridge columns by steel jacketing. A shear design equation was proposed:

$$V_n = V_c + V_s + V_p \tag{1.9}$$

where V_n = nominal shear strength;

V_c = shear strength from concrete mechanism;

V_s = shear strength from steel mechanism; and

V_p = shear strength from axial force mechanism.

In which

$$V_c = k\sqrt{f_c'}A_e \tag{1.10}$$

A_e is 0.8 of the section gross area for both circular and rectangular cross sections, and k is a factor that depends on displacement ductility and shear environment (figure 1.7). The shear carried by reinforcement in a rectangular column is:

$$V_s = \frac{A_v f_{yt} D'}{s}\cot\theta_{strut} \tag{1.11}$$

and for a circular column:

$$V_s = \frac{\pi}{2}\frac{A_{sp} f_{yh} D'}{s}\cot\theta \tag{1.12}$$

in which A_v = transverse reinforcement area for rectangular column;

A_{sp} = transverse reinforcement area for circular column;

f_{yh} = yield stress of transverse reinforcement;

D' = the distance between centre of hoop on opposite sides of the section;

s = spacing of transverse reinforcement; and

θ_{strut} = angle between column vertical axis and compression strut (30°)

The contribution of axial force to the shear resistance of an element is (figure 1.8):

$$V_p = \frac{k_c P(D-c)}{H} \tag{1.13}$$

where P = axial load;

k_c= 1 for double curvature and =0.5 for single curvature;

D= overall section depth or diameter;

c = the depth of the compression zone; and

H = the column height.

It was reported by Priestley et al. (1994) that the new proposed design equation reduces the conservatism inherent in previous shear design approaches, and provided excellent prediction of the shear strength of test columns.

Vecchio and Collins (1986) conducted experiments and theoretical work that yielded the "Modified compression-field theory". They tested 30 specimens to study the response of rectangular reinforced concrete elements subjected to in-plane shear and axial stresses. In their program, four specimens with nearly identical properties, were loaded at different ratios of shear stress to axial stress. Figure 1.9 shows the predicted cracking loads and the predicted failure loads using the modified compression-field theory. On the same figure, the observed cracking loads (hollow circles) and the observed failure loads (solid circles) for the four tested specimens are plotted. The predicted loads are shown to be in good agreement with the observed ones.

The behaviour shown in figure 1.9 indicates that there are three rather distinct regions in the shear strength-axial strength interaction diagram: 1) at high biaxial tension, yielding of the reinforcement at the cracks control failure; 2) concrete shear failure governs in the middle region, with concrete failing at compressive stresses considerably less than f_c'; and 3) at high biaxial compression levels, failure is controlled by f_{c2} reaching f_c'.

1.2.3 SUMMARY

Most biaxial test results (Takizawa and Aoyama, 1976; Otani et al., 1979) were limited to constant axial load and to imposed deflection paths that followed diagonal,

square, clover leaf, circular, or elliptical patterns. Few researchers conducted tests studying the variation of axial load effect on columns under uniaxial bending (Abrams, 1987) and biaxial bending (Bousias et al., 1995; and Saatcioglu and Ozcebe, 1989). Inspite of the importance of the effect of axial load variation on columns during an actual earthquake on the response and failure of the columns, the attempts to evaluate this effect analytically were rare. Perdomo et al. (1999) developed a finite element model that takes the variation of axial load into account and implemented the developed model in a commercial finite element program. No other models that use lumped plasticity global models and take the variation of axial load in the general three-dimensional deformation were reported in the literature.

1.3 OBJECTIVES

The main objectives of this research program are to analytically and experimentally evaluate the behaviour of non-ductile reinforced concrete columns under lateral cyclic deformations.

1.4 SCOPE

In order to achieve the study objectives, the scope of research is as follows:

1- Develop a bond-slip model that can be used in analyzing RC structures.

2- Develop an analytical procedure that uses the basic geometrical properties of beam-column elements and material properties of confined concrete and reinforcing steel

with the developed bond-slip model to obtain the moment-rotation and force-displacement relationships of beam-column elements to be used as input data for the three-dimensional element.

3- Examine the validity of the proposed procedure by comparing its results to the available experimental data.

4- Develop a three-dimensional lumped plasticity model to account for the combined interaction effects for flexure, variable axial load and shear in a beam-column element.

5- Validate the proposed model using available experimental data for reinforced concrete columns.

6- Conduct a testing program on three fixed-fixed reinforced concrete short column specimens to study the effect of confinement on their response when subjected to cyclic lateral excitation.

7- Experimentally compare the efficiency of two rehabilitation techniques for the tested columns using carbon-fibre-reinforced-polymer (CFRP).

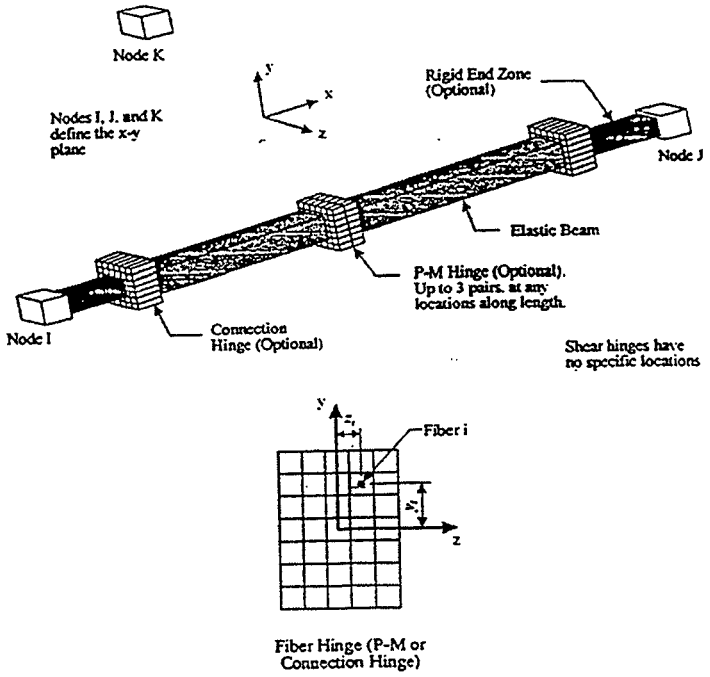

Element No. 08 (Powell and Campbell, 1994)

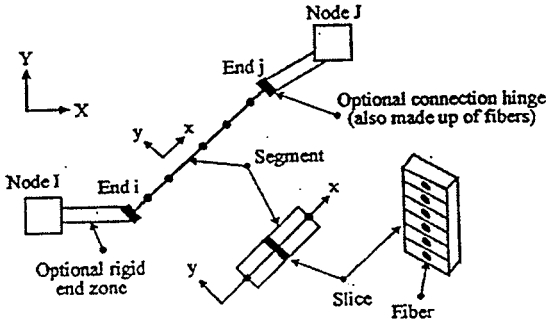

Element No. 15 (Powell and Campbell, 1994)

Figure 1.1 Fibre models

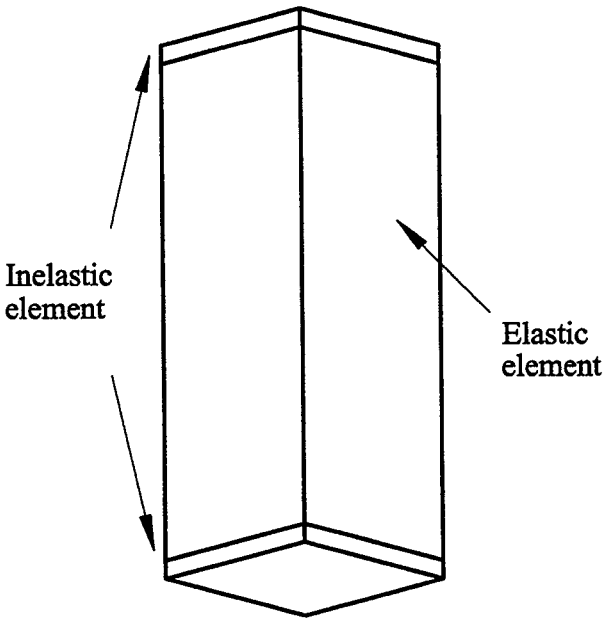

a) Member model

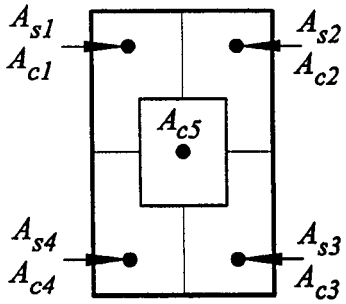

b) Nine-spring model
Lai et al. (1984)

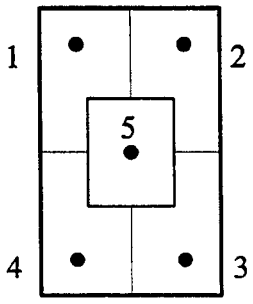

c) Five-spring model
Saiidi et al. (1986)

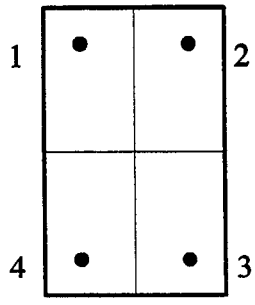

d) Four-spring model
Jiang and Saiidi (1990)

Figure 1.2 Multi-spring models

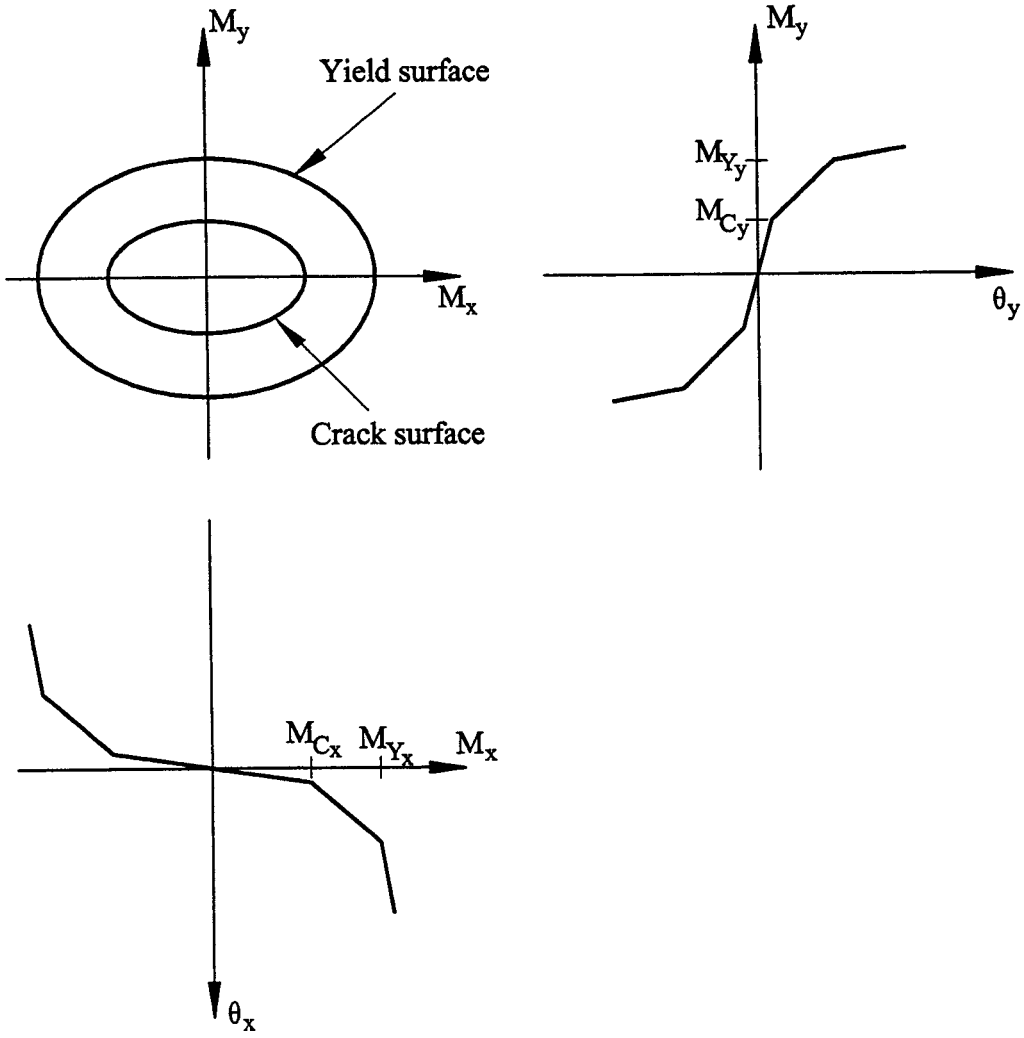

Figure 1.3 Skeleton curves and yield surfaces for yield surface models

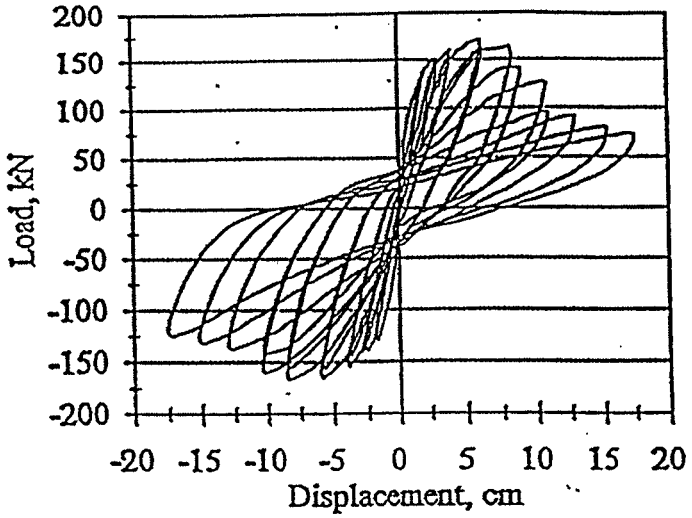

(a) Experimental-specimen 1 (Ghobarah et al., 1997)

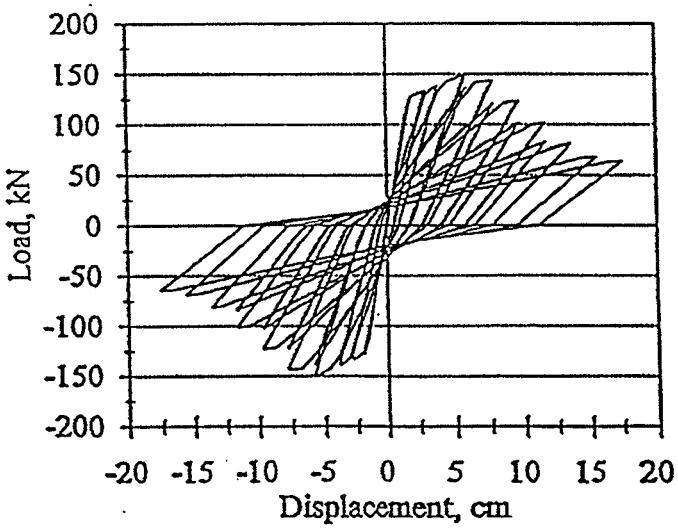

(b) Proposed model (Abou Elfath et al., 1998)

Figure 1.4 Analysis and test data of axially loaded reinforced concrete column subjected to lateral cyclic load

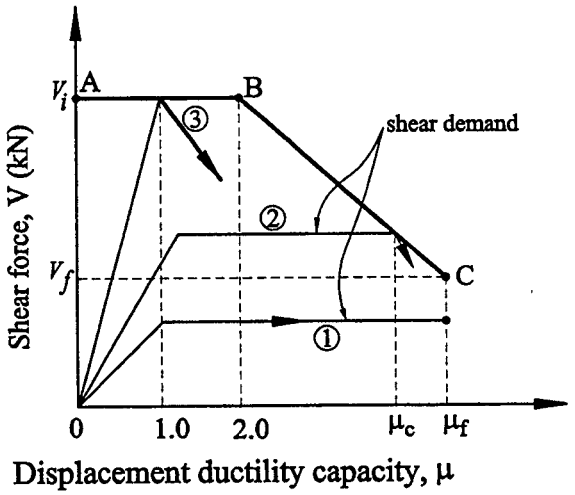

Figure 1.5 Relationship between shear strength and displacement ductility capacity (Ghee et al., 1989)

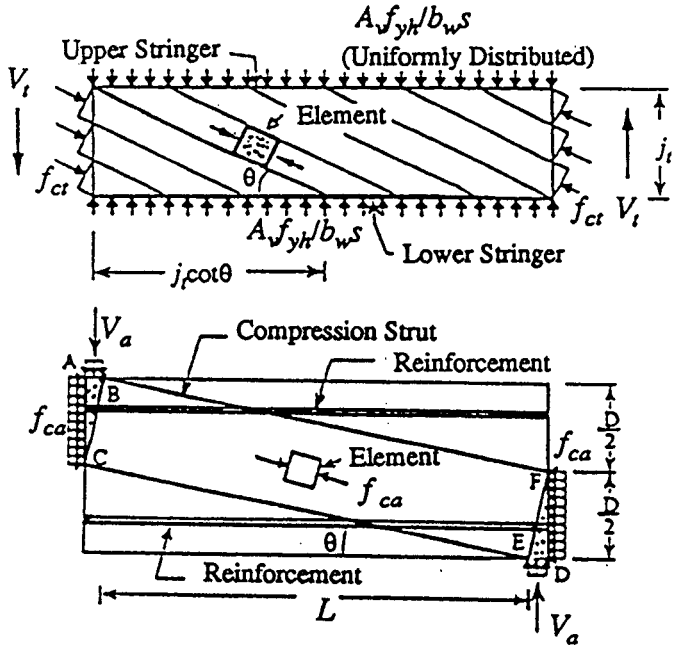

Figure 1.6 Analogous models in Watanabe and Ichinose (1991) approach; (a) Truss; and (b) Arch

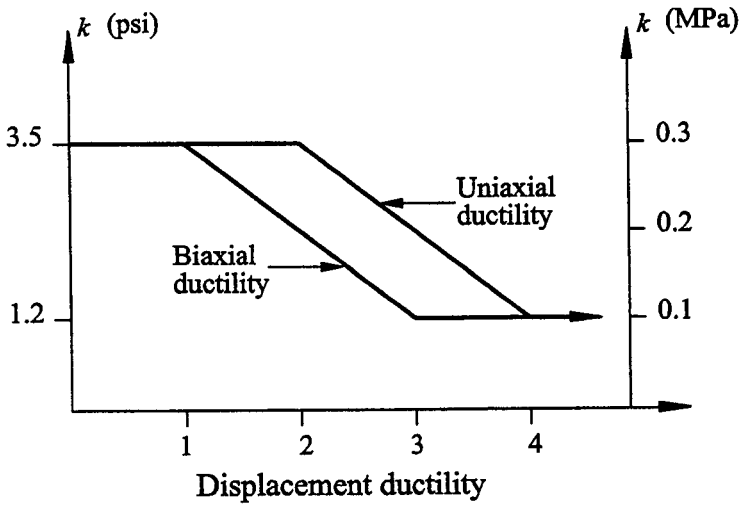

Figure 1.7 Degradation of concrete shear strength with ductility (Priestley et al., 1994)

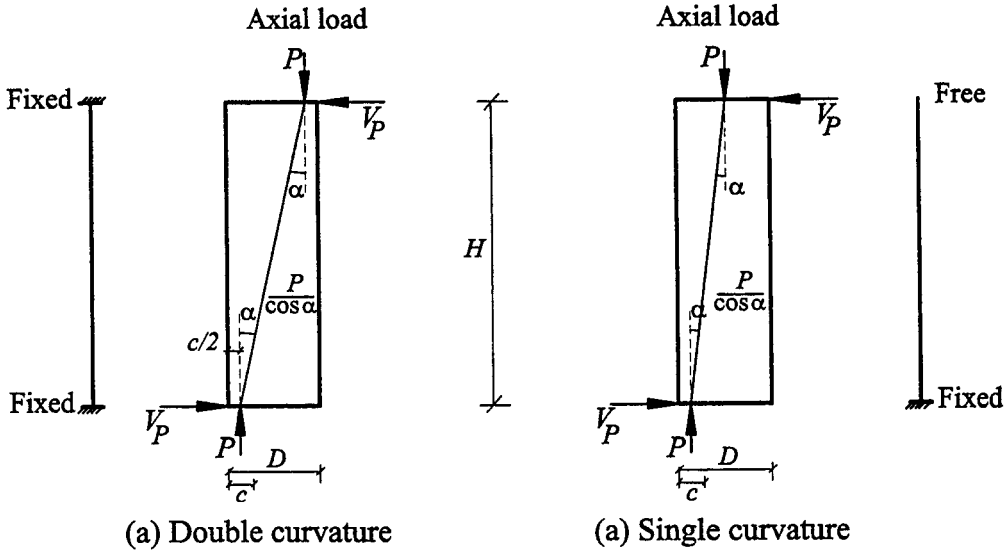

Figure 1.8 Contribution of axial force to column shear strength (Priestley et al., 1994)

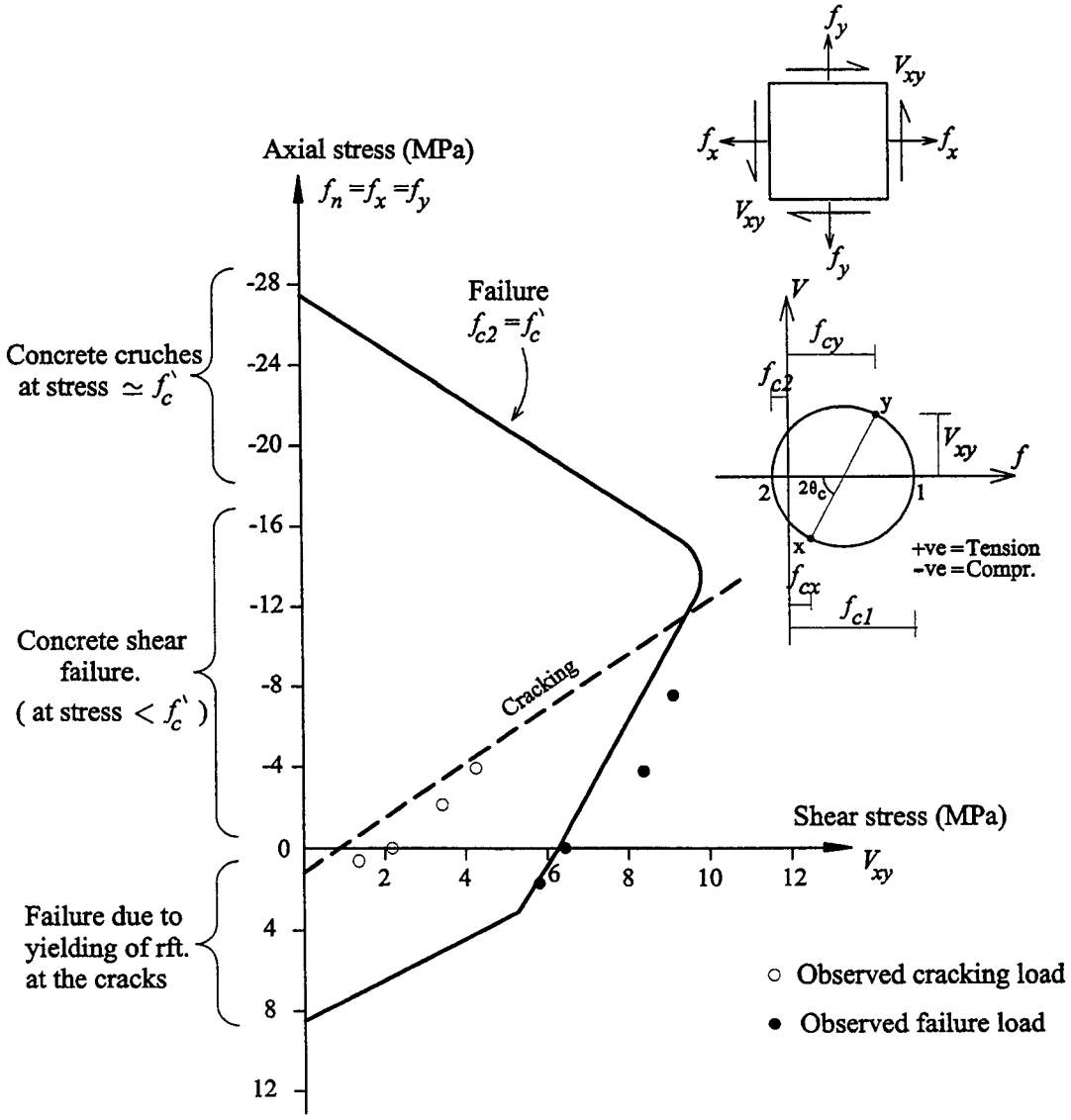

Figure 1.9 Shear strength-axial strength interaction diagram
(Vecchio and Collins, 1986)

CHAPTER 2

3D BEAM-COLUMN ELEMENT WITH FLEXURAL AND SHEAR FAILURE CRITERIA

2.1 GENERAL

Reinforced concrete members, especially those of non-ductile frames, have experienced both flexural and shear failures during recent earthquakes. Post-earthquake observations indicated that a brittle shear mode of failure might have been the cause of total collapse. During earthquakes, structures are subjected to lateral loads that impose biaxial flexural and shear forces on the columns. Analysis of such columns requires taking into consideration the effects of biaxial loading on the yielding, capacity, inelastic deformation, and degradation of strength and stiffness of the member in order to achieve realistic predictions of the seismic response of framed structures. Therefore, both shear and flexural effects must be included in the analysis of non-ductile frames, and in cases where shear failures are possible.

Shear is resisted primarily by concrete before cracking. After the shear cracks develop, the components of shear resistance are aggregate interlock, transverse reinforcement and dowel shear forces across the longitudinal reinforcement. The mathematical modeling of the member's behaviour after the initiation of the shear crack remains a challenging problem. While numerous analytical and experimental studies have been conducted on the flexural behaviour of reinforced concrete members under seismic loading, few studies have addressed the shear mode of failure of reinforced concrete structural members under seismic excitation.

The model developed in this chapter is based on the biaxial flexural model of Takizawa and Aoyama (1976) and Chen and Powell (1982) with improvements. The element is intended to model inelastic effects in reinforced concrete beams and columns under general cyclic loading. Particular emphasis is placed on accounting for axial force-biaxial bending moment interaction and torsional moment-biaxial shear force interaction, with shear strength degradation. The improvements involve accounting for the biaxial shear failure, post shear failure and shear pinching response and its interaction with axial load as well as the variation in axial load.

2.2 ELEMENT DESCRIPTION

The three-dimensional beam-column element is formulated to model inelastic hysteretic behaviour of reinforced concrete beams and columns, with particular emphasis on axial force-biaxial moment interaction, stiffness degradation under cyclic loading, shear failure and post shear failure response.

In the three dimensional space, the element may be arbitrarily oriented in a global *XYZ* coordinate system (figure 2.1), where the nodes *I*, *J*, and *K* define the element position and the local *xyz* coordinate. Nodes *I* and *J* define the x-axis, whereas node *K* together with nodes *I* and *J* define the local x-y plane. The element is selected to be straight. Eccentric end connections and slaving may be specified to model rigid joint regions and rigid diaphragms, respectively, as will be explained in the next section. Initial elastic flexural, torsional, axial and shear stiffnesses must be specified. The inelastic behaviour is assumed to be concentrated in the plastic hinge regions at each end of the

element (figure 2.2). For the case of constant torsion and axial loads, torsional and axial deformations are assumed to remain elastic throughout the analysis; however, interaction between different forces and moments is taken into consideration. For variable torsional moment and axial loads, the current level of these loads will continuously affect the plastic deformation. Each hinge is assigned an individual yield strength. The hinges are assumed to have elastic-plastic strain hardening characteristics when subjected to biaxial flexure, and strength degradation in shear. A set of three yield surfaces exists for bending moments, with one failure surface defined for shear. The flexural yield surfaces and shear failure surface are assumed to be independent, and the bending moment and shear force resultant are coupled only through equilibrium.

Each hinge is considered to have three subhinges for flexure, and one subhinge for shear (figure 2.3). Each subhinge has a rigid-plastic force-deformation response. Consequently, the axial and flexure force (P, M) - deformation (δ, θ) relationship is quadri-linear where M_i and P_i are the capacities for each subhinge (figure 2.4). Post-yield behaviour of the hinge follows kinematic hardening and stiffness degradation in flexure. The yield surface properties of each subhinge, in terms of flexural strength, elastic and post elastic stiffness, can be determined from moment curvature analysis for each principal axis. This relationship takes into consideration the bond-slip, as will be explained in Chapter 3.

The behaviour of the shear subhinge is based on the assumption that before the concrete cracks the subhinge remains rigid, where the shear resistance is provided by concrete. After the concrete develops shear cracks and reaches the member shear

capacity, the subhinge develops plastic shear deformations. Consequently, with further imposed deformation, the shear strength decreases and finally reaches the residual capacity provided by reinforcement alone. Upon load reversal, the shear subhinge unloads with a reduced pinching stiffness until the shear cracks are closed. When this is achieved, the subhinge becomes rigid until the shear capacity is reached in the opposite direction. The cyclic hysteretic envelope for the shear subhinge is shown in figure 2.5.

2.3 DEGREES OF FREEDOM

The element has two external nodes, *I* and *J*, as shown in figure 2.2. Each node has six degrees of freedom (DOF), namely three translations and three rotations along the global *XYZ* axes (figure 2.6). In the local element coordinate system, there exist six deformation degrees of freedom, as shown in figure 2.7. The transformation from global displacements to local deformations is determined by

$$d\underline{v} = \underline{a}_f \cdot d\underline{r} \tag{2.1}$$

where $\underline{a}_f$ = displacement transformation matrix;

$d\underline{r}$ = global displacement increment ; and

$d\underline{v}$ = local element deformation increment.

The element deformations include elastic beam deformations and plastic hinge deformations, hence

$$d\underline{v} = d\underline{q} + d\underline{\tilde{w}}_p \tag{2.2}$$

where $d\underline{q}$ = elastic beam deformation increments; and

$d\underline{\tilde{w}}_p$ = plastic hinge deformation increments.

The displacement transformation matrix $\underline{a_f}$ is determined from the coordinate transformation, end eccentricity, rigid diaphragm slaving, and deformation transformation. The following shows how to properly account for these properties.

2.3.1 Coordinate transformation

Figure 2.1 shows the global and local coordinate system for the element. The unit vector along the x-axis (longitudinal axis of member) is:

$$\bar{i} = \frac{1}{L}[(X_J - X_I),(Y_J - Y_I),(Z_J - Z_I)] \tag{2.3}$$

where L is the length of the element and X_I, Y_I, and Z_I are the global coordinates of node I, with X_J, Y_J, and Z_J are the global coordinates of node J. The I, J, and K nodes define the x-y plane for the local coordinate system. The relationship between the global and local coordinates can then be written as:

$$\begin{Bmatrix} x \\ y \\ z \end{Bmatrix} = [\underline{\lambda}] \begin{Bmatrix} X \\ Y \\ Z \end{Bmatrix} \tag{2.4}$$

where $\underline{\lambda}$ is a matrix of directional cosines for the local element coordinate system.

2.3.2 End eccentricity

Plastic hinges in frames and coupled frame-shear wall structures will form near the faces of the joints rather than at the theoretical joint centerlines. This effect can be approximated by postulating rigid, infinitely strong connecting links between the nodes and the element ends. Thus rigid offsets at the ends of the element are used to model the

effects of joint size, as shown in figure 2.8. The displacements at the ends of the element can be determined from nodal displacements, by considering the rigid offset to be an eccentricity, where:

$$d\underline{r}_u = \underline{a}_e \cdot d\underline{r} \tag{2.5}$$

in which $d\underline{r}$ are the global nodal displacements, $d\underline{r}_u$ are the element's end displacements in the global coordinate system, and $\underline{a}_e$ is the transformation matrix related to the end eccentricity. The transformation matrix $\underline{a}_e$ is defined as:

$$\underline{a}_e = \begin{bmatrix} 1 & 0 & 0 & 0 & e_5 & -e_3 & 0 & 0 & 0 & 0 & 0 & 0 \\ 0 & 1 & 0 & -e_5 & 0 & e_1 & 0 & 0 & 0 & 0 & 0 & 0 \\ 0 & 0 & 1 & e_3 & -e_1 & 0 & 0 & 0 & 0 & 0 & 0 & 0 \\ 0 & 0 & 0 & 1 & 0 & 0 & 0 & 0 & 0 & 0 & 0 & 0 \\ 0 & 0 & 0 & 0 & 1 & 0 & 0 & 0 & 0 & 0 & 0 & 0 \\ 0 & 0 & 0 & 0 & 0 & 1 & 0 & 0 & 0 & 0 & 0 & 0 \\ 0 & 0 & 0 & 0 & 0 & 0 & 1 & 0 & 0 & 0 & e_6 & -e_4 \\ 0 & 0 & 0 & 0 & 0 & 0 & 0 & 1 & 0 & -e_6 & 0 & e_2 \\ 0 & 0 & 0 & 0 & 0 & 0 & 0 & 0 & 1 & e_4 & -e_2 & 0 \\ 0 & 0 & 0 & 0 & 0 & 0 & 0 & 0 & 0 & 1 & 0 & 0 \\ 0 & 0 & 0 & 0 & 0 & 0 & 0 & 0 & 0 & 0 & 1 & 0 \\ 0 & 0 & 0 & 0 & 0 & 0 & 0 & 0 & 0 & 0 & 0 & 1 \end{bmatrix} \tag{2.6}$$

where e_1, e_3, e_5 = end eccentricity at node *I* in *X*, *Y*, and *Z* directions, respectively; and

e_2, e_4, e_6 = end eccentricity at node *J* in *X*, *Y*, and *Z* directions, respectively.

It's worth mentioning that the rigid joint assumption precludes consideration of joint shear failure in the model.

2.3.3 Rigid floor diaphragms

A frequently made assumption in the analysis of tall buildings is that each floor diaphragm is rigid in its own plane. To introduce this assumption, a master node at the

center of mass of each floor may be specified, as shown in figure 2.9. Each master node has only three degrees of freedom as shown, which are the displacements of the diaphragm horizontally as a rigid body. If any beam-column member is connected to these *master* displacements, its behaviour depends partly on these displacements and partly on the displacements that are not affected by the rigid diaphragm assumption. The displacement transformation relating the master (diaphragm) displacements, dr_m, to the displacement at a *slaved* node, dr_s, is as follows:

$$\begin{Bmatrix} dr_{s1} \\ dr_{s2} \\ dr_{s3} \\ dr_{s4} \\ dr_{s5} \\ dr_{s6} \end{Bmatrix} = \begin{bmatrix} 1 & 0 & 0 & 0 & dz & 0 \\ 0 & 1 & 0 & 0 & 0 & 0 \\ 0 & 0 & 1 & 0 & -dx & 0 \\ 0 & 0 & 0 & 1 & 0 & 0 \\ 0 & 0 & 0 & 0 & 1 & 0 \\ 0 & 0 & 0 & 0 & 0 & 1 \end{bmatrix} \begin{Bmatrix} dr_{mx} \\ dr_{sy} \\ dr_{mz} \\ d\theta_{sx} \\ d\theta_{my} \\ d\theta_{sz} \end{Bmatrix} \tag{2.7}$$

i.e., $\underline{dr}_s = \underline{a}_s \cdot \underline{dr}_m$

where $\underline{dr}_s$ = slaved displacement increment of slaved node;

$\underline{dr}_m$ = master nodal displacement increment (see figure 2.9);

$\underline{a}_s$ = master-slave displacement deformation matrix;

dr_{mx}, dr_{mz}, $d\theta_{my}$ = master nodal displacement increment; and

dr_{sy}, $d\theta_{sx}$, $d\theta_{sz}$ = independent displacements of slaved node.

2.3.4 Deformation transformation

The relationship between the element end displacements in the local coordinate system (figure 2.10) to the element deformations shown in figure 2.7 is:

$$\begin{Bmatrix} dv_1 \\ dv_2 \\ dv_3 \\ dv_4 \\ dv_5 \\ dv_6 \end{Bmatrix} = \begin{bmatrix} 0 & 0 & -1/L & 0 & 1 & 0 & 0 & 0 & 1/L & 0 & 0 & 0 \\ 0 & 0 & -1/L & 0 & 0 & 0 & 0 & 0 & 1/L & 1 & 1 & 0 \\ 0 & 1/L & 0 & 0 & 0 & 1 & 0 & -1/L & 0 & 0 & 0 & 0 \\ 0 & 1/L & 0 & 0 & 0 & 0 & 0 & -1/L & 0 & 0 & 0 & 1 \\ 0 & 0 & 0 & -1 & 0 & 0 & 0 & 0 & 1 & 0 & 0 & 0 \\ -1 & 0 & 0 & 0 & 0 & 0 & 1 & 0 & 0 & 0 & 0 & 0 \end{bmatrix} \begin{Bmatrix} dr_1 \\ dr_2 \\ dr_3 \\ dr_4 \\ dr_5 \\ dr_6 \\ dr_7 \\ dr_8 \\ dr_9 \\ dr_{10} \\ dr_{11} \\ dr_{12} \end{Bmatrix} \tag{2.8}$$

i.e. $\underline{dv} = \underline{a}_d \cdot \underline{dr}^*$

where $\underline{dv}$ = element deformation;

$\underline{dr}^*$ = element end displacements in local coordinates; and

$\underline{a}_d$ = deformation transformation matrix.

2.3.5 Total displacement transformation matrix

Thus, it can be shown that the transformation matrix $\underline{a}_f$ is the matrix product of the transformations described above, where

$$\underline{a}_f = \underline{a}_d \cdot \underline{T} \cdot \underline{a}_e \cdot \underline{A}_s \tag{2.9}$$

with

$$\underline{T}_{6\times 6} = \begin{bmatrix} \underline{\lambda} & \underline{0} & \underline{0} & \underline{0} \\ \underline{0} & \underline{\lambda} & \underline{0} & \underline{0} \\ \underline{0} & \underline{0} & \underline{\lambda} & \underline{0} \\ \underline{0} & \underline{0} & \underline{0} & \underline{\lambda} \end{bmatrix} \tag{2.10a}$$

and

$$A_s = \begin{bmatrix} \underline{a}_s^I & \underline{0} \\ \underline{0} & \underline{a}_s^J \end{bmatrix} \tag{2.10b}$$

The master-slaved displacement transformation matrices $\underline{a}_s^I, \underline{a}_s^J$ correspond to nodes I and J, respectively.

2.4 ELEMENT STIFFNESS

The element stiffness includes the contribution of the elastic beam and the two end hinges where the plastic behaviour of the element is concentrated. Before the element develops plastic deformations, the hinges are assumed to be infinitely rigid, and the stiffness of the element consists of only the elastic beam stiffness. After the hinge yields, the element flexibility will be the summation of the elastic beam's flexibility and plastic hinges' flexibility. The element stiffness is obtained from the inverse of the element flexibility.

2.4.1 Elastic beam flexibility

The local y and z axes are assumed to be the principal axes of the element cross section, with the local x-axis assumed to correspond to the centroidal axis and the axis of torsional twist.

The beam-column element stiffness relationships can be written as follows:

$$\begin{Bmatrix} dM_{yi} \\ dM_{yj} \end{Bmatrix} = \frac{EI_y}{L} \begin{bmatrix} K_{iiy} & K_{ijy} \\ K_{ijy} & K_{jjy} \end{bmatrix} \begin{Bmatrix} dw_1 \\ dw_2 \end{Bmatrix} \tag{2.11a}$$

$$\begin{Bmatrix} dM_{zi} \\ dM_{zj} \end{Bmatrix} = \frac{EI_z}{L} \begin{bmatrix} K_{iiz} & K_{ijz} \\ K_{ijz} & K_{jjz} \end{bmatrix} \begin{Bmatrix} dw_3 \\ dw_4 \end{Bmatrix} \tag{2.11b}$$

$$dM_x = \frac{GJ}{L} dw_5 \tag{2.11c}$$

$$dP_x = \frac{EA}{L} dw_6 \tag{2.11d}$$

in which

K_{ii}, K_{ij}, K_{jj} = flexural stiffness factors;

EI_y, EI_z = effective flexural rigidities;

M_y, M_z = bending moments;

$\underline{w}^T=[w_1,w_2,..,w_6]$ = vector of degrees of freedom for the elastic element;

I, J = element ends;

M_x = torsional moment;

P_x = axial force;

L = element length;

EA = effective axial rigidity; and,

GJ = effective torsional rigidity.

Flexural stiffness factors can be used to account for non-uniform elements. For a uniform element, $K_{ii} = K_{jj} = 4.0$ and $K_{ij} = 2.0$.

The shear flexibility of the elastic beam is taken into account, where

$$\underline{f}_s = \frac{1}{GA'L}\begin{bmatrix} 1 & 1 \\ 1 & 1 \end{bmatrix} \tag{2.12}$$

in which GA' is the effective shear rigidity. Combining the six components of forces, moments and deformations including the transverse shear effects, results in:

$$d\underline{q} = \underline{f}_{el} \cdot d\underline{S} \tag{2.13}$$

where $d\underline{S}$ = forces or moment increments;

$d\underline{q}$ = elastic beam deformation increments

and $\underline{f}_{el}$ is the elastic beam flexibility matrix, defined as:

$$\underline{f}_{el} = \begin{bmatrix} \frac{L}{EI_y}F_{iiy} + \frac{1}{GA'_yL} & -\frac{L}{EI_y}F_{ijy} + \frac{1}{GA'_yL} & 0 & 0 & 0 & 0 \\ -\frac{L}{EI_y}F_{ijy} + \frac{1}{GA'_yL} & \frac{L}{EI_y}F_{jjy} + \frac{1}{GA'_yL} & 0 & 0 & 0 & 0 \\ 0 & 0 & \frac{L}{EI_z}F_{iiz} + \frac{1}{GA'_zL} & -\frac{L}{EI_z}F_{ijz} + \frac{1}{GA'_zL} & 0 & 0 \\ 0 & 0 & -\frac{L}{EI_z}F_{ijz} + \frac{1}{GA'_zL} & \frac{L}{EI_z}F_{jjz} + \frac{1}{GA'_zL} & 0 & 0 \\ 0 & 0 & 0 & 0 & \frac{L}{GJ} & 0 \\ 0 & 0 & 0 & 0 & 0 & \frac{L}{EA} \end{bmatrix} \tag{2.14}$$

2.4.2 Plastic hinge flexibility

The plastic deformation increment of a hinge is the sum of the deformations of its yielded subhinges. i.e.,

$$d\underline{\tilde{w}}_p = \sum d\underline{\tilde{w}}_{spi} \tag{2.15}$$

where $d\underline{\tilde{w}}_{spi}$ is the plastic deformation increment of subhinge i. On the other hand, the force increment dS in a hinge, consisting of two bending moments, two shear forces, torsion, and axial force is given by

$$d\underline{S}^T = [\, dM_y \;\; dM_z \;\; dV_y \;\; dV_z \;\; dM_x \;\; dF_x \,] \tag{2.16}$$

with dV_y and dV_z representing the shear force increments acting along the y- and z- axes, respectively.

For the case of constant axial and torsional loads, dM_x and dF_x are zero. While for the case of variable axial and torsional loads, appropriate values for dM_x and dF_x are calculated to maintain an equilibrium state as explained in section 2.7. The plastic

deformation in each subhinge is therefore due to flexural and torsional moments; and axial and shear forces. The plastic hinge flexibility relationship is thus:

$$d\underline{\tilde{w}}_p = \underline{\tilde{f}}_p \cdot d\underline{S} = \sum \underline{f}_{spi} \cdot d\underline{S} \tag{2.17}$$

where $\underline{\tilde{f}}_p$ = plastic hinge flexibility matrix; and

$\underline{f}_{spi}$ = subhinge i plastic flexibility

For the hinge at node *I*, the plastic deformation increment is:

$$d\underline{\tilde{w}}_P^I = \begin{Bmatrix} d\theta_y^I \\ d\theta_z^I \\ d\gamma_y^I \\ d\gamma_z^I \\ d\psi_x^I \\ d\delta_x^I \end{Bmatrix} = \underline{\tilde{f}}_P^I \begin{Bmatrix} dM_y^I \\ dM_z^I \\ dV_y^I \\ dV_z^I \\ dM_x^I \\ dF_x^I \end{Bmatrix} = \underline{\tilde{f}}_P^I \begin{Bmatrix} dM_y^I \\ dM_z^I \\ (dM_z^I + dM_z^J)/L \\ (dM_y^I + dM_y^J)/L \\ dM_x^I \\ dF_x^I \end{Bmatrix} \tag{2.18a}$$

whereas for hinge at node *J*: the plastic deformation increment is:

$$d\underline{\tilde{w}}_P^J = \begin{Bmatrix} d\theta_y^J \\ d\theta_z^J \\ d\gamma_y^J \\ d\gamma_z^J \\ d\psi_x^J \\ d\delta_x^J \end{Bmatrix} = \underline{\tilde{f}}_P^J \begin{Bmatrix} dM_y^J \\ dM_z^J \\ dV_y^J \\ dV_z^J \\ dM_x^J \\ dF_x^J \end{Bmatrix} = \underline{\tilde{f}}_P^J \begin{Bmatrix} dM_y^J \\ dM_z^J \\ (dM_z^I + dM_z^J)/L \\ (dM_y^I + dM_y^J)/L \\ dM_x^J \\ dF_x^J \end{Bmatrix} \tag{2.18b}$$

where *I, J* identify the node;

$d\theta$ = incremental rotation due to flexural deformation;

$d\gamma$ = incremental rotation due to shear deformation;

$d\psi$ = incremental twist rotation due to torque; and

$d\delta$ = incremental extension due to axial force.

The total hinge deformation increment is the sum of its flexural rotational $d\theta$ and shear deformations $d\gamma$ in each direction;

i.e. at node I $$d\varphi_y^I = d\theta_y^I + d\gamma_y^I \tag{2.19a}$$

$$d\varphi_z^I = d\theta_z^I + d\gamma_z^I \tag{2.19b}$$

and at node J $$d\varphi_y^J = d\theta_y^J + d\gamma_y^J \tag{2.20a}$$

$$d\varphi_z^J = d\theta_z^J + d\gamma_z^J \tag{2.20b}$$

Expressing the plastic deformation increments in terms of local deformation degrees-of-freedom of the elastic beam and the external nodes, the incremental plastic force-deformation relationship at node I is:

$$d\underline{w}_P^I = \begin{Bmatrix} dv_1 - dq_1 \\ dv_3 - dq_3 \\ dv_5 - dq_5 \\ dv_6 - dq_6 \end{Bmatrix} = \underline{f}_P^I \begin{Bmatrix} dM_y^I \\ dM_z^I \\ dM_y^J \\ dM_z^J \\ dM_x^I \\ dF_x^I \end{Bmatrix} \tag{2.21a}$$

and at node *J*:

$$d\underline{w}_P^J = \begin{Bmatrix} dv_2 - dq_2 \\ dv_4 - dq_4 \\ dv_5 - dq_5 \\ dv_6 - dq_6 \end{Bmatrix} = \underline{f}_P^J \begin{Bmatrix} dM_y^I \\ dM_z^I \\ dM_y^J \\ dM_z^J \\ dM_x^J \\ dF_x^J \end{Bmatrix} \tag{2.21b}$$

The matrices $\underline{f}_P^I$ and $\underline{f}_P^J$ are 4x6 matrices, which represent coefficients of hinge flexibility matrices $\underline{\tilde{f}}_P^I$ and $\underline{\tilde{f}}_P^J$. These plastic hinge flexibility matrices can be simply added to the appropriate coefficients of the elastic beam flexibility matrix, to obtain the element's complete flexibility matrix.

2.4.2.1 Flexural subhinge flexibility

Let us now consider the flexural behaviour of a subhinge. The incremental force-deformation relationship can be written as:

$$d\underline{w}_{spm} = \underline{f}_{spm} \cdot d\underline{S}_m \tag{2.22}$$

where $d\underline{w}_{spm}$ = subhinge flexural, torsional and axial plastic deformation increment;

$\underline{f}_{spm}$ = subhinge flexural, torsional and axial plastic flexibility (*4x4*); and

$d\underline{S}_m$ = bending moment, torsional moment and axial load.

and
$$[d\underline{w}_{spm}]^T = [\, d\theta_y \;\; d\theta_z \;\; d\psi \;\; d\delta \,] \tag{2.23a}$$

$$[d\underline{S}_m]^T = [\, dM_y \;\; dM_z \;\; dM_x \;\; dP_x \,] \tag{2.23b}$$

To derive the flexibility matrix, three assumptions are made:

(1) $\Phi(\underline{S}_m)$ is the yield function in the force-moment space, where:

$$\Phi = \left(\frac{M_y}{M_y^y}\right)^2 + \left(\frac{M_z}{M_z^y}\right)^2 + \left(\frac{M_x}{M_x^y}\right)^2 + \left(\frac{P_x}{P_x^y}\right)^2 \tag{2.24}$$

and M_y, M_z = bending moment about y- and z- axes;

M_y^y, M_z^y = yield strength about y- and z- axes;

M_x, M_x^y = torsional moment and yield strength about x-axis;

P_x, P_x^y = axial force and yield strength along x-axis;

As an element develops plastic deformations, the yield surface is assumed to translate, such that the yield function becomes $\Phi(\underline{S}_m - \underline{\alpha})$, where $\underline{\alpha}$ is the new location of the yield surface's origin in two-dimensional stress space (figure 2.11).

(2) Drucker's postulate applies (Drucker and Palgen, 1981), implying that the plastic deformation increment is perpendicular to the yield surface and the yield function serves as a plastic potential.

(3) Translation of the yield surface is governed by Mroz strain hardening rule (Mroz, 1969).

Consequently, the unit vector $\underline{n}$ normal to the yield surface is:

$$\underline{n} = \frac{\underline{\Phi}_{,S}}{\sqrt{(\underline{\Phi}_{,S}^{T} \cdot \underline{\Phi}_{,S})}} \tag{2.25}$$

where $$\underline{\Phi}_{,S}^{T} = \left[\frac{\partial \underline{\Phi}}{\partial M_y} \quad \frac{\partial \underline{\Phi}}{\partial M_z} \quad \frac{\partial \underline{\Phi}}{\partial M_x} \quad \frac{\partial \underline{\Phi}}{\partial F_x} \right]$$

Applying Drucker's postulate, the plastic deformation increments will be in the direction of the unit normal vector $\underline{n}$, where

$$d\underline{w}_{spm} = \underline{n} \cdot d\lambda \tag{2.26}$$

where $d\lambda$ is the magnitude of plastic deformation of the subhinge.

The incremental force or moment in the direction parallel to the normal vector is

$$d\underline{S}_{nm} = \underline{n} \cdot (\underline{n}^{T} \cdot d\underline{S}_{m}) \tag{2.27}$$

The relationship between force or moment increments in the normal vector direction ($d\underline{S}_{nm}$) and plastic deformation ($d\underline{w}_{spm}$) increments is assumed to be

$$d\underline{S}_{nm} = \underline{K}_{spm} \cdot d\underline{w}_{spm} \tag{2.28}$$

where $\underline{K}_{spm}$ = diag [$\underline{K}_{pMy}$ $\underline{K}_{pMz}$ $\underline{K}_{pMx}$ $\underline{K}_{pFx}$], and is a diagonal plastic stiffness matrix in which the individual stiffness terms are related to individual axis force-deformation relationships. Substituting eqns. 2.27 and 2.28 into 2.26 and premultiply by $\underline{n}^{T}$ results in:

$$\underline{n}^T \cdot d\underline{S}_m = \underline{n}^T \cdot \underline{K}_{spm} \cdot \underline{n} \cdot d\lambda \tag{2.29}$$

From equation 2.29, $d\lambda$ is obtained as:

$$d\lambda = \frac{\underline{n}^T \cdot d\underline{S}_m}{[\underline{n}^T \cdot \underline{K}_{spm} \cdot \underline{n}]} \tag{2.30}$$

Thereby, from eqn. 2.26

$$d\underline{w}_{spm} = \frac{\underline{n} \cdot \underline{n}^T}{[\underline{n}^T \cdot \underline{K}_{spm} \cdot \underline{n}]} d\underline{S}_m \tag{2.31}$$

From eqn. 2.31 the flexibility matrix for each flexural subhinge can be written as:

$$d\underline{f}_{spm} = \frac{\underline{n} \cdot \underline{n}^T}{[\underline{n}^T \cdot \underline{K}_{spm} \cdot \underline{n}]} \tag{2.32}$$

2.4.2.2 Shear subhinge flexibility

Based on the experimental tests and the theoretical verifications of Vecchio and Collins (1986) (see Chapter 1, figure 1.9), a simplified shear strength-axial strength interaction diagram is proposed in the current research, as shown in figure 2.12. The interaction curve is approximated to an ellipse with its peak axial loads are P_{ult} and T_{ult}, while its peak shear capacity is $V_c+V_s+V_p$ with a shear capacity equal to V_c+V_s at zero axial load.

Where V_c = shear strength due to concrete mechanism;
V_s = shear strength due to steel mechanism; and
V_p = shear strength due to axial force mechanism.

When the shear cracks develop in a reinforced concrete member, inelastic shear deformation commences. The shear transferred by aggregate interlock and dowel action across the shear cracks will be reduced as the crack widens, therefore the element's shear

strength decreases. If large deformation is imposed, the shear will be resisted primarily by transverse steel reinforcement.

Based on the above physical behaviour and the postulated assumptions, the shear force-deformation V-Δ for the element in each direction, as well as the failure surface for shear in space are shown in figure 2.13. The failure surface for shear is assumed to be coupled in y and z axes. During post shear failure involving concrete cracking and steel yielding, the failure surface contracts. The incremental force-deformation relationship for the shear subhinge is:

$$d\underline{w}_{sps} = \underline{f}_{sps} . d\underline{S}_s \tag{2.33}$$

where $d\underline{w}_{sps}$ = shear subhinge plastic deformation increment;

$\underline{f}_{sps}$ = shear subhinge flexibility matrix [2x2]; and

$$dS_s^T = [dV_y , dV_z] \tag{2.34}$$

The shear force flexibility matrix is uncoupled during shear failure, but remains coupled with flexural forces through equilibrium, with the $\underline{f}_{sps}$ matrix in the form of 2x2 diagonal matrix:

$$\underline{f}_{sps} = \begin{bmatrix} \frac{1}{K_{vy}} & 0 \\ 0 & \frac{1}{K_{vz}} \end{bmatrix} \tag{2.35}$$

where K_{vy} and K_{vz} represent post shear failure plastic stiffness for shear subhinge about y and z axes, respectively. The values of K_{vy}, K_{vz} are determined according to the approach explained in Chapter 3, section 3.6.

There are minimum limiting values for K_{vy} and K_{vz} and are both equal to K_{vmin}. The value for K_{vmin} is established by having the shear resistance decrease abruptly without any change in deformation. This condition occurs when the element's flexibility matrix has a zero determinant. On this basis, K_{vy} and K_{vz} should be chosen with a higher value than K_{vmin}, where:

$$K_{v\min} = -\frac{1}{\frac{L}{(K_{ii}K_{jj} - K_{ij}^2)EI} + \frac{1}{GAL}} \tag{2.36}$$

2.4.3 Complete stiffness

All the plastic subhinges are initially rigid, thus the initial stiffness will be the stiffness of the elastic element. Under the action of flexural and shear forces, the subhinges experience some flexibility, therefore a reduction in the element stiffness occurs. The flexibility of the flexure subhinges is divided into elastic, $\underline{f}_{sem}^{I}$, (recoverable) and plastic, $\underline{f}_{spm}^{I}$, (non-recoverable upon load reversal) flexibilities. An isotropic contraction of the shear yield surface (shear failure) towards a residual shear surface (shear capacity of transverse reinforcement), which follows the shear subhinge flexibility $\underline{f}_{sps}$, is assumed.

The flexibility matrix for the entire element, $\underline{F}_{t}$, can be obtained by the appropriate addition of the elastic element, $\underline{f}_{el}$, and the end hinges' tangent flexibility matrices $\underline{f}_{p}^{I}$ and $\underline{f}_{p}^{J}$ at nodes I and J, respectively.

$$\text{i.e.: } \underline{F}_t = \underline{f}_{el} + \underline{f}_p^I + \underline{f}_p^J \tag{2.37}$$

After which, $\underline{F}_t$ can be inverted to obtain the element's total tangent stiffness matrix, $\underline{K}_t$ such that:

$$\underline{K}_t = \underline{F}_t^{-1} \tag{2.38}$$

Each end hinge tangent flexibility matrices $\underline{f}_p^I$ and $\underline{f}_p^J$ are calculated by appropriate summation of the flexibility of their constituting subhinges, such that:

$$\underline{f}_p^I = \sum_{i=1}^{3} \left(\underline{f}_{sem,i}^I + \underline{f}_{spm,i}^I \right) + \underline{f}_{sps} \text{ ; and} \tag{2.39a}$$

$$\underline{f}_p^J = \sum_{i=1}^{3} \left(\underline{f}_{sem,i}^J + \underline{f}_{spm,i}^J \right) + \underline{f}_{sps} \tag{2.39b}$$

where
$$\underline{f}_{sps} = \begin{bmatrix} \frac{1}{K_{vy}} & \frac{1}{K_{vy}} & 0 & 0 & 0 & 0 \\ \frac{1}{K_{vy}} & \frac{1}{K_{vy}} & 0 & 0 & 0 & 0 \\ 0 & 0 & \frac{1}{K_{vz}} & \frac{1}{K_{vz}} & 0 & 0 \\ 0 & 0 & \frac{1}{K_{vz}} & \frac{1}{K_{vz}} & 0 & 0 \\ 0 & 0 & 0 & 0 & 0 & 0 \\ 0 & 0 & 0 & 0 & 0 & 0 \end{bmatrix} \tag{2.40}$$

The complete element degree of freedom force-deformation relationship can be expressed as:

$$d\underline{S} = \underline{K}_t \,.\, d\underline{v} \tag{2.41}$$

where $d\underline{v}^{\mathrm{T}} = [\, dv_1 \;\; dv_2 \;\; dv_3 \;\; dv_4 \;\; dv_5 \;\; dv_6 \,]$

$$d\underline{S}^{T} = [\ dM_{Iy}\ \ dM_{Jy}\ \ dM_{Iz}\ \ dM_{Jz}\ \ dM_{x}\ \ dP_{x}\ ]$$

$$dV_y^I = dV_y^J = \frac{dM_z^I + dM_z^J}{L} \tag{2.42a}$$

$$dV_z^I = dV_z^J = \frac{dM_y^I + dM_y^J}{L} \tag{2.42b}$$

2.5 HARDENING RULE

2.5.1 Flexural subhinge hardening rule

The original yield surfaces of a hinge are shown in figure 2.15 consisting of three concentric subhinge yield surfaces. After initial yield develops, the behaviour of a subhinge follows the Mroz theory, (Mroz, 1969), strain hardening rule for yielding of metals.

Assuming that the current state has reached point S1 on yield surface YS1, and loading continues, yield surface YS1 will translate towards yield surface YS2 (figure 2.15a) where point S_1 is assumed to move towards the corresponding point S_2 on yield surface YS2. The relationship between stress state S_1, and S_2 can be written as:

$$\underline{S}_2 = \underline{S}_{u12}(\underline{S}_1 - \underline{\alpha}_1) + \underline{\alpha}_2 \tag{2.43}$$

where $\underline{\alpha}_1$, $\underline{\alpha}_2$ is the location of origins of yield surfaces YS1 and YS2; and

$\underline{S}_{u12}$ is the square diagonal matrix, representing the relative size of yield surface YS2 to YS1 on the y and z axes for example:

$$\underline{S}_{u12} = diag[\frac{M_{y2}^y}{M_{y1}^y} \quad \frac{M_{z2}^y}{M_{z1}^y} \quad \frac{M_{x2}^y}{M_{x1}^y} \quad \frac{F_{x2}^y}{F_{x1}^y}] \tag{2.44}$$

where M_{y2}^y, M_{z2}^y, M_{x2}^y, F_{x2}^y = yield strength of yield surface YS2; and

M^y_{y1}, M^y_{z1}, M^y_{x1}, F^y_{x1} = yield strength of yield surface YS1.

The translation of yield surface YS1 is assumed to be parallel to vector ($\underline{S}_1 - \underline{S}_2$), that is,

$$d\underline{\alpha}_1 = (\underline{S}_2 - \underline{S}_1)\, d\alpha_1^* \tag{2.45}$$

where $d\underline{\alpha}_1$ = vector defining the direction of YS1 translation; and

$d\alpha_1^*$ = scalar defining the magnitude of YS1 translation.

Substituting eqn. 2.43 into eqn. 2.45 leads to:

$$d\underline{\alpha}_1 = [\, (\underline{S}_{u12} - \underline{I})\, \underline{S}_1 - (\underline{S}_{u12} \cdot \underline{\alpha}_1 - \underline{\alpha}_2)\,]\, d\alpha_1^* \tag{2.46}$$

with $\underline{I}$ being the identity matrix.

Point S_1 lies on the yield surface YS1 when:

$$\Phi(\underline{S}_1 - \underline{\alpha}_1) = 1 \tag{2.47}$$

in which Φ is the yield function, as defined in equation 2.24.

To satisfy loading, point S_1 must remain on yield surface YS1 during its translation, hence

$$d\Phi = 0 = \underline{\Phi}^T_{,S} \cdot d\underline{S}_1 - \underline{\Phi}^T_{,S} \cdot d\underline{\alpha}_1 \tag{2.48}$$

Upon substituting eqn. 2.40 into eqn. 2.42, one obtains:

$$\underline{\Phi}^T_{,S} \cdot d\underline{S}_1 - \underline{\Phi}^T_{,S} \cdot \left[(\underline{S}_{u12} - \underline{I})\underline{S}_1 - (\underline{S}_{u12} \cdot \underline{\alpha}_1 - \underline{\alpha}_2)\right]\, d\underline{\alpha}_1^* = 0 \tag{2.49}$$

which leads to

$$d\underline{\alpha}_1^* = \frac{\underline{\Phi}^T_{,S} \cdot d\underline{S}_1}{\underline{\Phi}^T_{,S}\left[(\underline{S}_{u12} - \underline{I})\underline{S}_1 - (\underline{S}_{u12} \cdot \underline{\alpha}_1 - \underline{\alpha}_2)\right]} \tag{2.50}$$

Hence the translation of the yield surface YS1 is determined by substituting eqn. 2.50 and eqn. 2.43 into eqn. 2.45 which give:

$$d\underline{\alpha}_1 = \frac{\left[(\underline{S}_{u12} - \underline{I})\underline{S}_1 - (\underline{S}_{u12} \cdot \underline{\alpha}_1 - \underline{\alpha}_2)\right]\underline{\Phi}_{,S}^T \cdot d\underline{S}_1}{\underline{\Phi}_{,S}^T\left[(\underline{S}_{u12} - \underline{I})\underline{S}_1 - (\underline{S}_{u12} \cdot \underline{\alpha}_1 - \underline{\alpha}_2)\right]} \tag{2.51}$$

In the current state, $\underline{\alpha}_1$, $\underline{\alpha}_2$, and $\underline{S}_1$ are known. Once the increment of force $d\underline{S}_1$ is computed, the yield surface YS1 translation can be determined from eqn. 2.51. The translation of yield surface YS1 continues according to eqn. 2.51 until yield surface YS2 is reached. Yield surfaces YS1 and YS2 will then both translate together to the corresponding point S3 on yield surface YS3 (figure 2.15b), where the translation increment of both surfaces is determined from the general form of eqn. 2.50. This general form for the translation increment is written as:

$$d\underline{\alpha}_i = \frac{\left[(\underline{S}_{uij} - \underline{I})\underline{S}_j - (\underline{S}_{ij} \cdot \underline{\alpha}_i - \underline{\alpha}_j)\right]\underline{\Phi}_{,S}^T \cdot d\underline{S}_i}{\underline{\Phi}_{,S}^T\left[(\underline{S}_{uij} - \underline{I})\underline{S}_i - (\underline{S}_{uij} \cdot \underline{\alpha}_i - \underline{\alpha}_j)\right]} \tag{2.52}$$

Where subscript i implies the yield surface YSi has been reached and subscript j is to indicate that yield surface YSj is the target surface.

The Mroz strain hardening rule is applied as described above, before the outermost yield surface (YS3) is reached. If the current state lies on the yield surface YS3, the translation increment of the yield surfaces is determined by assuming an infinitely large yield surface which surrounds the three subhinge yield surfaces and applying the Mroz theory. This leads to the translation of yield surface YS3 based on Ziegler's hardening rule (Zeigler, 1959), where the direction of translation $d\alpha_3$ is in the radial direction:

$$d\underline{\alpha}_3 = \frac{(\underline{S}_3 - \underline{\alpha}_3)\underline{\Phi}_{,S}^T \cdot d\underline{S}_3}{\underline{\Phi}_{,S}^T(\underline{S}_3 - \underline{\alpha}_3)} \tag{2.53}$$

In which $\underline{\alpha_3}$ = origin of yield surface YS3;

$\underline{S_3}$ = stress state on yield surface YS3; and

$d\underline{S_3}$ = force vector increment.

2.5.2 Shear subhinge failure surface contraction rule

The post shear failure force-deformation response follows a softening branch as the concrete shear failure surface contracts gradually. The rate of softening is specified by K_{vy} and K_{vz}. After contraction of the failure surface, it is required that the shear force state remains on the failure surface. Considering a current state at the beginning of a load step, the following must hold:

$$\Phi_s(V_y, V_z, P, V_y^f, V_z^f) = \left(\frac{V_y}{V_y^f}\right)^2 + \left(\frac{V_z}{V_z^f}\right)^2 + \left(\frac{P - P_{av}}{P_{ult} - P_{av}}\right)^2 = 1 \qquad (2.54)$$

where P_{av} and P_{ult} are shown in figure 2.12.

While after loading:

$$\Phi_s = \left(\frac{V_y + FACS \cdot dV_y}{V_{fac}\, V_y^f}\right)^2 + \left(\frac{V_z + FACS \cdot dV_z}{V_{fac}\, V_z^f}\right)^2 + \left(\frac{P + FACS \cdot dP - P_{av}}{P_{ult} - P_{av}}\right)^2 = 1 \qquad (2.55)$$

Where FACS = event factor for shear subhinge failure (as explained in section 2.10);

V_{fac} = contraction factor for shear subhinge shear forces capacity (figure 2.16);

V_y , V_z = shear force along the y and z axes;

dV_y , dV_z = shear force decrease along y and z axes;

dP = increment of variation in axial force;

V_y^f , V_z^f = shear capacity along y and z axes; and

dV_y^f , dV_z^f = increment of shear capacity deterioration along y and z axes.

An isotropic contraction model is adopted, where the failure surface is assumed to uniformly contract from the original failure surface to the residual shear capacity along axes y and z (figure 2.16). After the initial shear failure occurs, the new shear failure surface is a linearly contracted surface according the coefficient V_{fac} in equation 2.55. This model has an influence on the reduction in shear capacity in the opposite loading direction of each axis. The transition failure surface depends on the current stress state in the stress space. The contraction of the failure surface is determined by solving for V_{fac} in equation 2.55.

Upon reversal of loading, the stiffness of the shear subhinge reduces when the shear force reaches a zero value and resumes when the element total deformation reaches zero. This is done to model the pinching behaviour in the moment-rotation hysteresis response. The shear subhinge flexibility matrix during pinching is defined as:

$$\underline{f}_{sps} = \alpha_p \cdot \underline{f}_s \tag{2.56}$$

where α_p = arbitrary coefficient (from $0 \rightarrow 1$ where 0 indicates no pinching) with a practical range from 0.01 to 0.025; and

$\underline{f}_s$ = initial shear flexibility matrix

2.6 LOADING / UNLOADING CRITERION

The loading/unloading criterion enables continuous plastic flow at a subhinge to be distinguished from elastic unloading for any plastic state for any specified deformation

increment. The procedure used here was based on the criterion that the elastic load increment, $d\underline{S}_e$, must point outwards from the yield surface during continuous loading:

$$d\underline{S}_e^T \cdot \underline{n} \geq 0 \tag{2.57}$$

where the given state must be on the yield surface:

$$\underline{\Phi}(\underline{S}\text{-}\underline{\alpha}) = 1 \tag{2.58}$$

The elastic loading increment $d\underline{S}_e$ is calculated as

$$d\underline{S}_e = \underline{K}_e \cdot d\underline{v} \tag{2.59}$$

where $\underline{K}_e$ = elastic stiffness matrix;
$d\underline{v}$ = deformation increment;
$d\underline{S}_e$ = elastic force increment.

If the elastic force increment vector, $d\underline{S}_e$, has positive components in the normal vector direction of the yield surface (figure 2.17), the force state is moving outside the yield surface and the elastic assumption is correct, the hinge thereby continues to develop plastic flow. Otherwise, if the elastic action increment has negative components in the direction of the yield surface normal vector, then the elastic assumption is incorrect and the element unloads. Flexural and shear elastic unloading must be checked independently.

In general, the flexural behaviour of each hinge should be checked. Generally, due to translation, the flexural subhinges' yield surface are not concentric, hence the subhinges do not have the same normal vector at their corresponding points. Under this circumstance the yield surfaces can overlap, where it is possible that some subhinges satisfy the loading criterion while others do not. In the element formulation elastic

unloading is controlled by the outermost subhinge's yield surface that the force state has reached, as shown in fig 2.18.

2.7 STIFFNESS DEGRADATION

2.7.1 Flexural stiffness degradation

As mentioned in section 2.4.3, a flexure subhinge flexibility is divided into two parts; elastic and plastic flexibilities. Both flexibilities are initially zero. Continuous loading follows kinematic strain hardening, where a triggered yield surface (in case of occurrence of certain event such as crack, yield or ultimate) translates in the force space till it reaches the following yield surface. Both yield surfaces move without change of size or shape till they reach the following yield surface, and so on. The process of occurrence of a certain event (reaching a yield surface) results in a finite plastic flexibility, $\underline{f}_{spm,i}^{IorJ}$, of such subhinge. Upon load reversal, a finite elastic flexibility, $\underline{f}_{sem,i}^{IorJ}$, is assigned to a triggered flexure subhinge (in addition to the plastic flexibility). Having both, elastic and plastic flexure subhinge flexibilities, gives the advantage of having elastic stiffness degradation which results in a reduced overall element stiffness (and consequently strength) when subjected to reversed loading at the same displacement level.

The plastic flexibility matrix $\underline{f}_{spm,i}$ of a yielded flexure subhinge was derived before in section 2.4.2.1, and was shown to be equal to:

$$\underline{f}_{spm,i} = \frac{\underline{n} \cdot \underline{n}^T}{\underline{n}^T \cdot K_{spm,i} \cdot \underline{n}} \tag{2.60}$$

where n is the outward normal vector to the yield surface at the action point; and $\underline{K}_{spm,i}$ is the diagonal plastic stiffness matrix from the individual flexural action-deformation relationships for each force component, defined as:

$$K_{spm,i} = diag\left[\ K^{p}_{My,i} \quad K^{p}_{My,i} \quad K^{p}_{My,i} \quad K^{p}_{My,i}\ \right] \tag{2.61}$$

in which the plastic stiffness after yield for each force component is given by:

$$K^{p}_{i} = \frac{K_i \cdot K_{i+1}}{K_i - K_{i+1}} \tag{2.62}$$

in which the stiffnesses K_i are the initial (elastic beam, input data) stiffnesses.

A typical force-deformation relationship of a tested cantilever column (Ghobarah et al., 1997) is shown in figure 2.19. From the shown relationship, it is observed that the level of degradation in stiffness increases as the ductility of the element increase or in case of repeated cycles at the same level of ductility. The effect of ignoring the stiffness degradation on the force-displacement relationship is shown in figure 2.20. Stiffness degradation is introduced in the model when reversed loading is applied. In the formulation of the 3D element, it is assumed that the stiffness degrades independently for each moment or force component for each subhinge. The degraded stiffness is inversely proportional to the previous hinge secant stiffness, K_s.

Thus the elastic subhinge flexibility after unloading for each force component are shown in figure 2.21 and are given by:

$$f_{sem,i} = \alpha_m \left(\frac{d^{p}_{i}}{\sum_{i=1}^{3} d^{p}_{i}} \right) \frac{1}{K_s} \tag{2.63}$$

where K_s is the secant stiffness of the previous cycle and α_m is an arbitrary degradation coefficient that ranges from 0 to 1 where 0 indicates no stiffness degradation. A practical range for α_m was found to be in the rage from 0.03 to 0.1. The technique of assigning each plastic subhinge *elastic and plastic* flexibilities, will allow for the decrease in the total element's strength for repeated cycles at the same displacement level. The strength degradation depends on the plastic deformation of each subhinge in proportion to the total plastic deformation of all subhinges at the previous cycle. It is possible to assign different degradation coefficients α_{my} and α_{mz} in each loading direction. The model can be extended to have a different coefficient α_m^i for each subhinge; this means that the degradation level for each subhinge can be different. This feature was not used in the current applications in order not to increase the number of parameters that need to be defined. It should be mentioned that Bauschinger effect is implicitly taken into consideration when using the aforementioned quadri-linear degrading force-displacement relationship.

2.7.2 Shear stiffness degradation

Shear stiffness degradation is introduced after unloading. A reduced initial shear stiffness $\underline{f}_s^u$ according to the following equation was used:

$$\underline{f}_s^u = \alpha_s \times \frac{1}{K_s} \tag{2.64}$$

where $\underline{f}_s^u$ = unloading shear stiffness matrix; and

α_s = arbitrary coefficient (from $0 \rightarrow 1$ where 0 indicates no elastic shear stiffness degradation) with a practical ranges from 0.025 to 0.09.

and the secant stiffness is shown in figure 2.21.

2.8 VARIATION IN AXIAL LOAD

There are two ways to incorporate the effect of variation of axial load on the state of the yield surfaces of a hinge. First approach is to consider the variation in axial deformation (elongation/shortening), while the second approach is to consider the variation of axial force as the control input, as shown in figure 2.22. It is more convenient to use the first approach when there are considerable differences in the force-extension stiffnesses of each subhinge, thus keeping track of the appropriate axial force corresponding to a certain level of axial deformation. Figure 2.23 shows the axial load deformation relationship for tied and spiral columns. From that figure it can be postulated that the force-deformation relationship is almost linear (i.e. with a constant initial stiffness) up to the point of failure. From the aforementioned assumption and from the fact that the variation in axial load is experimentally conducted using a force mode control (therefore allowing the element's end to elongate or shorten while applying the planned axial force path), the second approach was adopted.

2.8.1 Effect of variation of axial load on flexure subhinges

Since the "event to event" solving technique rather than the "iterative" technique is used (on the element level), thus the factor "FACM" which will cause a certain flexure event occurrence (reaching a yield surface and change in stiffness) is calculated assuming

a linear interpolation along the axial load path, as shown in figure 2.24. A curved path can be achieved (if required) by subdividing the axial force variation increment into several linear sub-increments.

2.8.2 Effect of variation of axial load on shear subhinge

Figure 2.16 shows the effect of variation of axial load on the force state determination on the contracting shear subhinge yield surface (i.e. post shear failure response). In that figure, the element is assumed to be subjected to cyclic lateral displacement from point 0 to 9 (loading 0→2, unloading 2→6, reloading 6→9). The shear subhinge failure event "FACS" is dependent on the contraction factor V_{fac} as explained in section 2.5.2.

Figure 2.16a shows the determination of the factor V_{fac} in case of constant axial load, while figure 2.16b shows the change in the force state (and consequently V_{fac}) in case of variable axial force as shown in the same figure where the axial force is varying through the points 0 to 9 (increasing 0→2, decreasing 2→6, increasing 6→9).

It is worth mentioning that in addition to the influence of axial load variation on the force state on the yield surfaces of the subhinges, it affects the flexibility matrix for the active flexural subhinges (consequently affects the element's total flexibility and stiffness matrices) as well. Equation 2.60 shows that the plastic flexibility matrix $\underline{f}_{spm,i}$ of a yielded flexure subhinge is dependent on the outward normal vector to the yield surface, n, which in turn depends on the current force state.

2.9 YIELD SURFACE TOLERANCE

The amount of yield surface translation is only affected by the load increments that are parallel to the yield surface normal vector. Consequently, the amount of yield surface translation $d\underline{\alpha}$ is not the same as the load increments $d\underline{S}$ (figure 2.25). It is possible that the new action point Q will lie outside the new yield surface.

To deal with this, if the yield function exceeds the allowable tolerance, it is assumed that the error varies linearly with the element deformation. A scale-back factor is determined to subdivide the load step to satisfy a tolerance for which the yield function is close to 1.0. Once the tolerance is satisfied, the new force point is scaled back to the yield surface. A tolerance value of about 1-2% of the yield surface size is recommended. After the point is moved to the yield surface, the tangent stiffness is recalculated, and the determination for the remaining element deformation is performed.

2.10 STATE DETERMINATION

In an inelastic analysis, once the increment of global displacement is computed, it is necessary to evaluate the unbalanced global nodal forces $\underline{R}^U$ based on updated internal resisting force $\underline{R}^I$. This procedure is called state determination. The unbalanced global forces are

$$\underline{R}^U = \underline{R}^E - \underline{R}^I \tag{2.66}$$

Here, $\underline{R}^E$ is the external applied loads. If the unbalanced nodal forces are less than the allowable tolerance, then it is assumed that equilibrium is satisfied. Otherwise, iterations

are required, which involve imposing the unbalanced load on the structure and determining the resulting increment of global displacements.

Two well-known procedures are the Newton Raphson iteration (e.g. tangent stiffness iteration) and the Modified Newton Raphson iteration (e.g. constant stiffness iteration) as illustrated in figure 2.26.

The procedure for the state determination to update global resisting force is as follows:

(1) Calculate the element deformation increment from the given nodal displacement increment:

$$d\underline{v} = \underline{a}_f \cdot d\underline{r}$$

where $d\underline{v}$ = element deformation increment;
$\underline{a}_f$ = displacement transformation matrix; and
$d\underline{r}$ = nodal displacement increment.

(2) Calculate linear loading increment for the element:

$$d\underline{S} = \underline{K}_t \cdot d\underline{v}$$

and determine hinge force increment:

$$d\underline{S}_h = \underline{b} \cdot d\underline{S}$$

where $d\underline{S}$ = linear force increment for the element based on given deformation increment $d\underline{v}$;
$\underline{K}_t$ = element tangent stiffness matrix;
$d\underline{S}_h$ = linear action increment for hinges; and
$\underline{b}$ = force transformation matrix from dS to $d\underline{S}_h$.

(3) Check for an "event" in the given deformation increment, and calculate the event factor FACi (and FACj) for each hinge. Possible events are:

Flexure

(a) Reaching a flexural yield surface of a subhinge:

If the proportion of deformation increment to reach this surface is greater than 1.0, then the event factor FACMi (or FACMj) is 1.0. Otherwise, the event changes the status, and event factor is set equal to the calculated proportion.

(b) If unloading occurs, the elastic degrading flexural stiffness is calculated. The stiffness matrix is reconstructed, and the event factor is set to 0.0. The calculation proceeds to step (2) above.

Shear

(a) Check $\Phi_s(V_y, V_z, P) = \left(\frac{V_y}{V_y^f}\right)^2 + \left(\frac{V_z}{V_z^f}\right)^2 + \left(\frac{P - P_{av}}{P_{ult} - P_{av}}\right)^2$

If less than 1, then FACS = 1.

If greater than 1, calculate FACS such that the above equation equal to 1.

(b) If unloading, then elastic degraded shear stiffness is calculated.

(4) Calculate plastic deformation increment, and the translation of yield surfaces.

(5) Choose the smallest event factor for the whole element, FAC, from the two hinges' factors. (i.e. for hinge I: FACi=smaller(FACMi, FACS), similarly FACj= smaller(FACMj, FACS). Therefore, FAC=smaller(FACi, FACj)).

(6) Update the new hinge forces, new subhinge plastic deformation, new origin of subhinges.

$$\underline{S_h} = \underline{S_h} + \text{FAC} \cdot d\underline{S_h}$$

$$\underline{\alpha_i} = \alpha_i + \text{FAC} \cdot d\underline{\alpha_i}$$

$$\underline{w}_{spi} = \underline{w}_{spi} + \text{FAC} \cdot d\underline{w}_{spi}$$

where $\underline{w}_{spi}$ = flexural subhinge i plastic deformation;

$d\underline{w}_{spi}$ = flexural subhinge i plastic deformation increment;

$\underline{\alpha}_i$ = flexural subhinge i origin; and

$d\underline{\alpha}_i$ = flexural subhinge i origin translation.

(7) Calculate the complement of event factor, SS:

$$\text{SS} = 1.0 - \text{FAC}$$

(8) If the element event status has changed, reconstruct the element tangent stiffness matrix.

(9) If the displacement increment has been completely developed (i.e. SS=0.0), go to step (11)

(10) Calculate remaining element displacement increment:

$$d\underline{v} = \text{SS} \cdot d\underline{v}$$

go to step (2)

(11) Obtain element actions $\underline{S}$: $\underline{S} = \underline{b}^{\text{T}} \cdot \underline{S}_h$

(12) Compute the internal force $\underline{\text{R}}^{\text{I}}$: $\underline{R}^I = a_f^T \cdot \underline{S}$

2.11 ELEMENT LIMITATIONS

It is important to recognize that the element development is based on several simplifying assumptions, and that the element does not capture a number of potentially important aspects of beam-column behaviour. The main assumptions and limitations are as follows:

1. All inelastic behaviour is considered to be lumped into end hinges.

2. Shear deformations are included but moment-shear interaction is ignored.
3. There are currently no provisions for element loads, pre-stressing, or initial stresses.
4. Induced membrane forces due to end restraint are not considered.

2.12 SUMMARY

A mathematical description of the force-deformation response of inelastic biaxial beam-column element has been presented in a form suitable for incorporation in 3D inelastic analysis programs. The element is based on the lumped plasticity modeling, which is particularly suitable for the analysis of building frames under seismic loads. The model represents flexural response by quadrilinear force-deformation relationship, and shear response by strength and stiffness degrading relationship. The model takes into account the effect of axial load variation on lateral deformation and its interaction with biaxial moments and shear.

The yield surface properties for each subhinge in terms of flexural strength and elastic and post elastic stiffness (which is needed as an input data), can be determined from the moment-rotation analysis about each principal axis. This analysis should account for the major components of deformation such as flexure, shear and bond slip of tensile reinforcement. The following chapter explains the procedure for developing moment-rotation and force-deflection relationships from the basic mechanical and geometrical properties.

The model described above, which is presented in Appendix C, has been coded using the MATLAB® V5.3 programming language.

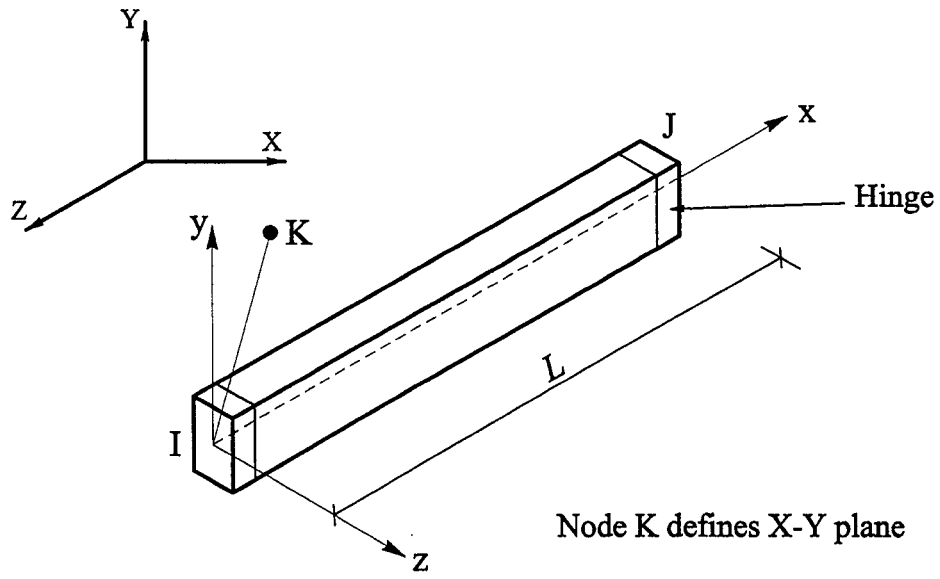

Figure 2.1 Element position and axes

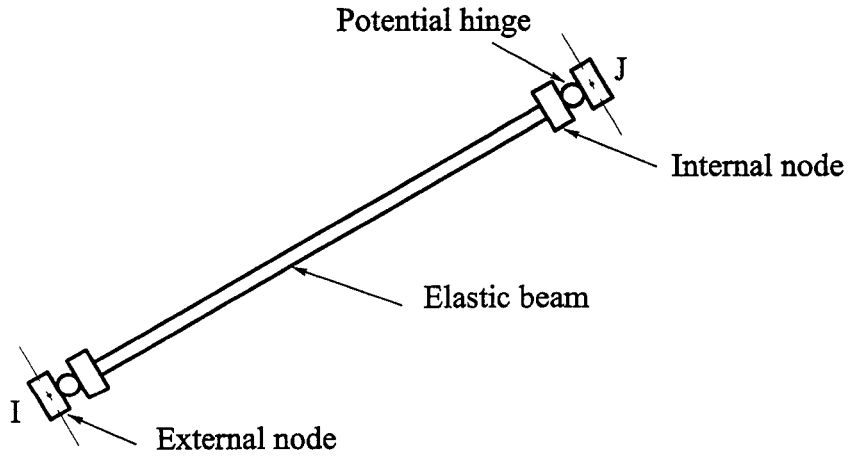

Figure 2.2 Element idealization

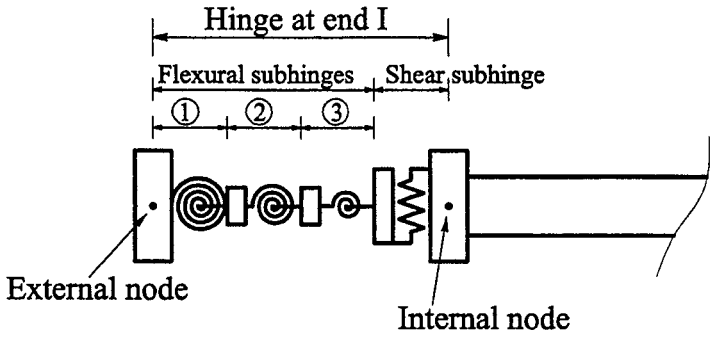

Figure 2.3 Plastic hinge idealization

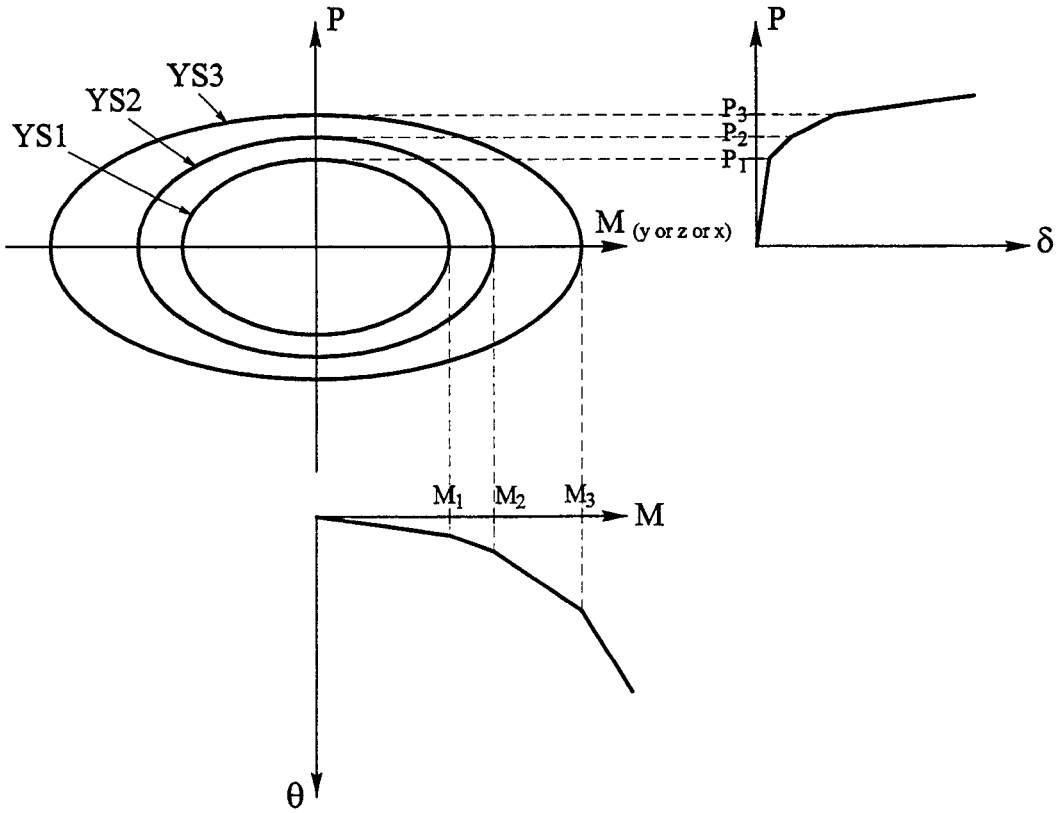

Figure 2.4 Flexural hinge force-deformation and moment rotation relationships

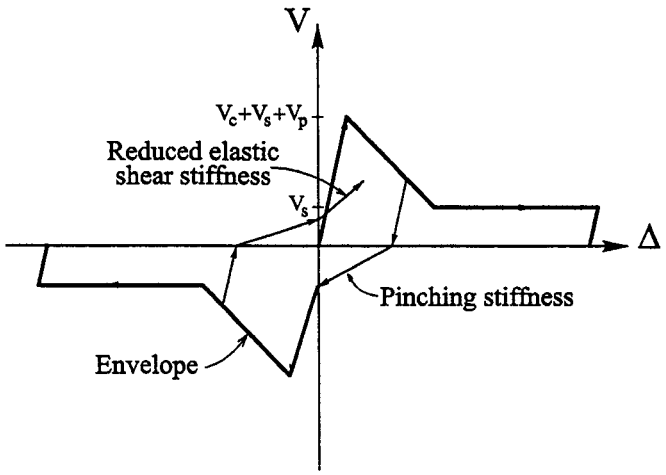

Figure 2.5 Shear hinge-shear deformation relationship envelope

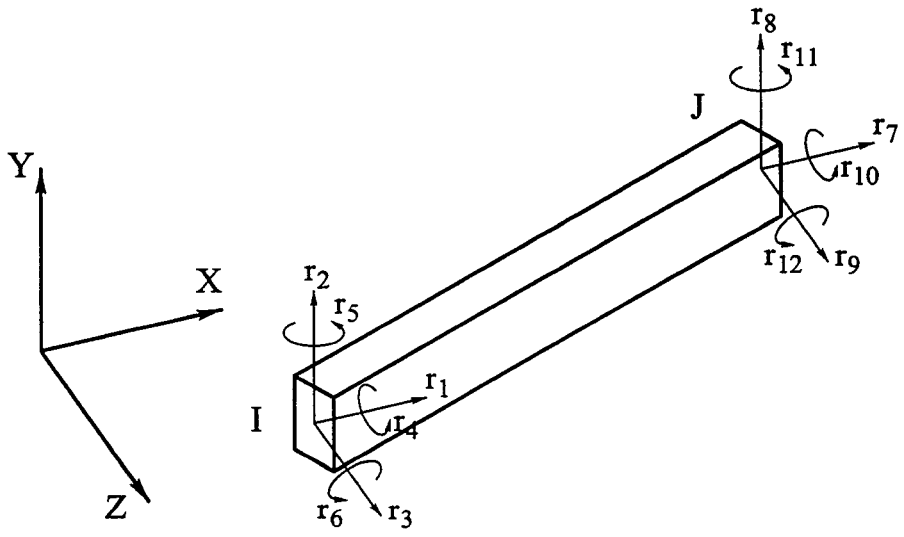

Figure 2.6 Element global degrees of freedom

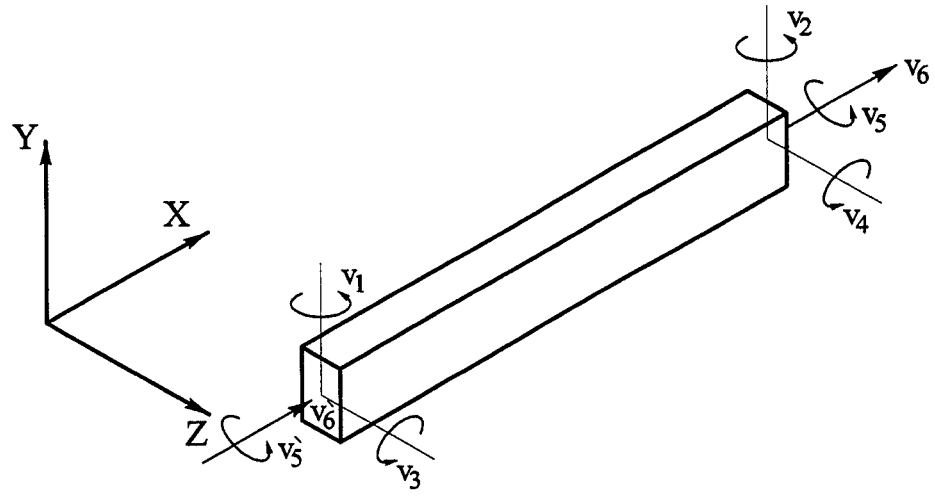

Figure 2.7 Element local degrees of freedom

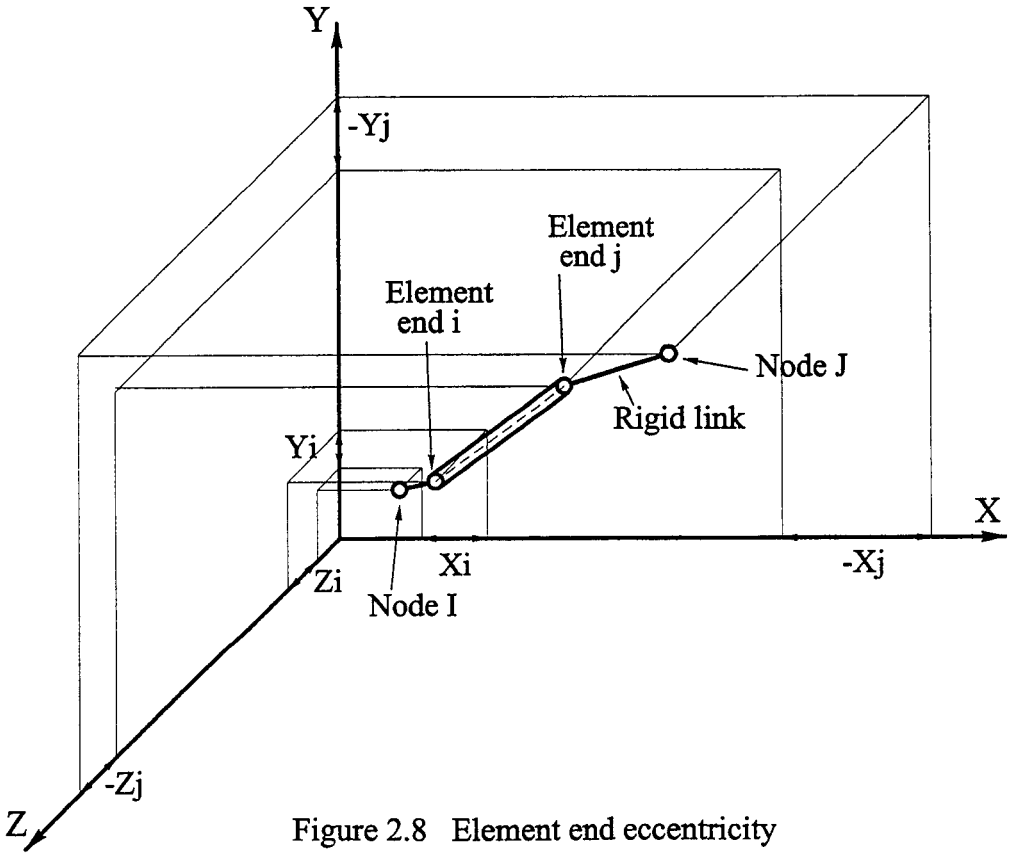

Figure 2.8 Element end eccentricity

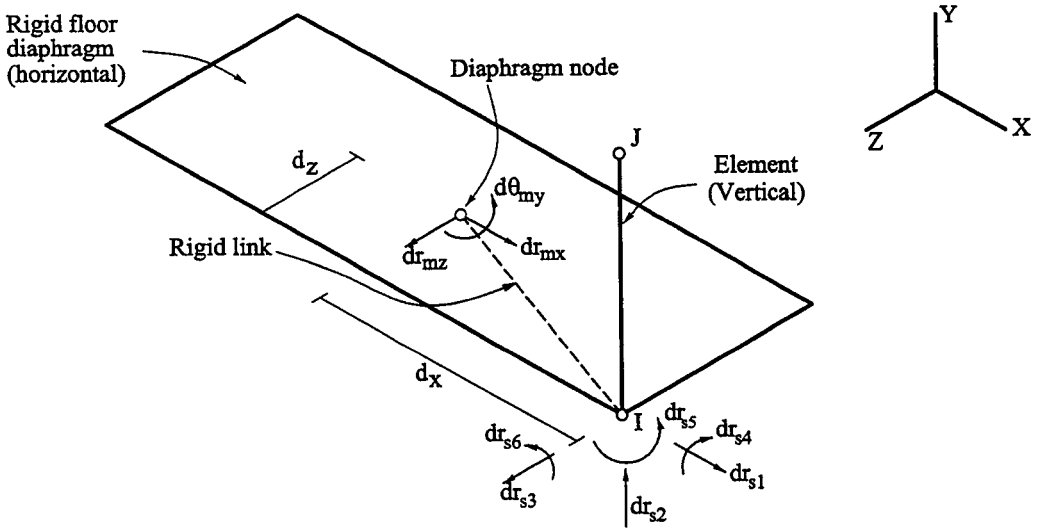

Figure 2.9 Rigid floor diaphragm

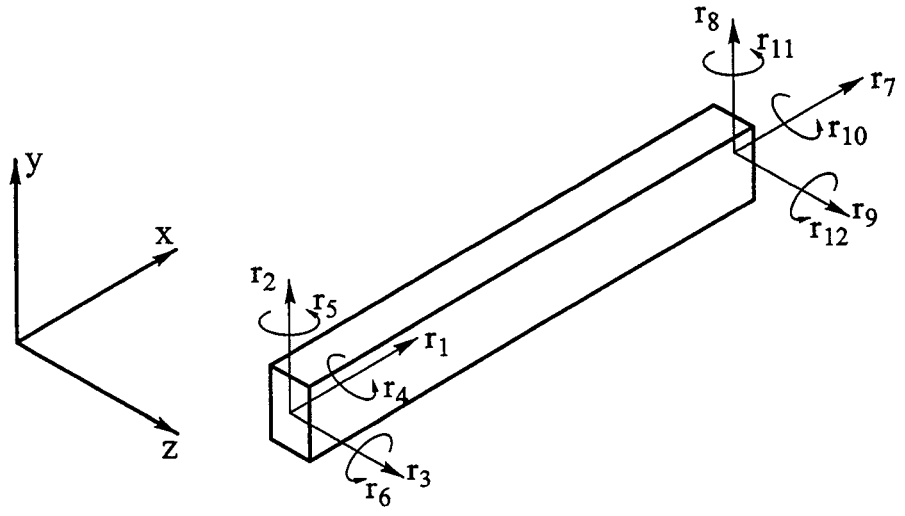

Figure 2.10 Element displacements in local coordinate system

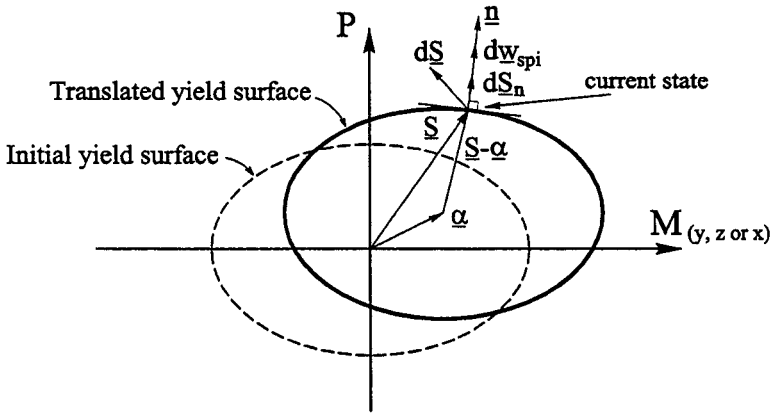

Figure 2.11 Flexural subhinge yield surface translation

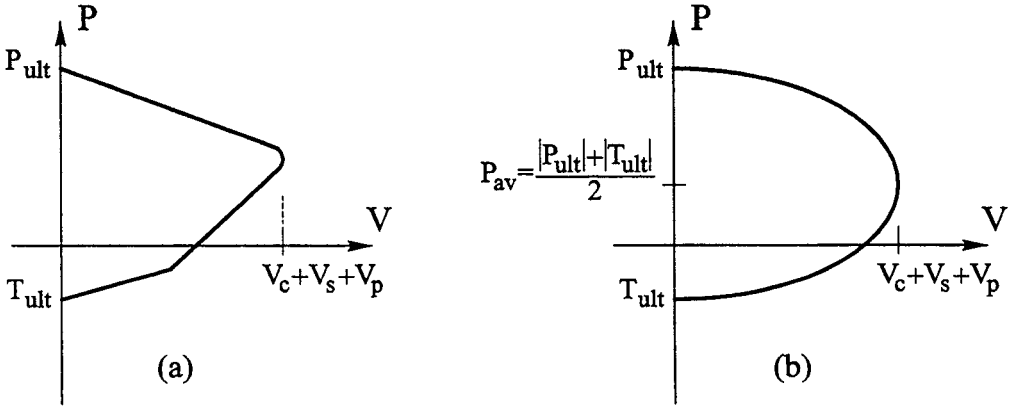

Figure 2.12 Shear strength - axial strength interaction diagram;
(a) Experimental (Vecchio and Collins, 1986);
(b) Approximate model

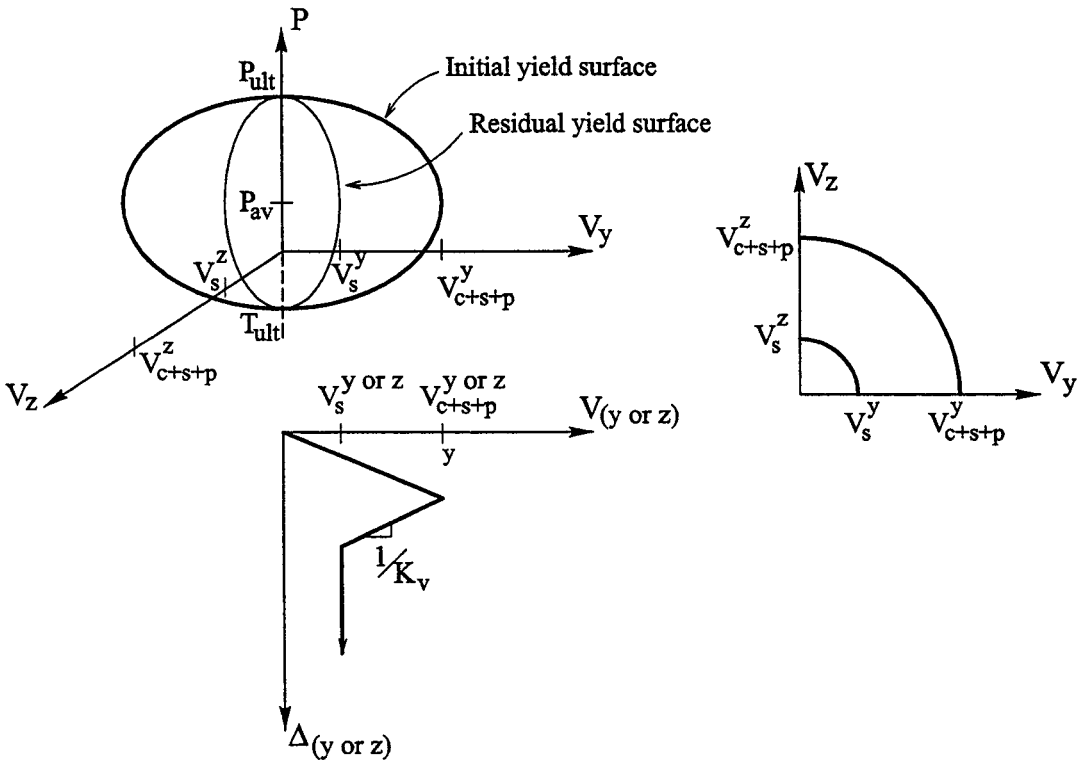

Figure 2.13 Failure surface for shear subhinge

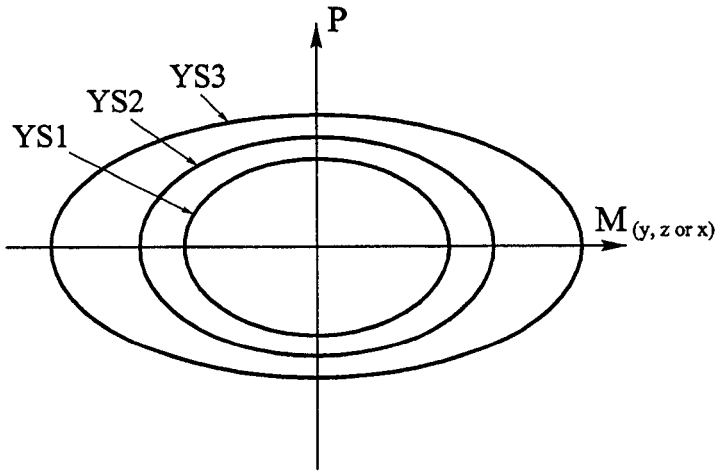

Figure 2.14 Original yield surface for flexure

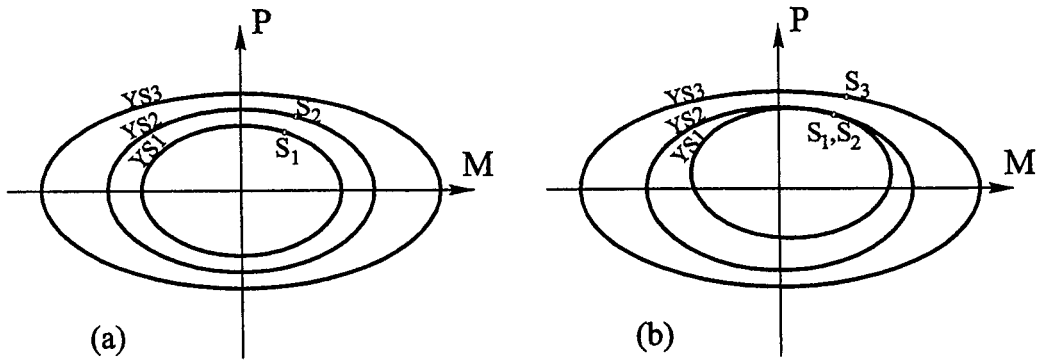

Figure 2.15 Translation of flexural subhinges

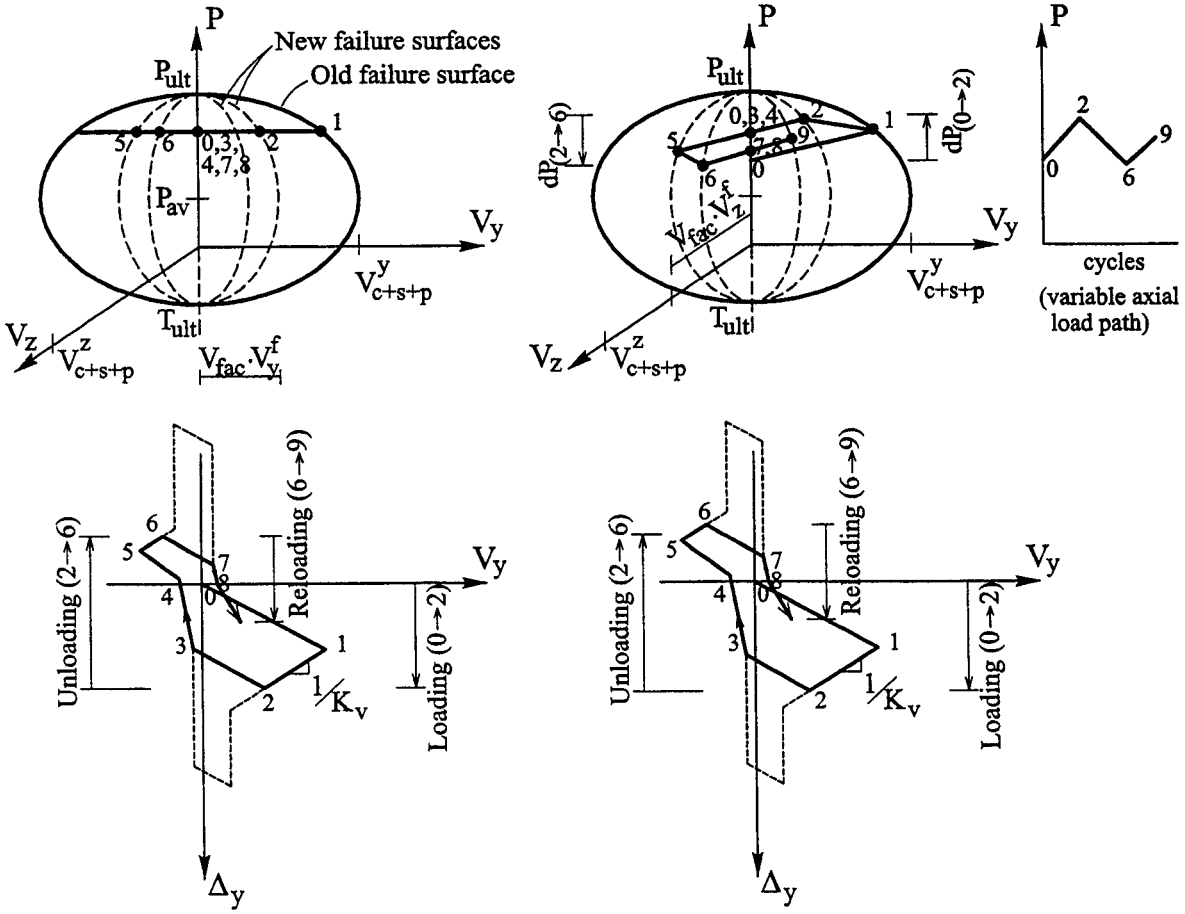

a) Case of constant axial load b) Case of variable axial load

Figure 2.16 Shear subhinge failure surface contraction

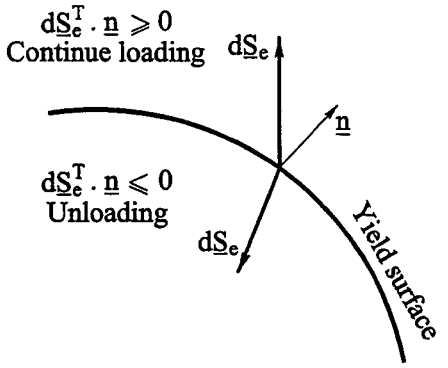

Figure 2.17 Loading / unloading criterion

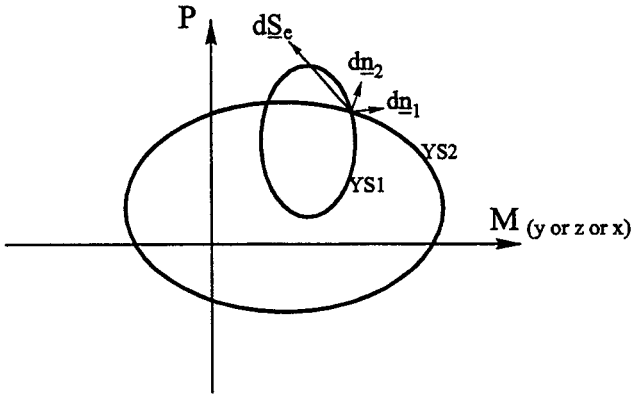

Figure 2.18 Overlaping of flexural yield surfaces

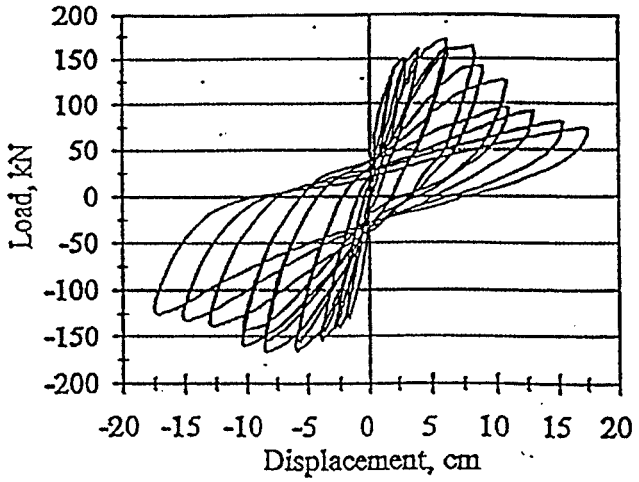

Figure 2.19 Typical force-displacement relationship (Ghobarah et al., 1997)

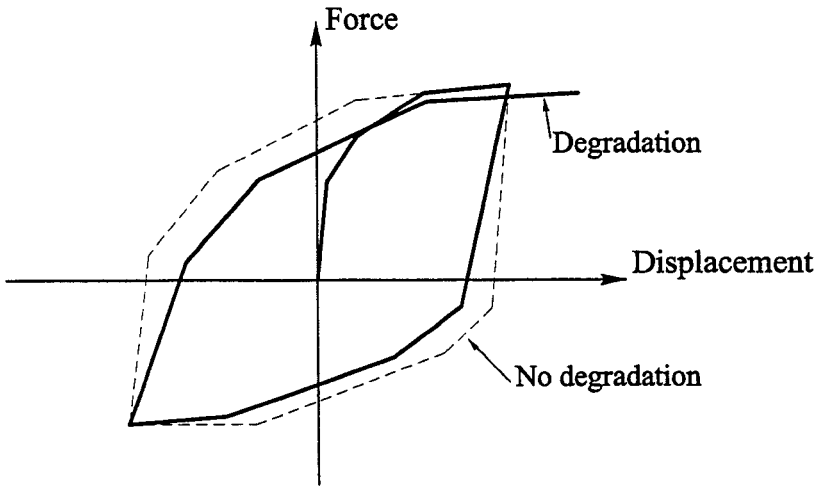

Figure 2.20 Stiffness degradation of cyclic loading

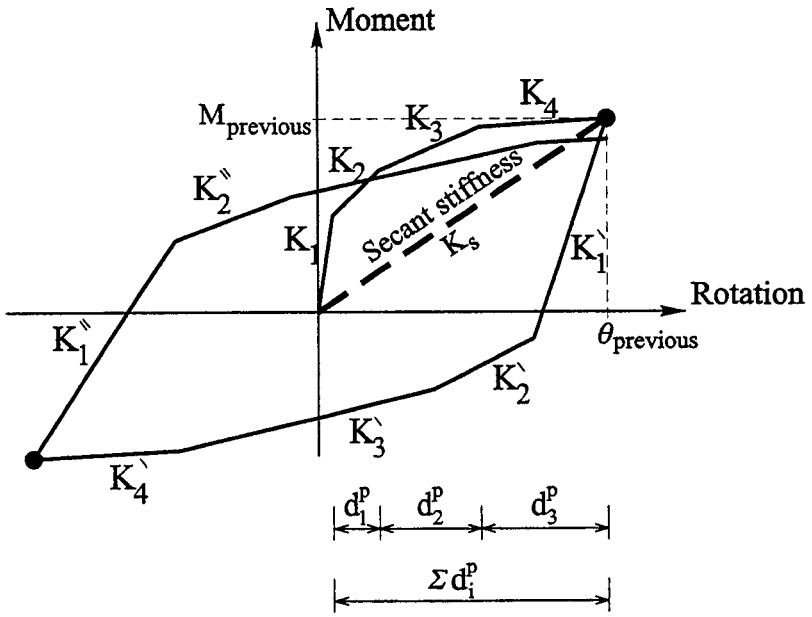

Figure 2.21 Degradation coeffecients

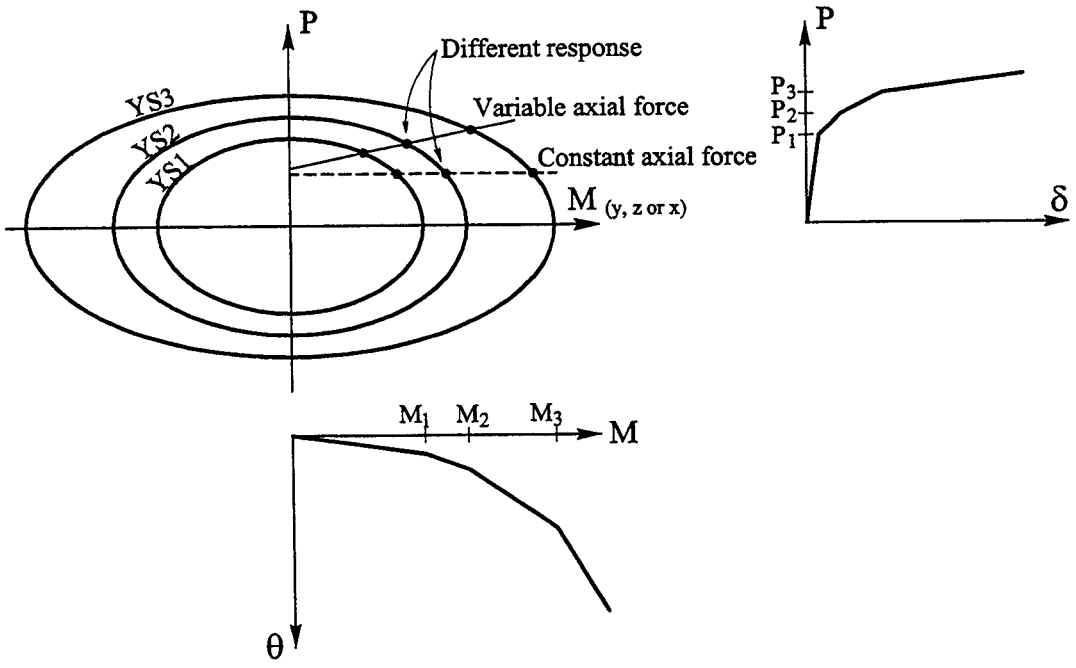

Figure 2.22 Effect of variable axial load

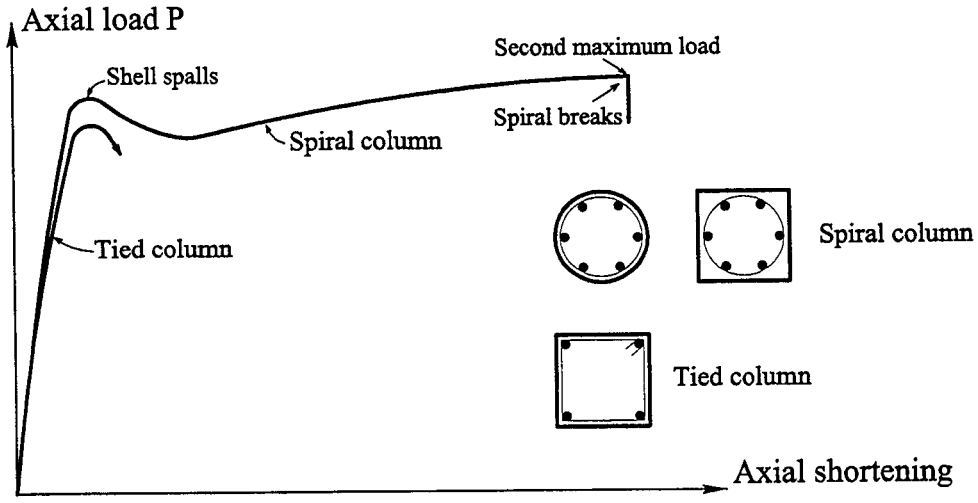

Figure 2.23 Axial load-deformation curves of tied and spiral columns (Park and Paulay, 1975).

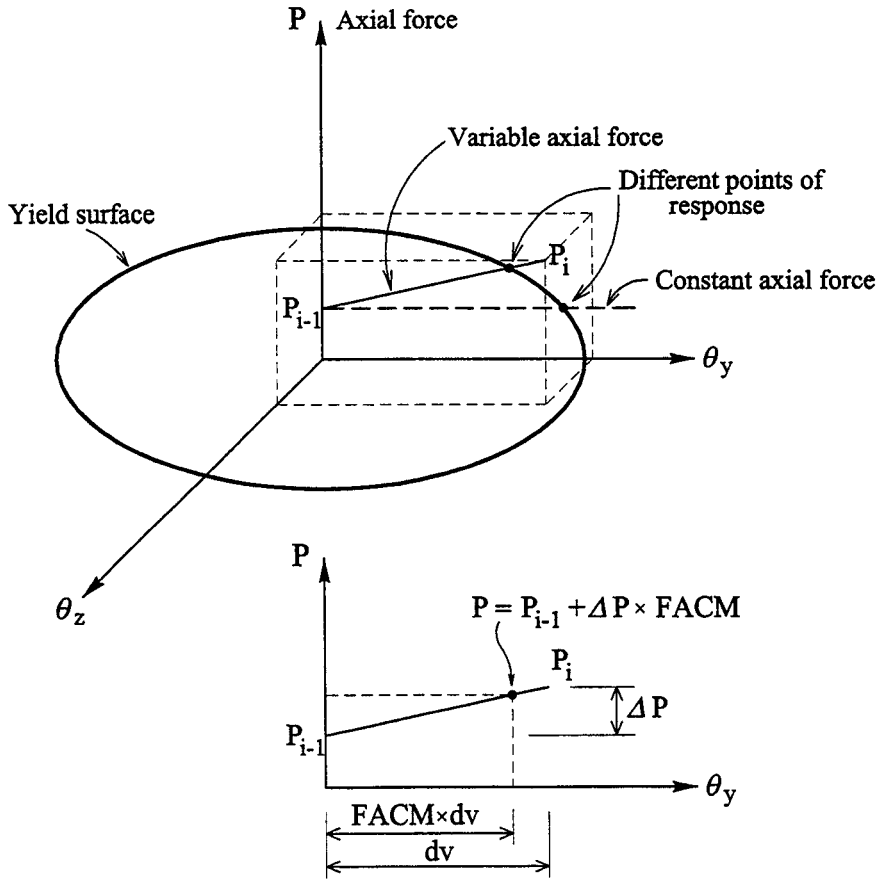

Figure 2.24 Effect of variable axial load on response

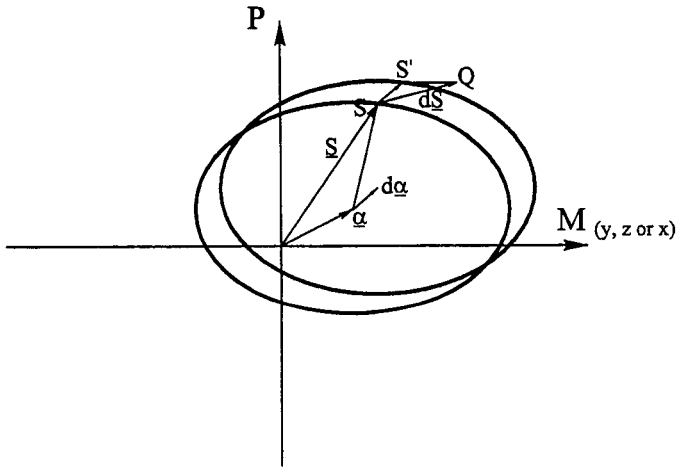

Figure 2.25 Tolerance control of state determination

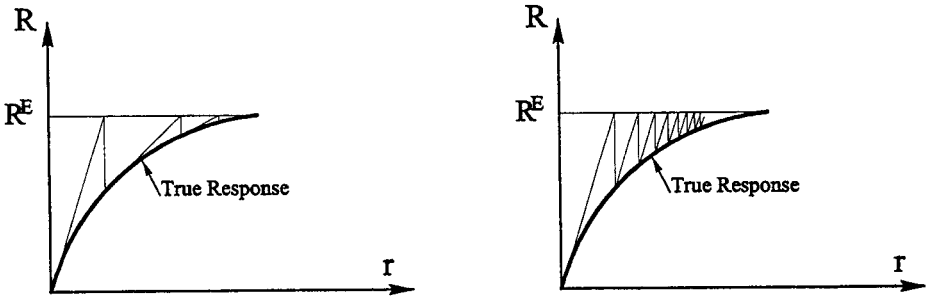

Newton Raphson Iteration
Tangent stiffness iteration

Modified Newton Raphson Iteration
Constant stiffness iteration

Figure 2.26 Iteration techniques for nonlinear analysis

CHAPTER 3

LATERAL RESPONSE ANALYSIS OF RC MEMBERS

3.1 INTRODUCTION

The proposed 3D beam-column model is based mainly on the backbone envelope of the moment-rotation relationships (M-θ) in two directions perpendicular to the element longitudinal axis, and their interaction with the applied axial load. Thus it is important to develop efficient analytical tools, as well as evaluate their sensitivity to various parameters.

The principal sources of deformation in reinforced concrete structures are axial, biaxial flexural, shear deformations including shear sliding, and bond-slip. The hysteretic load-deformation behaviour of frame members arises from the combination of these deformation mechanisms. A rational analysis of the hysteretic behaviour of reinforced concrete members needs to be based on the representation of all deformation sources and the interactions between the different mechanisms.

In this chapter, an analytical technique to obtain the moment-rotation and force-deflection relationships for reinforced concrete columns is presented. The main advantage of this procedure is that it uses the basic mechanical properties of the constitutive materials, i.e. concrete and steel, along with the geometric properties of the cross section and the element. From this basic data, and without making many

assumptions, the force-deformation response of the element is developed taking into consideration the effect of bond-slip of tensile bars, buckling of compression bars as well as flexure and shear deformations. The elementary, yet efficient, technique was verified using available experimental data. The comparison showed good agreement. A parametric study to evaluate the effect of variation in section and material properties was also conducted.

Otani and Cheung (1981) calculated the theoretical response of axially loaded columns under monotonically increasing load. They did not consider the contribution of bond slip of tensile steel bars to the rotation and deflection of the column. Moreover, a predetermined plastic hinge length based on experimental observation was used. Priestley and Park (1987) adopted a simple method for analytically predicting the plastic hinge length. The formula is based on the results of 100 tests on columns with different aspect ratios and vertical steel bar diameters. The plastic hinge length appeared to be a function of the column height and the diameter of the vertical reinforcement bar.

Soroushian et al. (1991) conducted section analysis and parametric study on chosen beam and column cross sections. Their analysis included the moment-curvature, axial load-axial strain and axial load-moment relationships. The analysis did not include prediction of the moment-rotation or the force-displacement relationships.

The available models have the disadvantages of either ignoring or oversimplifying one or more of the major components of lateral deformations, namely; flexure, bond-slip, and shear.

The objective of this chapter is to develop a simple technique to predict reliable moment-rotation and the force-deflection relationships for axially loaded columns using the available mechanical properties of concrete and steel and the geometrical properties of the element. The developed reliable simple analytical constitutive model has the advantage of accounting for all components of deformation. The predicted response of the column using this analytical method is compared to the predictions of available methods as well as test results.

3.2 PARAMETERS AFFECTING DEFORMATION AND STIFFNESS

The lateral deformation of a reinforced concrete column is a combination of flexure, bond-slip, and shear deformations. Figure 3.1 shows typical inelastic column behaviour. Failure of reinforced concrete elements may be due to any of these mechanisms, either individually or combined. Park and Ang (1985) defined the ultimate state of monotonically loaded columns and beams by categorizing them into four groups according to their ultimate failure mode, as defied in figure 3.2. Some of the parameters that affect the force-deformation relationship (i.e. stiffness, strength and ductility) of a reinforced concrete column are:

- Longitudinal steel area, yield and ultimate strength.
- Concrete compressive strength and ultimate strain.
- Transverse reinforcement content and its yield strength.
- Embedded length of the longitudinal reinforcement.

- Shear span ratio ($\frac{M}{V \cdot t}$); where M is the maximum moment in a region of constant shear V along the element length; and t is the total depth of the section.
- Level of axial load.

In the global macromodels, the flexural plasticity is separated from the shear plasticity, yet the final total behaviour is due to both plasticities. The most important input property for the flexure plasticity is the envelope of the force-deformation relationship for the element.

3.3 STRATEGY OF ANALYSIS

The procedure for developing moment-rotation and force-deflection relationships for the column involve the following steps:

Step 1: Use the mechanical properties of concrete and steel as well as the length of embedment of steel bars in concrete, along with the definition of local bond-slip relationship, to obtain the force-displacement relationship of embedded bars. The mechanical properties of concrete are f_c' and ε_{cmax}; where f_c' is the concrete cylinder compressive strength and ε_{cmax} is the maximum concrete strain. The properties of steel are: ε_y, ε_{sh}, ε_u, f_y, and f_{ult}; where ε_y is the steel yield strain, ε_{sh} is the steel strain hardening, ε_u is the ultimate steel strain, f_y is the steel yield strength and f_{ult} is the ultimate steel strength. This relationship is developed using an imposed incrementally increasing strain at the end of the bar under tension. An idealized stress-strain relationship of embedded bars is thus obtained.

Step 2: Use the cross section geometrical properties along with the stress-strain curve of confined concrete and the idealized stress-strain relationship of the tensile steel (defined from the outcome of step 1) as well as the stress-strain of compression steel (considering bar buckling), to obtain the moment-curvature relationship of the critical section. The section properties include: b, t, d, A_s, A_s', ρ_s, and s; where b, t, and d are the width, total depth and the depth to tensile reinforcement of the section, A_s, A_s' are the steel areas in tension and compression, ρ_s is the ratio of transverse steel volume to volume of concrete core and s is the spacing between ties.

Step 3: The approximated 6-points moment-curvature relationship of the critical cross section and the bond-slip properties of the tensile reinforcing bars as well as the shear stiffness of the element are then used to obtain the moment-rotation and the force-displacement relationships of the column through a procedure that takes into consideration the different stages of loading and response of an axially and laterally loaded RC column.

3.4 MODELING OF BOND-SLIP

One of the components of inelastic deformation in reinforced concrete is anchorage slip (Alsiwat and Saatcioglu, 1992). Anchorage slip occurs when the critical section of a member for flexure is located near its ends, which is the main assumption in lumped plasticity type of modeling. Formation of a flexural crack at the interface of two members strains the reinforcement crossing the crack. Widening of the crack may produce inelastic strains in the reinforcement. This results in penetration of yielding into

the anchorage zone for the reinforcement, causing extension of reinforcement. Additional rigid-body deformations may also occur due to slippage of reinforcement. The combined effect of reinforcement extension and slip in the anchorage zone may be referred to as bond-slip. Bond-slip contributes to the member end rotations. Neglecting the contribution of bond-slip in computing inelastic deformations may lead to erroneous results, especially when significant yielding of longitudinal tensile reinforcement is expected under low levels of axial compression (Razvi and Saatcioglu, 1999).

3.4.1 Anchorage slip relationships for bars subjected to pull only

Evaluation of the inelastic force-deformation relationship of reinforcement embedded in concrete requires consideration of *extension* and *slip* of reinforcement in concrete. The extension of reinforcement is the result of accumulation of strains along the length of the embedded bar. A steel bar embedded in concrete develops elastic and plastic regions. This behaviour was investigated experimentally (Viwathanatepa et al., 1979) and analytically (Filippou, 1985). The plastic region includes three sub-regions, namely, the yield plateau, strain-hardening and pullout cone sub-regions as shown in figure 3.3. In a reinforced concrete assemblage (beam-column or column-footing), it was shown experimentally that the yield plateau and the pullout cone sub-regions do not contribute much to the bar extension due to their small length (observed from test results of Viwathanatepa et al., 1979, and Ueda et al., 1984).

Slippage of reinforcement in concrete may occur if the bar is stressed up to the cutoff point. This takes place when the embedment length of the bar is not sufficiently long or when the bar pulled end is strained beyond the yield strain. Bar slip can be

obtained from a local bond-slip relationship. The bond stress at the far end of the bar q_e, can be used to determine the corresponding slip. The characteristic bond stress and slip values in this local bond slip model (q_1, q_2, q_3, δ_1, δ_2, δ_3) shown in figure 3.4 depend on the bar diameter, the concrete strength, the clear distance between lugs of the reinforcing bars and the local confinement. The local confining action varies depending on both concrete mechanical properties and geometrical characteristics of the specimen.

A simple approach with reasonable accuracy and generality was proposed by Alsiwat and Saatcioglu (1992) to establish the monotonic force-deformation relationship of reinforcement embedded in concrete. This model was found to correlate well with experimental results. After some refinements, it was utilized in the present model to determine the force bond-slip relationship. This relationship will be used to evaluate the idealized stress-strain curve of an embedded bar, taking bond-slip into consideration. The introduced refinements include accounting for the post-peak (falling branch) effects in the local bond stress-slip relationship through an incrementally increasing slip-displacement controlled procedure. Also, the extension plateau along the embedded tensile bar was limited to the elastic and strain-hardening regions only.

The first part of the solution scheme is based on applying an incrementally increasing strain at the pull side of the bar until first slippage at the cutoff side occurs. The corresponding length of each region is calculated giving the strain distribution at each increment. Once the strain distribution is known, the extension of the bar, δ_{ext}, can be computed by integrating the strains. The integration of strains can be expressed in terms of the area under the strain diagram shown in figure 3.5.

$$\delta_{ext} = \tfrac{1}{2}\, \varepsilon_y\, l_e + \tfrac{1}{2}\, (\, \varepsilon_s + \varepsilon_{sh}\,)\, l_{pl} \tag{3.1}$$

where ε_y is the steel yield strain;

l_e is the length of the tensile bar elastically stressed;

ε_s is the steel strain at the pull side of the bar;

ε_{sh} is the steel strain hardening; and

l_{pl} is the length of the tensile bar inelastically stressed.

The second part of the solution scheme is based on applying incrementally increasing slip displacement $\Delta\delta_{slip}$, at the cutoff end (from δ_{slip}=0 to δ_{slip}=δ_3). The bond stress at the cutoff end will obey the predefined local bond slip relationship (figure 3.4). Again, the corresponding length and strain at each region can be calculated and δ_{ext} is given by equation 3.1. Appendix A contains a detailed explanation of the solution scheme.

Therefore, the total bar displacement δ_s is the sum of the bar extension δ_{ext} and the bar slip δ_{slip}.

i.e. $$\delta_s = \delta_{ext} + \delta_{slip} \tag{3.2}$$

In the development of the idealized stress-strain relationship of an embedded bar taking bond-slip into consideration, the following assumptions were made:

$$\varepsilon_{(i)} = \varepsilon_s + \frac{\delta_{slip}}{l_{bar}} \tag{3.3a}$$

$$f_{(i)} = f_s \tag{3.3b}$$

where $\varepsilon_{(i)}$ and $f_{(i)}$ are the embedded steel bar strain and stress at the pull side ofthe bar at increment step i;

ε_s is the steel bar strain at the pull end;

δ_{slip} is the bar displacement due to slip; and

f_s is the steel stress associated with strain ε_s

This idealized stress-strain relationship can be used to calculate the moment-curvature (and then the moment-rotation) relationships for the critical cross section, taking bond slip into consideration.

Figure 3.6 shows the idealized stress-strain relationship for tensile steel, taking bond-slip into consideration. In case of perfect bond between concrete and steel bar with a sufficient anchorage bar length, the stress-strain curve is identical to the conventional tensile coupon test stress-strain relationship. On the other hand, insufficient anchorage length will result in reduced stiffness (this agrees with the findings of Spacone et al., 1996) and strength, which might not reach the yield strength of the bar (this agrees with the findings of Monti and Spacone, 2000). In this case, the whole bar pulls out as a one unit, and the residual strength is that resisted only by friction along the bar surface.

3.4.2 Anchorage slip relationships for bars subjected to pull and push

To simulate the simultaneous push-pull conditions of a beam bar in an interior joint, excluding the complexities of dowel action which is generated by the presence of shear at the column faces and an interaction from the adjacent bars, a simplified model

was derived. The combined effect of pull and push occurs when development lengths in tension and compression overlap inside the joint. In this case, the compression force contributes to the slippage of the bar. The slip can be computed as before, by assuming a constant bond stress over the elastic region. The elastic region has parts in tension and compression.

Tests conducted by Viwathanatepa at al. (1979) indicate that yield penetration on the compression side is very small. This implies that the bond at the pushed end increases significantly at the onset of compression yielding. This observation may be used to limit the maximum compressive stress to yield stress (i.e. $f_{sc} \leq f_y$; *where* f_{sc} is the steel stress at the push side), resulting in linear strain distribution in compression. The compressive stress distribution only affects the slip component as shown in figure 3.7.

3.4.3 Verification of the anchorage slip model

Analytical results for the two cases; monotonic pull only, monotonic pull and push are compared with available experimental data from Viwathanatepa at al. (1979) in figure 3.8 and from Ueda et al. (1986) in figure 3.9. Table 3.1 shows the properties and type of failure of each test. The comparison shows good correlation prior to the peak stress. For some specimens, the experimental data were not available for the post-peak point. The analytical method predicted the post-peak behaviour through an incremental displacement technique, which was not used in the tests.

Comparisons between the proposed model and the available different analytical models are shown in figures 3.10 and 3.11. These comparisons show that the proposed

model can be used efficiently to predict the pre- and post-peak force-displacement relationship for reinforcement bars embedded in concrete.

3.5 M-ϕ RELATIONSHIP

To develop the moment-curvature relationship of a reinforced concrete member, a section analysis needs to be conducted. Such analysis requires material models, incorporating concrete confinement and steel strain hardening. Furthermore, deformations due to yield penetration into adjoining members and resulting anchorage slip have to be considered.

To establish the ascending and descending parts of the moment-curvature relationship, an incremental curvature control (i.e. increasing curvature ϕ from 0 to failure), rather than a moment control should be conducted. Force equilibrium and strain compatibility must be maintained at each increment. Figure 3.12 shows the strain distribution over the cross section at various stages of loading. The following equations constitute the section equilibrium and the compatibility conditions:

Force equilibrium:

$$P = C_c + C_s - T \tag{3.4}$$

where P is the external axial load on the column;

C_c is the compressive force in the compression zone of the section;

C_s is the compressive force in the compression steel bars; and

T is the tensile force in the tension steel bars.

Strain distribution

Linear strain distribution is assumed throughout all incremental loading stages.

$$\frac{\varepsilon_c}{c} = \frac{\varepsilon_s'}{c - d'} = \frac{\varepsilon_s}{d - c} \tag{3.5}$$

where c is the depth of the concrete compression zone;

d is the depth to tensile reinforcement of the section;

d' is the depth to compressive reinforcement of the section; and

ε_c, ε_s and ε_s' are the strains in concrete, tensile and compressive steel bars, respectively.

Thus the moment resisted by the critical cross section at any loading increment is calculated as the sum of moments of all the forces about any arbitrary axis.

Definition of concrete stress-strain relationship

Several investigators proposed stress-strain relationships for concrete confined by rectangular hoops. Some of the proposed curves may have parabolic, tri-linear or even linear approximation for the actual stress-strain relationship. In this study, the modified Kent and Park model (Park et al., 1982) shown in figure 3.13 was used. In this model, the maximum concrete stress reached (at point B) and its corresponding strain are assumed to be dependent on the degree of confinement provided by the lateral hoops through the multiplier factor K. The maximum confined concrete compressive strain ε_{cmax}, was determined using the following equation proposed by Corley (1966) in MPa units:

$$\varepsilon_{c\max} = 0.003 + 0.02\left(\frac{b}{z}\right) + \left(\frac{\rho_s \cdot f_y}{140}\right)^2 \tag{3.6}$$

where z is the distance along the span from section of maximum moment to adjacent section of zero moment, and ρ_s is the ratio of transverse steel volume to volume of concrete core.

Definition of compression steel stress-strain relationship

The stress-strain relationship of compression steel will be the same as that of a tensile coupon test, provided that the bar stability is maintained under compression. Stability of compression reinforcement can be expressed in terms of the bar slenderness ratio, where slenderness ratio is defined as the ratio of unsupported bar length between two ties, s, to its diameter, d_b. If the slenderness ratio of rebar is high, the stress-strain relationship may show unloading immediately after yielding.

Experimental and analytical verification were done by several researchers to investigate the buckling of reinforcing bars in compression (Mau and El-Mabsout, 1989; Mau, 1990; Yalcin and Saatcioglu, 2000; Bayrak and Sheikh, 2001). The empirical relationships suggested by Yalcin and Saatcioglu (2000) were adopted in the current analysis. Figure 3.14 illustrates the stress-strain relationship for compression reinforcement as a function of bar slenderness ratio $\frac{s}{d_b}$.

Figure 3.15 shows a general moment-curvature relationship. A simplified six point M-ϕ diagram is developed to approximate the curve. The six points are chosen such that they represent different stages of behaviour of a reinforced concrete section subjected to axial load and increasing curvature, such that:

Point (1); M_{cr}: cracking moment, when the principal tensile stress reaches the concrete tensile strength taken to be $0.33\sqrt{f_c'}$ (MPa).

Point (2); M_y: moment at the first yield of the tension steel.

Point (3); ϕ_3: intermediate ϕ between ϕ_y and ϕ_{ult}.

Point (4); M_{ult}: maximum moment with corresponding curvature ϕ_{ult}.

Point (5); ϕ_5: intermediate ϕ between ϕ_{ult} and ϕ_{fail}.

Point (6); ϕ_{fail}: maximum curvature with corresponding moment M_{fail}.

3.6 MODELING OF SHEAR STIFFNESS AND STRENGTH

The shear deflections were calculated using the elastic shear stiffness expression derived by Park and Paulay (1975). The shear stiffness per unit length of the element, K_v, was defined by the following expression:

$$K_v = \frac{\rho_s \sin^2 \alpha \cos^2 \alpha}{\sin^4 \alpha + n\rho_s} E_s bd \qquad (3.7a)$$

where E_s is the elastic modulus of shear reinforcement, n is the modular ratio E_s/E_c, E_c is the elastic modulus of concrete taken to be $4500\sqrt{f_c'}$ (MPa) and α is the inclination of diagonal shear cracks.

In the case of assumed 45° diagonal cracks, the previous equation reduces to:

$$K_{v,45} = \frac{\rho_s}{1+4n\rho_s} E_s bd \tag{3.7b}$$

In the presence of axial compression, the diagonal cracks tend to be flatter than 45°, therefore equation 3.7b, which is based on the truss analogy with 45° struts, is conservative.

Figure 3.16 shows the combined flexure and shear response of axially and laterally loaded reinforced concrete column. Curves denoted cases 1, 2 and 3 represent the column's total flexural response calculated using the aforementioned procedures and section 3.7. The broken line represents the shear strength envelope calculated using the equations proposed by Priestley et al. (1994) and explained in Chapter 1. Three cases of combined responses might arise, namely: (1) Ductile behaviour where the total flexure response is less than V_f; (2) Moderate ductility behaviour with shear failure when the total flexure response is in between V_f and V_i; and (3) Limited ductility behaviour with brittle shear failure when the total flexure response is higher than V_i.

For cases 2 and 3 a shear failure is expected. The determination of the unloading stiffness in case of shear failure (post-peak failure response) has been explored by few researchers. Ricles et al. (1998) proposed an unloading stiffness for a moderate ductility failure (case 2) with a negative value of the element's initial elastic shear stiffness. In case of brittle shear failure (case 3), a negative unloading shear stiffness in the range of 25 to 50% of the elastic shear strength was adopted. More recently, Aschheim (2000), used the degrading Mohr-Coulomb failure surface in an attempt to analytically model the

shear strength degradation in RC members. The tentative model was verified using seven specimens. More refinement to the model was recommended.

In the current analysis, a simple approach was adopted for the determination of the unloading post-shear stiffness. It is assumed that the column will undergo post-shear stiffness degradation, K_{vy}, which is equivalent to the loss of strength from V_i to V_r through a lateral displacement equivalent to twice the yield displacement. This postulate is valid for a moderate ductility type of response (case 2). On the other hand, a limited ductility response (case 3) will be accompanied by brittle shear failure with a higher unloading stiffness, which is equivalent to the loss of strength from V_i to V_r through a lateral displacement equivalent to the yield displacement.

i.e. $$K_{vy} = -\frac{V_i - V_r}{2\Delta_y} \qquad \text{for moderate ductility} \qquad (3.8a)$$

$$K_{vy} = -\frac{V_i - V_r}{\Delta_y} \qquad \text{for limited ductility} \qquad (3.8b)$$

3.7 M-θ AND M-Δ RELATIONSHIPS

The rotation θ and deflection Δ of a reinforced concrete member at any point along its length is due to the distributed curvature of the member along its length and the lumped rotation near the fixed end due to the slippage of steel bars at the tension side of the member as well as the member shear deformation. The total rotation and deflection at any point along the RC member is the algebraic sum of these three components as illustrated in figure 3.17.

i.e. $$\Delta_{tot} = \Delta_f + \Delta_s + \Delta_v \tag{3.9a}$$

$$\theta_{tot} = \theta_f + \theta_s + \gamma_v \tag{3.9b}$$

where Δ_{tot} is the total lateral tip displacement corresponding to the total rotation θ_{tot};

Δ_f and θ_f are the lateral deflection and rotation due to flexure;

Δ_s and θ_s are the lateral deflection and rotation due to reinforcement bond-slip;

Δ_v and γ_v are the lateral deflection and rotation due to shear.

The rotation θ_f and deflection Δ_f of a member may be calculated by integrating the distributed curvatures along the member. Since the curvature is defined as the rotation per unit length of member, the rotation between any two points A and B of the member as shown in figure 3.17 is given by:

$$\theta_f^{AB} = \int_A^B \phi \, dx \tag{3.10a}$$

The transverse deflection of point B from the tangent to the axis of the member at point A due to curvature along the whole length of member between those points is given by:

$$\Delta_f^{AB} = \int_A^B x\phi \, dx \tag{3.10b}$$

Equations 3.10a and 3.10b are generalizations of the moment-area theorems, and they apply whether elastic or plastic curvatures are involved.

The lumped rotation at the fixed end point, θ_s, due to tensile reinforcement bond-slip can be defined as:

$$\theta_s = \frac{\delta_s}{d-c} \tag{3.11a}$$

The corresponding deflection at any point at distance x from support will be equal to $\theta_s \cdot x$ and the maximum tip deflection will be:

$$\Delta_s = \theta_s L = \delta_s \frac{L}{d-c} \tag{3.11b}$$

The value of δ_s is determined through the bond-slip analysis of the embedded reinforcement bar under monotonic pull, as explained in section 3.4.

The shear deformation γ_v and shear deflection Δ_v can be calculated from the element's shear stiffness assuming 45° cracks, $K_{v,45}$. Thus:

$$\theta_v = \frac{V}{K_{v,45}} \tag{3.12a}$$

$$\Delta_v = \frac{VL}{K_{v,45}} \tag{3.12b}$$

where V is the lateral force on the column tip.

Thus at each stage of loading, the following holds:

$$\theta_{tot} = \int_0^L \phi \, dx + \frac{\delta_s}{d-c} + \frac{V}{K_{v,45}} \tag{3.13a}$$

$$\Delta_{tot} = \int_0^L x\phi \, dx + \frac{\delta_s}{d-c} L + \frac{VL}{K_{v,45}} \tag{3.13b}$$

The following subsections explain the behaviour at each stage of loading.

Stages of M-ϕ relationship

Stage 1; M=0 to M_{cr}

At this stage the member is not cracked and it resists the applied forces with its gross inertia. Figure 3.18a shows the external moment distribution as well as the corresponding curvature along the member length.

Stage 2; M_{cr} to M_y

The top bars are stressed to the yield point. A vertical crack at the section with maximum moment will appear. Other vertical cracks will be initiated and start to open at the location of the maximum tensile stress at the fixed end. Although the distribution of the external moments is linear, the distribution of the curvature will be bilinear along the member length as shown in figure 3.18b.

Stage 3; M_y to M_3 and Stage 4; M_3 to M_u

At these two stages, vertical cracks will widen and inclined cracks will open and widen. Figures 3.18c and 3.18d illustrate that at the vicinity of the fixed end (maximum moment), the diagonal cracks, instead of being parallel will tend to radiate from the compression zone at the load point. When the flexural reinforcement has yielded, these cracks increase in width. At this stage, it is prudent to assume that little shear can be transferred by either aggregate interlock or dowel action. Consequently, nearly the whole shear force will have to be transferred across the compression zone of the vertical section adjacent to the support.

After the yielding of tensile steel, a plastic hinge starts to develop at the vicinity of the critical section. Flexural plastic rotation due to the formation of the plastic hinge starts to develop (Park and Paulay, 1975). An idealized constant curvature along a plastic hinge length to account for the flexural plastic rotation, is adopted as shown in figures 3.18c and 3.18d.

Various empirical expressions have been proposed by researchers for the equivalent length of plastic hinge L_p. These are reviewed below.

Baker (1956): $$L_p = 0.8k_1k_3\left(\frac{L}{d}\right)c \tag{3.14a}$$

Where c is the neutral axis depth at ultimate moment;

L is the distance of the critical section to the point of contraflexure;

D is the effective depth of the member; and

K_1 and k_3 are factors depending on the steel and concrete strengths.

Sawyer (1964): $$L_p = 0.25d + 0.075L \tag{3.14b}$$

Corley (1966): $$L_p = 0.5d + 0.2\sqrt{d}\left(\frac{L}{d}\right) \tag{3.14c}$$

Mattock (1967): $$L_p = 0.5d + 0.05L \tag{3.14d}$$

Priestley and Park (1987): $L_p = 0.08L + 0.02d_b$ (MPa) (3.14e)

Xiao et al. (1998): $$L_p = 0.08L\left(\frac{f_s}{f_y}\right) + 0.02d_b f_s \quad \text{(MPa)} \tag{3.14f}$$

Where d_b is the longitudinal bar diameter;

f_s is the stress in extreme tensile longitudinal bar; and

f_y is the yield strength of longitudinal reinforcement.

The second term in the last two equations accounts for the strain penetration of longitudinal bars into the foundation. The length of the hinge in the last equation varies according to the stress in the extreme tensile longitudinal bars.

In the current analytical procedure, the strain penetration of the longitudinal bars into the foundation is explicitly accounted for through the bond-slip modeling, thus the last two equations should not be used herein. Mattock's equation 3.14d was used to model the equivalent length of plastic hinge L_p to be used in estimating ultimate curvature requirements.

A linear variation of the plastic hinge length from zero to L_p at yield and ultimate stages, respectively was assumed. A full equivalent plastic hinge length, L_p, is assumed to form at ultimate stage as shown in figure 3.15.

Stage 5; M_u to M_5 and Stage 6; M_5 to M_{fail}

Although the moment capacity of the member decreases after its ultimate moment value M_u, the curvature, rotation and tip-deflection of the member increases. Figures 3.18e and 3.18f show the external moment distribution and the corresponding idealized curvature distribution.

3.8 COMPARISONS WITH EXPERIMENTAL RESULTS

Comparisons between the proposed analysis procedure and available measured experimental curves for force-deformation relationship and its components are shown in figure 3.19. The specimens used for comparison were chosen to emphasis the

contribution of different sources of deformations (flexure, bond-slip and shear) to the total column's response. Specimens U6 and U4 have a significant bond-slip deformation (due to the reduced anchorage length $l_{bar}/d_b = 20$), while specimen R3A failed by brittle shear (due to the reduced shear capacity). The comparisons indicate that the inelastic force-deformation relationships for reinforced concrete columns can be computed with a reasonable degree of accuracy using the analytical models and the procedure employed in this study. It can be also seen that results from the presented analytical procedure showed closer agreement to the experimental results as compared to other analytical models.

3.9 EFFECT OF VARIATION IN SECTION AND MATERIAL PROPERTIES

In order to verify the results of the proposed procedures and to demonstrate its applicability, some of the parameters that affect the force-deformation behaviour of reinforced concrete columns were examined for their influence on such behaviour. A typical column as shown in figure 3.20 was selected as a control column. The influence of variations in concrete strength, steel yield stress, vertical steel ratio, horizontal confinement, tensile bars embedded length, and the axial load level was investigated.

Figure 3.21 shows the influence of these variables on the force-tip displacement relationship of a fixed-fixed reinforced concrete column. The results of the numerical study indicated that:

1- Variations in concrete compressive strength have relatively small effect on lateral load carrying capacity and lateral stiffness (15% change in the range from f'_c=20MPa to

40MPa). These variations have significant effects on drift ratio (≈40% change in the range from f_c'=20MPa to 40MPa) as shown in figure 3.21a. The drift ratio is taken to be ratio of the total lateral displacement to the column height.

2- Variations in steel yield strength have considerable effect on the lateral load carrying capacity. A decrease in the steel yield strength of 25% results in a decrease in the lateral load capacity by 20%, while an increase of steel yield strength of 25% results in an increase in the lateral load capacity by 10%. However, variations in steel strength have almost no effect on lateral stiffness and drift (figure 3.21b).

3- Variations in the area of longitudinal steel strongly influence the lateral load carrying capacity and stiffness of a reinforced concrete column, while having almost no effect on the lateral drift ratio. Decreasing the vertical steel content to its half decreases the lateral load capacity and stiffness by 25%, while increasing the vertical steel content to double its value increases the lateral load capacity and stiffness by 50% as shown in figure 3.21c.

4- Variations in lateral confinement have a substantial influence on the lateral drift ratio, while having little influence on the lateral load carrying capacity or stiffness. A 300% increase in the lateral steel ratio (by reducing the tie spacing to its third) will result in a 200% increase in the lateral drift ratio as shown in figure 3.21d.

5- Decreasing the embedded length of the tensile bars of a reinforced concrete column below 25 d_b decreases the lateral load capacity and stiffness by approximately 25% (due to the increase in the contribution of bond-slip deformation at the fixed end to the column's total deformation), while increasing the lateral drift ratio by approximately 75% as shown in figure 3.21e.

6- The level of applied axial load changes the behaviour of the RC columns lateral response noticeably. For axial load levels below the balanced load ($\approx 0.4P_o$ where P_o is the axial load capacity of the column), increasing the axial load decreases the lateral load drift ratio while increasing the lateral load capacity. However, increasing the axial load level higher than the balanced load decreases the lateral load capacity as shown in figure 3.21f.

3.10 SUMMARY

In this chapter, a rational analytical procedure that depends on the basic properties of a reinforced concrete member to achieve the force-deflection envelope of axially and laterally loaded columns, was developed. This method takes the effect of bond-slip of tensile bars, buckling of compression bars as well as flexure and shear deformations into account. The effect of concrete tension stiffening was not considered. The procedure showed good correlation with experimentally measured force-displacement relationships for RC columns and its corresponding deformation components.

As an example of the application of the procedure, a numerical study was performed on the sensitivity of the reinforced concrete columns' lateral response characteristics to the changes in concrete and steel strength, vertical and horizontal steel ratios, embedment length of tensile steel, and the level of axial load.

It is concluded that the described analytical procedure can be used to predict the backbone relationships for cyclically loaded columns.

Table 3.1 Test data

Specimen	Type of loading	Bar dia. d_b (mm)	Embedded length l_{bar} (mm)	$\frac{l_{bar}}{d_b}$	f_c' (MPa)	f_y (MPa)	f_u (MPa)	ε_y	ε_{sh}	ε_u	Mode of failure	
											Test	Model
#3[1]	Pull	25.4	635	25	32	469	690	0.00232	0.016	0.12	Bar fracture	Bar fracture
#13[1]	Pull & push	25.4	635	25	32	469	737	0.00232	0.016	0.1	Bar pullout	Bar pullout
#10[1]	Pull & push	19	508	27	30	475	737	0.00232	0.017	0.1	Bar fracture	Bar pullout
#16[1]	Pull & push	32	635	20	29	471	737	0.00232	0.015	0.1	Bar pullout	Bar pullout
S61[2]	Pull	19	405	21	24	438	775	0.00215	0.00405	0.0609	Bar pullout	Bar pullout
S64[2]	Pull	19	610	32	29	438	775	0.00215	0.00405	0.0609	No failure†	Bar fracture
S101[2]	Pull	32	610	19	20	414	660	0.00203	0.01003	0.052	Bar pullout	Bar pullout

[1] Viwathanatepa et al. (1979)

[2] Ueda et al. (1986)

† Failure of connection between the bar and the loading equipment limited the capacity and the ductility achieved in test

Table 3.2a Steel bars anchorage data

Specimen	Type of loading	Bar dia. d_b (mm)	Embedded length l_{bar} (mm)	$\frac{l_{bar}}{d_b}$	f_c' (MPa)	f_y (MPa)	f_u (MPa)	ε_y	ε_{sh}	ε_u
U6[1]	Pull	25	500	20	37.3	437	700	0.0022	0.0115	0.140
U4[2]	Pull	25	500	20	32	438	700	0.0022	0.0115	0.140
R3A[3]	Pull	19.5	790	40.5	34.5	470	690	0.0024	0.01	0.150

Table 3.2b Specimen details

Specimen	P (kN)	b (mm)	t (mm)	d (mm)	d' (mm)	A_s (mm^2)	A_s' (mm^2)	ρ_s %	s_h (mm)	b'' (mm)
U6[1]	600	350	350	305	45	1473	1473	0.975	65	298
U4[2]	600	350	350	305	45	1473	1473	1.27	50	298
R3A[3]	500	405	610	570	40	1500	1500	0.22	127	570

[1] Saatcioglu and Ozcebe (1989)
[2] Saatcioglu and Ozcebe (1987)
[3] Priestley et al. (1993)

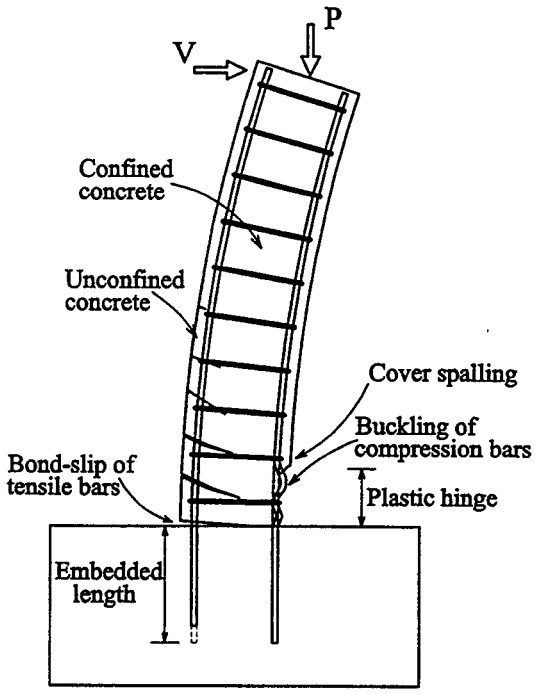

Figure 3.1 Typical inelastic column behaviour

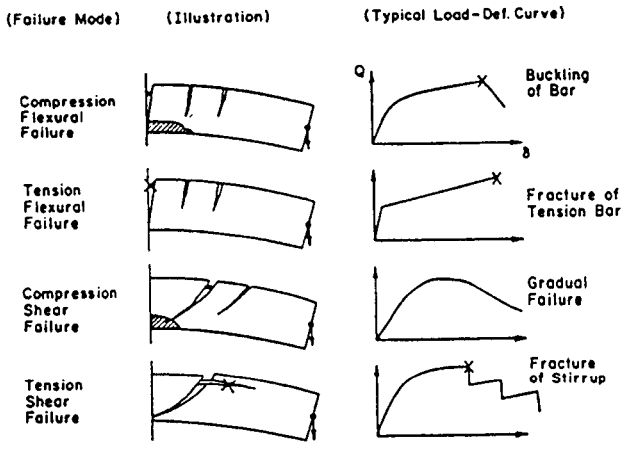

Figure 3.2 Ultimate failure modes (Park and Ang, 1985)

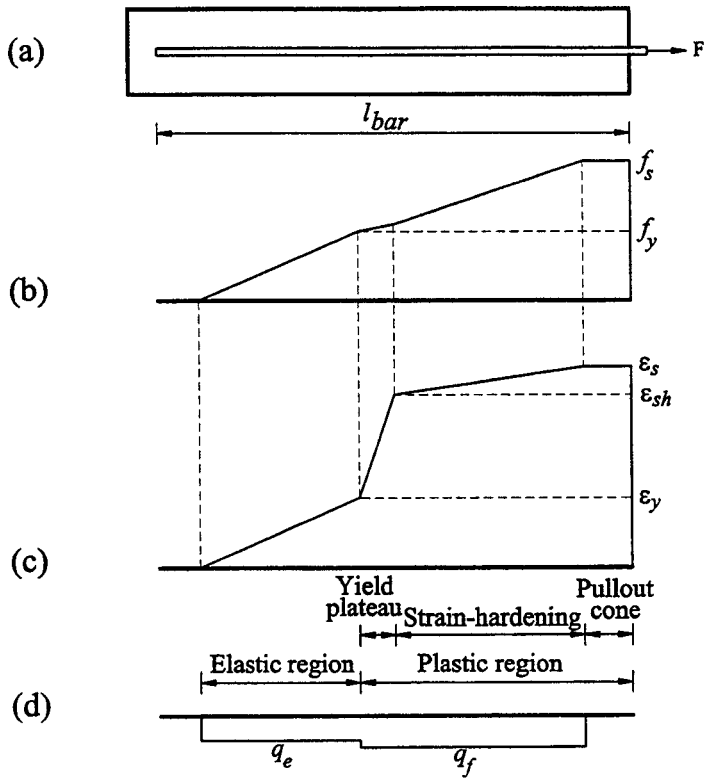

Figure 3.3 (a) Reinforcing bar embedded in concrete; (b) Stress distribution; (c) Strain distribution; (d) Bond stress between concrete and steel (Alsiwat and Saatcioglu, 1992)

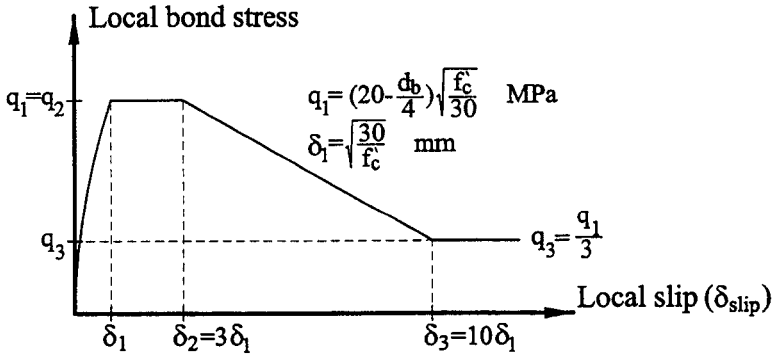

Figure 3.4 Local bond stress-slip model (Ciampi et al., 1982, and Eligehausen et al., 1983)

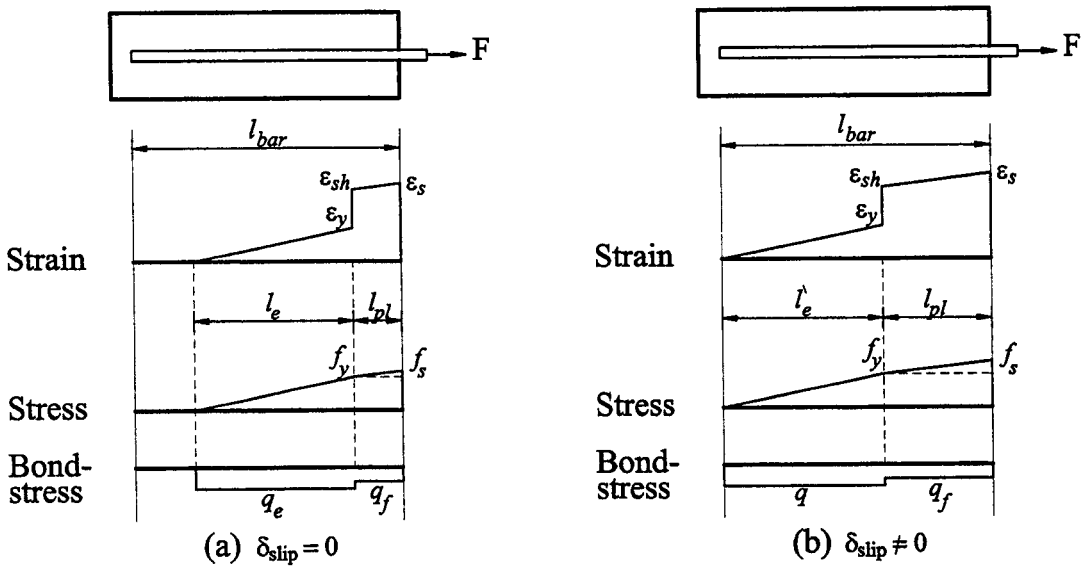

Figure 3.5 Embedded bar properties (a) before bar slip; (b) after bar slip (case of pull only)

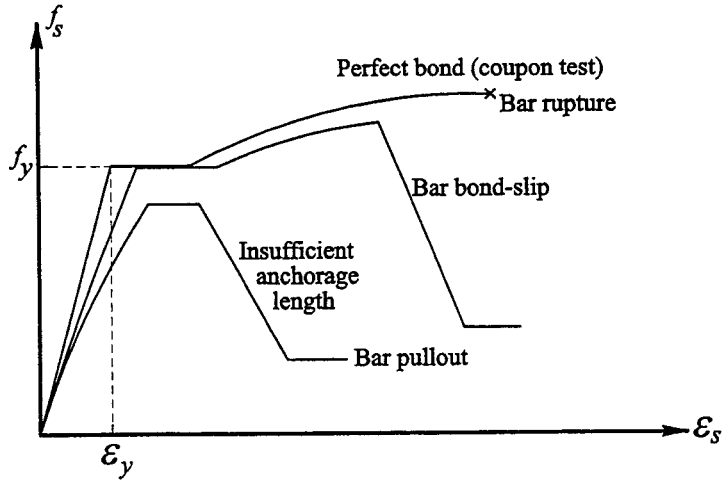

Figure 3.6 Idealized stress-strain relationship for tensile steel, taking bond-slip and anchorage with concrete into consideration

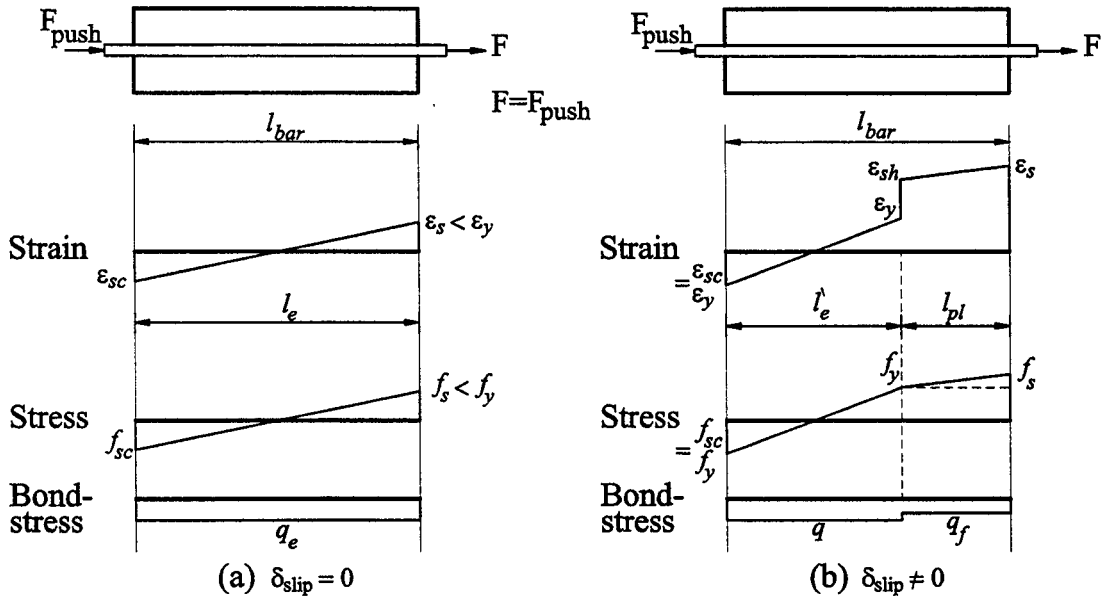

Figure 3.7 Embedded bar properties (a) before yield; (b) after yield (case of pull and push)

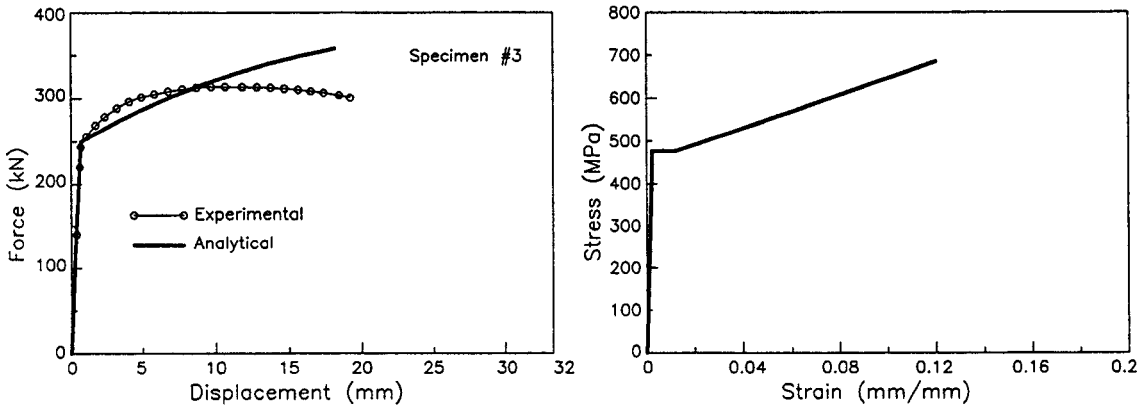

Figure 3.8 Force-displacement and stress-strain relationships for embedded bars tested under monotonic pull, and monotonic pull and push (Viwathanatepa et al., 1979). (a) Specimen 3, pull only (Continued)

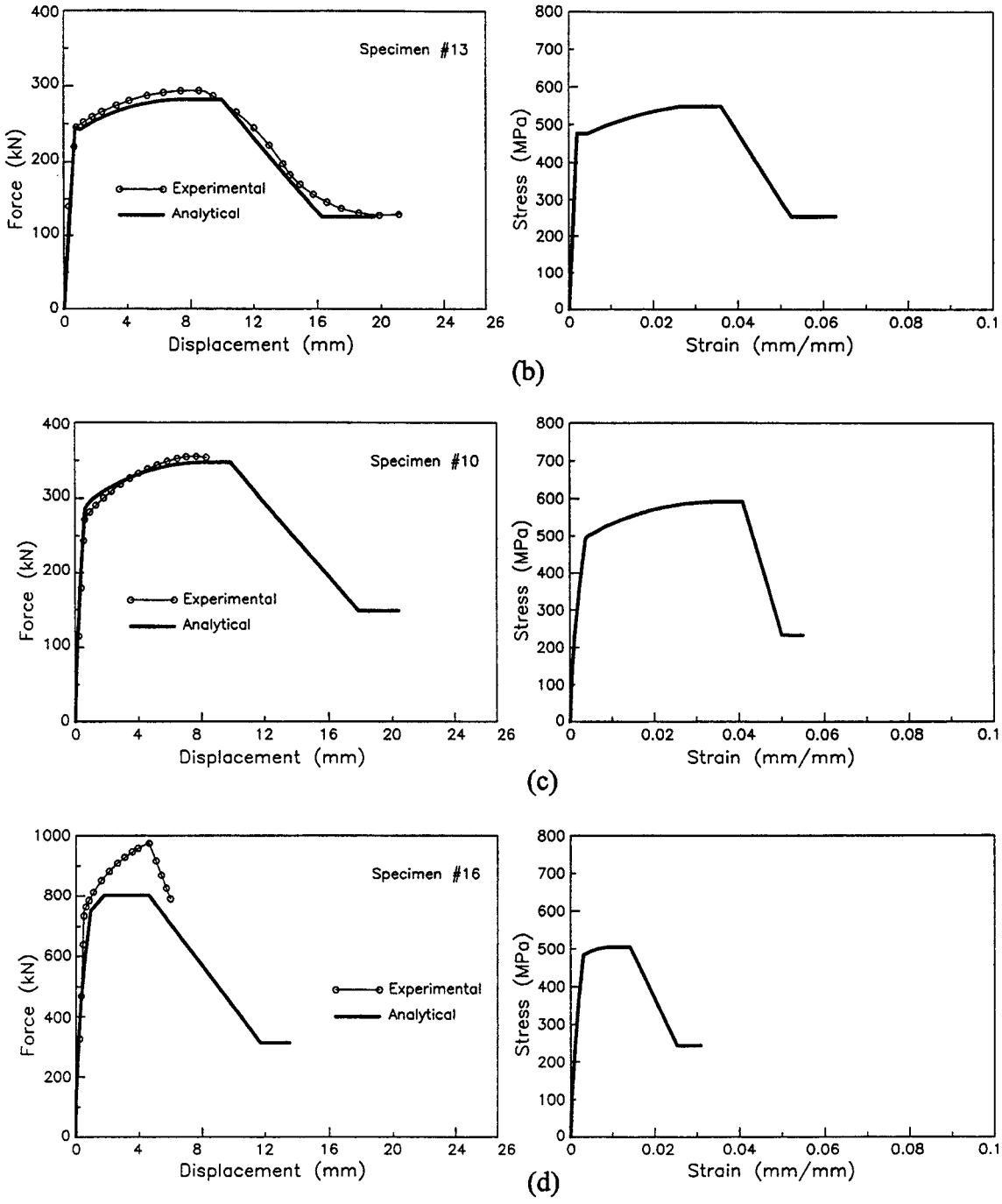

Figure 3.8 Force-displacement and stress-strain relationships for embedded bars tested under monotonic pull, and monotonic pull and push (Viwathanatepa et al., 1979). (b) Specimen 13, pull and push; (c) Specimen 10, pull and push; (d) Specimen 16, pull and push

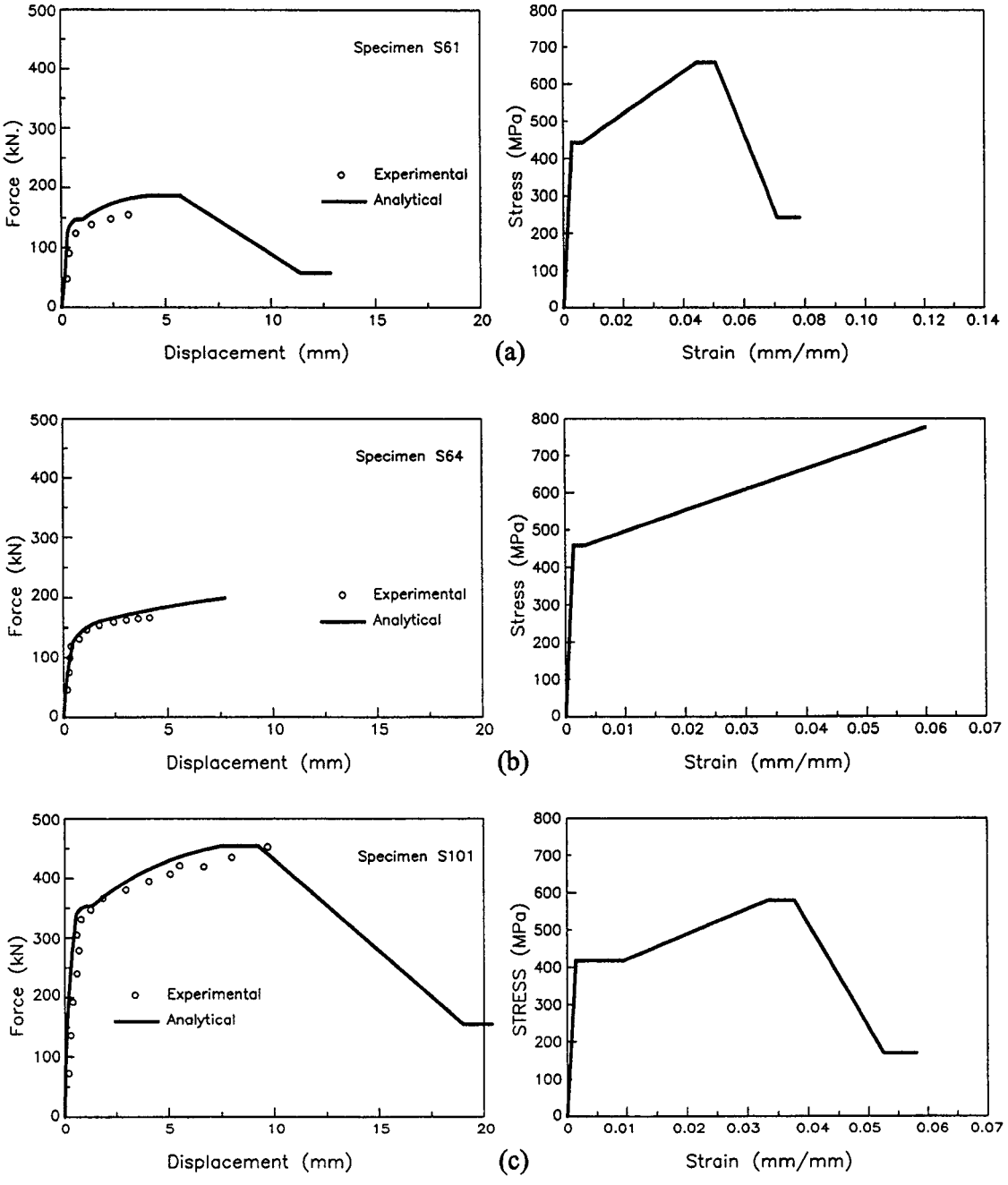

Figure 3.9 Force-displacement and stress-strain relationships for embedded bars tested under monotonic pull (Ueda et al., 1986).
(a) Specimen S61; (b) Specimen S64; (c) Specimen S101

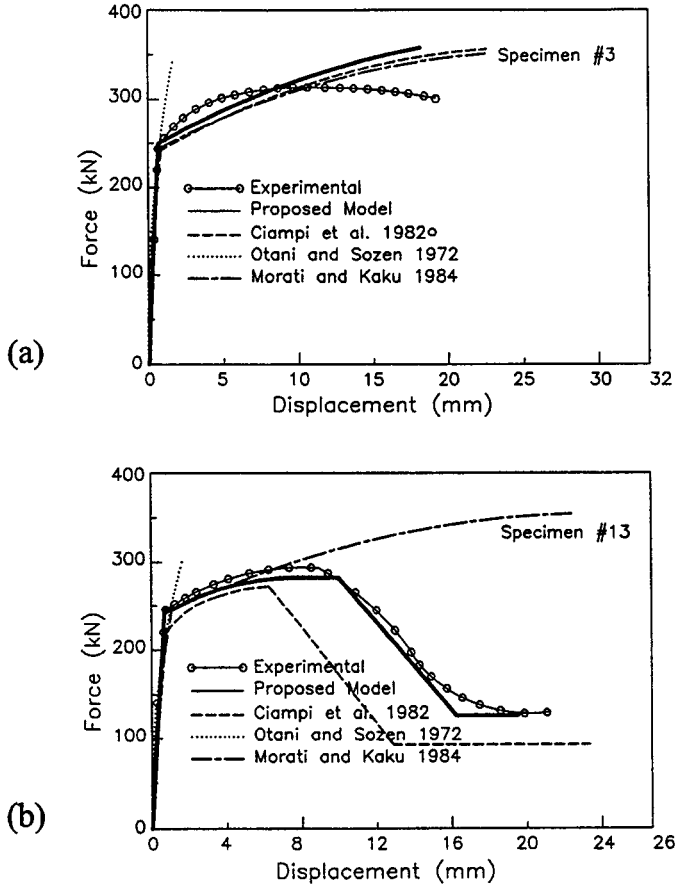

Figure 3.10 Comparisons with previous analytical predictions (Viwathanatepa et al., 1979) (a) pull only; (b) pull and push

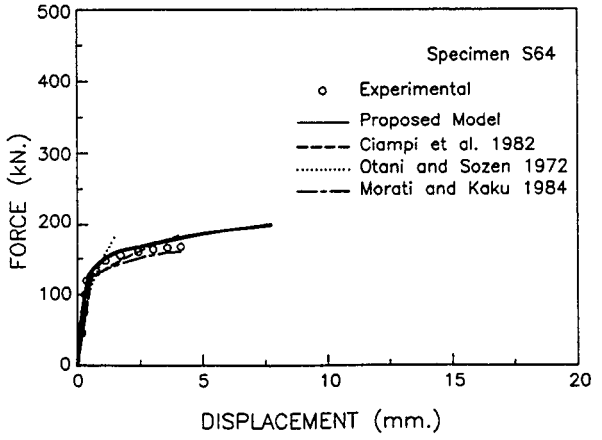

Figure 3.11 Comparison with previous analytical predictions (Ueda et al., 1986)

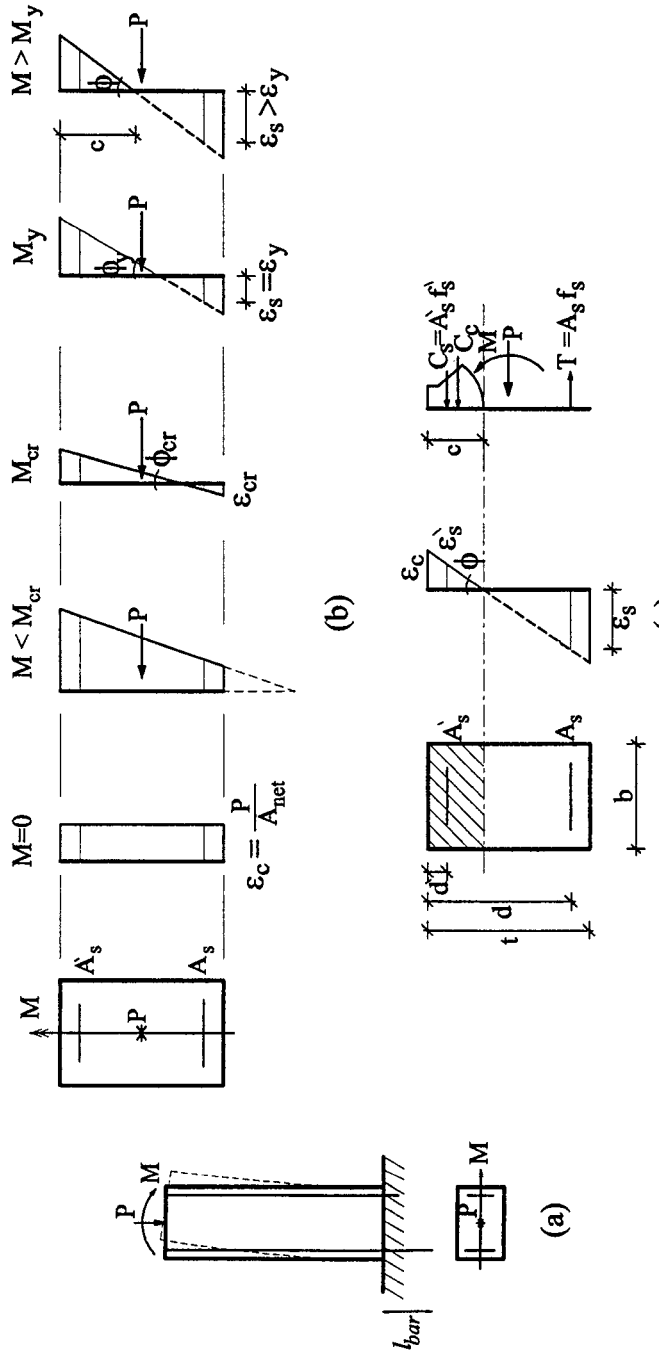

Figure 3.12 (a) Axially loaded RC column subjected to increasing curvature; (b) Strain diagram at different stages; (c) Force equilibrium and compatibility condition

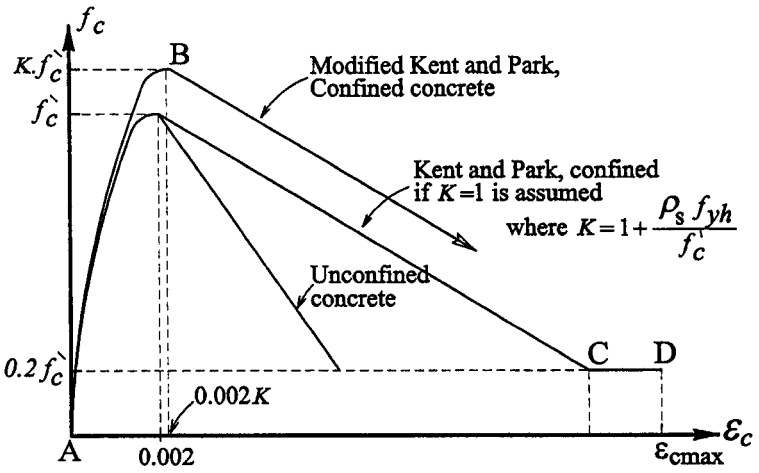

Figure 3.13 Stress-strain curve for concrete confined by rectangular hoops, modified Kent and Park (Park et al., 1982)

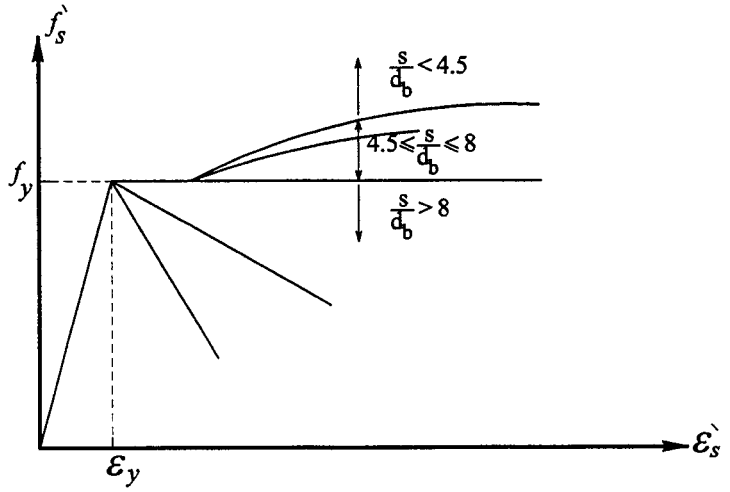

Figure 3.14 Stress-strain relationship for compression steel (Yalcin and Saatcioglu, 2000)

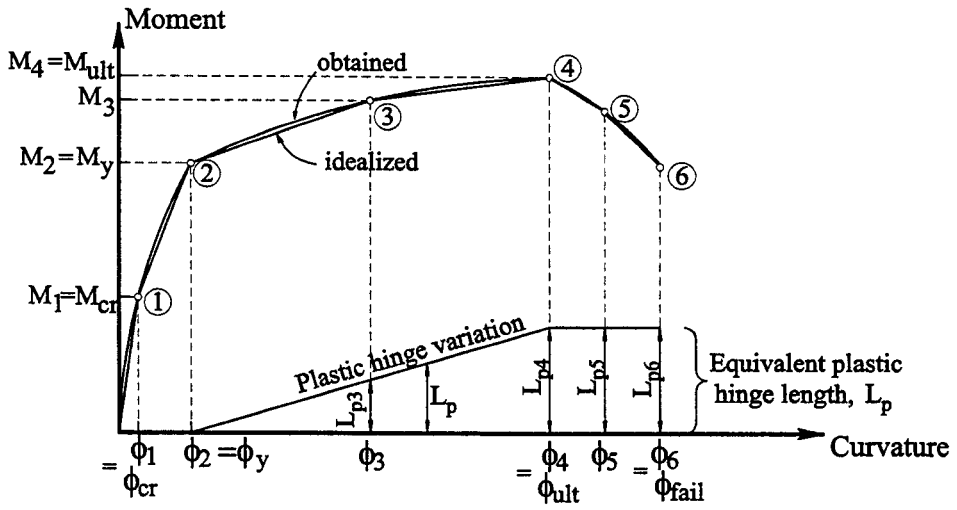

Figure 3.15 Obtained and idealized M-ϕ relationships

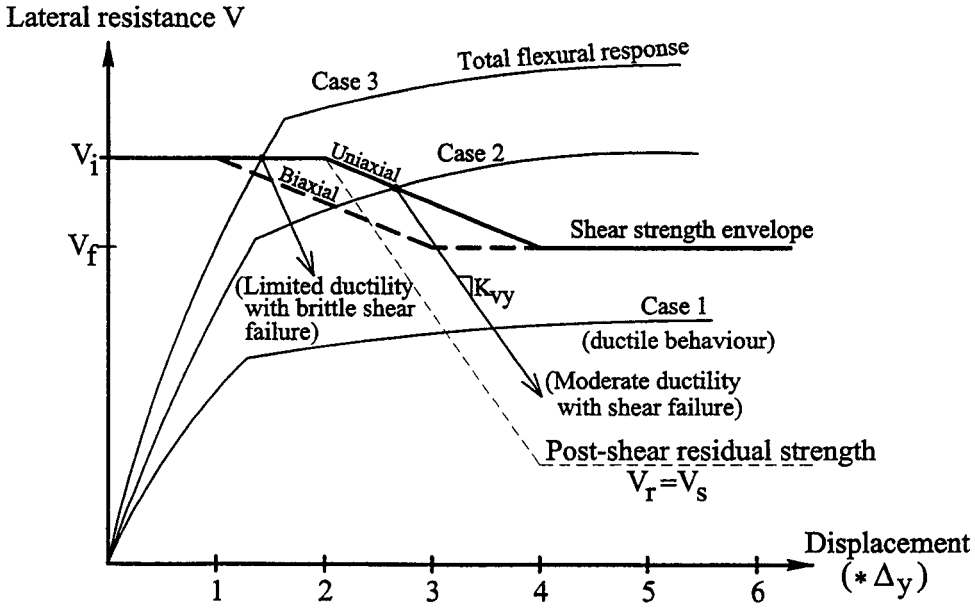

Figure 3.16 Combined flexure and shear response for columns

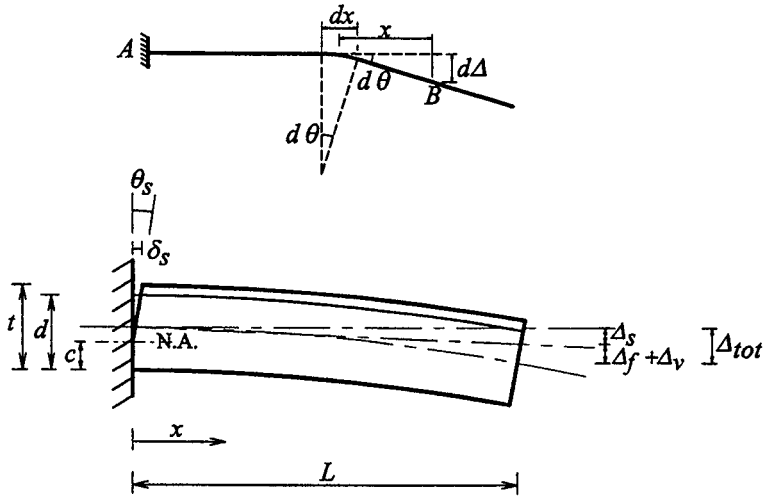

Figure 3.17 Deformation components of an element

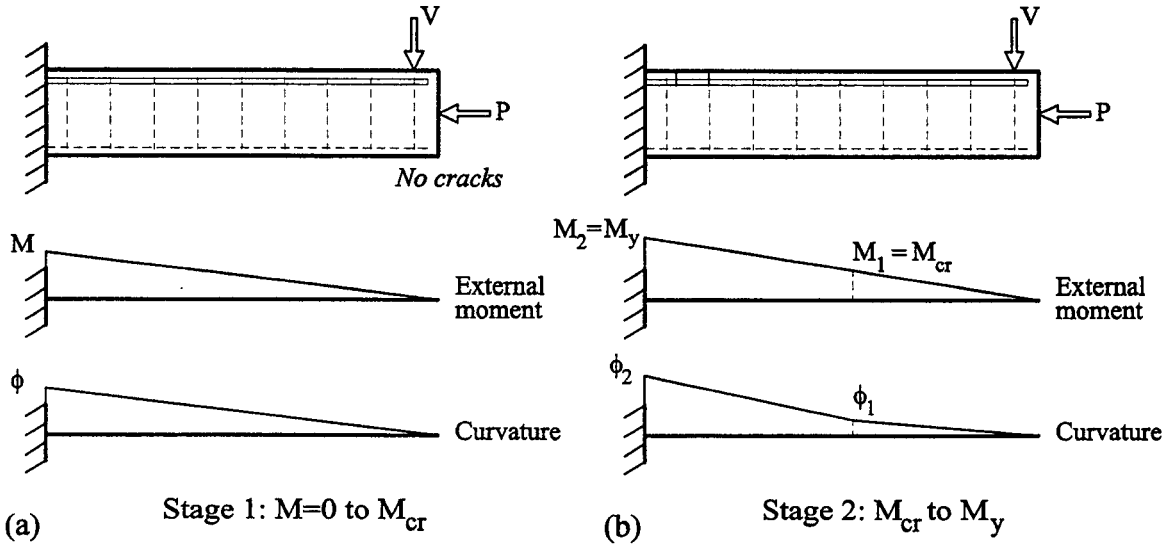

Figure 3.18 Various stages of laterally and axially loaded RC member (Continued)

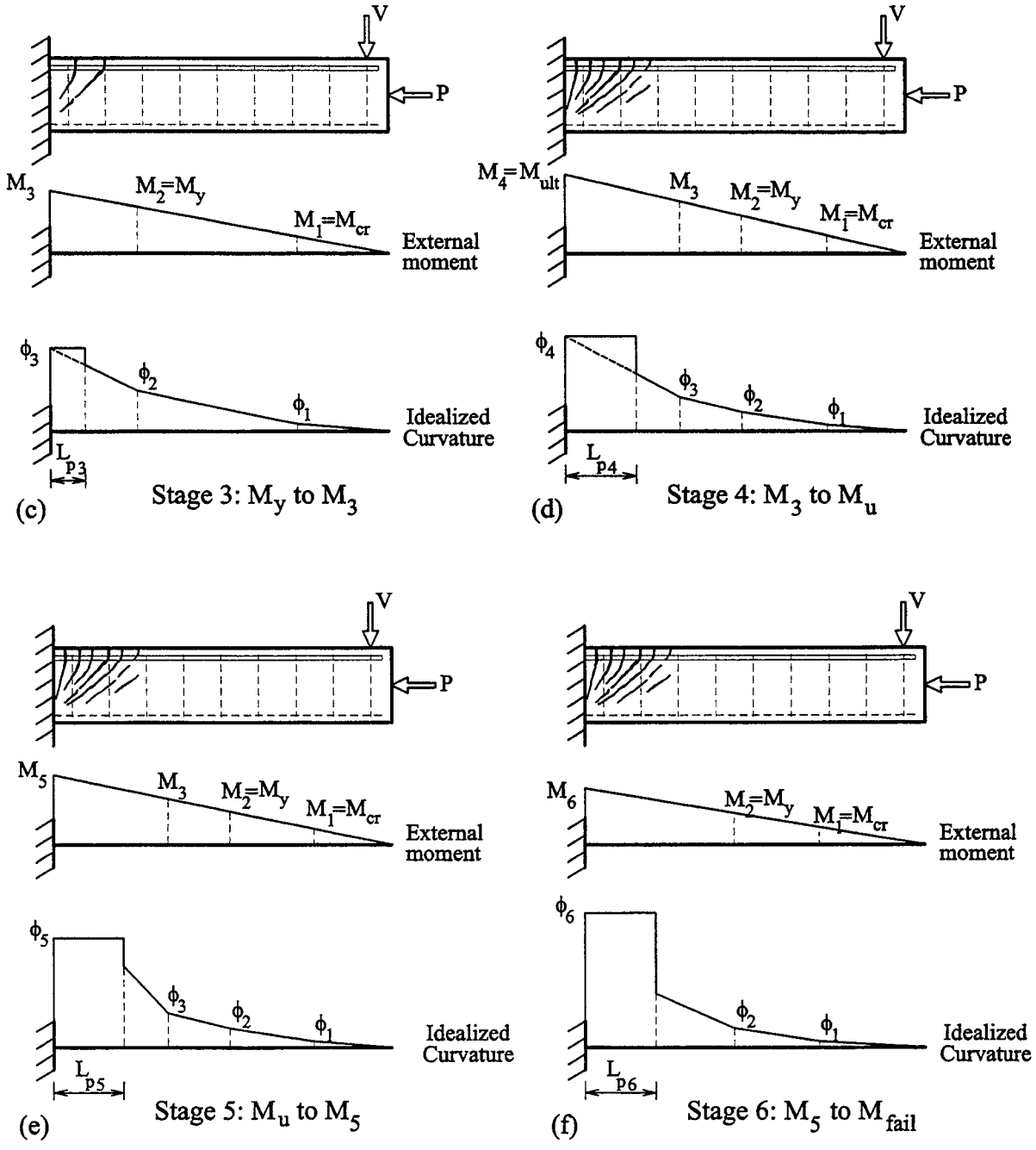

Figure 3.18 Various stages of laterally and axially loaded RC member (Continued)

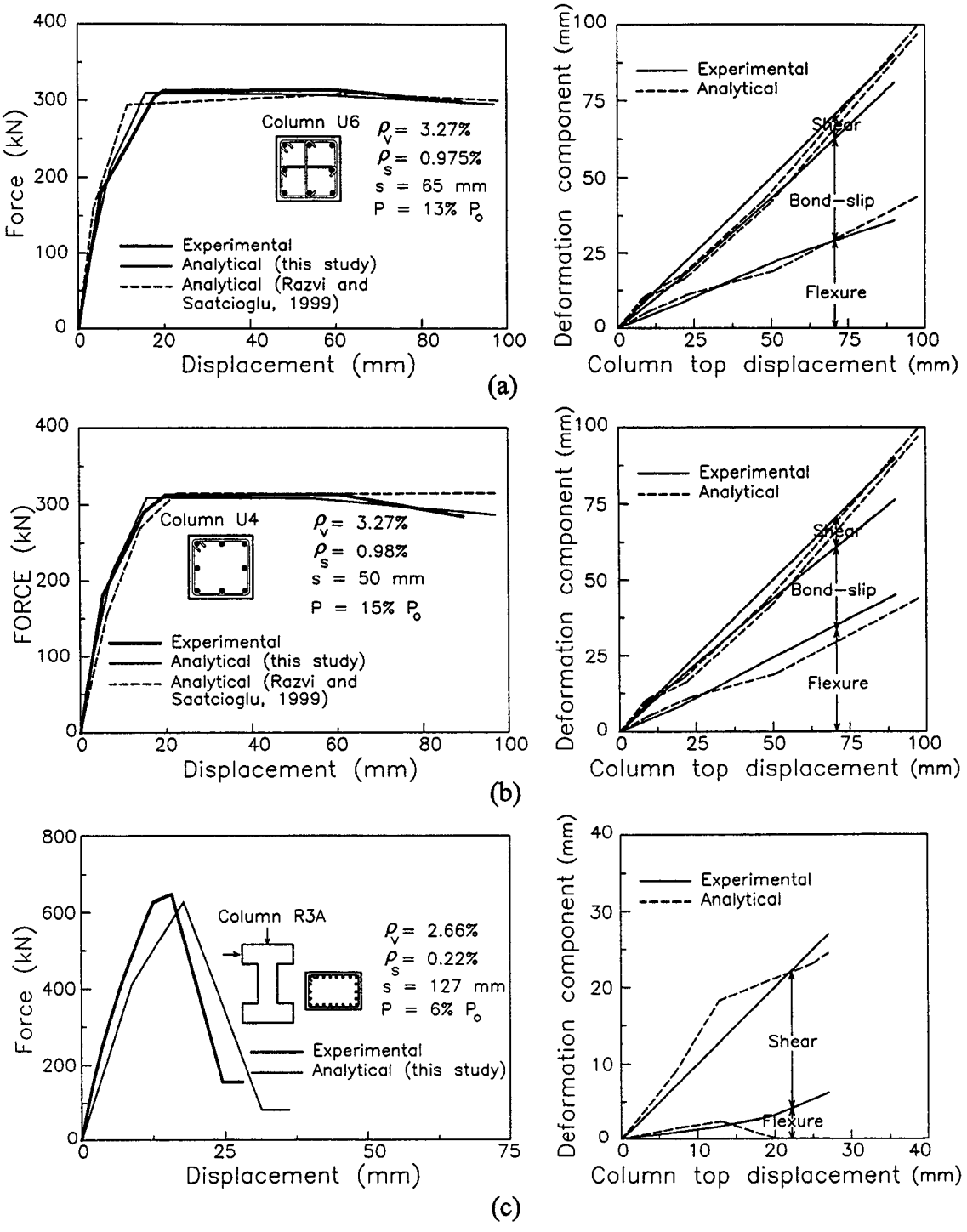

Figure 3.19 Comparisons between experimental and analytical force-displacement relationships and corresponding deformation components; Column test by (a) Saatcioglu and Ozcebe (1989); (b) Saatcioglu and Ozcebe (1987); (c) Priestley et al. (1993)

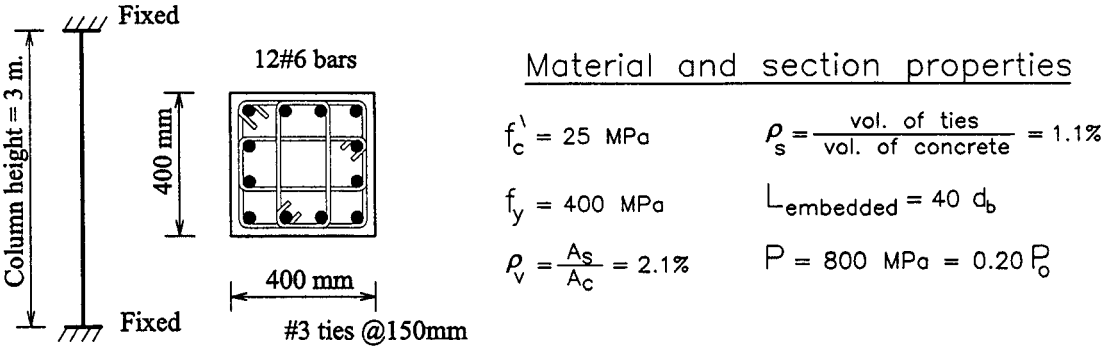

Figure 3.20 Typical column dimensions and properties

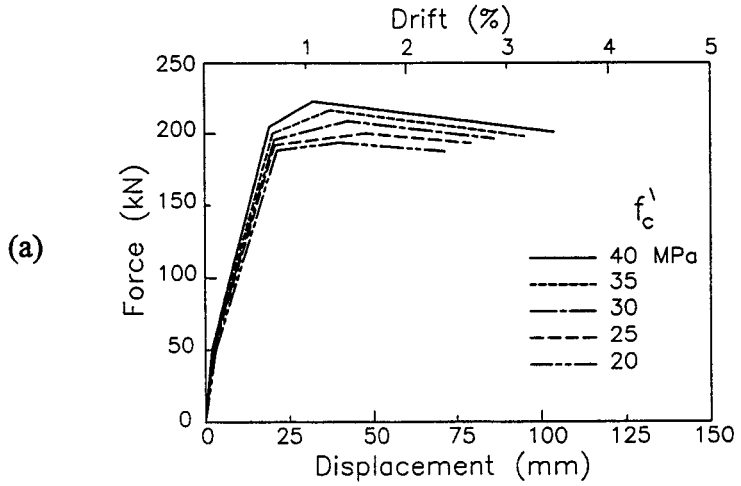

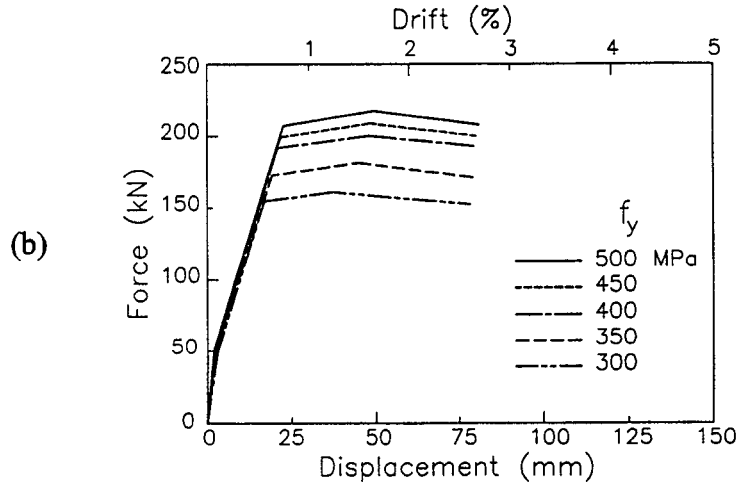

Figure 3.21 Influence of variables on force-deflection relationship of fixed-fixed column; (a) Concrete strength; (b) Steel yield stress; (Continued)

(c)

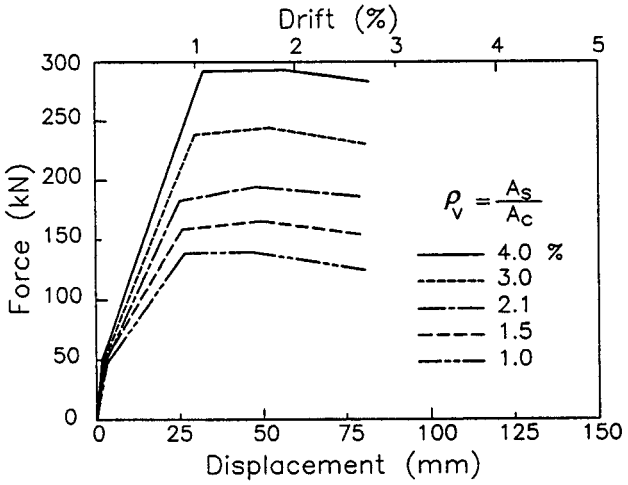

(d)

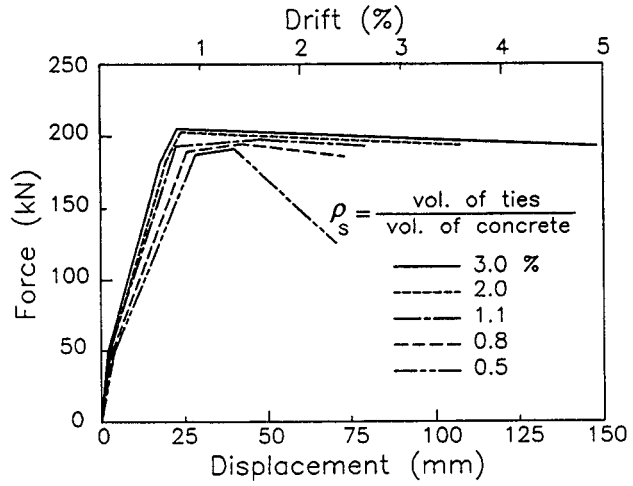

Figure 3.21 Influence of variables on force-deflection relationship of fixed-fixed column; (c) Vertical steel ratio; (d) Horizontal steel ratio (Confinement) (Continued)

(e)

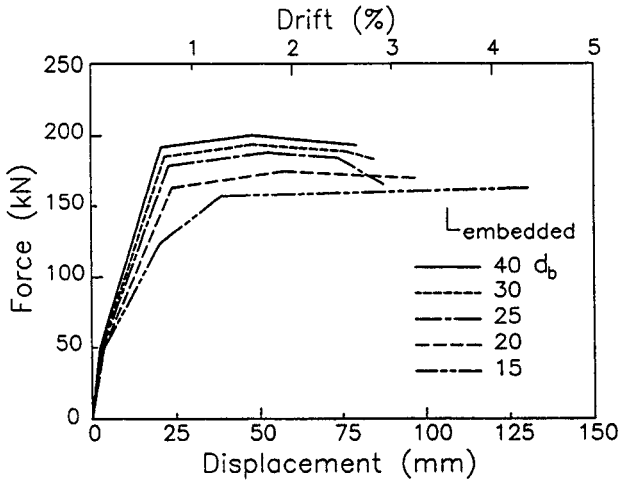

(f)

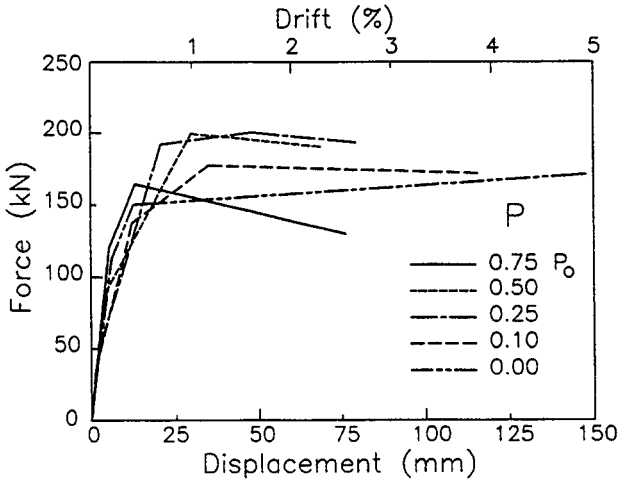

Figure 3.21 Influence of variables on force-deflection relationship of fixed-fixed column; (e) Embedded length of tensile bars; (f) Axial load. (Continued)

CHAPTER 4

VERIFICATION AND APPLICATION OF THE 3D MODEL

4.1 INTRODUCTION

The model developed in Chapter 2 to represent the behaviour of reinforced concrete members subjected to three-dimensional shear, flexure and variable axial loads was coded using the MATLAB® V5.3 programming language. To illustrate the use of this element and to verify the algorithm, five examples were analyzed. These examples were chosen to cover a wide range of cases involving different lateral deformations and various axial load paths. The five selected examples of the analysis are:

1- Flexural behaviour of biaxially loaded square cantilever RC column under constant axial load tested by Takizawa and Aoyama (1976).

2- Flexural behaviour of diagonally loaded square cantilever RC column with variable axial load tested by Saatcioglu and Ozcebe (1989).

3- Brittle shear failure of uniaxially loaded rectangular fixed-fixed RC column under constant axial load tested by Verma et al. (1993).

4- Limited flexural ductility with biaxial shear failure of biaxially loaded circular cantilever RC column under constant axial load tested by Wong et al. (1990).

5- Biaxial shear failure of biaxially loaded square fixed-fixed RC column with variable axial load tested by Ramirez and Jirsa (1980).

Figure 4.1 shows the general dimensions, details of reinforcement and the loading history for the analyzed column cases. The flexural yield surfaces and shear failure surfaces used in these analyses were determined using the analytical procedure outlined in Chapter 3.

4.2 ANALYZED CASES

4.2.1 Biaxial flexural behaviour:

The first analysis example is a reinforced concrete cantilever column subjected to biaxial bending, tested by Takizawa and Aoyama (1976) in Japan. Figure 4.2 shows the dimensions and the lateral displacement path used for the experiment. Takizawa and Aoyama (1976) as well as Chen and Powell (1982) have analytically modeled the test specimen and experimental data using the lumped plasticity method. Zeris and Mahin (1991) also studied this problem by using a fiber filament model. The specimen response involved inelastic biaxial flexural behaviour with flexural stiffness deterioration under non-proportional cyclic loading.

The analytical flexural yield surfaces were provided using the procedure explained in chapter 3. Table 4.1 contains the data used to evaluate the force-deflection relationship that was used to define the three flexural yield surfaces and the four flexural stiffnesses of the element in each direction. Figures 4.3a and 4.3b show the force-displacement and stress-strain relationship of an embedded bar subjected to incrementally increasing pulling displacement, respectively. Figure 4.3c shows the moment-curvature relationship of the cross-section while figure 4.3d shows the predicted moment-rotation

backbone relationship of the column. Table 4.2 lists all the data for the flexure and shear subhinges.

Comparison between the load-deflection relationships in E-W and N-S directions from both experimental and analytical models are shown in figure 4.4. The calculated and experimental results are encouragingly close, especially considering the complexity of the response. Comparison between the measured and calculated yield and ultimate moments in E-W and N-S directions is shown in table 4.3. The results show good agreement between the experimental and the predicted results.

4.2.2 Flexural behaviour with variation in axial load:

This analysis example consists of a RC cantilever column tested by Saatcioglu and Ozcebe (1989). The geometric details of the test specimen are shown in figure 4.5a. The lateral deflection and axial load histories are shown in figure 4.5b. The column was subjected to uniaxial cyclic displacements along the section diagonal as well as variable axial load. The applied axial load varied linearly between 500 kN (112 kips) tension when the column was displaced horizontally 6 percent of the column height in one direction and 500 kN (112 kips) compression when the specimen was displaced the same amount in the opposite direction. This loading was selected to simulate an axial load couple counteracting moment resulting from lateral loading. Table 4.1 includes the data used to evaluate the force-deflection relationship that was used to define the three flexural yield surfaces and the four flexural stiffnesses of the element in each direction. Figures 4.6a and 4.6b show the force-displacement and stress-strain relationship of an

embedded bar subjected to incrementally increasing pulling displacement, respectively. Figure 4.6c shows the moment-curvature relationship of the cross-section while figure 4.6d shows the predicted moment-rotation backbone relationship of the column. Table 4.2 lists all the data for the flexure and shear subhinges.

Figure 4.7 shows the comparison between the experimental and analytical lateral load-top deflection hysteretic relationships in the direction of loading. Both the experimental results and the analytical simulation model indicate that the yield and ultimate moments are affected by the level of the concurrent axial load. Also, the analytical model was able to simulate the degradation in stiffness upon reloading. The stiffness degradation was increasing with the increase of the displacement level. Table 4.3 shows a comparison between the measured and calculated lateral loads and deflections in the direction of loading at the yield and ultimate stages. Close agreement between the test results and that of the analysis was demonstrated.

4.2.3 Brittle shear failure:

In order to demonstrate the ability of the analytical model to simulate the brittle shear failure behaviour in RC columns, the column tested by Verma et al. (1993) was analyzed. Details of the shear test setup, loading conditions and specimen's cross section are shown in figure 4.8a, while the applied cyclic loading history is shown in figure 4.8b. The data used to evaluate the force-deflection relationship is listed in table 4.1. This data was used to define the three flexural yield surfaces and the four flexural stiffnesses of the element in each direction. Figures 4.9a and 4.9b show the force-displacement and stress-

strain relationship of an embedded bar subjected to incrementally increasing pulling displacement, respectively. Figure 4.9c shows the moment-curvature relationship of the cross-section while figure 4.9d shows the predicted moment-rotation backbone relationship of the column.

The column developed flexural cracking and shear failure during the load application process. The calculated initial shear strength is 828 kN (186 kips). The predicted shear failure was 688 kN (155 kips), while the experimental shear failure occurred at 750 kN (169 kips). Tables 4.2a and 4.2b contain the data for the flexure and shear subhinges. The response of the tested column included a complete shear failure, where the transverse shear reinforcement contributed the residual shear capacity as shown in figure 4.10a. Figure 4.10a also shows the brittle shear failure during the loading to achieve the first peak of the yield displacement 0.67 inches. In addition to the calculated shear strength and residual strength, the falling branch shows calculated unloading stiffness of -48 kN/mm (-274 kips/in), for the shear strength degradation.

The analytical load-deflection relationship is shown in figure 4.10b. The results of the analysis correlate well with the experimental measurements. It is concluded that the model does capture the uniaxial brittle shear failure by using appropriate shear strength degradation stiffness and coefficients. Table 4.3 shows the comparison between the experimental and analytical yield, ultimate lateral loads and deflections. The comparison indicates that the model predict the column's response with good accuracy.

4.2.4 Limited flexural ductility with biaxial shear failure:

This analysis example is a squat circular reinforced concrete cantilever column tested by Wong et al. (1990) under non-proportional biaxial cyclic loading in conjunction with a constant axial load of 930 kN (210 kips). The specimen's dimensions and the loading path for a cycle of displacement imposed on the specimen, are shown in figure 4.11a and 4.11b, respectively. The shown path was followed repeatedly, increasing the displacement ductility μ in each successive pair of loading cycles. Table 4.1 lists the data used to evaluate the force-deflection relationship that was used to define the three flexural yield surfaces and the four flexural stiffnesses of the element in each direction. When analyzing the column for the backbone load-deflection relationship, the circular cross section was approximated with a square one having the same moment of inertia about the section's principal axis. An equivalent square section was needed for the moment-rotation relationship analysis, since the procedure formulation was based on rectangular cross sections. Figure 4.11c shows the cross section dimensions of the equivalent square section. Figures 4.12a and 4.12b show the force-displacement and stress-strain relationship of an embedded bar subjected to incrementally increasing pulling displacement, respectively. Figure 4.12c shows the moment-curvature relationship of the cross-section while figure 4.12d shows the predicted moment-rotation backbone relationship of the column.

The experimental lateral load-displacement hysteretic responses in the North-South and East-West directions are shown in 4.13a and 4.13c. The column's response consists of initial flexural cracking, followed by inelastic flexural deformations as the

amplitude of the displacement history was increased. The flexural ductility demand imposed by the displacement history led to degradation in the shear strength of the specimen. This caused the onset of a shear failure to occur at an imposed displacement ductility of μ=4.0 in the north direction, and a subsequent reduction in shear capacity to about 166 kN with continued loading. The displacement ductility of 4.0 corresponds to a lateral deflection of about 24 mm. All properties for the flexural subhinges and the shear subhinge are listed in table 4.2. The initial shear strength was 610 kN (137 kips) at displacement ductility of 2.0, then decreased to 487 kN (109.5 kips) at displacement ductility of 4.0. The residual shear strength (which is the shear strength from steel mechanism V_s) was equal to 178 kN (40 kips). A value of -36 kN/mm (-206 kips/in) was calculated for coefficients K_{vy} and K_{vz} to account for shear strength degradation effects. The effect of flexural ductility demand on the degradation of shear strength in the plastic hinge zone was accounted for using Priestly's model (figure 1.7). Therefore, the initial shear strength surface decreases as the displacement ductility demand imposed on the column increases (for circular column the value used for k in equation 1.10 was based on the uniaxial case).

The predicted response based on the analysis of the test specimen is shown in figures 4.13b and 4.13d as well as table 4.3. The comparison between the analytical and experimental response is shown to be in good agreement, where the analysis predicts limited lateral strength and displacement ductility before a shear failure occurred at a displacement ductility of 4.0 in the north direction. After the occurrence of the shear

failure, the analytical model captured the pinching behaviour and stiffness deterioration that occurred in the experimental hysteretic response.

The results of this analysis demonstrates that the element formulation is capable of modeling the hysteretic response of a reinforced concrete column that develops deterioration in shear capacity in the plastic flexural hinge zone due to excessive flexural ductility demand.

4.2.5 Biaxial shear failure with variable axial load:

The fifth analysis example is a squat square fixed-fixed RC column tested by Ramirez and Jirsa (1980) under non-proportional biaxial cyclic loading in conjunction with an alternating compressive and tensile axial load. Figure 4.14 shows the specimen's dimensions and details of reinforcement as well as the deflection history in N-S and E-W directions and the sequence of variation of axial load. The lateral displacement and axial load paths were designed to simulate the loads induced by an earthquake on an interior column of a slender reinforced concrete building. In such a case, axial tension alternates with compression for lateral displacement in one direction and only axial compression for lateral displacement in the other direction. Table 4.1 contains the data used to evaluate the force-deflection relationship that was used to define the three flexural yield surfaces and the four flexural stiffnesses of the element in each direction. Figures 4.15a and 4.15b show the force-displacement and stress-strain relationship of an embedded bar subjected to incrementally increasing pulling displacement, respectively. Figure 4.15c shows the

moment-curvature relationship of the cross-section while figure 4.15d shows the predicted moment-rotation backbone relationship of the column.

The experimental lateral load-displacement hysteretic response in the north-south and east-west directions, are shown in figures 4.16a and 4.16c. The specimen experienced initial flexural cracking followed by inelastic flexural deformations in both NS and EW directions. Shear failure occurred when displacement first reached 0.6 inches in the NS direction leading to subsequent reduction in shear strength with a highly pinched hysteretic behaviour, as seen in figures 4.16a and 4.16c. All the calculated properties for the flexural subhinges and the shear subhinge are listed in tables 4.2a and 4.2b. The initial shear strength was 366 kN (82.1 kips) at displacement ductility of 1.0 and then decreased to 283 kN (63.4 kips) at displacement ductility of 3.0. The residual shear strength was equal to 110 kN (25 kips). A value of -22 kN/mm (-126 kips/in) was calculated for coefficients K_{vy} and K_{vz} to account for shear strength degradation effect. However, these values did not have much effect on the analytical results since the degradation in stiffness upon reversal of loading combined with variation of axial load dominated the shear strength capacity. Therefore at each new cycle the reduced stiffness led to a reduced shear strength capacity.

The predicted response based on the analysis of the test specimen in the N-S and E-W directions are shown in figures 4.16b and 4.16d. Table 4.3 includes a comparison between the yield and ultimate forces and displacements for both, the experimental and analytical results. The analytical and experimental overall responses are shown to be in good agreement. It should be mentioned that the analytical model did not predict the peak

response in the south direction at displacement 0.6 inches. This is attributed to the isotropic contraction modeling for the shear subhinge yield surface, where the first shear trigger occurred in the east direction at displacement 0.6 inches. An anisotropic contraction model could have allowed for independent shear capacities in different directions.

4.3 EFFECT OF DIFFERENT AXIAL LOAD PATTERNS

Having verified the analytical model using experimental results, the next step was to study the effect of different axial load variation patterns on the response of laterally loaded columns. Testing of columns under varying axial load patterns is difficult. In addition to the fact that there are few experimental results available in the published literature, the axial load variations during severe earthquakes have not been measured or accurately predicted by a reliable analysis. Thus, an available analytical tool can achieve results and conclusions that have not yet been verified by experimental work.

In this study, a RC cantilever column with given moment-rotation properties, was subjected to eight different axial load paths as shown in figure 4.17. The axial load paths were selected to cover different possibilities of axial load variation with respect to the lateral deformation.

Path 1 had a constant axial load of -0.5 P_b (P_b is the balanced compressive axial load). Path 2 had a variable axial load between 0 and -P_b (i.e. $\pm$0.5 P_b from the initially applied load of -0.5P_b). In path 3, the axial load was varied from 0 to -2 P_b. In path 4, the axial load was varied between 0 and -0.5 P_b. In path 5, the axial load was varied between

$\pm$ 0.5 P_b (i.e. compression and tension). Paths 2 to 5 were 'in phase' loading cycles; such that the axial load was proportional to the lateral load with maximum axial load coinciding with maximum lateral deflection. Path 6 was an 'out of phase' loading case, with a phase shift of a quarter cycle between the axial load and lateral deformation. In the 'out of phase' loading of case 6, the maximum axial load coincided with zero lateral displacement. Paths 7 and 8 represent an axial load that was varied at twice the number of cycles with which the lateral load was varied. In the case of path 7, the axial load was varied such that no axial load was applied at maximum lateral displacement while the maximum axial load was applied when the lateral displacement was zero. In the case of path 8, the axial load variation was such that the maximum axial load occurred at maximum lateral displacement while no axial load was applied at zero lateral displacement.

The moment-rotation relationships for the eight imposed variable axial load paths are shown in figure 4.18. The cumulative dissipated energy-displacement ductility factor relationship for the eight different axial load paths are plotted in figure 4.19. From the two figures, the following behaviour is observed:

1- Comparing the cases of axial load paths 2, 3 and 4 with path 1, it is observed that the lateral moment capacity of the column subjected to a variable compressive axial load corresponds to the force-moment interaction relationship for the column section. In effect, the maximum moment capacity occurs when the axial load reaches the balanced compressive axial load.

2- Comparing the column behaviour when subjected to an axial load varying according to path 2 (0 to $-P_b$) to the response of path 5 ($\pm 0.5\ P_b$) loading, it is observed that the axial load with reversing sign (i.e. compression and tension) causes approximately a 25% decrease in the lateral moment capacity of the column that is subjected to axial load that remains compressive. The decrease in the lateral moment capacity in the case of an axial load with reversing sign is accompanied by an increase in the unloading stiffness which results in an accumulated energy dissipation capacity approximately equal to the case of an axial load of the same amplitude but remaining compressive.

3- Comparing cases of axial load path 6 with path 2, it is observed that 'out of phase' loading (path 6) causes slight decrease in the moment capacity and approximately 15% decrease in the energy dissipating capacity of the RC column as compared to the 'in phase' loading. The 'in phase' loading of path 2 refers to the case when the maximum axial load is applied at the maximum lateral push while the minimum axial load is applied at the maximum lateral pull. The 'out of phase' loading of path 6 represents the case when the maximum and minimum axial loads coincide with zero lateral displacement.

4- Comparing the column behaviour with an axial load following paths 7 and 8 with that of an axial load following paths 2 to 6, it is noted that applying two axial load cycles for every one lateral load cycle will decrease the energy dissipating capacity of the columns.

5- Comparing the results of cases of axial load path 7 with that of path 8, it is observed that varying the compressive axial load such that the maximum axial load is applied at maximum lateral displacement and zero axial load is applied at zero lateral displacement (path 8) will decrease the lateral moment capacity, stiffness and energy dissipating capacity of RC column as compared to the reverse load pattern (i.e. zero axial load at maximum lateral displacement and maximum axial load at zero lateral displacement, path 7). This can be attributed to the fact that increasing the axial load while increasing the lateral deformation will decrease the lateral stiffness of the column.

Table 4.1a Steel bars anchorage data

Column test	Bar diameter d_b	Embedded length l_{bar}	$\frac{l_{bar}}{d_b}$	f_c'	f_y	f_u	ε_y	ε_{sh}	ε_u
	mm (in)	mm (in)		MPa (kip/in^2)	MPa (kip/in^2)	MPa (kip/in^2)			
1- Takizawa and Aoyama (1976).	13 (4/8")	500 (20")	38	16.2 (2.3)	394 (57)	600 (87)	0.002	0.014	0.13
2- Saatcioglu and Ozcebe (1989).	25 (1")	1000 (40")	40	49.3 (7.2)	430 (62)	650 (94)	0.0022	0.01	0.1
3- Verma et al. (1993).	19.5 (6/8")	790 (31")	41.3	34.6 (5)	413 (60)	600 (87)	0.0021	0.013	0.12
4- Wong et al. (1990)*.	20 (6/8")	800 (31.5")	40	39 (5.6)	475 (69)	625 (91)	0.0024	0.019	0.35
5- Ramirez and Jirsa (1980).	19.5 (6/8")	760 (30")	40	34.6 (5)	448 (65)	690 (100)	0.0022	0.01	0.08

* Equivalent square section.

Table 4.1b Specimen details

Column test	P_{av}	b	t	d	$A_s=A_s'$	ρ_s	s_h	f_{yh}	b''
	kN (kip)	mm (in)	mm (in)	mm (in)	mm^2 (in^2)	%	mm (in)	MPa (kip/in^2)	mm (in)
1- Takizawa and Aoyama (1976).	300 (67)	200 (8)	200 (8)	168.5 (6.6)	265 (0.41)	1.34	50 (2)	252 (36.5)	162 (6.4)
2- Saatcioglu and Ozcebe (1989).	2000 (450)	350 (14)	350 (14)	305 (12)	1470 (2.28)	0.66	150 (5.9)	470 (68)	305 (12)
3- Verma et al. (1993).	3225 (725)	405 (16)	610 (24)	570 (22.5)	1500 (2.33)	0.22	127 (5)	300 (43.5)	570 22.5
4- Wong et al. (1990)*.	2000 (450)	350 (14)	350 (14)	315 (12.4)	1256 (1.95)	1.18	30 (1.18)	343 (50)	312 (12.3)
5- Ramirez and Jirsa (1980).	1335 (300)	305 (12)	305 (12)	265 (10.38)	858 (1.33)	0.74	65 (2.57)	448 (65)	254 (10)

* Equivalent square section.

Table 4.2a Properties of flexure subhinges

Column test	M_1	M_2	M_3	K_1	K_2	K_3	K_4	α	P_{ult}	T_{ult}	P_{av}
	kN.m (kip.ft)	kN.m (kip.ft)	kN.m (kip.ft)	kN.m (kip.ft)	kN.m (kip.ft)	kN.m (kip.ft)	kN.m (kip.ft)		kN (kip)	kN (kip)	kN (kip)
1- Takizawa and Aoyama (1976)*.	9 (6.6)	19.5 (14.4)	28.8 (21.2)	8200 (6050)	3900 (2875)	2400 (1770)	20 (15)	0.1	800 (180)	200 (45)	300 (67)
2- Saatcioglu and Ozcebe (1989)*.	158 (116)	252 (186)	292 (214)	54000 (40000)	15400 (11350)	7700 (5675)	1550 (4000)	0.065	6000 (1350)	2000 (450)	2000 (450)
3- Verma et al. (1993)*.	214 (158)	650 (480)	730 (540)	135600 (100200)	81360 (60000)	27500 (20300)	6880 (5075)	0.03	9340 (2100)	2890 (650)	3225 (725)
4- Wong et al. (1990)**.	150 (111)	365 (270)	405 (299)	70400 (51925)	49280 (36350)	21120 (15580)	2110 (1555)	0.05	6000 (1350)	2000 (450)	2000 (450)
5- Ramirez and Jirsa (1980)*.	45 (33)	136 (100)	176 (130)	54000 (39820)	22780 (16800)	9520 (7020)	4680 (3450)	0.035	3560 (800)	890 (200)	1335 (300)

* Properties are the same in y and z directions.

** Listed propertries are in the direction of analysis.

Table 4.2b Properties of shear subhinge

Column test	V_c		V_s	V_p	V_n		V_r	K_v	α_s	α_p
	Max.	Min.			V_i	V_f				
	kN (kip)	kN (kip)	kN (kip)	kN (kip)	kN (kip)	kN (kip)	kN (kip)	kN/mm (kip/in)		
1- Takizawa and Aoyama (1976)*.	38.6 (8.7)	13.3 (3)	77 (17.3)	30 (6.7)	145.6 (32.7)	120.3 (27)	77 (17.3)	--	--	--
2- Saatcioglu and Ozcebe (1989)*.	206 (46)	71 (15.9)	251 (56)	115 (26)	572 (128)	437 (97.9)	251 (56)	--	--	--
3- Verma et al. (1993)**.	338 (76)	116 (26)	156 (35)	334 (75)	828 (186)	606 (136)	156 (35)	-48 (-274)	0.095	0.025
4- Wong et al. (1990)*.	188 (42)	65 (14.5)	178 (40)	244 (55)	610 (137)	487 (109.5)	178 (40)	-36 (-206)	0.025	0.02
5- Ramirez and Jirsa (1980)*.	127 (28.5)	44 (9.8)	110 (15.2)	129 (38.4)	366 (82.1)	283 (63.4)	110 (15.2)	-22 (-126)	0.029	0.01

* Properties are the same in y and z directions.

** Listed propertries are in the direction of analysis.

Maximum V_c and V_i occur at displacement ductility 1.0 and 2.0 for biaxial and uniaxial lateral loading, respectively (see figure 1.6).

Minimum V_c and V_i occur at displacement ductility 3.0 and 4.0 for biaxial and uniaxial lateral loading, respectively (see figure 1.6).

Table 4.3 Comparison between measured and calculated loads and deflections at yield and ultimate levels

Column test	Measured								Calculated							
	E-W				N-S				E-W				N-S			
	Yield		Ultimate		Yield		Ultimate		Yield		Ultimate		Yield		Ultimate	
	kN (kip)	mm (in)	kN (kip)	mm (in)	kN (kip)	mm (in)	kN (kip)	mm (in)	kN (kip)	mm (in)	kN (kip)	mm (in)	kN (kip)	mm (in)	kN (kip)	mm (in)
1- Takizawa and Aoyama (1976).	30 (7)	3 (0.1)	45 (10)	9 (0.4)	28 (6)	4 (0.2)	44 (10)	9 (0.4)	32.5 (7)	2.5 (0.1)	48.5 (11)	9 (0.4)	30 (7)	3 (0.1)	48.5 (11)	9 (0.4)
2- Saatcioglu and Ozcebe (1989)*.	190 (43)	10 (0.4)	245 (55)	35 (1.4)	--	--	--	--	180 (41)	10 (0.4)	220 (50)	35 (1.4)	--	--	--	--
3- Verma et al. (1993).	169 (38)	15 (0.6)	169 (38)	15 (0.6)	--	--	--	--	155 (35)	14 (0.6)	155 (35)	14 (0.6)	--	--	--	--
4- Wong et al. (1990).	355 (80)	6 (0.2)	500 (112)	18 (0.7)	355 (80)	6 (0.2)	500 (112)	18 (0.7)	380 (85)	6 (0.2)	485 (109)	16 (0.6)	380 (85)	6 (0.2)	485 (108)	18 (0.7)
5- Ramirez and Jirsa (1980).	190 (43)	5 (0.2)	310 (70)	10 (0.4)	200 (45)	5 (0.2)	322 (72)	15 (0.6)	210 (47)	6 (0.2)	290 (65)	10 (0.4)	220 (49)	5 (0.2)	312 (70)	11 (0.4)

* Values are in the direction of loading.

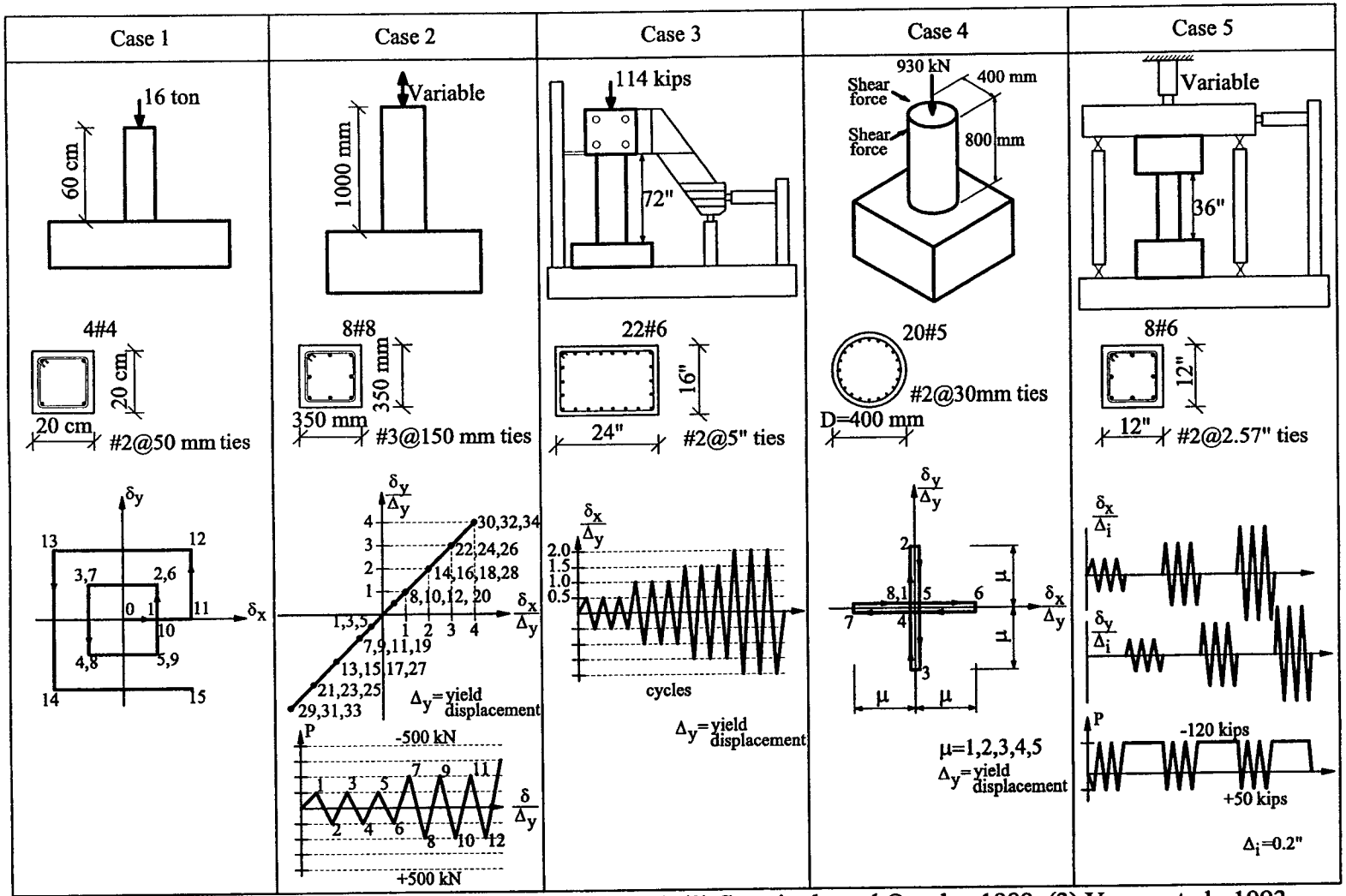

Figure 4.1 Analysis cases: (1) Takizawa and Aoyama, 1976; (2) Saatcioglu and Ozcebe, 1989; (3) Verma et al., 1993; (4) Wong et al., 1990; (5) Ramirez and Jirsa, 1980

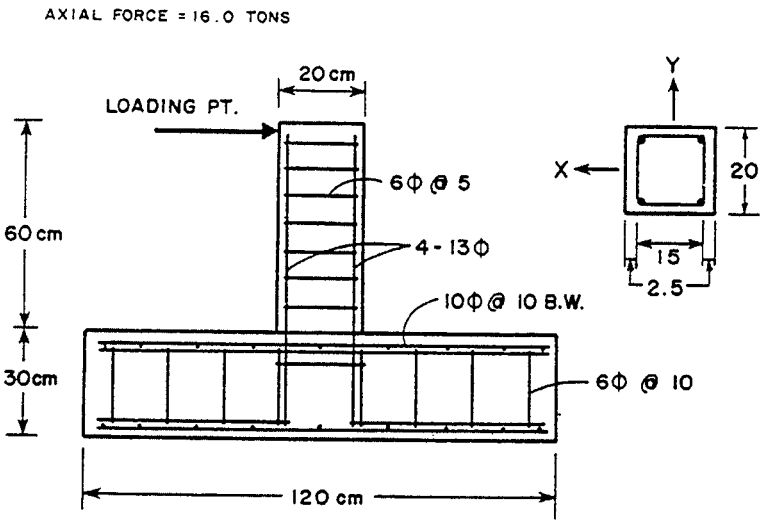

(a)

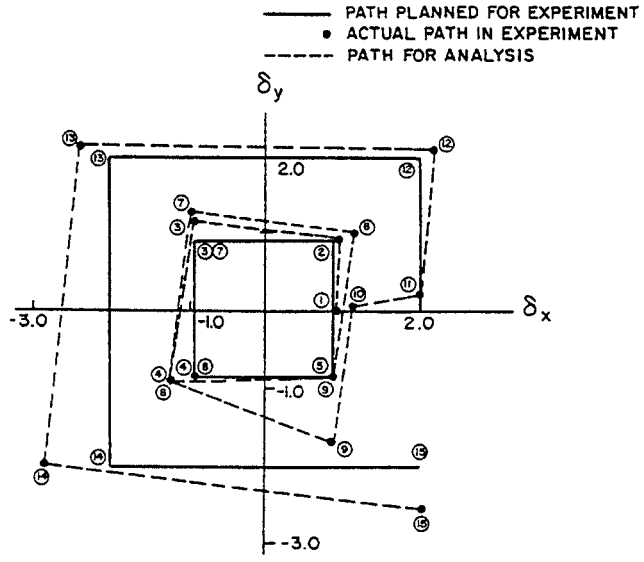

(b)

Figure 4.2 Case 1 (Takizawa and Aoyama, 1976): (a) Dimensions of test specimen; (b) Applied deflection path

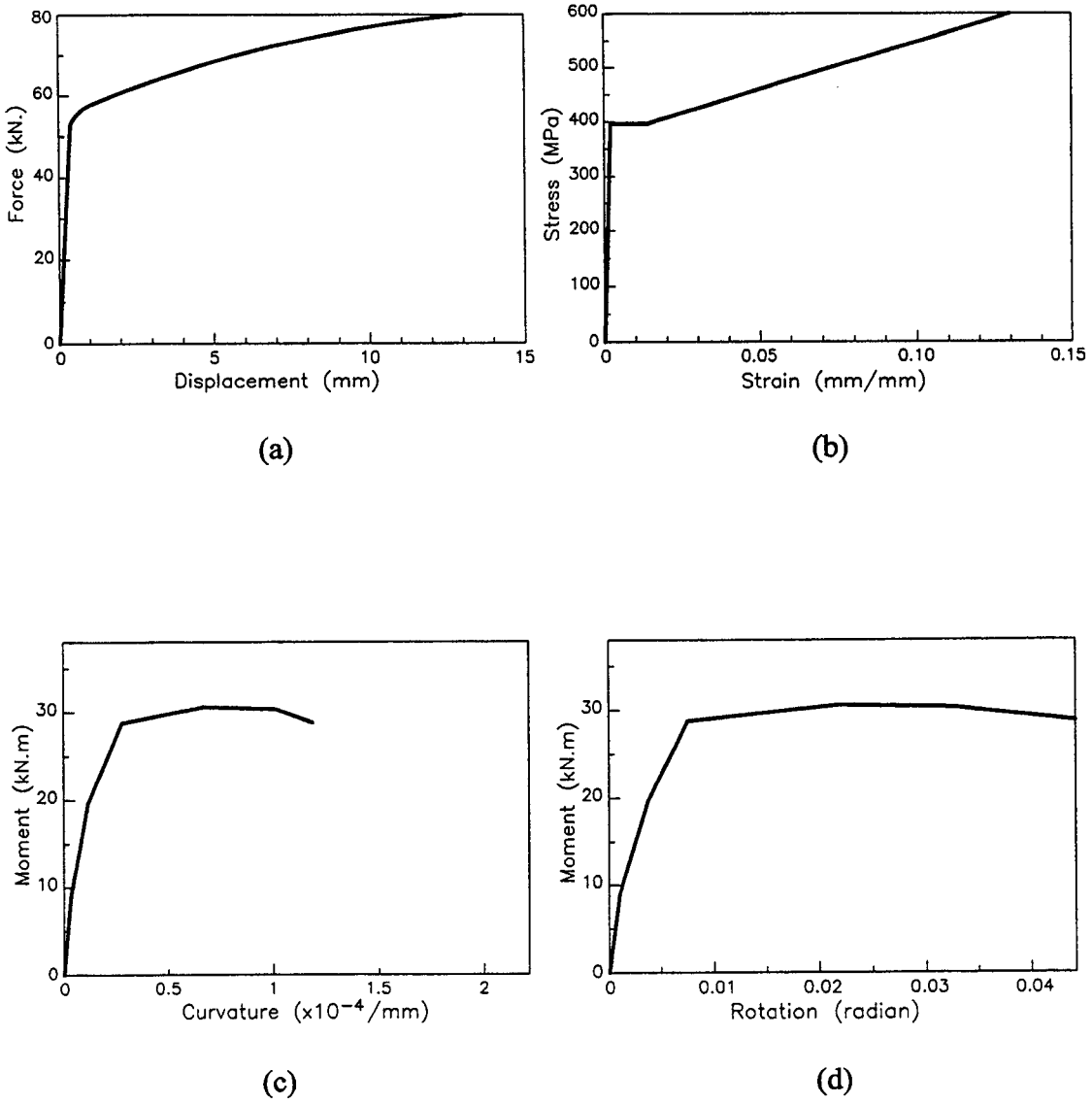

Figure 4.3 Section analysis results: (a) Force-displacement relationship for embedded bar; (b) Stress-strain relationship for embedded bar; (c) Moment-curvature relationship for the section; (d) Moment-rotation relationship for the element

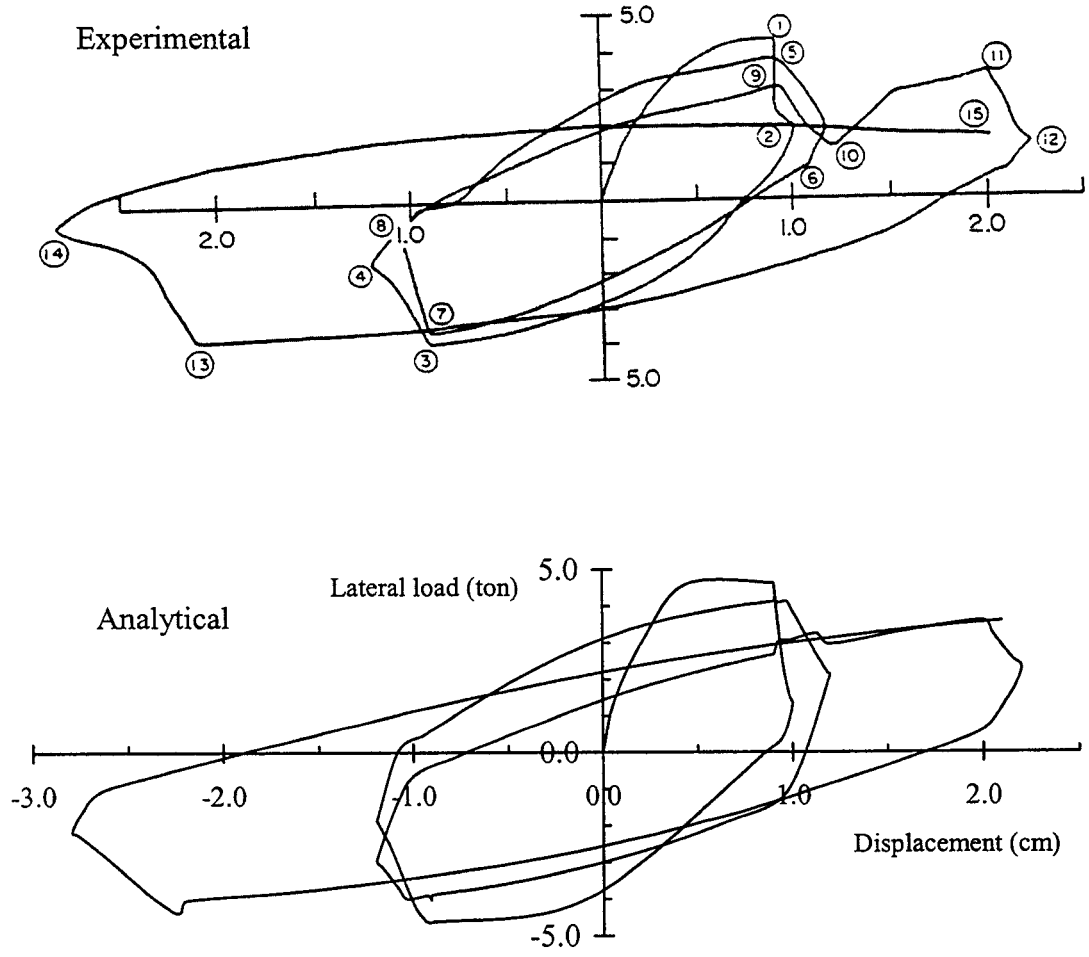

(a) E-W direction

Figure 4.4 Biaxial load-displacement response for case 1 (Takizawa and Aoyama, 1976): (a) E-W direction; (b) N-S direction. (Continued)

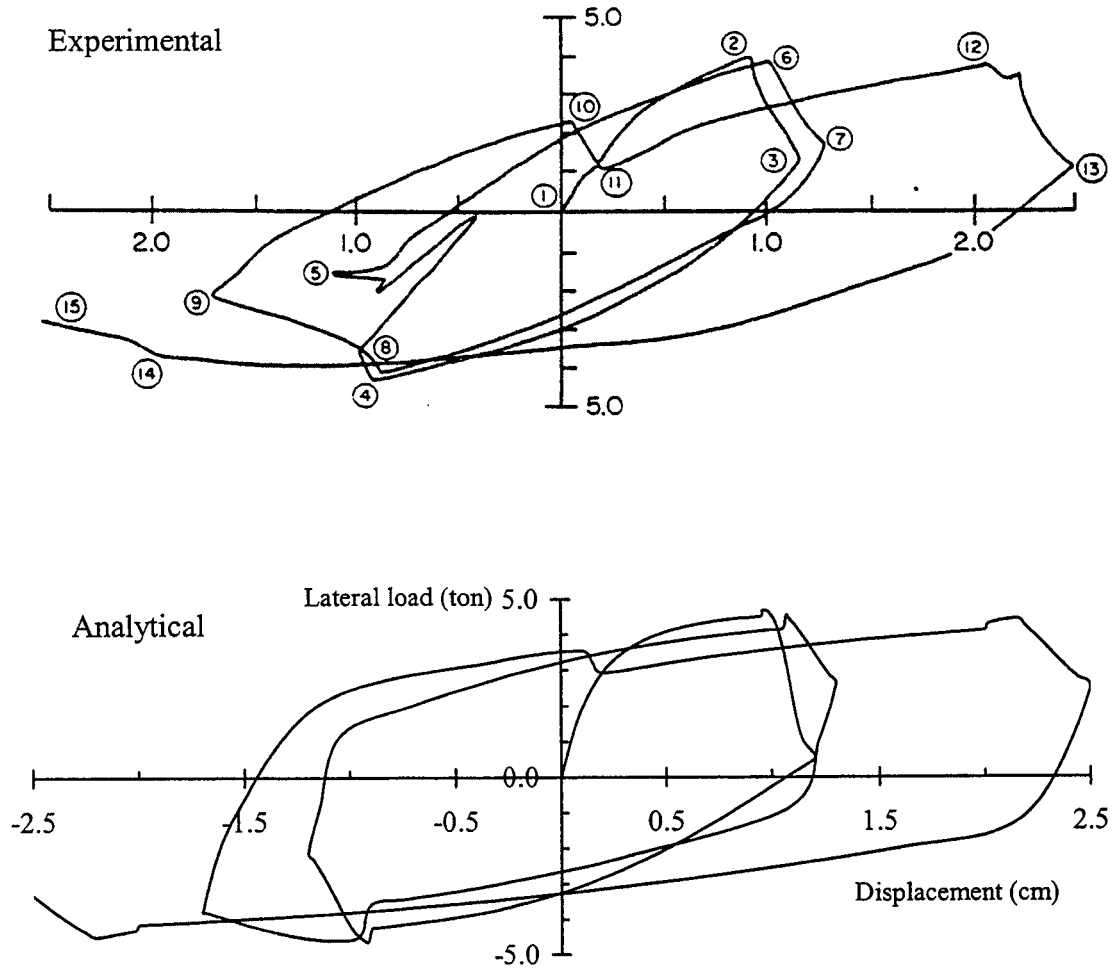

(b) N-S direction

Figure 4.4 Biaxial load-displacement response for case 1 (Takizawa and Aoyama, 1976): (a) E-W direction; (b) N-S direction. (Continued)

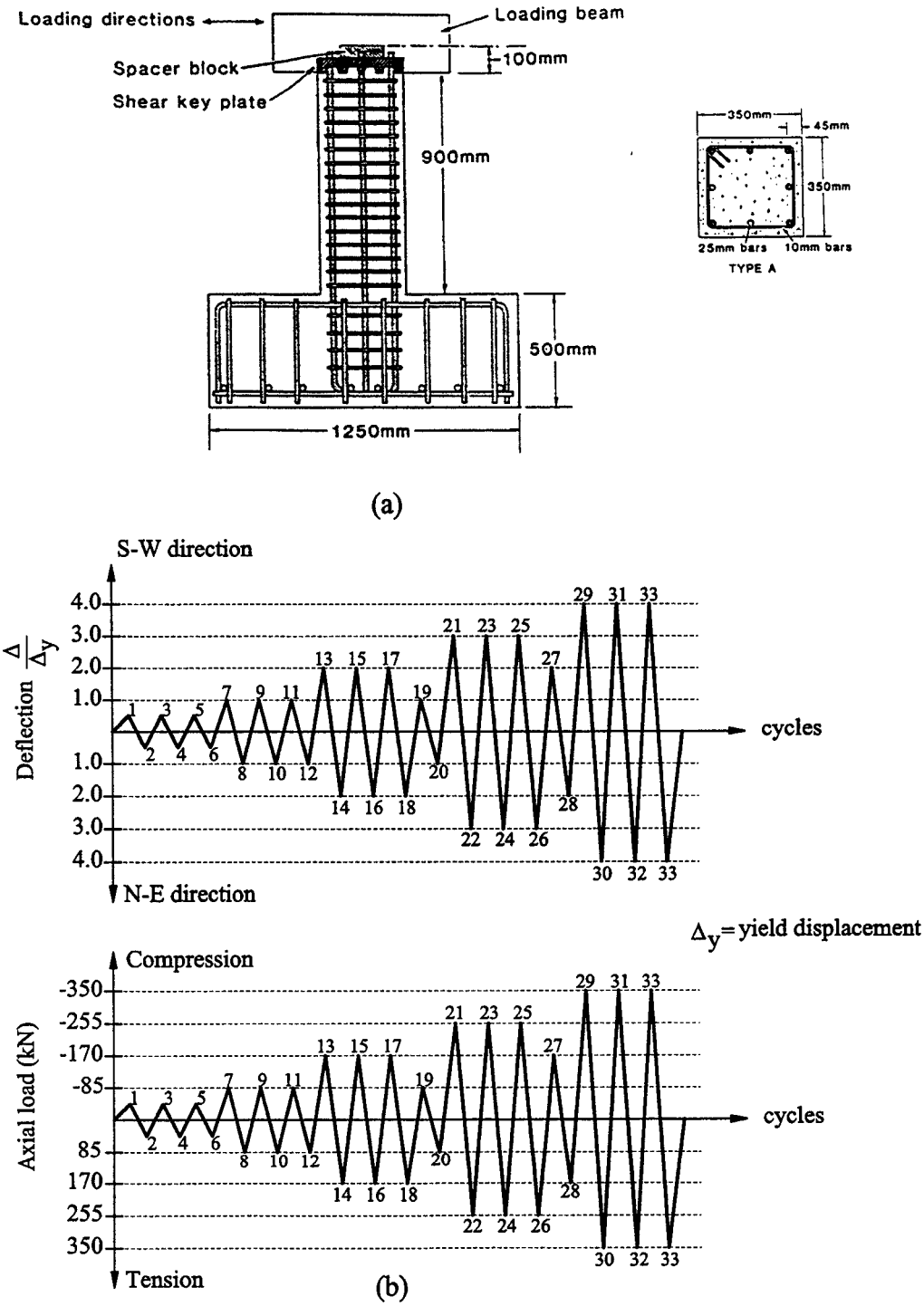

Figure 4.5 Case 2 (Saatcioglu and Ozcebe, 1989): (a) Dimensions of test specimen; (b) Planned deflection and axial load paths

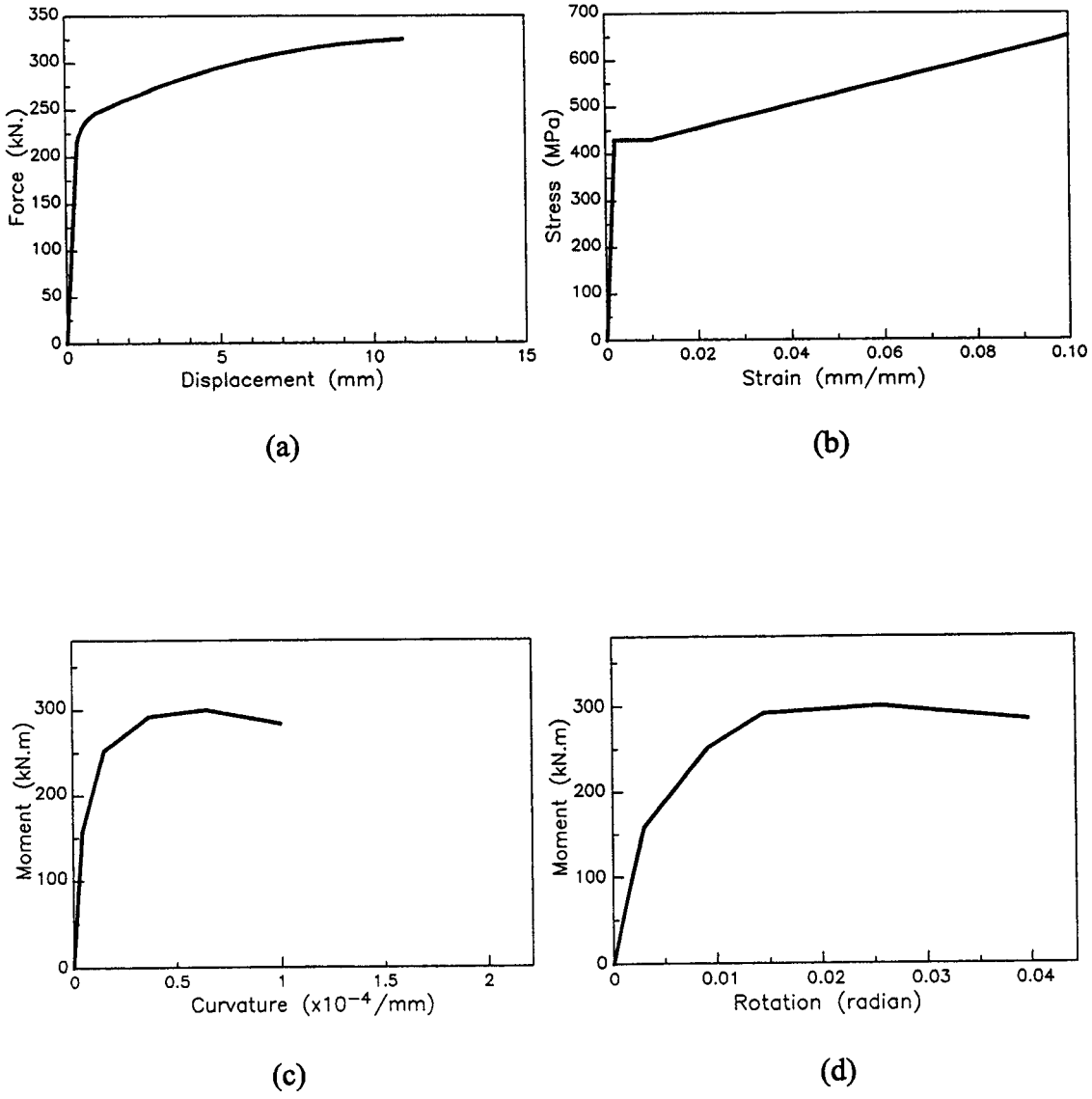

Figure 4.6 Section analysis results: (a) Force-displacement relationship for embedded bar; (b) Stress-strain relationship for embedded bar; (c) Moment-curvature relationship for the section; (d) Moment-rotation relationship for the element

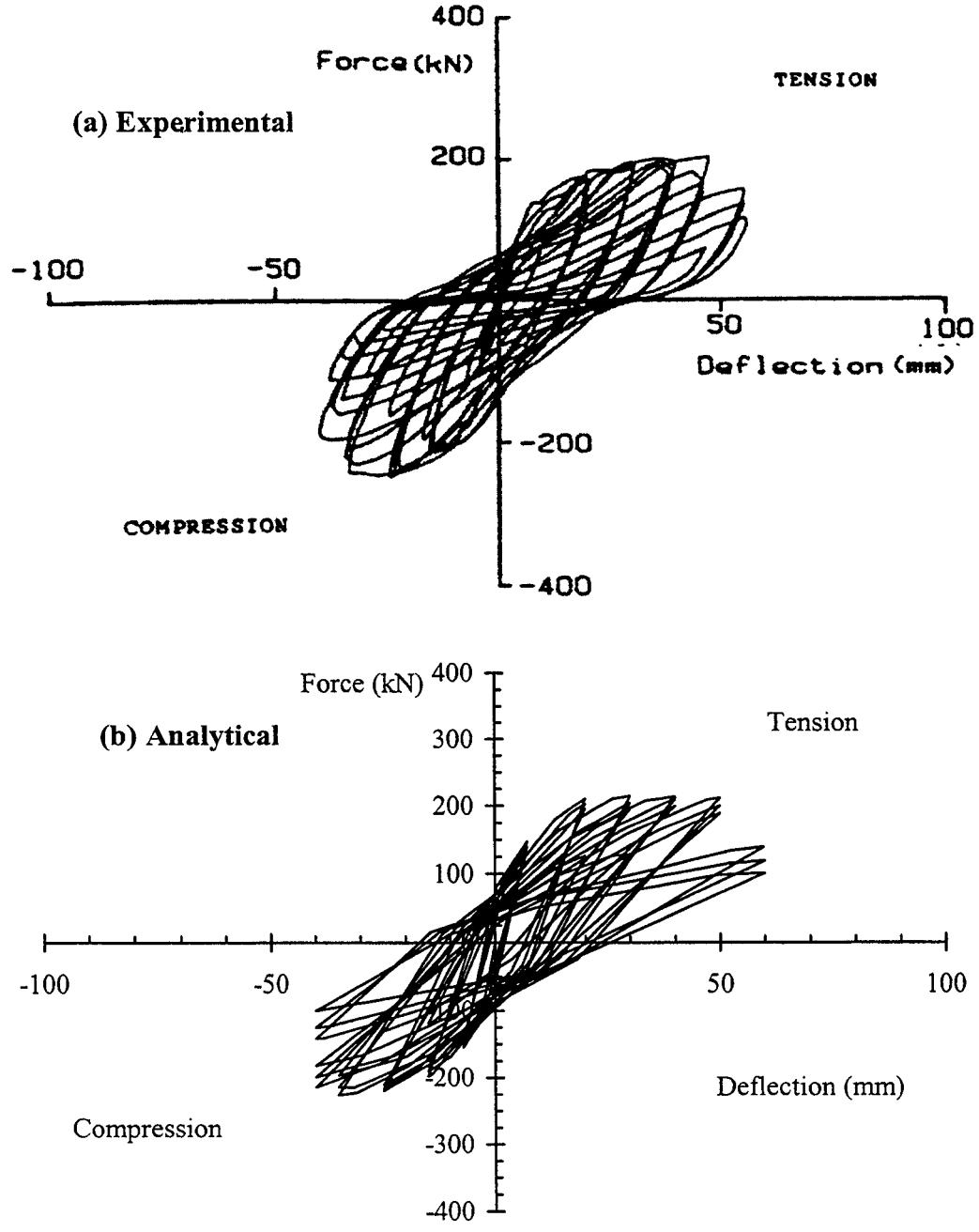

Figure 4.7 Lateral load-top deflection relationship in the direction of loading for case 2 (Saatcioglu and Ozcebe, 1989): (a) Experimental; (b) Analytical

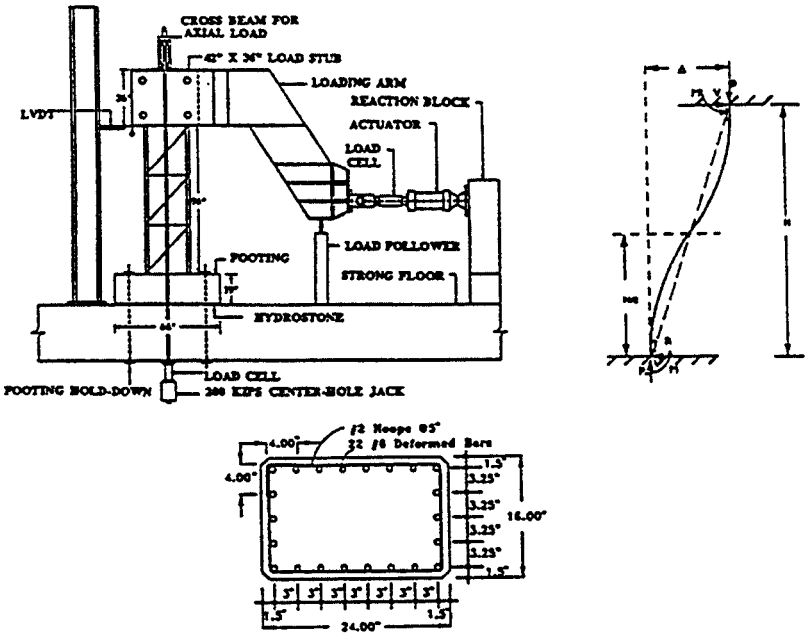

(a)

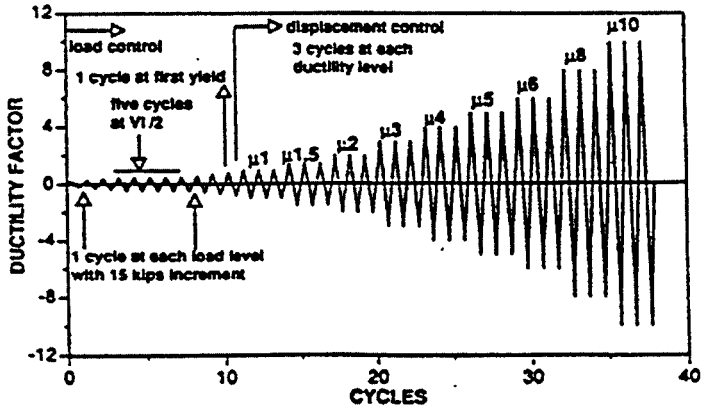

(b)

Figure 4.8 Case 3 (Verma et al., 1993): (a) Dimensions of test specimen; (b) Planned deflection path

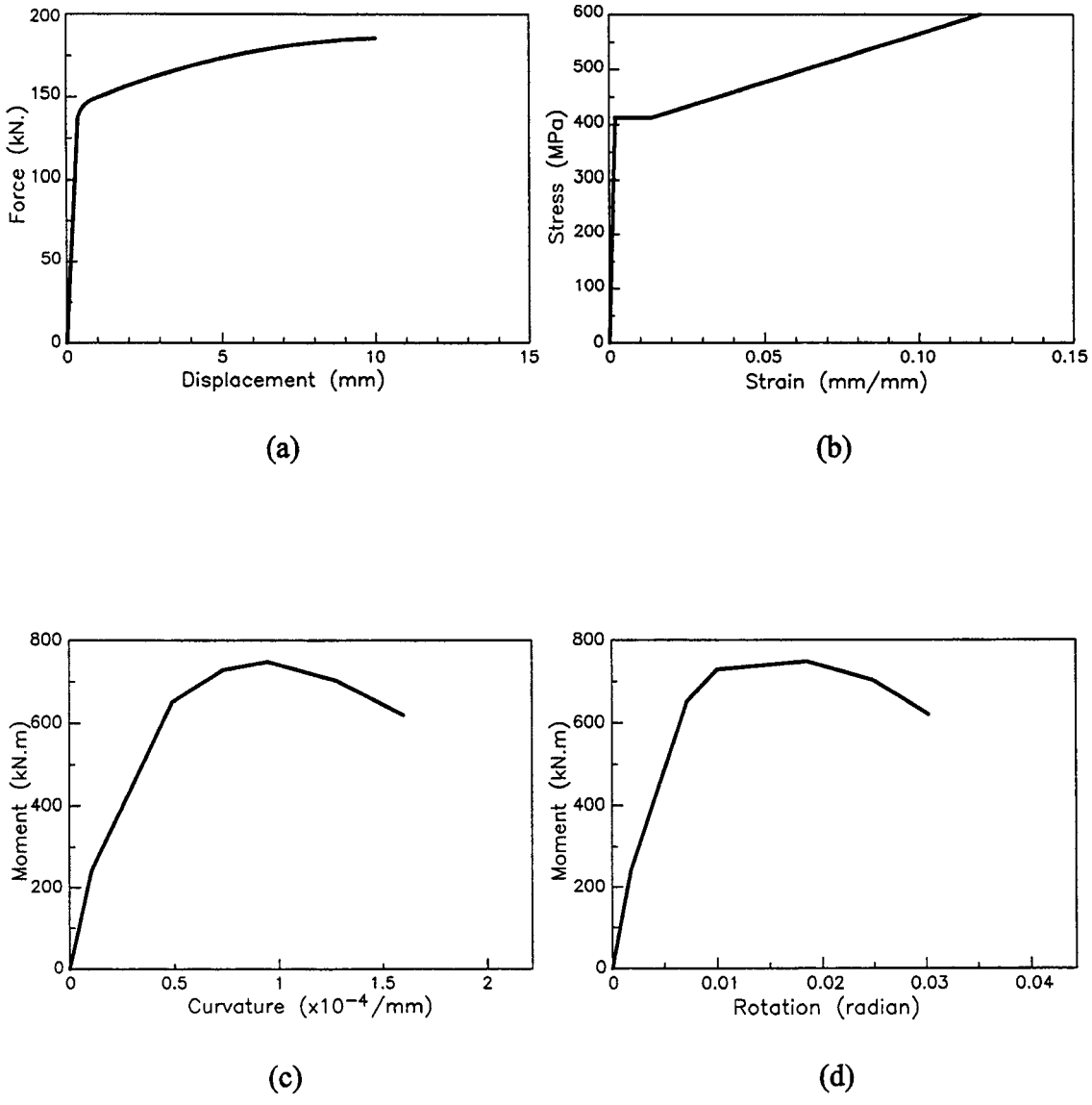

Figure 4.9 Section analysis results: (a) Force-displacement relationship for embedded bar; (b) Stress-strain relationship for embedded bar; (c) Moment-curvature relationship for the section; (d) Moment-rotation relationship for the element

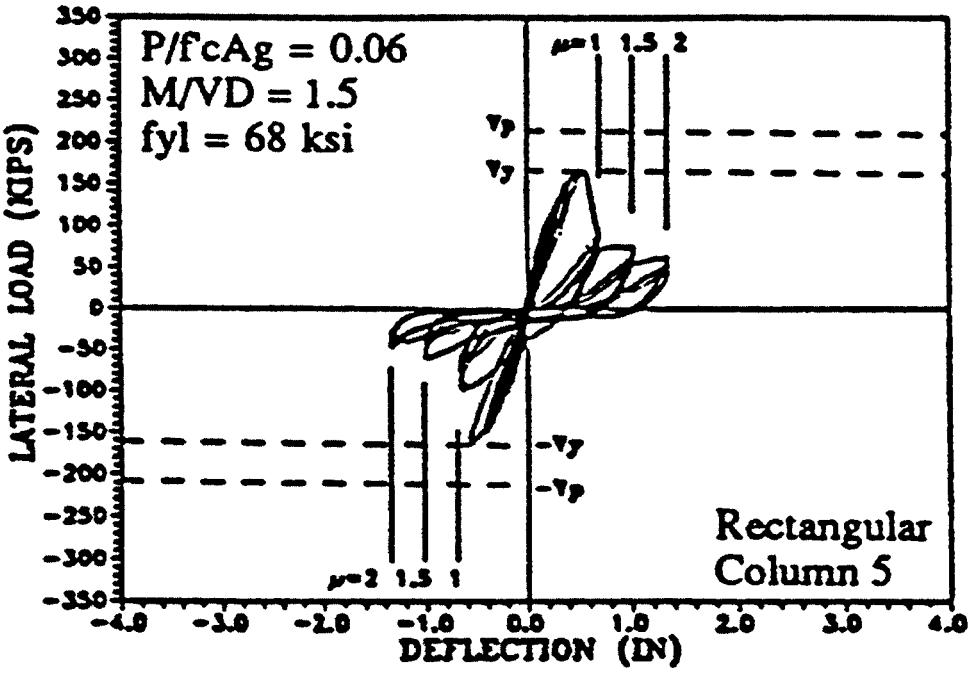

(a) Experimental

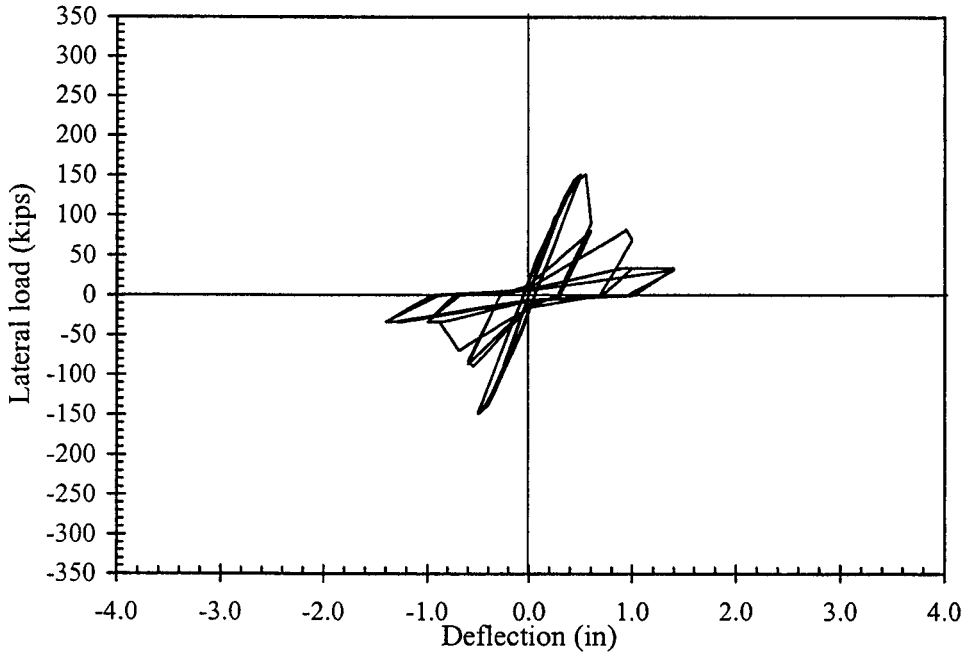

(b) Analytical

Figure 4.10 Lateral load-deflection relationship for case 3 (Verma et al., 1993): (a) Experimental; (b) Analytical

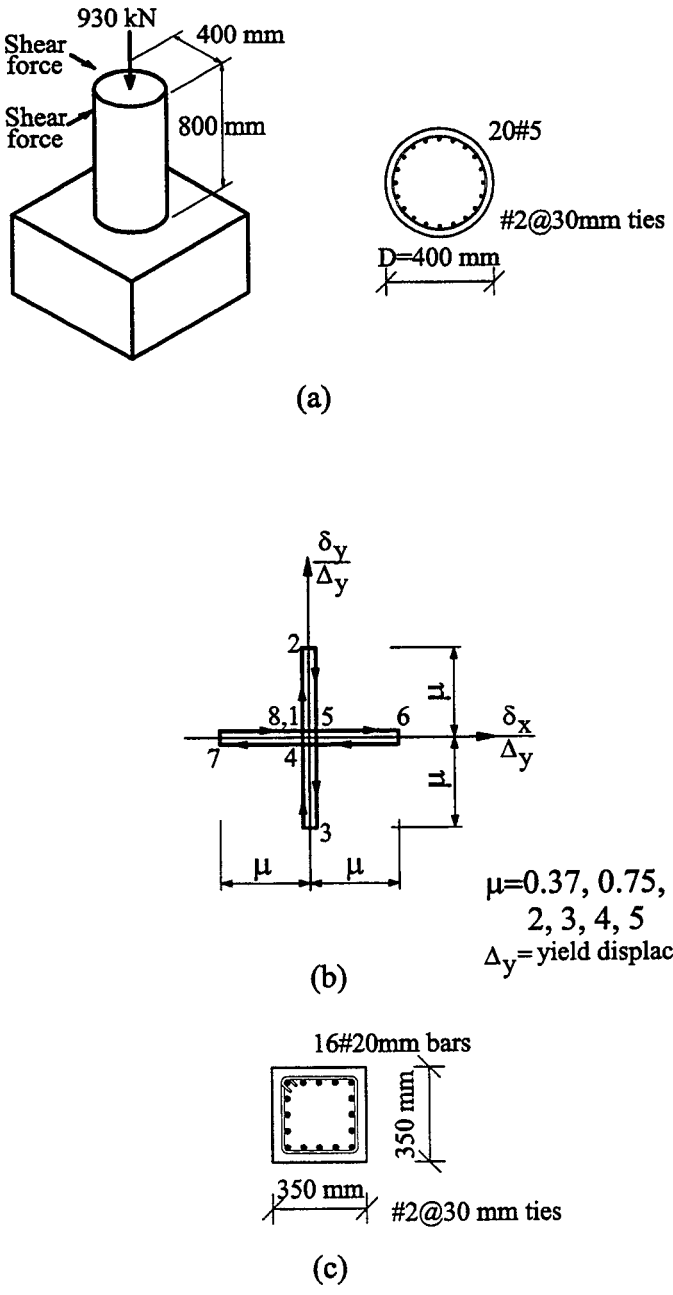

Figure 4.11 Case 4 (Wong et al., 1990): (a) Dimensions of test specimen; (b) Imposed deflection path; (c) Equivalent square section for analysis

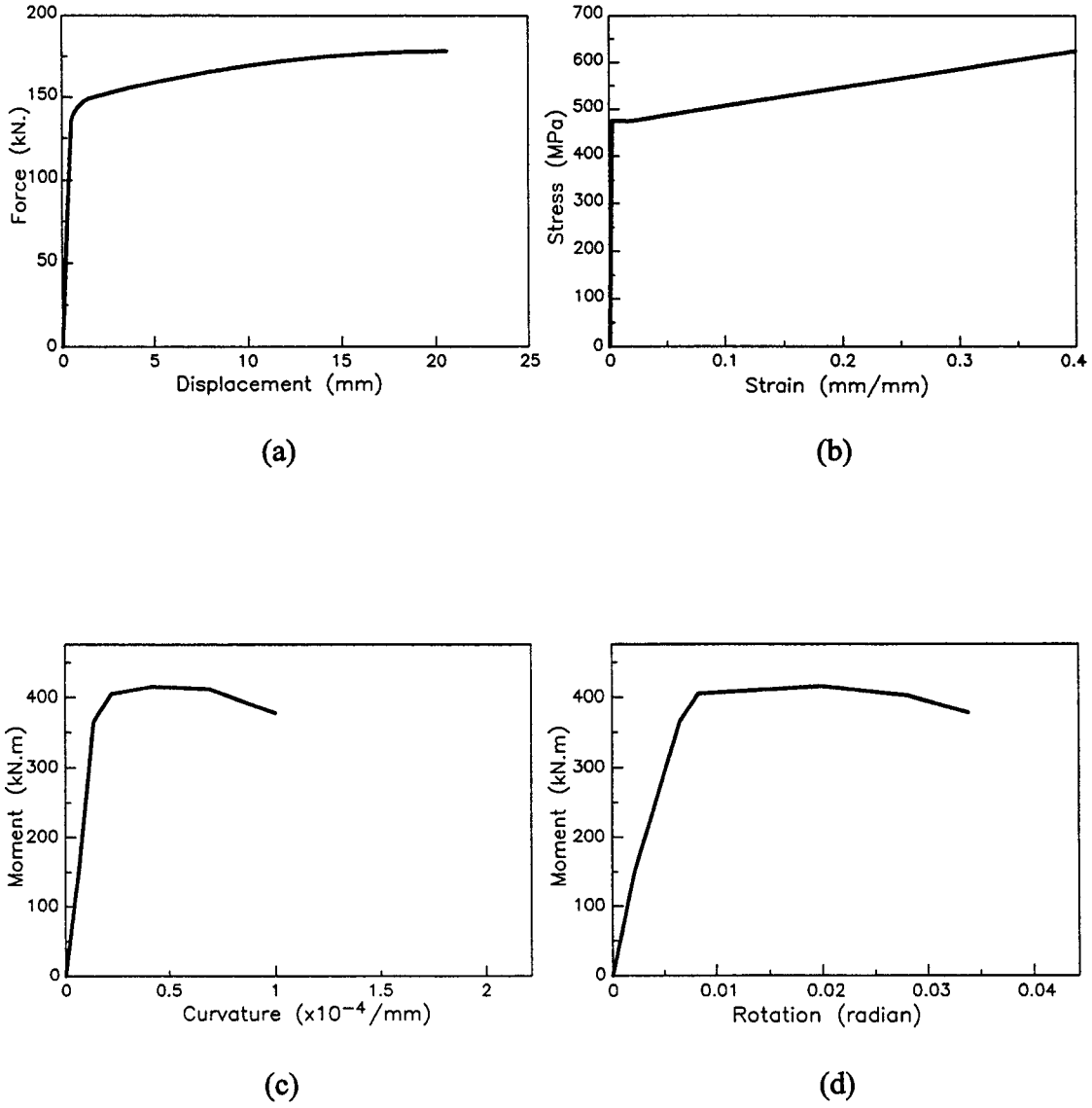

Figure 4.12 Section analysis results: (a) Force-displacement relationship for embedded bar; (b) Stress-strain relationship for embedded bar; (c) Moment-curvature relationship for the section; (d) Moment-rotation relationship for the element

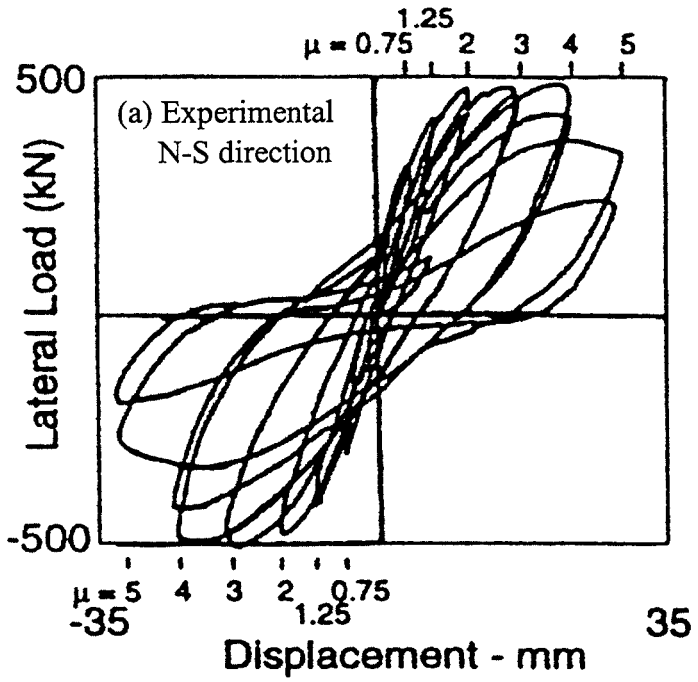

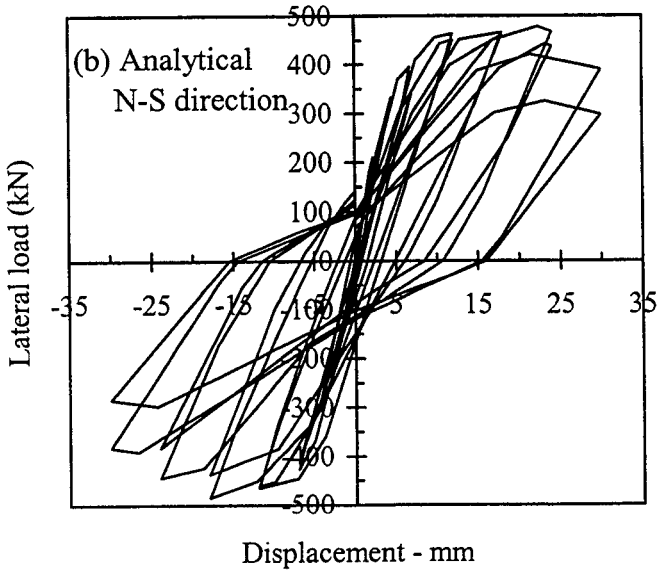

Figure 4.13 Biaxial load-displacement response for case 4 (Wong et al., 1990); (a) Experimental N-S direction; (b) Analytical N-S direction (continued)

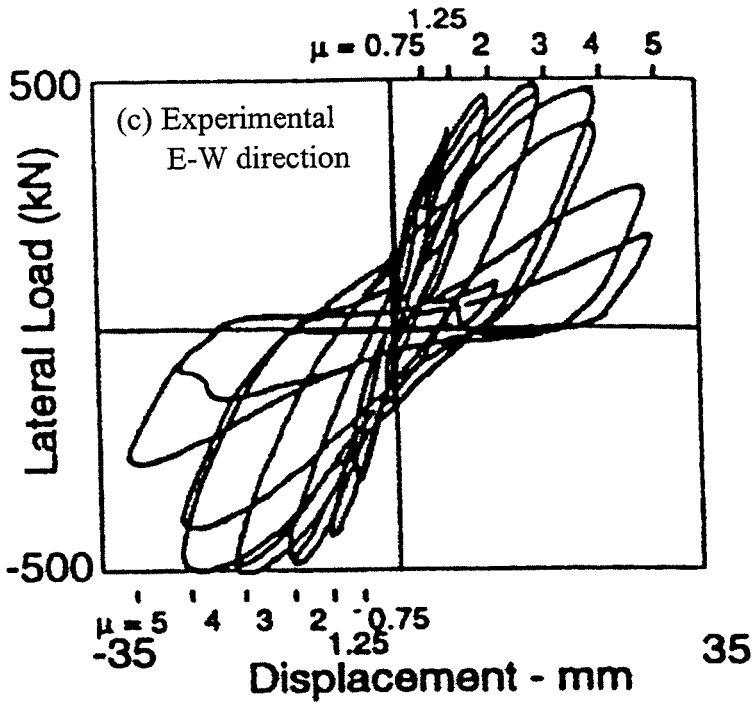

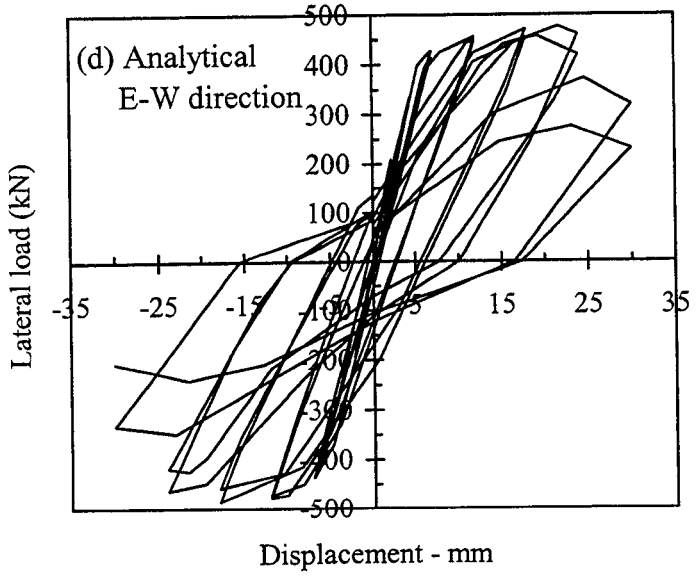

Figure 4.13 Biaxial load-displacement response for case 4 (Wong et al., 1990)
(a) Experimental E-W direction; (b) Analytical E-W direction (continued)

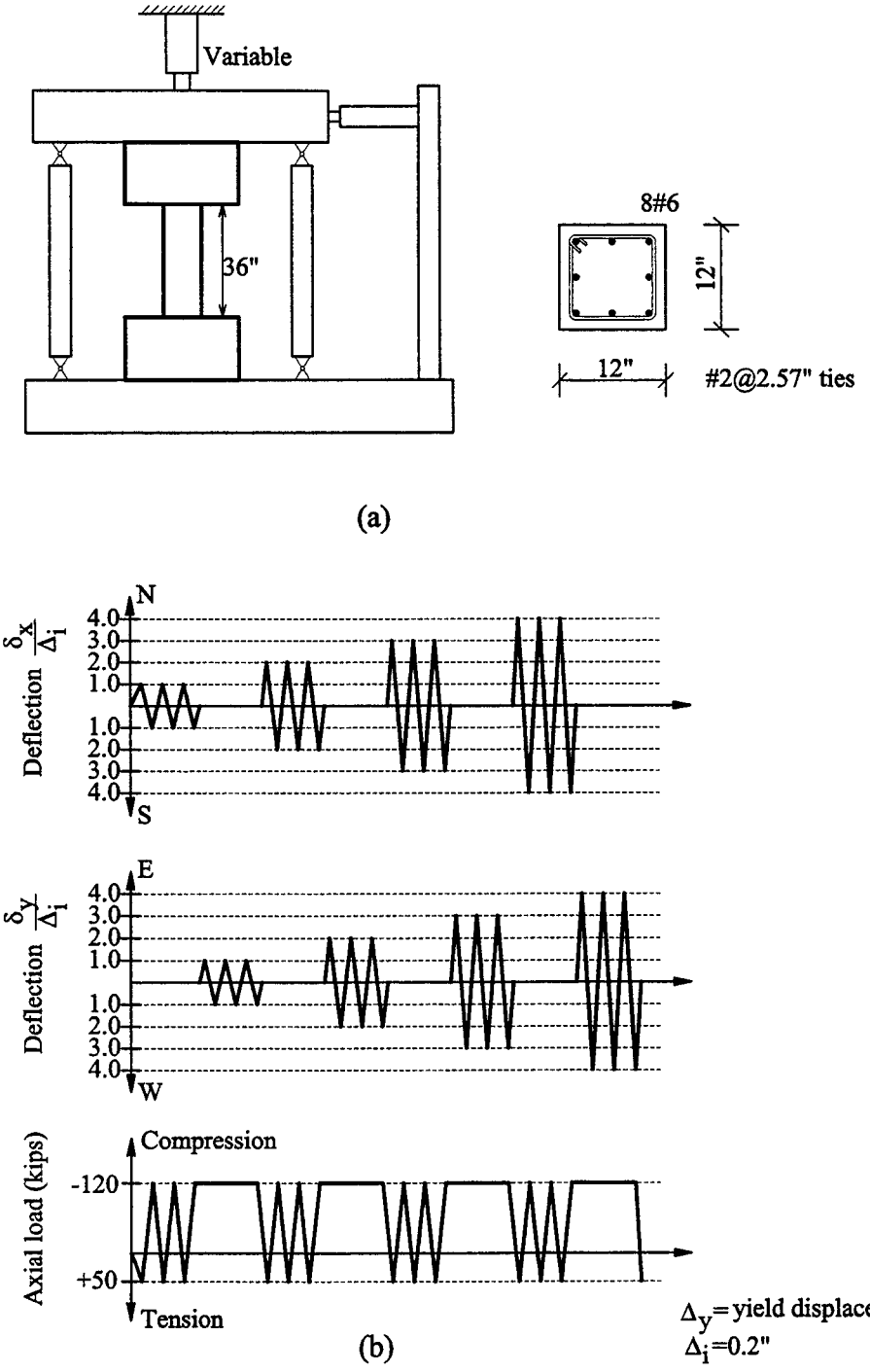

Figure 4.14 Case 5 (Ramirez and Jirsa, 1980): (a) Dimensions of test specimen; (b) Planned deflection and axial load paths

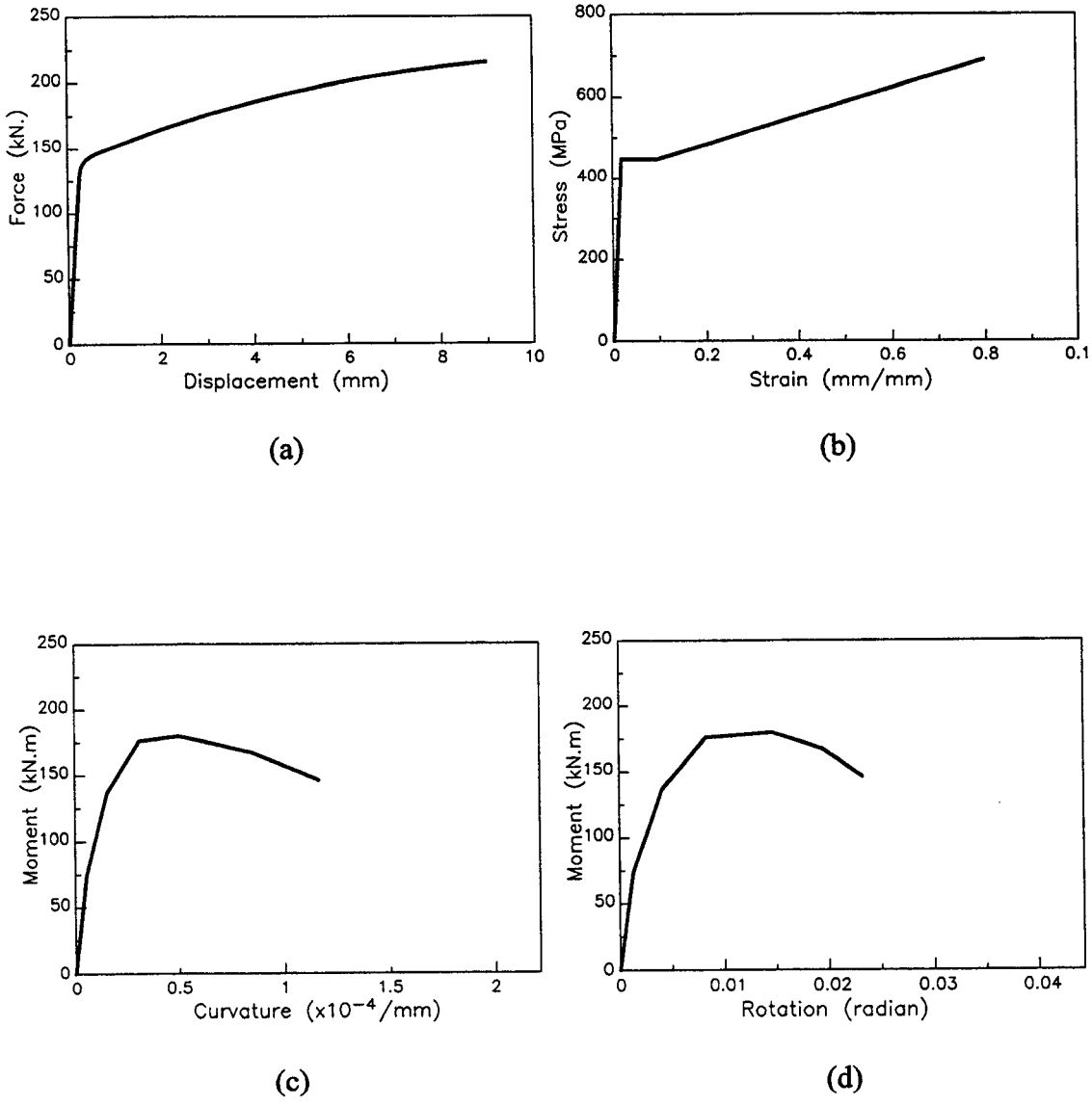

Figure 4.15 Section analysis results: (a) Force-displacement relationship for embedded bar; (b) Stress-strain relationship for embedded bar; (c) Moment-curvature relationship for the section; (d) Moment-rotation relationship for the element

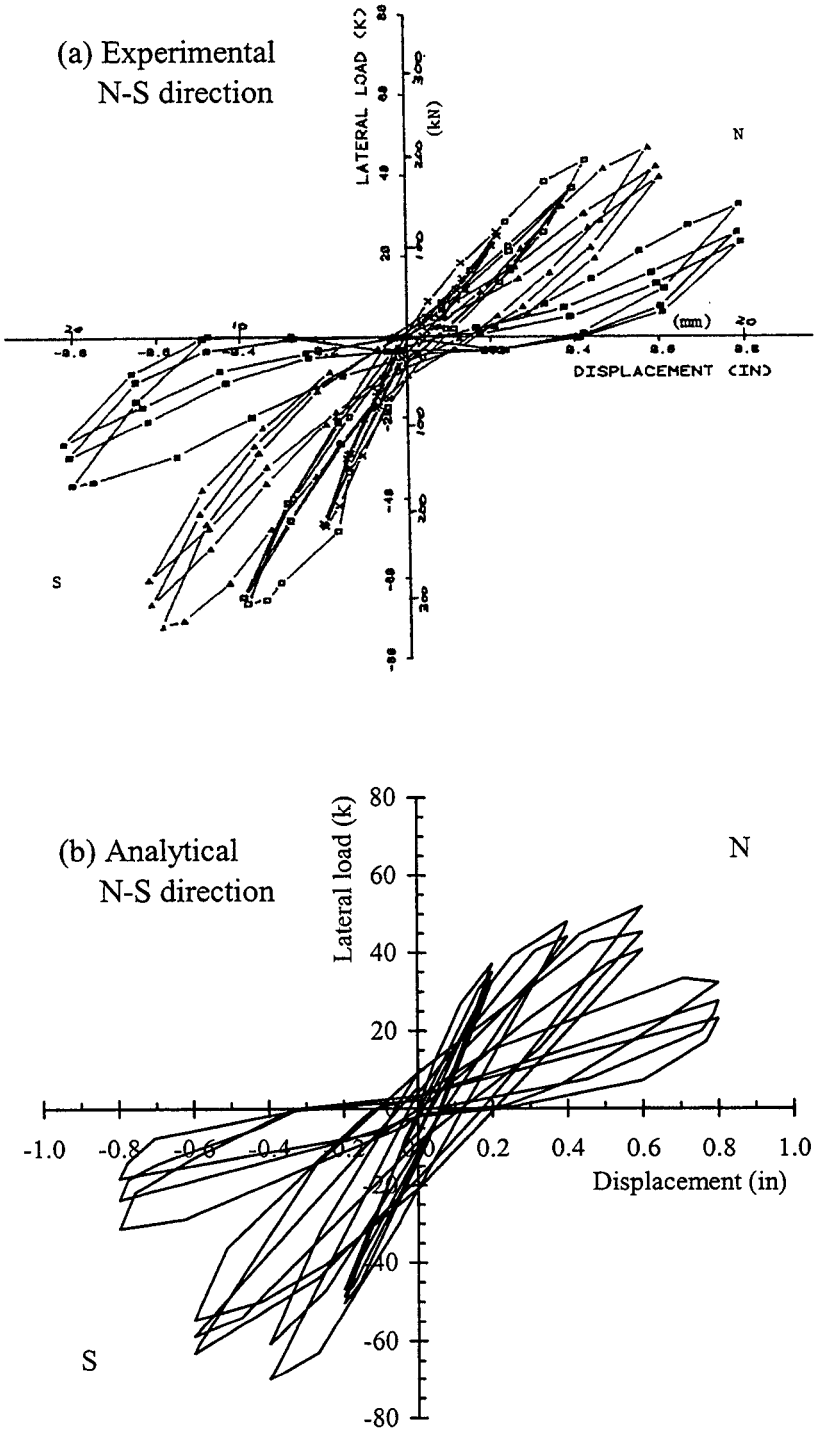

Figure 4.16 Biaxial load-displacement response for case 5 (Ramirez and Jirsa, 1980)
(a) Experimental N-S direction; (b) Analytical N-S direction (continued)

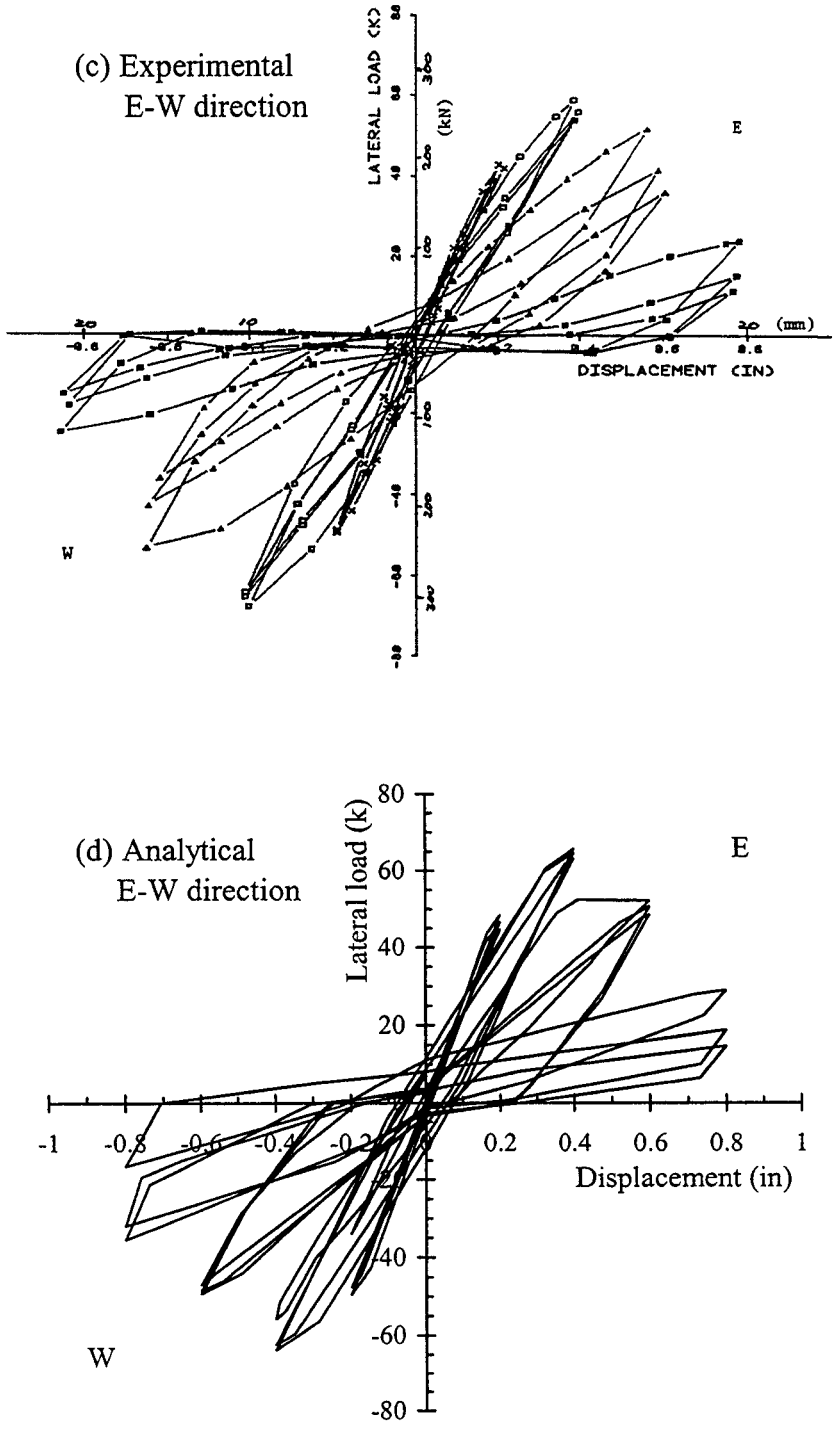

Figure 4.16 Biaxial load-displacement response for case 5 (Ramirez and Jirsa, 1980)
(a) Experimental E-W direction; (b) Analytical E-W direction (continued)

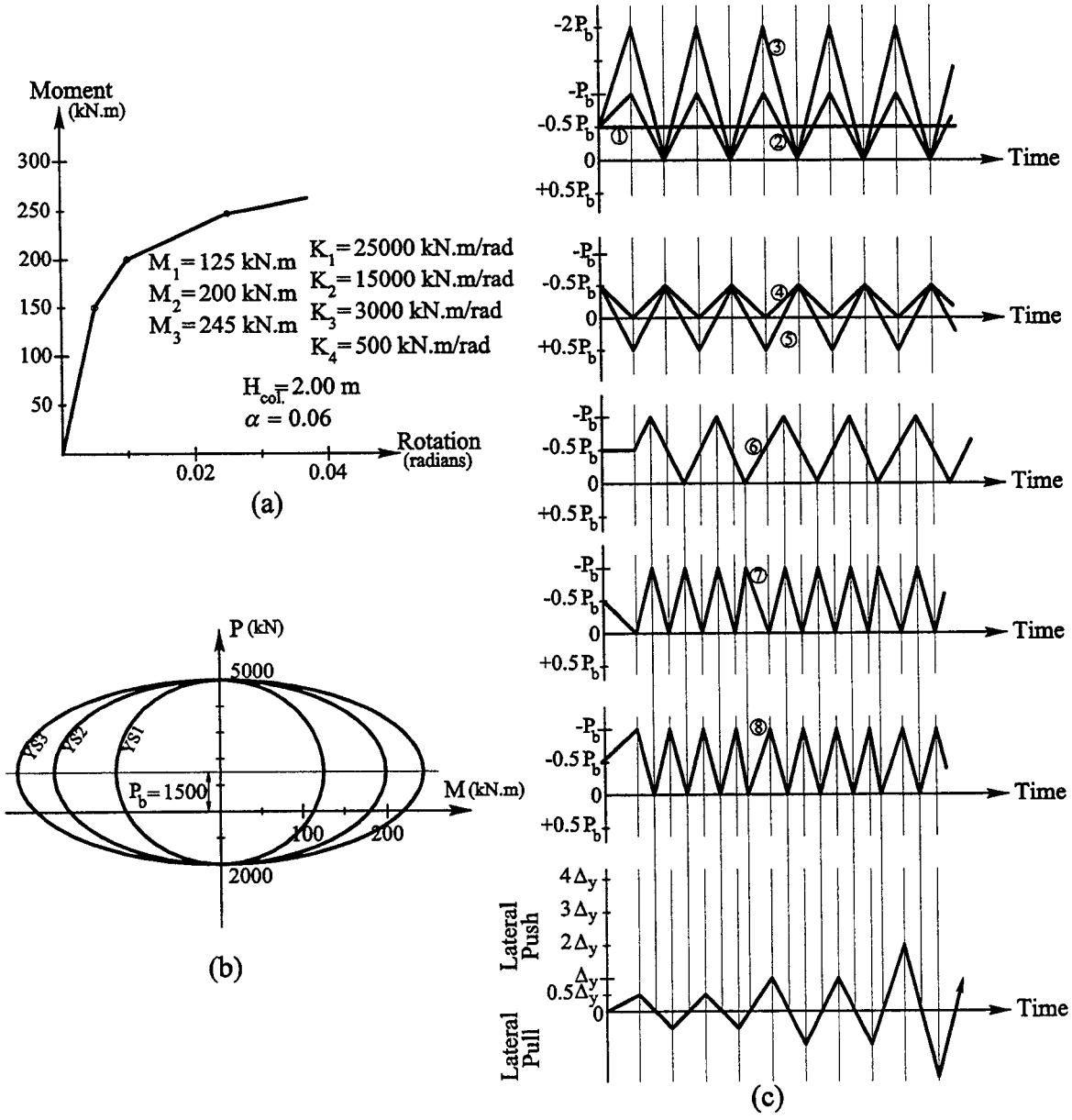

Figure 4.17 Hypothetical cantilever column properties; (a) Moment-rotation relationship; (b) Moment-axial force interaction diagram; (c) Eight axial load paths

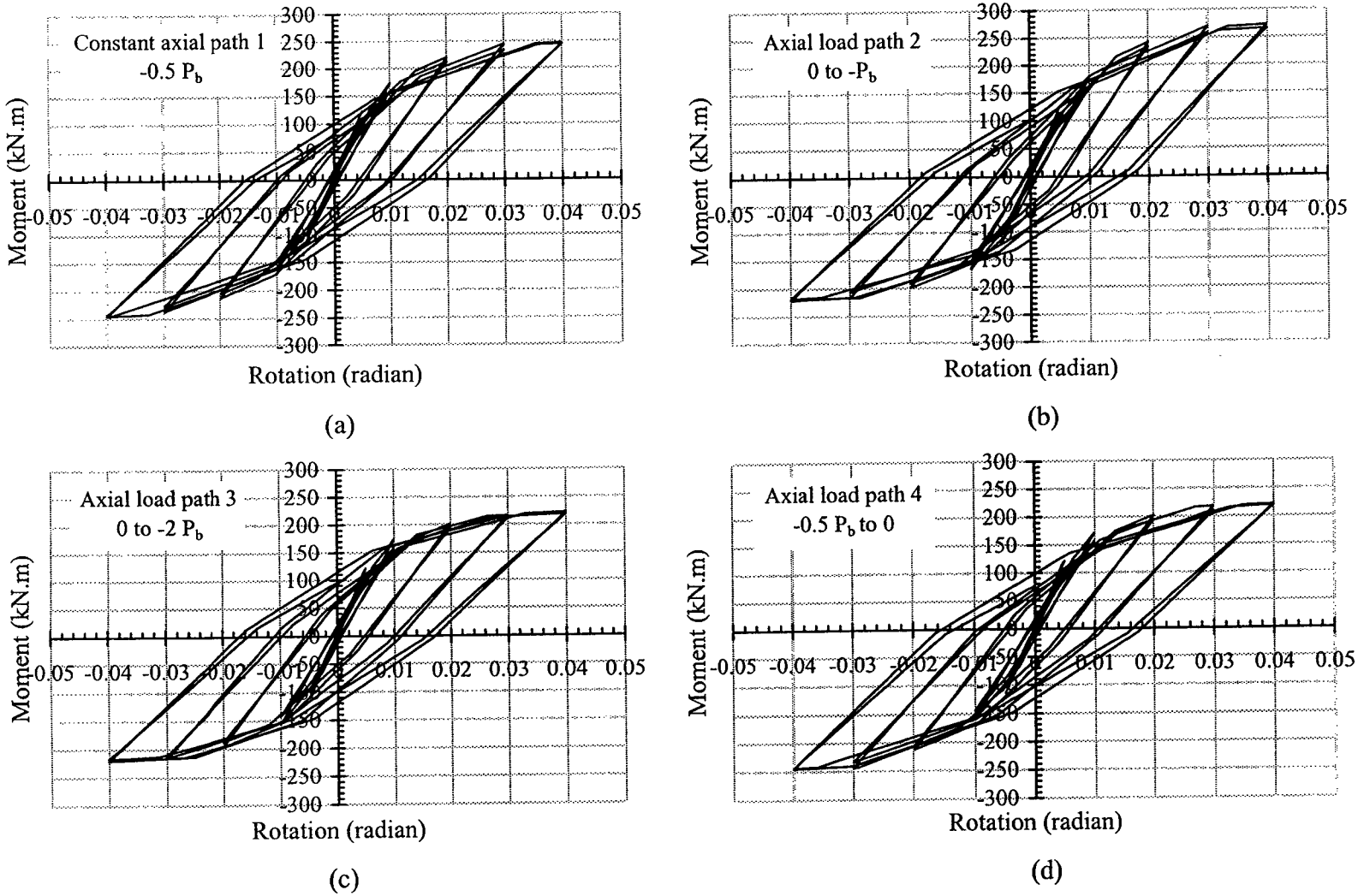

Figure 4.18 Moment-rotation relationship for different axial load paths (continued)

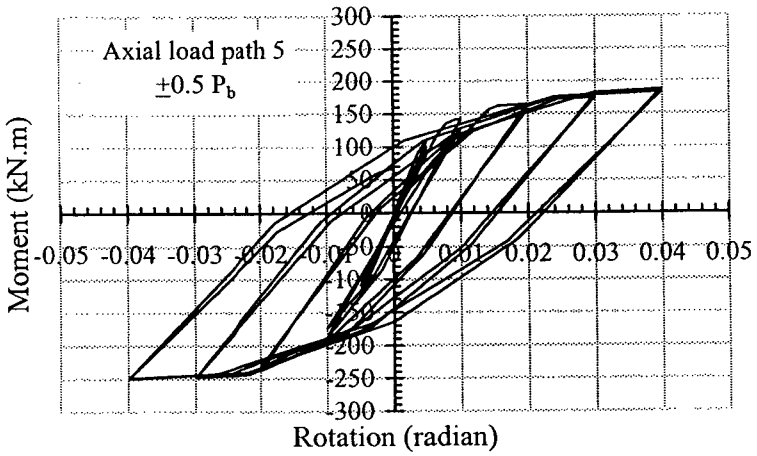

(e)

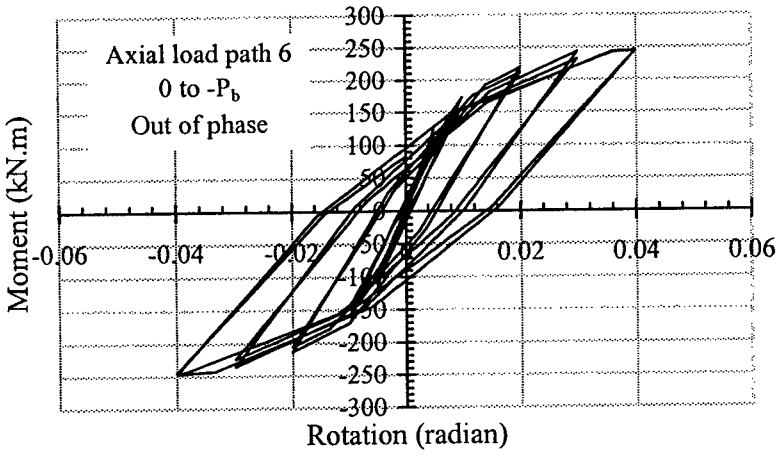

(f)

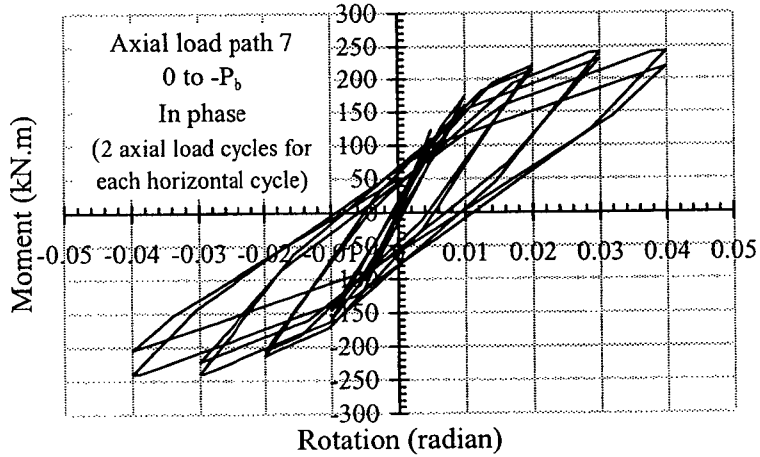

(g)

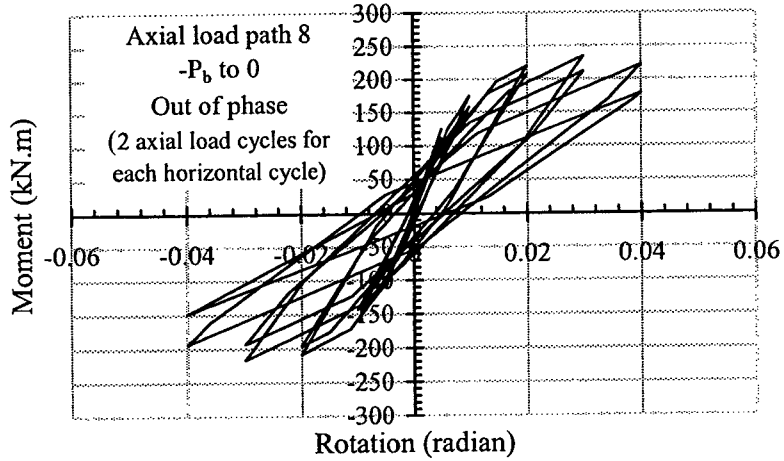

(h)

Figure 4.18 Moment-rotation relationship for different axial load paths (continued)

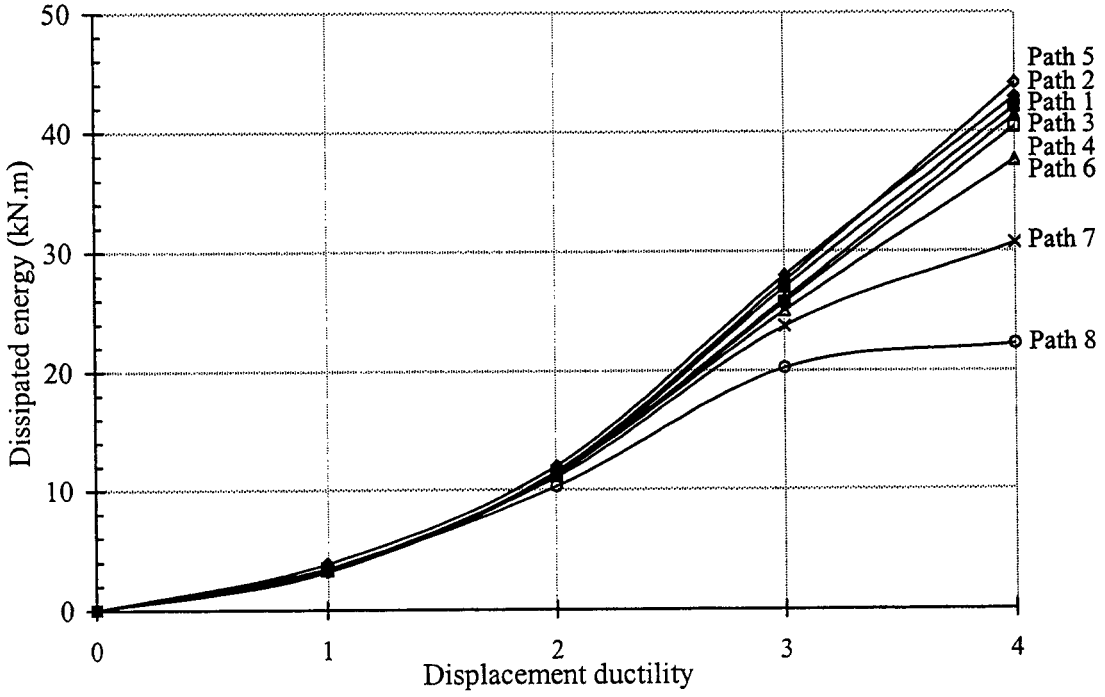

Figure 4.19 Cumulative dissipated energy - displacement ductility factor relationship for different axial load paths

CHAPTER 5

BEHAVIOUR OF NON-DUCTILE AND REHABILITATED SHORT COLUMNS

5.1 BACKGROUND

One of the observed common reinforced concrete structural failures during recent earthquakes is column shear failure. The types of columns that are susceptible to shear failure are those with a reduced height/depth ratio; i.e. short columns. A short column is defined as a column with clear height to depth ratio of less than 5. Figure 5.1 shows one of the cases where columns will behave as a short column due to the lateral stiffening effect of other structural or non-structural elements on a part of the column height.

The shear capacity of short columns is a function of several parameters:

- Longitudinal reinforcement area and strength
- Transverse reinforcement area
- Concrete compressive strength and section confinement
- Bond between main reinforcement and concrete
- Level and variability of axial load

All columns including short columns, built prior to 1970 were designed according to a strength capacity perspective. This led to brittle non-ductile behaviour under moderate to severe earthquake ground motion. Once the strength of the short column is reached, abrupt non-ductile deterioration follows, which reduce the energy dissipating capacity of the columns and consequently of the whole structure.

Recently, performance based seismic design methodology is being adopted by several codes. The ductility of the column past initial steel bar yielding has become the target for good design. This should decrease the probability of failure of the structure, and increase its energy dissipating capacity, when subjected to the design ground motions.

There are three different mechanisms of non-ductile failure in a RC short column; namely, shear capacity mechanism, concrete confinement mechanism and main rebars-concrete debonding mechanism.

With the shear capacity mechanism, the column fails prematurely without reaching the yield limit of the main rebars.

The concrete confinement mechanism is more likely to occur either in columns with flexural-dominant behaviour (high height/depth ratio) that have low transverse reinforcement ratio, or in columns with shear-dominant behaviour (low height/depth ratio) having high transverse reinforcement ratio. In both cases, the concrete cover crushes on the compression side under reversed loading. The spalling of the concrete cover reduces the column effective cross section and increases the strains on core of the column, which in turn losses its compressive capacity due to the deterioration and crushing of the core concrete. Also loss of cover will allow steel reinforcement to buckle. These types of columns usually do not reach medium to high ductility levels.

The main rebar-concrete debonding mechanism is more likely to occur in columns with moderate to high amounts of vertical reinforcement along with low to medium concrete compressive strength. In this type of failure, the bond stress between the longitudinal reinforcement bars and the surrounding concrete reaches high values due

to the high capacity of the main rebars and the low strength of the concrete, which leads to debonding between the two materials at the interface layer.

The use of composites in a wide variety of industrial applications has been rapidly increasing in recent years. Advanced composite materials are being used to strengthen and to enhance the performance of various structural elements, particularly RC columns. Composites are made up of fibres or filaments of glass or carbon, bonded together with a resin matrix. The fibres provide the composites with their unique structural properties. The matrix serves as a bonding agent for the fibre filaments and layers.

Two types of resin-impregnated unidirectional composite fabric are widely used; namely, glass and carbon fibre materials. Typical stress-strain relationships for both types of fibres are shown in figure 5.2. The glass fibres have low strength high strain capacity while the carbon fibres have high strength low strain capacity. Thus the carbon fibres are stiffer than the glass fibres, yet both materials fail in a brittle manner. Wrapping a short column with Carbon Fibre Reinforced Polymer (CFRP) is expected to increase the concrete confinement and provide additional lateral shear resistance, thus enhancing the ductility of the column.

Wrapping a circular column with CFRP produces a uniform passive confining pressure along the column circumference, which reduces the chances of delamination or debonding between the CFRP wraps and the concrete. When a rectangular column is wrapped with CFRP high passive confining pressure occurs at the corners and lower confining pressure is generated along the four edges, with minimum confining pressure at

the midpoint of each side. In this case delamination between the CFRP wraps and the concrete will occur. Similarly, the core of the column confined by steel ties has high confining pressure at the location of each vertical bar and lower confining pressure between the vertical bars. Two anchoring techniques to prevent debonding of CFRP were explored.

One technique for anchoring the fibre wrap is to use through rods. These through rods clamp steel plates on the column sides using hand-tightened nuts. Another technique is to use fibre ties that are anchored into the confined core at one end while the other end is sandwiched between the CFRP wraps. Anchored CFRP wrapping is expected to improve the ductile performance of the short brittle concrete column.

The predictions of the analytical model need to be verified for cases of different confinement. This is best accomplished by controlled confinement using selective FRP wrap design for axially loaded brittle short RC columns.

A pilot experimental program was conducted with the following objectives:

1- To evaluate the behaviour of RC short columns with high transverse reinforcement ratio (designed according to current codes).

2- To evaluate the performance enhancement of such columns when strengthened using CFRP wraps.

3- To evaluate the performance of CFRP rehabilitated short columns with low transverse reinforcement ratio (designed according to pre-1970 codes).

5.2 TEST PROGRAM

Three reinforced concrete short columns were tested to evaluate their behaviour under constant axial load and cyclic lateral displacements. The tested specimens represented a column attached to stiff framing members that restrain its end rotations. The columns were subjected to cyclic displacements applied to the top end while the bottom end was fixed. The horizontal actuator used to apply the horizontal displacements and shear forces was centered at the mid height level of the tested columns. The load was transmitted to the specimen by a stiff L-shaped beam. The moment/shear ratio was maintained equal to $^{h}/_{2}$ according to the used test setup (where h is the column height). The dimensions of the columns were taken similar to those tested by Woodward and Jirsa (1984) in order to have a benchmark for the column's performance. However, the current rehabilitation techniques and the studied parameters are new.

5.2.1 Specimen details

The three specimens had similar column overall dimensions. The columns dimensions were a $^{2}/_{3}$-scale model of a prototype column. One column was designated the control column while the other two had different transverse reinforcement and were strengthened using different systems. All columns were of 305 mm (12") square section with eight #20 (nominal diameter 19.5 mm) longitudinal bars (ρ_g=0.026), and #10 (nominal diameter 11.3 mm) transverse reinforcement bars. The column height was 914 mm (36") and the column height/depth ratio was 3.0. The tested columns were subjected to double curvature with the point of contraflexure being maintained at the mid-height of the column, thus the shear span to depth ratio ($\frac{M}{V.t}$) for the tested columns was 1.5. The

top and bottom ends of the column were fixed to the test setup by means of rigid block of dimensions 457x914x508 mm (18"x36"x20") and with higher reinforcement content compared to that of the column. Figures 5.3 to 5.8 show the details of the three specimens and their construction.

Specimen SC1 had a high transverse reinforcement ratio of ρ_v=2.42% (#10 bars @ 65 mm) and was not strengthened. The transverse reinforcement was designed according to the CSA (1994) design practice code so as to resist the maximum shear force resulting from the flexure capacity of the section. The behaviour of this specimen should represent the expected behaviour of a reinforced concrete short column designed according to the current code of practice.

Specimen SC2 had the same shear reinforcement as specimen SC1 (#10 bars @ 65 mm with ρ_v=2.42%) but was strengthened using three layers of CFRP. The enhancement in the behaviour as compared to specimen SC1 was examined. To prevent the delamination between the CFRP wraps and the concrete, four clamping plates with hand tightened threaded rods through the column section, were used. The through rods were 12 mm (½") diameter and the clamping plates were $^3/_8$" thick.

Specimen SC3 had a low transverse reinforcement ratio of ρ_v=0.5% (#10 @ 305 mm). This low percentage was chosen so as to satisfy the minimum transverse reinforcement requirement according to the ACI (1968) design practice code, providing negligible shear capacity. Without strengthening, specimen SC3 would have experienced non-ductile shear failure due to its low transverse reinforcement ratio. The test specimen SC3 was strengthened with 3 layers of CFRP wrap. Therefore, the behaviour of specimen

SC3 represents a pre-1970 designed RC short column rehabilitated using CFRP wrap. In this specimen, another anchoring technique was used to enhance confinement and reduce the bulging of the columns sides; five 75mm (3") deep CFRP anchors were used for each of the two sides of the specimen.

5.2.2 Materials

5.2.2.1 Concrete

The three specimens were cast at the same time. The mix properties proportions per m^3 for a 25 MPa concrete were as follows:

Cement:	Type 10	236 kg.
	Slag	34.5 kg.
	Type CI	15.5 kg.
Water		122.5 kg.
W/C ratio		0.428
Sand		960 kg.
20 mm gravel		1060 kg.
Admixture		900 ml.

The slump of the concrete mix was 80 mm, which provided adequate concrete workability during the concrete casting in the forms. No segregation or bug holes in the cast concrete were noticed. Eighteen control cylinders were cast. Three cylinders were tested at the age of 7 and 28 days. Three cylinders were tested for compressive strength for each specimen on the day of testing. In addition, three cylinders were tested for the tensile strength of concrete using the split cylinder test at 28 days. The specimens and the cylinders were cured for seven days after pouring the concrete using a 100% moistured

burlap covered by plastic sheet. A summary of the cylinder test results is given in table 5.1.

5.2.2.2 Reinforcement

Deformed bars #20 (19.5 mm nominal diameter) were used for longitudinal reinforcement and #10 (11.3 mm nominal diameter) deformed bars for transverse reinforcement. Coupons of the deformed bars were tested to obtain yield stress and ultimate stress as summarized in table 5.1.

5.2.2.3 Carbon fibre reinforced polymer (CFRP)

The MBrace CF 130 carbon fibre system was used in the rehabilitation of specimens SC2 and SC3. The MBrace system consists of five components:

- MBrace Primer
- MBrace Putty filler
- MBrace Saturant resin
- MBrace CF 130 carbon fibres
- MBrace Topcoat (not used)

The mechanical properties of the used materials as provided by the supplier (Master Builders, 2001), are shown in table 5.1.

5.2.3 Loading system

The loading system consisted of a lateral reaction frame supporting the lateral hydraulic jack and a vertical setup supporting the vertical hydraulic jack and the 'pantograph' to restrain the top fixed end of the tested column against rotation. Figures 5.9 and 5.10 show details of the test setup.

5.2.3.1 Hydraulic jacks

Two MTS hydraulic jacks were used to control the specimens' displacements and forces. A 1200 kN capacity actuator was used to provide the horizontal lateral load. The jack was in a force control mode until yield was reached in both push and pull directions of the specimen. After the initial yield of the steel reinforcement, displacement control mode was used to provide displacements as a multiplier of the yield displacement. Another 1000 kN capacity hydraulic jack was used to provide the axial load to the column. The load was kept constant at 500 kN during the test. The axial load tended to increase or decrease during the lateral cyclic displacement of the specimen due to the elongation or shortening of the specimen's height. Although attempts were made to maintain the axial load constant, fluctuation in the order of ± 3 to 5 % of the required 500 kN load, were measured.

5.2.3.2 Pantograph system

To restrain the top of the column against rotation, so as to represent fixed end conditions, a pantograph system was used. The system of the pantograph is shown in figure 5.11. It consisted of four inclined link members supported by a horizontal member at the mid height of the pantograph. The higher ends of the two top links were attached to a stiff horizontal beam, which also acted as a reaction beam for the axial load applied to the column. The lower end of the two bottom links were attached to a stiff L-shaped beam which translated the horizontal force provided by the horizontal actuator as shear, V, and moment, $M = V\frac{h}{2}$ at the top end of the column. The pantograph restrained the top of the column from rotation (thus applying the required moment) and allowed free lateral

and vertical displacements. The pantograph also provided an out-of-plane stiffness, thus preventing any torque or out of plane loading on the specimen.

5.2.4 Instrumentation

During testing, loads, deflections and strains were measured to monitor the behaviour of the specimen. A 66-channel capacity data acquisition system was used for recording the readings at 5 seconds intervals. The data were saved after each cycle for subsequent data analysis.

5.2.4.1 Loads

The lateral loads corresponding to the lateral displacement and the axial load were measured using load cells that were integral with the loading rams. The load cells were calibrated more than once prior to conducting the tests and were found to give consistent measurements.

5.2.4.2 Deflections

Lateral deflections of the specimen, relative rotation of the two end blocks of the column, as well as the curvature of the column were measured during the test. Each specimen was instrumented using twenty linear voltage displacement transformers LVDTs, ranging from ±12 mm (±½") to ±125 mm (±5") capacity, depending on the monitored position. The lateral deflections were measured with respect to an independent vertical stiffened tubular frame that was fixed to the strong floor. Figure 5.12 shows the deflection instrumentation for each specimen. The signals from the lateral LVDT attached to the top block and the lateral load cell were used to produce the load deflection curves on x-y plots during the test.

5.2.4.3 Strains

Strains in the longitudinal and transverse reinforcement, as well as in the CFRP wraps, were measured by means of 5 mm electrical strain gauges. The locations of the strain gauges are shown in figure 5.13. For each specimen, four strain gauges were placed on each of the four corner longitudinal bars and located at the bottom, $^1/_3$ height, $^2/_3$ height, and the top of each bar. Two strain gauges were placed on three ties for each specimen. The three ties were chosen to have consistent locations for the three specimens, thus the position of the three ties of specimen SC3 was measured for the three specimens. Six strain gauges were placed on the outer surface of the CFRP wraps; three of them were at the centerline axis of the column while the other three were near the edge of the column and were located at the bottom, mid height and top end of the column.

5.2.5 Loading history

All specimens were subjected to a 500 kN constant axial load. The basic lateral deflection pattern is shown in figure 5.14. For specimen SC1, the lateral load was applied in increments of 10 kN until cracking of concrete. A cycle at cracking level was then conducted and the propagation of cracks were observed and marked. For specimens SC2 and SC3 the cracking load was not recorded because the concrete cracking was obscured by the CFRP wraps. For all specimens, two load cycles at half the yield strain of the longitudinal bars were applied. The yield deflection Δ_y for each specimen was defined as the deflection at first yielding of the longitudinal bars. After yield, the lateral displacement level was increased incrementally as a multiplier of Δ_y, applying two cycles at each displacement level. For specimens SC2 and SC3, the CFRP wrap was removed

after the test was completed in order to examine the state of the column concrete. Figure 5.15 shows a typical deformed shape and the associated distribution of axial load, shear and moment in the push and pull directions for the tested columns.

Table 5.1 Material properties

Concrete

	Age (days)	f_c' (MPa)
Control 1	7	28.0
Control 2	28	38.0
Day of test of Specimen SC1	160	39.4
Day of test of Specimen SC2	205	39.5
Day of test of Specimen SC3	240	39.5

Concrete split cylinder strength = 3.2 MPa (28 days)

Reinforcement

Bar	**Nominal bar area (mm^2)**	**Yield stress (MPa)**	**Ultimate strength (MPa)**
#20	300	432	684
#10	100	421	662

Carbon fibre reinforcement system MBrace CF 130 as provided by the supplier (Master Builders, 2001)

Fibre density: 18.2 N/mm^3

Fibre modulus: 2.35 x 10^5 MPa

Fibre areal weight density: 3 N/mm^2

Design thickness: 0.165 mm

Design tensile strength: 3550 MPa

Design tensile modulus: 2.35 x 10^5 MPa

Ultimate tensile elongation: 1.5%

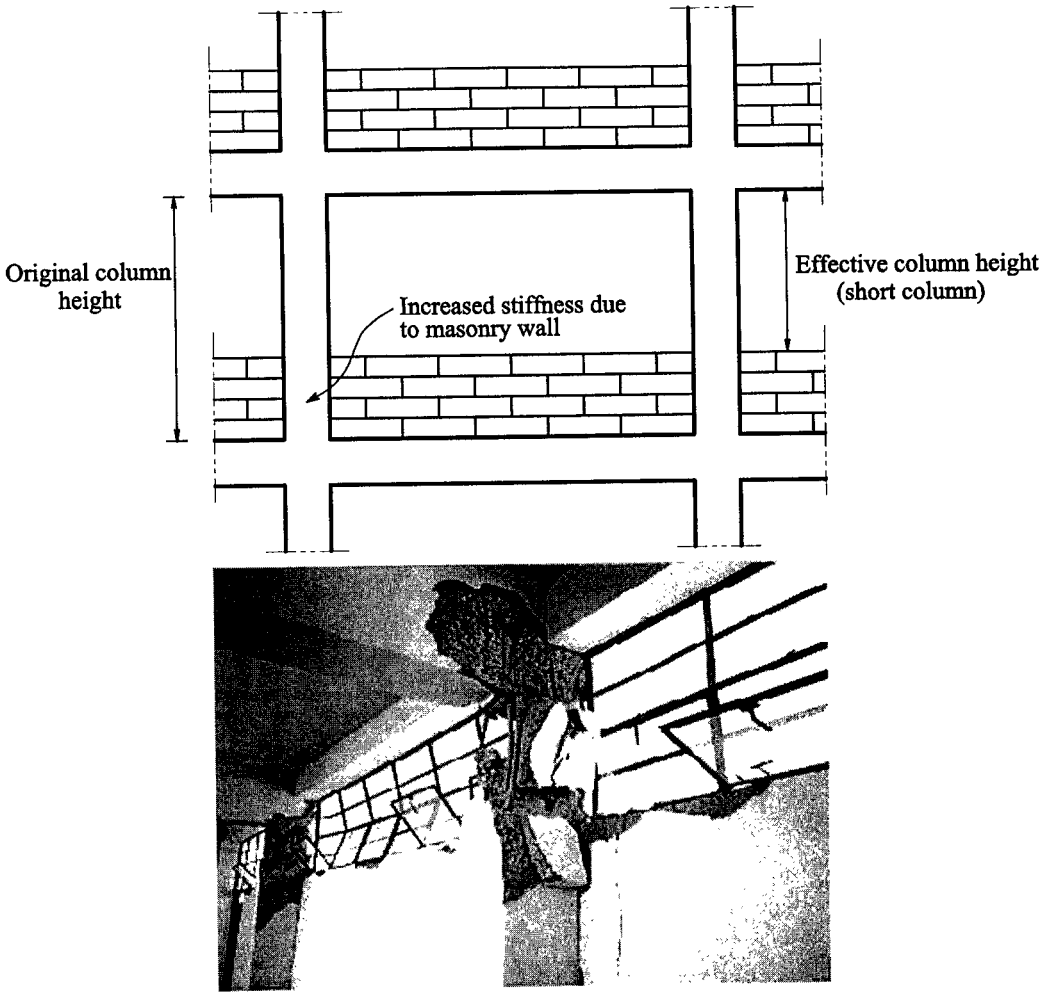

Example of damaged captive column: failure in short column created by the increased stiffness due to masonry walls (EERI, 2002)

Figure 5.1 Short columns

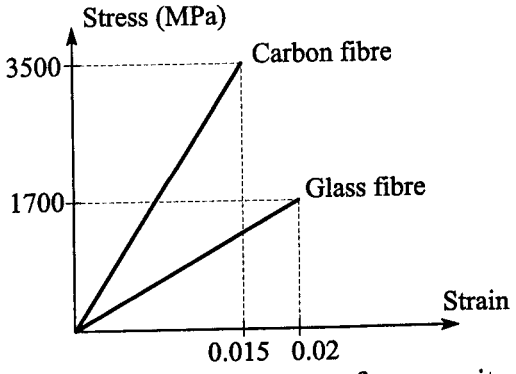

Figure 5.2 Stress-strain curves of composite materials

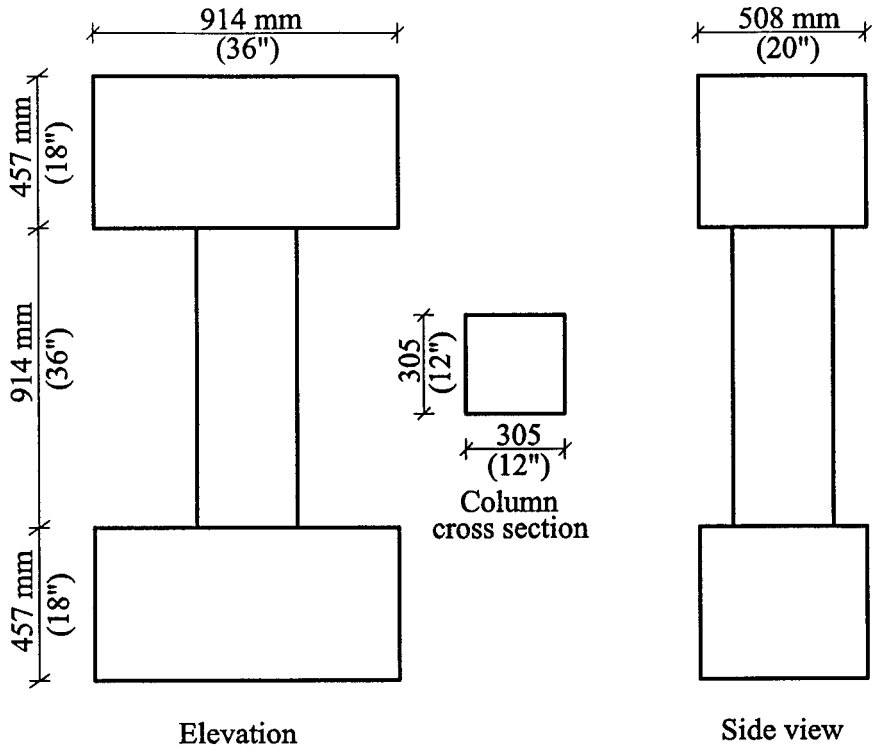

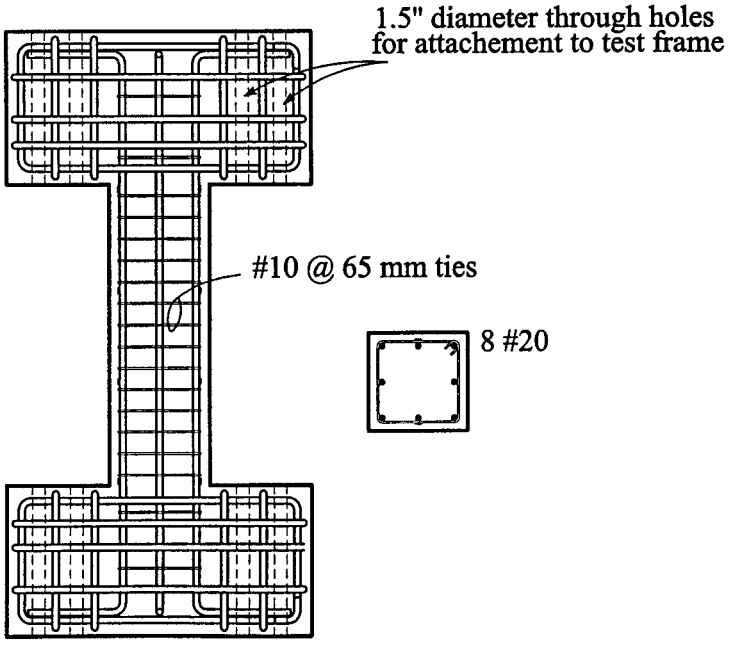

Reinforcement details

Figure 5.3 Specimen SC1

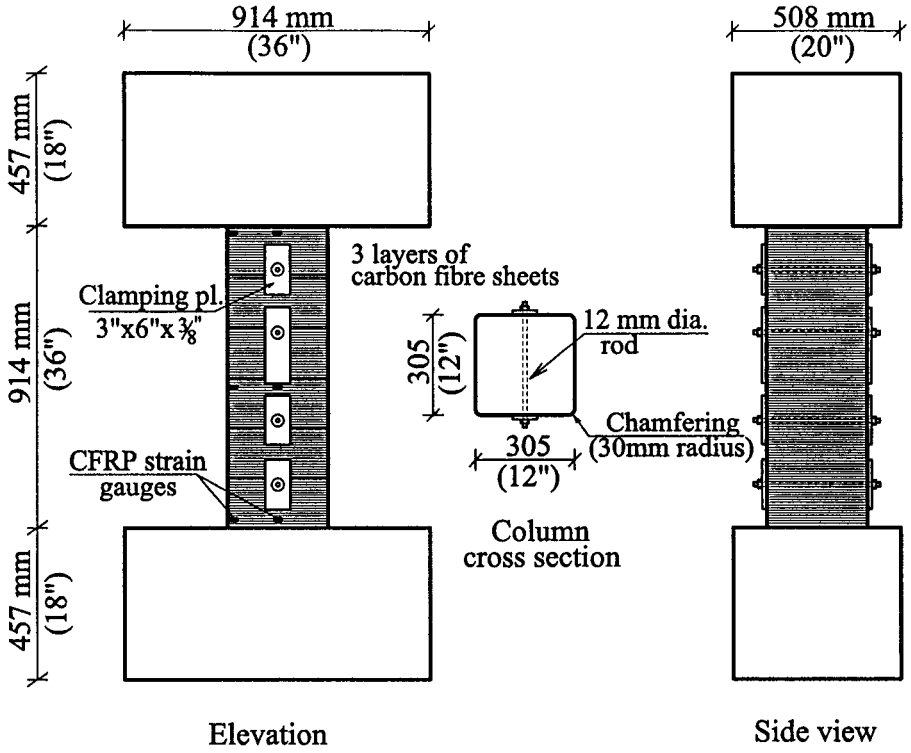

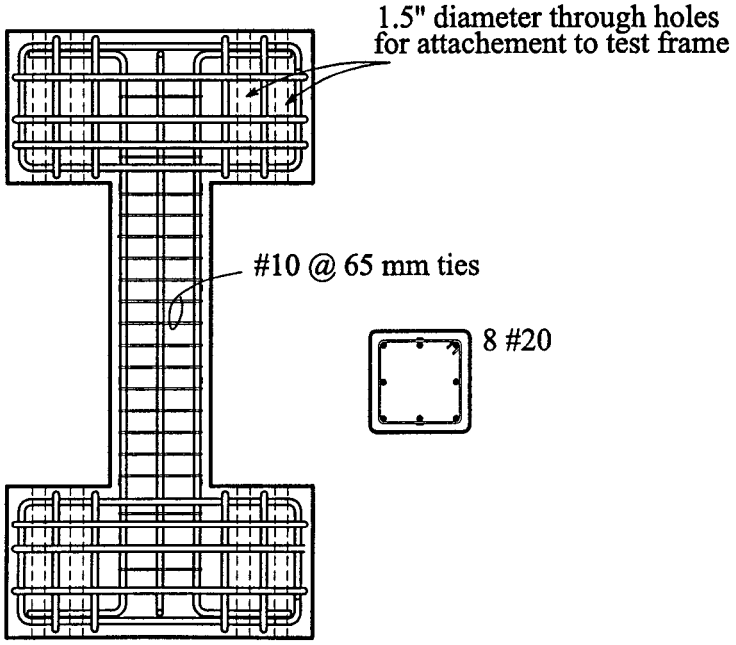

Reinforcement details

Figure 5.4 Specimen SC2

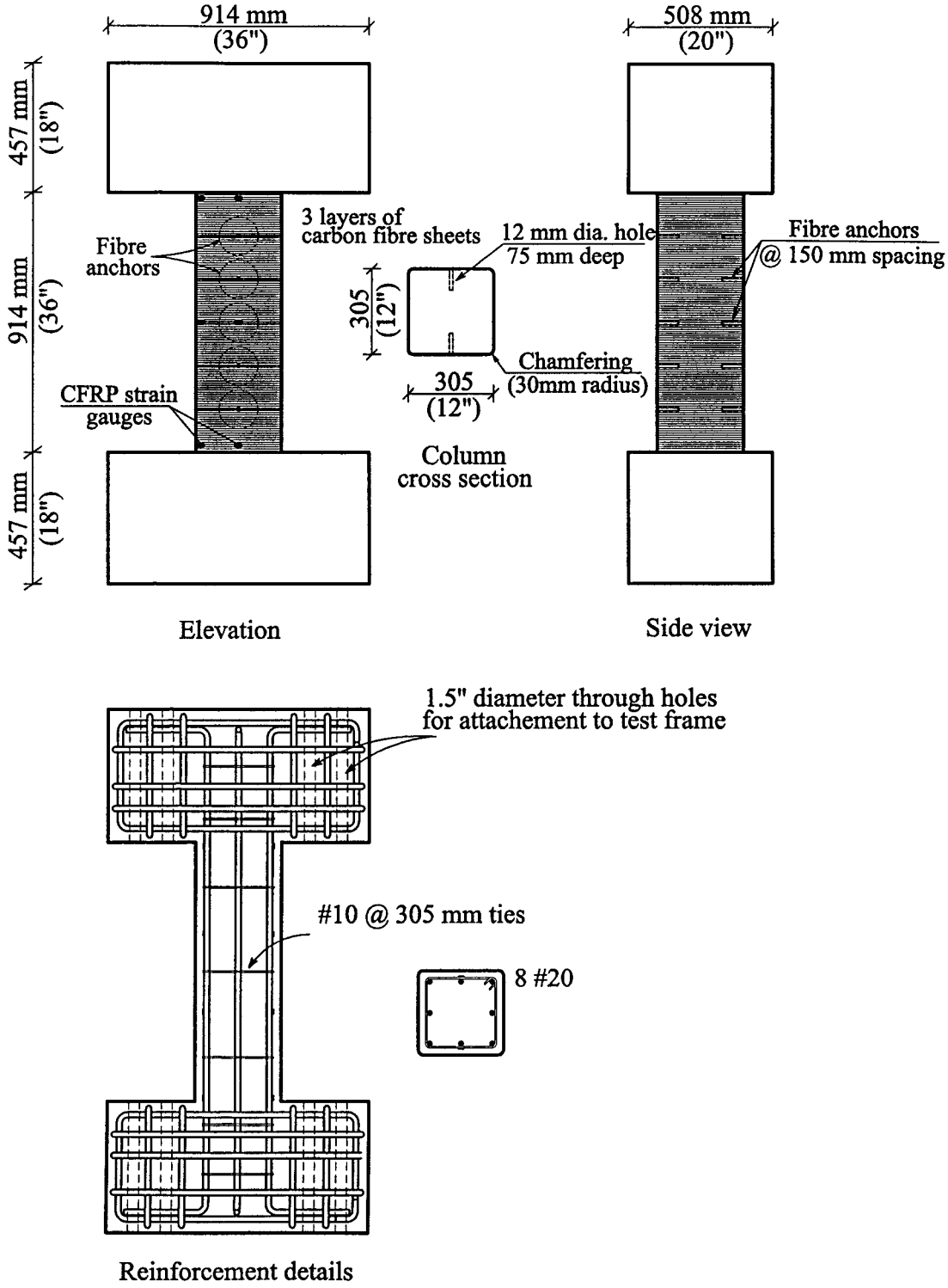

Figure 5.5 Specimen SC3

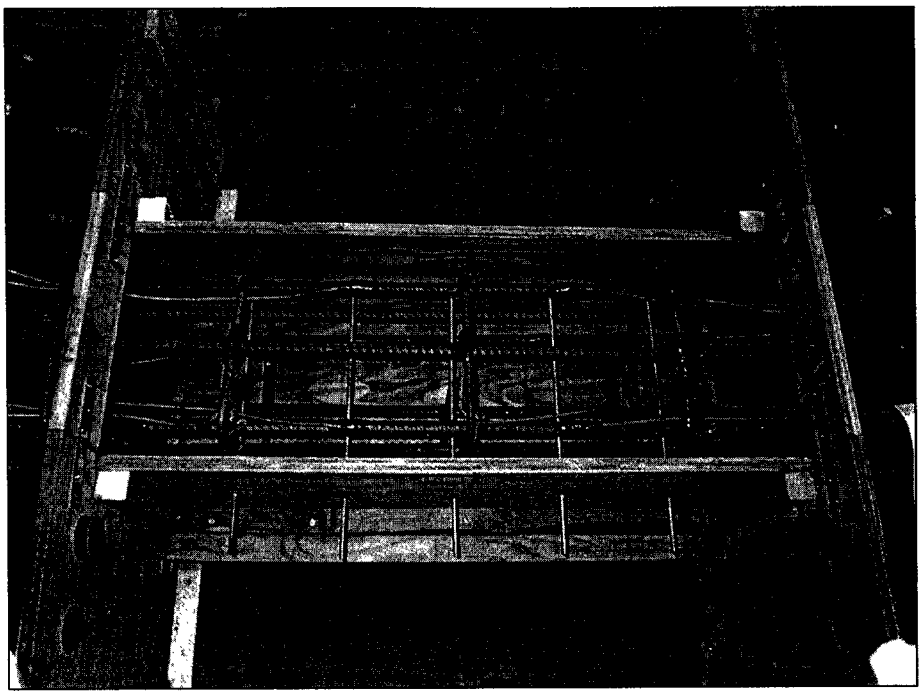

Specimen SC3

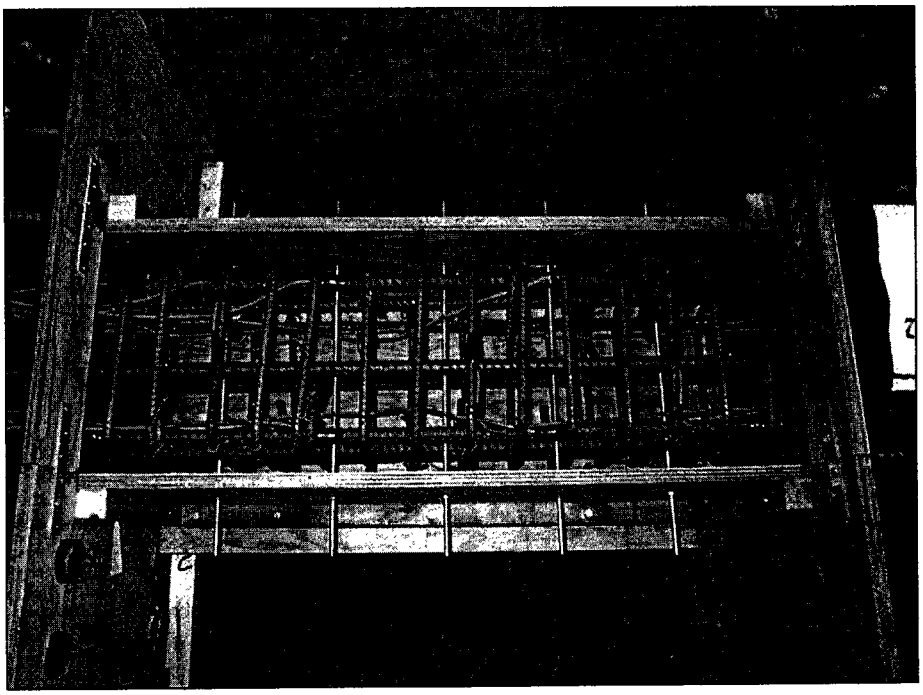

Specimens SC1 and SC2

Figure 5.6 Details of reinforcement for the three specimens

(a)

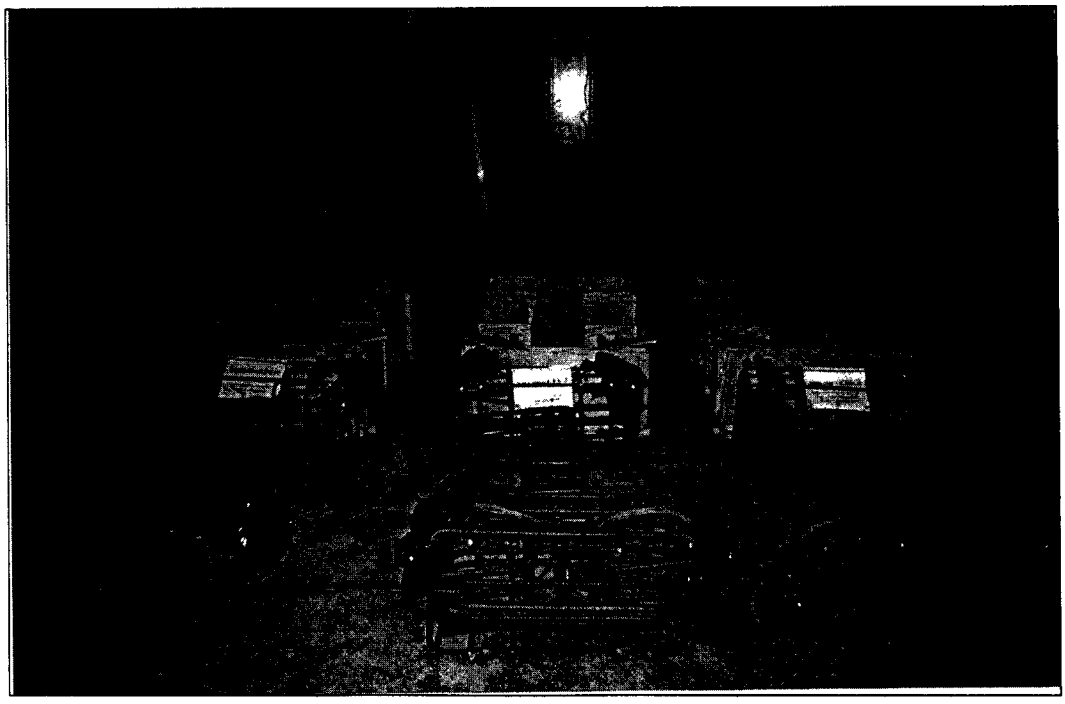

(b)

Figure 5.7 (a) Wooden forms; and (b) steel cages before casting concrete

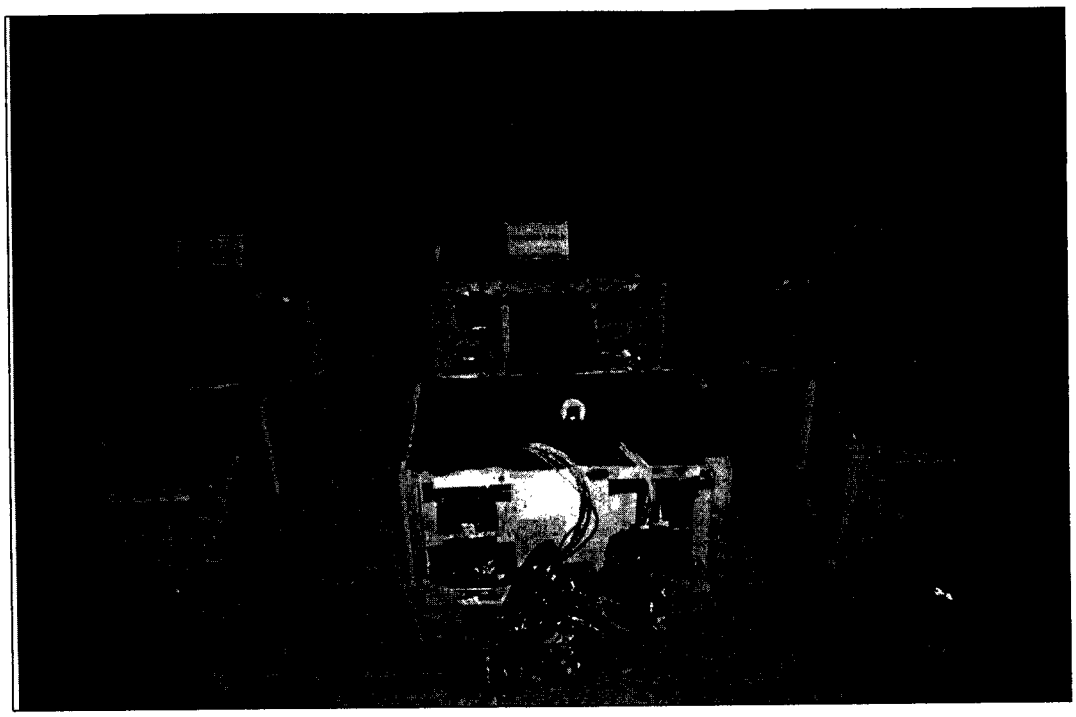

(a)

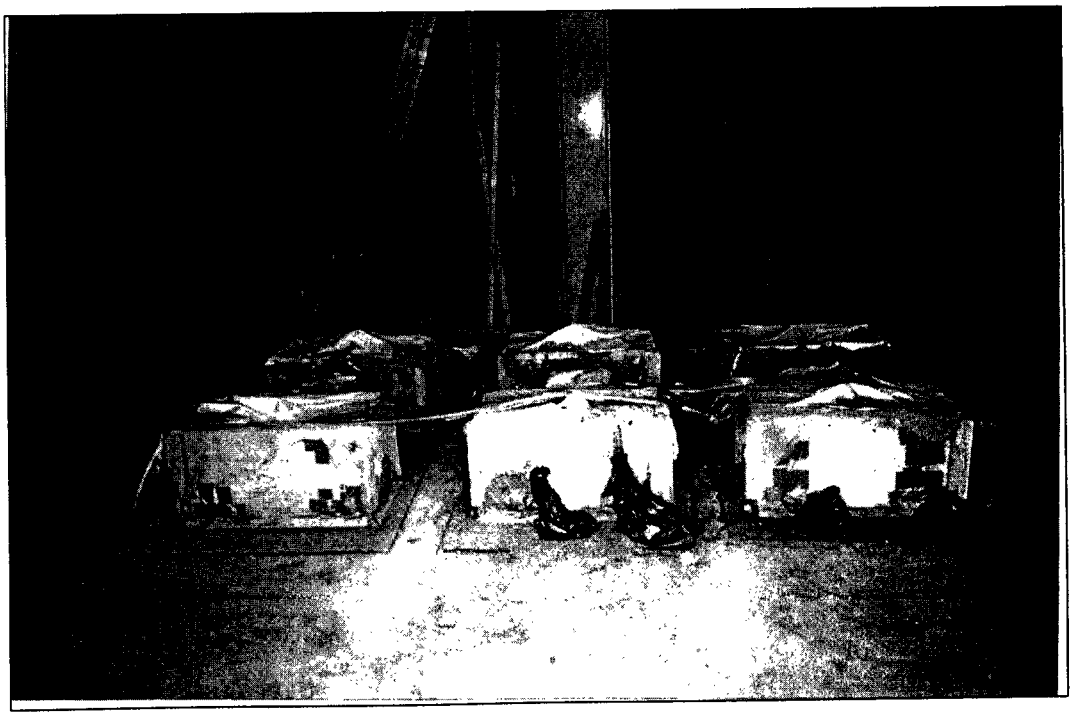

(b)

Figure 5.8 (a) Concrete after casting; and (b) Curing

NOTE TO USERS

Page(s) not included in the original manuscript and are unavailable from the author or university. The manuscript was scanned as received.

179-181

This reproduction is the best copy available.

UMI®

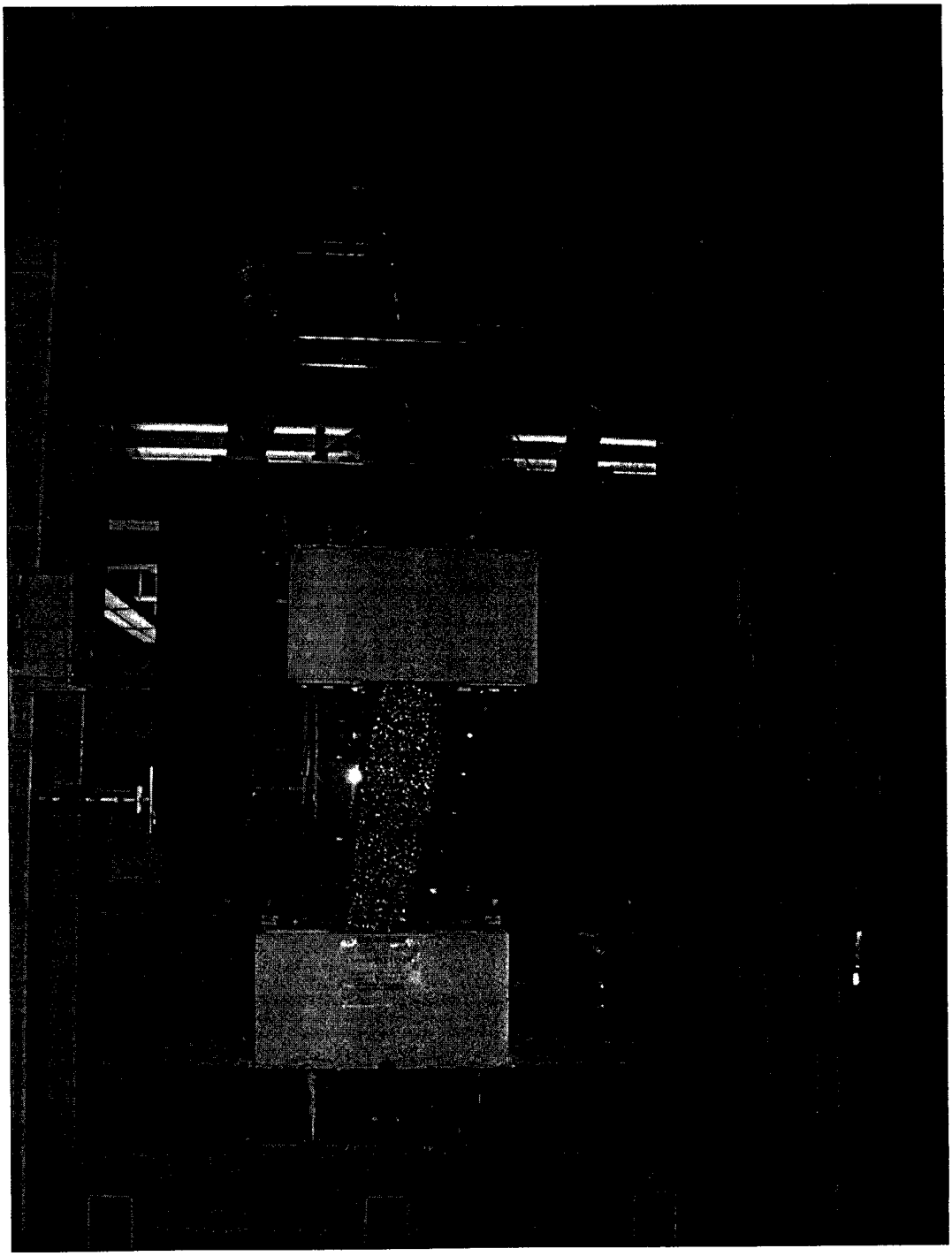

Figure 5.10 Test setup

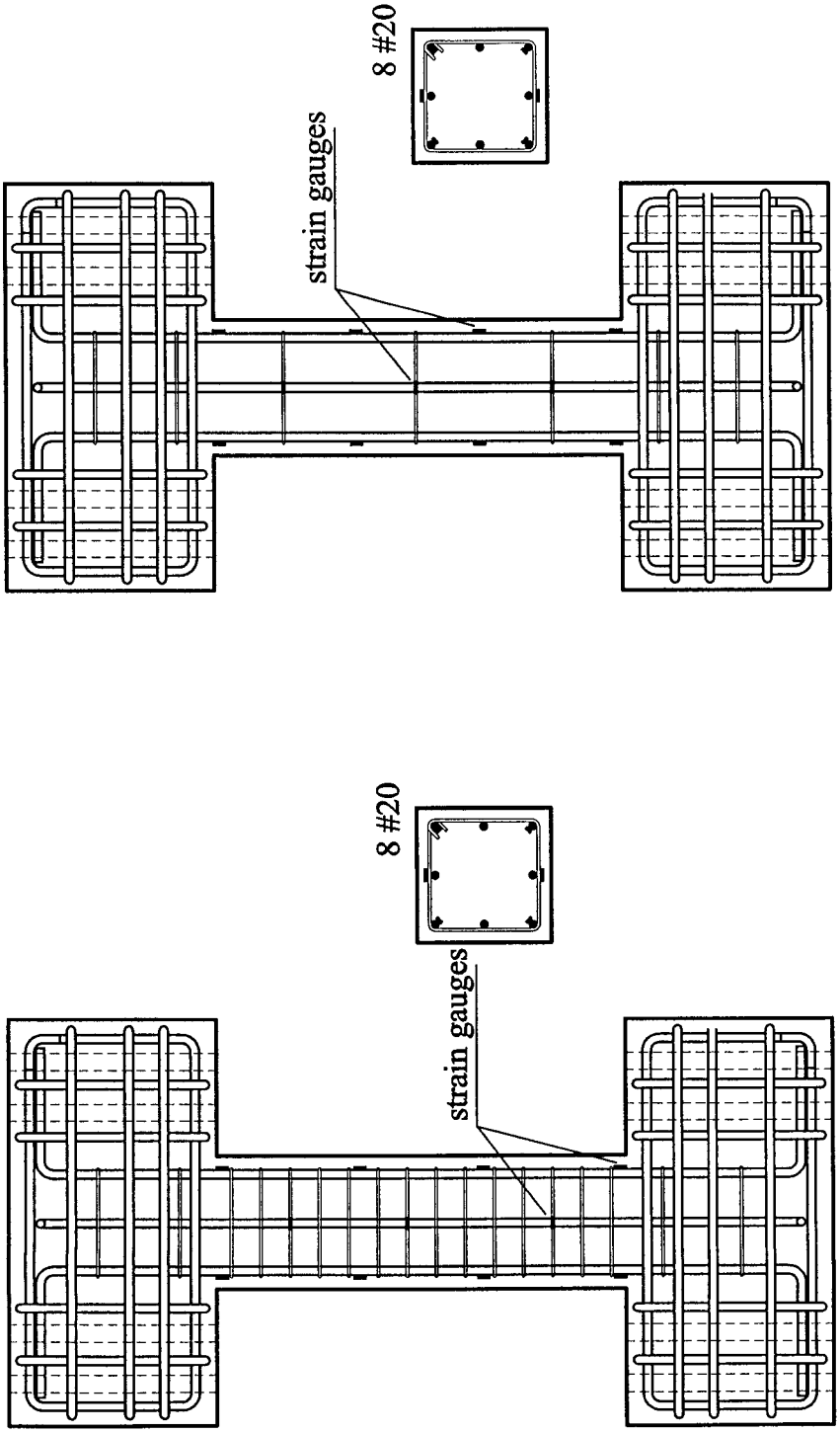

Figure 5.13 Strain gauge locations

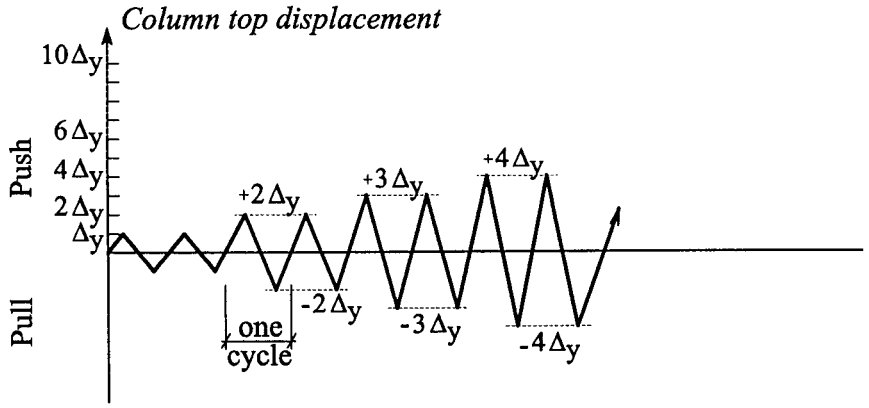

Figure 5.14 Lateral deflection route

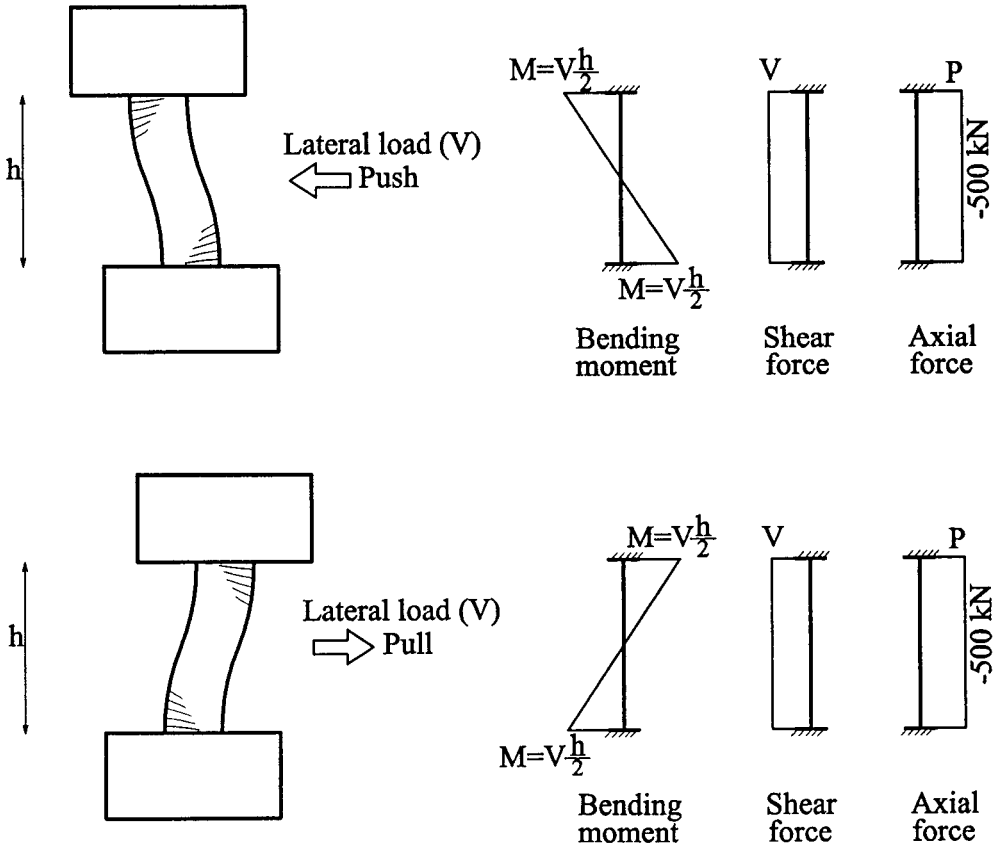

Figure 5.15 Deformed shape and distribution of axial force, shear and bending moment in the push and pull loading

CHAPTER 6

TEST RESULTS

6.1 GENERAL

The behaviour of the test specimens is described in terms of load-deflection curves, strains in reinforcing bars and wrapping fibre, lateral displacement and curvature profile. Comparisons between test results and explanation of the observed behaviour of specimens are presented.

All specimens were subjected to a 500 kN constant axial load (compression) and to lateral cyclic displacement in the east-west direction (push cycle is towards west as shown in figure 6.1). The axial load level was equivalent to 14% of the axial load capacity of the column ($A_g f_c'$) which is in the range of typical design loads. The lateral load-deflection relationship was plotted using deflection of the top block (close to the column top end). The lateral load was adjusted to include the contribution of the horizontal component of inclined axial load:

$$V_{adj} = V + P\sin\theta$$

$$= V + P\frac{\Delta}{H_p} \qquad (6.1)$$

where V_{adj} is the adjusted lateral load;

V and P are the measured lateral and axial loads, respectively;

θ is the inclination of the axial load with respect to vertical axis;

Δ is the measured horizontal displacement at the top of the specimen; and

H_p is the vertical distance between the hinges of the axial load cell setup.

The horizontal component of the axial load becomes significant at high drift ratios. Figure 6.1 shows the adjusted lateral load configuration.

For specimen SC1 the crack pattern during the test is discussed, while for specimens SC2 and SC3 the CFRP wrap was removed after the completion of the test in order to examine the cracked condition of the column.

For specimen SC2, the last repeated cycle was at displacement level $6\Delta_y$, after which a half cycle in push mode reaching $9.5\Delta_y$ (11.5% drift ratio) was conducted. Although it was believed that the specimen could still carry significant load, the test was terminated due to the high drift reached and because of the limitation of the horizontal jack stroke.

6.2 SPECIMEN SC1

The specimen was initially subjected to an increasing lateral load in push mode applied in 10 kN increments to seek the crack load. The first crack occurred at load of 70 kN at the top west side of the column. A complete cycle was conducted at the same level of load. There was no sign of change in stiffness in the push and pull loading directions. The next deflection limit was selected to develop a lateral resistance approximately half of the calculated yield resistance. For this specimen, the lateral force causing the main bars to yield was calculated to be 350 kN. The developed 3D model was used to predict the lateral deformation response for specimen SC1. Figure 6.2 shows the experimental load-deflection relationship for the specimen. Section 6.6 contains comparison between

the analytically predicted and experimental load-deflection relationship for specimen SC1. Two half-yield cycles were conducted at load level ± 170 kN. At that load level, flexure cracks developed at the top and bottom of column at the connection with the end blocks. Inclined shear cracks also developed in the push and pull modes. On the east and west sides of the column, the cracks were horizontal and were closely spaced towards the top and bottom ends of the column.

The yield of the reinforcement occurred at a lateral displacement of 11 mm and a lateral load equal to 344 kN. A vertical crack at the centerline of the east side of the column was observed. This bond crack can be attributed to the decreased cover at the east side compared to the west side, due to a 12 mm (½") shift in the steel cage towards the east during pouring of the concrete. The strain in the longitudinal bars at yield reached 0.0027.

At a displacement level ± $2\Delta_y$, the lateral load capacity of the specimen increased to ± 380 kN. The concrete cover started to crush at the corners of the top and bottom ends of the column, and spalled at the top east side. The second cycle at the same displacement ductility level of 2 showed a drop in the lateral load capacity due to the opening of diagonal shear cracks.

An excessive reduction in the lateral load resistance occurred at $3\Delta_y$, and the shape of the hysteretic loops became increasingly pinched near the origin and the strength and stiffness of the specimen deteriorated rapidly.

Figure 6.3 shows the crack patterns at levels $1\Delta_y$, $2\Delta_y$, $3\Delta_y$ and at failure. Several 45° cracks formed at $1\Delta_y$. The number of cracks increased and cracks from the push and

pull modes crossed forming a diamond shaped crack pattern at the middle of the column and zigzag shapes near the edges. Spalling of the concrete as well as the formation of wide diagonal shear crack at the mid-height of the column decreased the column strength and were the causes of failure.

Figures 6.4 and 6.5 show the strains in the ties at $^1/_6$ and $^1/_2$ the column height, respectively. From the figures, it is noticed that the strains were close in magnitude with a maximum in the range of half the yield strain. The strains in the ties were high which indicates that the shear cracks formed at increasing displacement levels were sufficient to produce a shear failure. The shear cracks were distributed uniformly in the specimen with no one large crack of width bigger than 0.5 mm which precludes local yielding of the ties away from the strain gauge locations. The concrete shear failure significantly decreased the column strength.

Figures 6.6 and 6.7 show the lateral displacement and curvature distribution along the column height throughout the loading history at different displacement ductilities μ. From both figures, a double curvature behaviour can be observed. In the late stages of loading, there were some signs of initiation of rotations at the column ends. However, there was no evidence of formation of complete flexural plastic hinge at the column ends.

6.3 SPECIMEN SC2

Specimen SC2 had the same concrete dimensions and reinforcement details as specimen SC1 (14 #10 ties with ρ_v=2.42%), but wrapped with 3 layers of carbon fibre sheets. Four side-plates with through tying bars were used to clamp the CFRP to

eliminate debonding between the fibre wraps and the concrete of the column. Specimen SC2 was representative of a rehabilitated column that was initially designed according to recent codes. Figure 6.8 shows the adjusted force-deflection relationship under cyclic loading. The lateral force is adjusted using equation 6.1 to account for the horizontal component of the inclined axial load. Two cycles at load ± 170 kN were conducted to represent half the expected yield capacity of the column. The following cycle was to reach the yield strain of the main longitudinal bars. The yield displacement Δ_y was 11 mm, and the corresponding lateral load was 363 kN. The yield strain of the main reinforcement was measured at 0.0027.

In subsequent cycles, the specimen showed high load carrying capacity that was maintained without significant deterioration up to $6\Delta_y$. There was a decrease in the loading stiffness that was proportional to the increase in the displacement ductility level induced. The second cycle conducted at the same displacement level did not show significant strength deterioration, which indicates that new cracks were not forming and old cracks were not widening. The areas enclosed by the hysteretic loop of each cycle showed high energy dissipation. A final half cycle with $9.5\Delta_y$ and drift ratio 11.5% was conducted. The load carrying capacity decreased by only 12% of the ultimate capacity. The test was halted because the drift was excessive and the loading actuator was out of stroke.

Figure 6.9 shows the test column at maximum displacement and after removing the fibre wrap from the top part of the column. The concrete column under the fibre wrap had several shear and flexure cracks, yet the crack widths were small (from visual

inspection) and the concrete was not severely deteriorated, due to the confining effect of the CFRP. The high stiffness of the CFRP (compared to that of concrete) provided substantial lateral confinement of concrete that was generated by the high axial compressive strain and crack formation in concrete at high ductility levels.

Figures 6.10 and 6.11 show the strains in the steel ties at $^1/_6$ and $^1/_2$ the column height, respectively. From the figures it can be seen that the strains were close in magnitude, and were in the range of half the yield strain.

Figures 6.12 to 6.14 show the lateral strains of the CFRP wraps at the top end, mid-height and the bottom end of the column, respectively. The plots on the left hand side of figures 6.12 to 6.14 show the strains near the corner of the column, while the plots on the right hand side show the strains near the centre of the column side. The strain in the ties at half the height (figure 6.11) and the strain in the CFRP at half height (figure 6.13) are approximately equal. From the figures it can be seen that the CFRP strain was higher at the column ends than at the column mid-height due to the higher moment at the column ends. The strains along the corner of the column were higher than those at the centerline of the column sides. This is due to the increased confining effect of the CFRP fibres at the column corners as compared to the middle of the column side. The fibre strains at the corner of the column (at the top and bottom ends) were approximately twice the strains at the centerline of the column side. At a drift ratio of 11.5% ($9.5\Delta_y$), the fibre strains reached approximately 0.004 at the top and bottom ends of the column. A bulge underneath the wrapping fibre was observed in the compressed side of the column near the top and bottom ends at high displacement levels. However, there was no sign of

tensile rupture in the fibre sheet itself. This bulge was due to the sliding and dislocation of the highly strained concrete in compression along the cracks that formed at the ends of the column.

Figures 6.15 and 6.16 show the strain in the tie rods (used as anchors for the CFRP wraps) at mid-height and bottom end of the column, respectively. From the figures it can be observed that the strains at the mid-height of the column were small and those at the column end were quite significant at approximately 0.001 at drift ratio of 11.5%. The high strains in the tie rods near the column's ends indicate that the rods were effective in increasing the confinement due to the CFRP wraps, which led to a higher lateral capacity. The tension force in the rods resisted bulging of the concrete at the middle of the sides.

Figures 6.17 and 6.18 show the lateral displacement and curvature distribution along the column height throughout the loading history up to displacement ductility factor μ=6. From figure 6.17 and from observation during the test, the column behaved as a stiff element with two plastic hinges at the top and the bottom. The plastic hinge length was about 75 mm (3 inches) and it can be identified visually by means of the alternating bulging of the concrete underneath the CFRP wrap at the compression sides during push and pull cycles. A lumped curvature localized at the top and the bottom of the column shown in figure 6.18 is another indication of the elastic element with two end plastic hinge behaviour of the specimen.

6.4 SPECIMEN SC3

Specimen SC3 had the same number of CFRP layers as specimen SC2, but was wrapped by reduced number of steel ties (3#10 ties with ρ_v=0.5%). A different technique was used to eliminate delamination and improve the concrete confinement. Five three-inch deep carbon fibre anchors were used at each side of the column. The fibre anchors were installed after the first layer of CFRP was wrapped. One end of the fibre anchor was anchored into the column's confined core in a 80 mm deep hole, while the fibres at the other end were spread in a fan-blades shape between the first and second layers of CFRP. The CFRP anchors are shown in figure 6.19. Specimen SC3 was representative of a rehabilitated column that was designed according to the pre-1970's codes. Figure 6.20 shows the adjusted force-deflection relationship under lateral cyclic loading and a constant 500 kN axial load. Two cycles at load ± 170 kN were conducted to represent half the expected yield capacity of the column. The following cycle was to reach the yield strain of the main longitudinal bars. The yield displacement Δ_y was 13 mm, and the corresponding lateral load was 385 kN. The yield strain of the main longitudinal reinforcement was 0.003. The higher yield displacement and load for specimen SC3 as compared to specimens SC1 and SC2 was attributed to the higher yield strain of the longitudinal reinforcement bars and to the higher shear displacement component of the column due to its reduced transverse reinforcement.

In the following cycles, the specimen showed an increasing load carrying capacity until $3\Delta_y$ was reached. The second loading cycle at each displacement level up to $3\Delta_y$ did not show significant loss in the specimen strength. Strength deterioration of the

specimen started at displacement level of $4\Delta_y$. Formation of new cracks and widening of the old cracks was evident from the loss in strength at the same ductility level. The increasing pinching of the hysteretic loops for loading cycles of $4\Delta_y$ suggest that shear cracks were developing in the concrete under the CFRP wrapping. The rate of energy dissipation associated with each cycle decreased after $4\Delta_y$ was reached. A final half cycle with $8\Delta_y$ and drift ratio of 11.5% was conducted. In that cycle, rupture of one inch width of the fibres occurred at the bottom corner of the column. The specimen was still capable of resisting approximately 70% of its ultimate lateral load.

Figures 6.21 and 6.22 show the specimen at maximum lateral displacement and after removing the fibre wraps from the bottom part of the column. The fibre anchors used to improve the CFRP confinement of concrete were successful and there was no sign of debonding or delamination observed (as can be seen in figure 6.22). The concrete under the fibre wraps near the plastic hinge location at the two ends of the column was severely crushed. The absence of ties at the plastic hinge locations coupled with crushing of concrete cover led to buckling of the longitudinal steel bars in compression. With the steel bars buckling, the interior concrete of the column failed by crushing. At the plastic hinge locations, limited confinement of the column was provided by the CFRP wraps only. For this reason the lateral strain in the CFRP was high and reached its ultimate. The lateral profile of the column after displacement ductility level 5 (i.e. $5\Delta_y$) consisted of three parts separated by wide cracks. Two 150 mm (6") parts at each end with a middle 600 mm (24") part of the column are shown in figure 6.21b. The wide cracks separating the three parts were approximately at the locations of the top and bottom ties. As the test

progressed, it was apparent that most of the rotation of the column was occurring at four discrete locations: the top and bottom column ends and the locations of two wide cracks.

Figures 6.23 and 6.24 show the measured strain in the steel ties at $^1/_6$ and $^1/_2$ the column height, respectively. The figures show that the strains at $^1/_6$ (and $^5/_6$) the column heights are slightly higher than those at the mid-height. This is due to the combined flexure and shear at $^1/_6$ and $^5/_6$ the column height as compared to shear only at column mid-height. An increased normal stress due to flexure generates tensile forces in the ties for confinement.

Although the contribution to the lateral shear strength from the steel mechanism provided by the ties was low (due to the low transverse reinforcement content ρ_v=0.5%), the three layers of CFRP wraps provided sufficient additional shear resisting mechanism to prevent the column from sustaining a brittle shear failure. This emphasizes the dual action of the CFRP wrapping in increasing the column lateral load carrying capacity due to its confining effect in addition to increasing the shear strength due to the additional FRP resisting mechanism.

Figures 6.25 to 6.27 show the lateral strains in the CFRP wraps at the top end, mid-height and the bottom end of the column, respectively. The left hand plots in figures 6.25 to 6.27 show the strains near the edge of the column, while the right hand side plots show the strains near the centre of the column side. The figures show that the CFRP strains were higher at the column ends as compared to the column mid-height due to the higher flexural stresses. The strains along the corner of the column were higher than those at the centre of the column side. This is due to the increased confining effect of the

wrapping CFRP fibres at the column corners as compared to the middle of the column sides. The fibre strains at the corner of the column (at the top and bottom ends) were almost twice those at the centre of the column side. At a drift ratio of 11.5% ($8\Delta_y$), the CFRP strains reached approximately 0.007 at the top and bottom ends of the column. This strain was sufficient to cause rupture of the fibres at the bottom end of the column.

Figures 6.28 and 6.29 show the lateral displacement and curvature distribution along the column height throughout the loading history until displacement ductility factor μ=5. From figure 6.28 and from observation during the test, the specimen behaved as a stiff element with two 75 mm (3") plastic hinges at the top and the bottom ends of the column until $4\Delta_y$. At lateral displacement of $5\Delta_y$, the length of the plastic hinge suddenly increased to 150 mm (6"). This led to an increase in the curvature of the specimen as shown in figure 6.29. The middle 600 mm (24") section of the column between the two plastic hinges behaved elastically.

6.5 COMPARISON OF EXPERIMENTAL RESULTS

6.5.1 Load-deflection relationship

The lateral load-deflection relationships of the three specimens are compared in figure 6.30. The lateral load capacities of the three specimens for the first and second loading cycles throughout the loading history at every ductility level are compared in figure 6.31. From the two figures, the following can be concluded:

1- Using a large number of ties at small spacing as per current code (CSA A23.3-94, see Appendix B) for a short RC column did not eliminate the shear failure and did not

improve the limited displacement ductility capacity. A short RC column with ρ_v=2.42% failed in shear at a ductility factor of 3.0 (drift ratio 3.5%).

2- Rehabilitating a short RC column that contains high percentage of transverse reinforcement using CFRP wraps significantly improved the displacement ductility. A short RC column with ρ_v=2.42%, rehabilitated using three wraps of CFRP reached a displacement ductility factor of 9.5 (drift ratio of 11.5%) without failure and still maintained 88% of the column's maximum lateral load carrying capacity.

3- Rehabilitating a short RC column that contains low percentage of transverse reinforcement using CFRP wraps increased the lateral load capacity and displacement ductility. A short RC column with ρ_v=0.5% and rehabilitated using three wraps of CFRP failed at ductility factor of 8.0 (drift ratio of 11.5%) having 70% of the column's maximum lateral load capacity.

4- Decreasing the lateral reinforcement content of CFRP-rehabilitated short RC columns from ρ_v=2.42% to ρ_v=0.5% decreased the post-peak lateral load capacity and the lateral stiffness and increased the pinching behaviour of the column.

5- CFRP wrapping provided both confinement to the concrete and additional lateral load resistance mechanism. Thus a proposed total shear design equation is:

$$V_n = V_c + V_s + V_p + V_{FRP} \tag{6.2}$$

where V_n = nominal shear strength;
V_c = shear strength from concrete mechanism;
V_s = shear strength from steel mechanism; and
V_p = shear strength from axial force mechanism; and
V_{FRP} = shear strength from the CFRP mechanism.

Appendix D includes a detailed explanation of the contribution of different mechanisms to the column's total shear strength.

6- Both anchoring techniques used in specimen SC2 (through steel rods) and specimen SC3 (fibre anchors) were effective in reducing bulging at the column sides.

Table 6.1 shows the calculated and measured yield and ultimate lateral loads for the three specimens. The comparison shows good correlation between the tested and the predicted results.

Table 6.2 and figure 6.32 show the peak-to-peak stiffness values for the first and second cycles for the three specimens. From the table and the figure it can be seen that specimen SC1 showed higher loss in stiffness upon load reversals at the same ductility level than specimens SC2 and SC3. It can be also seen that the rate of degradation of stiffness for the first cycles is higher for specimen SC1 than specimens SC2 and SC3. This is due to the low confinement of specimen SC1, which allowed the formation of new cracks and widening of the old ones thus reducing the column stiffness.

6.5.2 Energy dissipation

For each specimen, the energy dissipated in each cycle was obtained by calculating the area enclosed by the corresponding load-displacement hysteretic loop. The cumulative energy dissipated was obtained by summing the energy dissipated in consecutive loops throughout the test. Figure 6.33 shows the cumulative dissipated energy with the displacement ductility factor for the tested specimens. Figure 6.34 shows the drift ratio-energy absorption capacity relationship, where the "energy absorption capacity" at each displacement ductility level is defined as the current dissipated energy divided by the corresponding displacement amplitude (2Δ). The energy absorption

capacity gives a measure for the specimen potential to absorb energy with respect to different drift ratios. From these two figures it can be concluded that the CFRP rehabilitated RC short columns have higher energy dissipation capacity when compared to the control column (even with code specified transverse reinforcement). It can be also concluded that decreasing the lateral reinforcement ratio of CFRP-rehabilitated RC short columns from ρ_v=2.42% to ρ_v=0.5% will have the same energy content up to drift ratio ≈ 5%, after which the higher lateral reinforcement content column will dissipate larger amount of energy.

6.5.3 Curvature

Figure 6.35 shows the curvature distribution along the column height for the three specimens at drift ratios of 3.5% and 7.0% (equivalent to lateral displacement of 33 mm and 66 mm, respectively). From the figure it can be concluded that specimen SC2 has a higher curvature capacity than specimens SC1 and SC3. The curvature capacity of specimen SC2 is almost twice that of specimen SC3 at its ultimate drift ratio (11.5%).

6.5.4 Longitudinal strain

Figure 6.36 shows the main bars strain distribution along the column height at the onset of first bar yielding. The longitudinal strain distribution along the column height follows a typical fixed-fixed double moment pattern.

6.5.5 Lateral strain

Figures 6.37 and 6.38 show the lateral tie and fibre strain distribution along the height at the onset of yield of the longitudinal steel bars, at maximum lateral load and at the ultimate lateral displacement for the three specimens. The strain in the ties in all the

tests remained well below the yield strain. Comparing the strains in the ties of specimen SC1 to specimen SC2, indicates that the CFRP-rehabilitated RC short columns have similar tie strain level, which is about half the yield strain. Figure 6.38 shows that the anchored CFRP wraps did not develop significant strains, and therefore did not provide high confining pressures and lateral resistance, until large column displacements were applied. On the other hand, figure 6.37 shows a reduction in the tie strains, which is proportional to the reduction in the lateral column resistance from the point of maximum lateral load to the point of ultimate lateral displacement.

Comparing the CFRP strains in specimens SC2 and SC3, it can be concluded that the strain in the CFRP increases with the increase of the applied displacements at much higher rate in the column with less transverse reinforcement (specimen SC3). This indicates that at high displacement ductility levels, the CFRP wraps tend to complement the column's shear resistance, which is primarily provided by the steel mechanism.

6.6 ANALYTICAL PREDICTION OF TESTED SPECIMENS' RESPONSE

The developed 3D model is used to predict the lateral response of the three tested specimens. Tables 6.3a and 6.3b show the data for the flexure and shear subhinges for the three specimens. Figures 6.39 to 6.41show the comparison between the analytical and experimental force-displacement relationship. The comparison shows that the model was capable of predicting response of specimens with good accuracy.

Table 6.1 Calculated and measured lateral loads in kN

Specimen	Calculated												Measured		Behaviour	Failure
	Yield						Ultimate						Yield	Ultimate		
	Flexure	Shear					Flexure	Shear								
		V_c	V_s	V_p	V_{FRP}	V_n		V_c	V_s	V_p	V_{FRP}	V_n				
SC1	350†	92	336	83	--	511	425	25	336	42	--	403††	344	380	Low ductility	Shear failure
SC2	375†	169	336	83	476	1064	450††	28	336	--	476	840	363	428	High ductility	No failure
SC3	365†	43	71	83	476	673	425††	--	--	--	476	476	385	425	Moderate ductility	No failure§

† Governing calculated yield lateral load capacity
†† Governing calculated ultimate lateral load capacity
§ Rupture of fibres occurred at column bottom end at drift ratio of 11.5%

Table 6.2 Experimentally measured peak-to-peak stiffnesses (N/mm) at different displacement ductilities for the three specimens

		$1\Delta_y$	$2\Delta_y$	$3\Delta_y$	$4\Delta_y$	$5\Delta_y$	$6\Delta_y$	$8\Delta_y$	$9.5\Delta_y$
Specimen SC1	1st cycle	32000	19000	10500	NA				
	2nd cycle	32000	15000	6000	NA				
Specimen SC2	1st cycle	33000	19500	13000	9500	7500	6000	--	4000
	2nd cycle	32000	18000	12000	9000	7000	5500	--	--
Specimen SC3	1st cycle	30000	16500	11000	8000	5000	--	3000	NA
	2nd cycle	28000	15000	9500	6500	4000	--	--	NA

Table 6.3a Properties of flexure subhinges

Specimen	M_1	M_2	M_3	K_1	K_2	K_3	K_4	α	P_{ult}	T_{ult}	P_{av}
	kN.m	kN.m	kN.m	kN.m	kN.m	kN.m	kN.m		kN	kN	kN
SC1	45	136	176	54000	22780	9520	100	0.06	3560	890	1335
SC2	71	171	206	65000	20000	4580	100	0.06	3560	890	1335
SC3	55	165	199	62000	21325	6850	100	0.06	3560	890	1335

Table 6.3b Properties of shear subhinge

Specimen	V_c		V_s	V_p	V_{FRP}	V_n		V_r	K_v	α_s	α_p
	Max.	Min.				V_i	V_f				
	kN	kN	kN	kN	kN	kN	kN	kN	kN/mm		
SC1	92	25	336	42	--	511	403	100	-25	0.03	0.015
SC2	169	28	336	--	476	1064	840	336	-25	0.03	0.015
SC3	43	--	--	--	476	673	476	--	-25	0.03	0.015

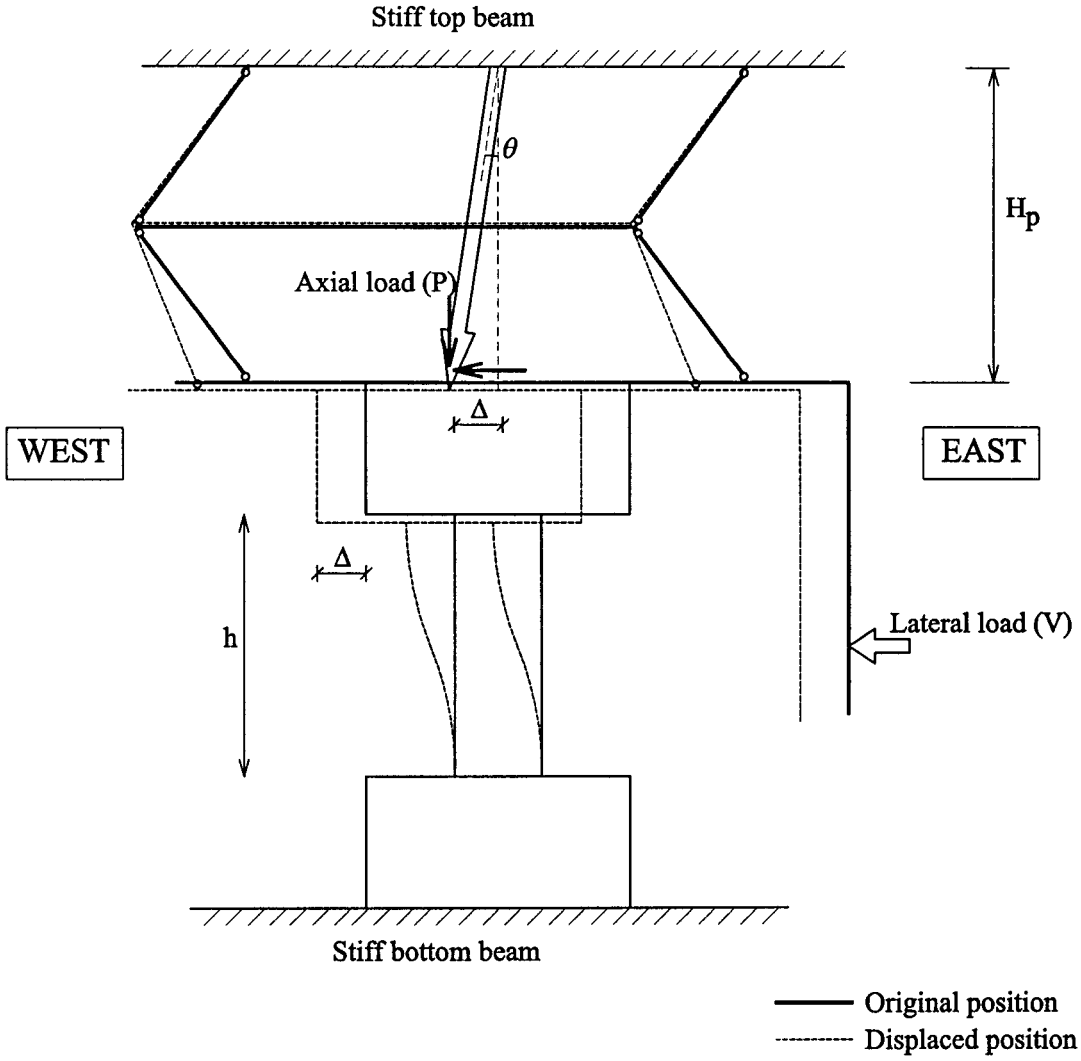

Figure 6.1 Adjusted lateral load

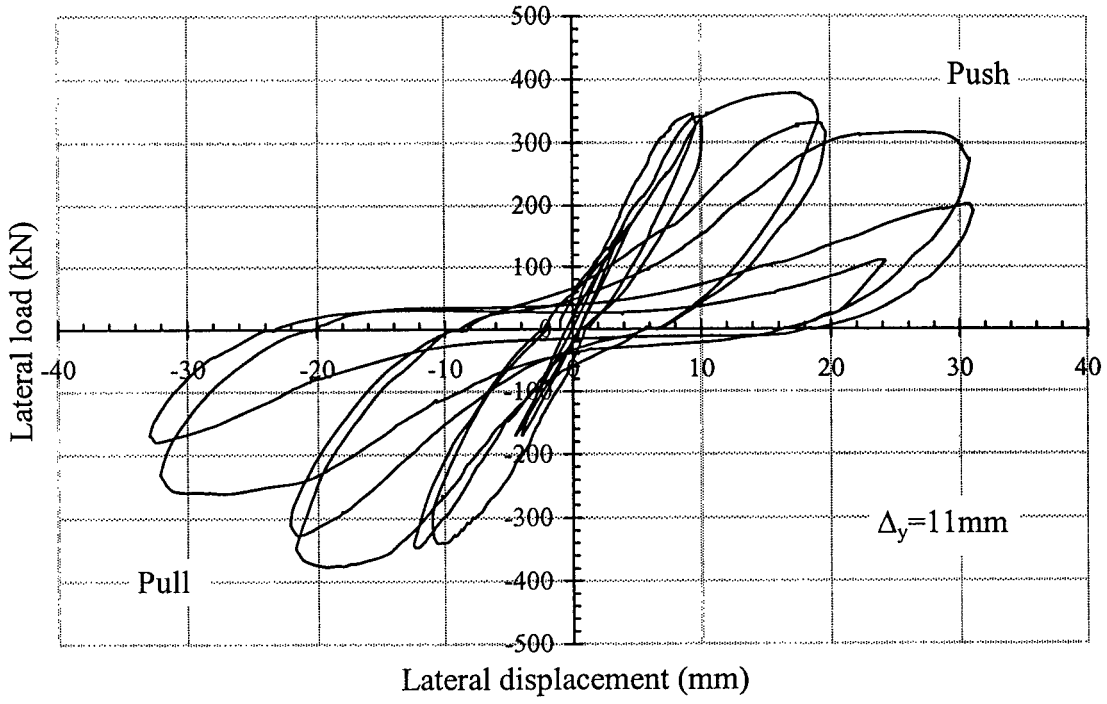

Figure 6.2 Lateral force-displacement relationship for specimen SC1

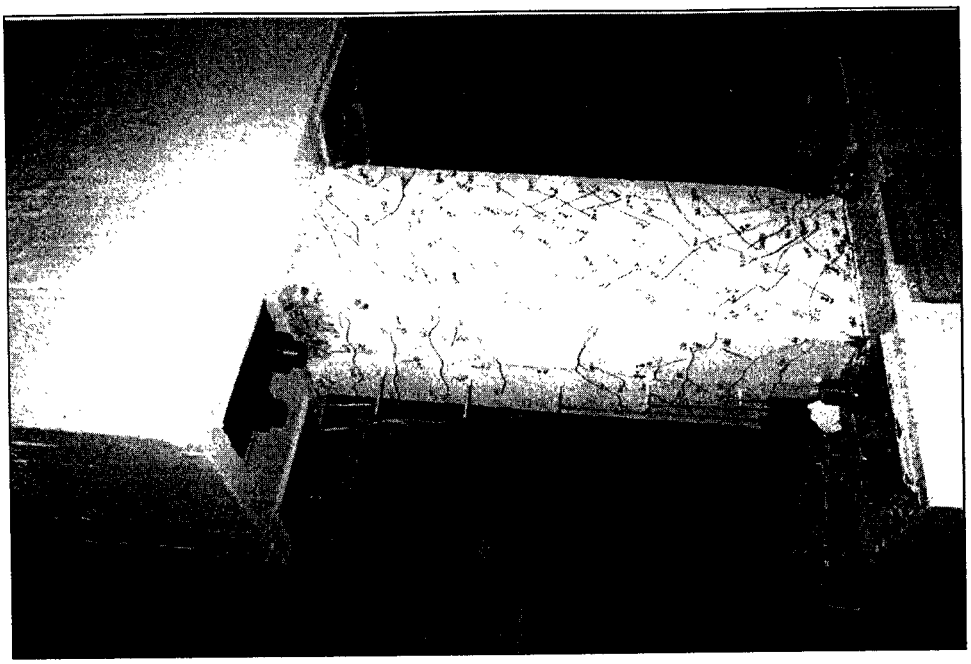

(b) after $2\Delta_y$ (second cycle)

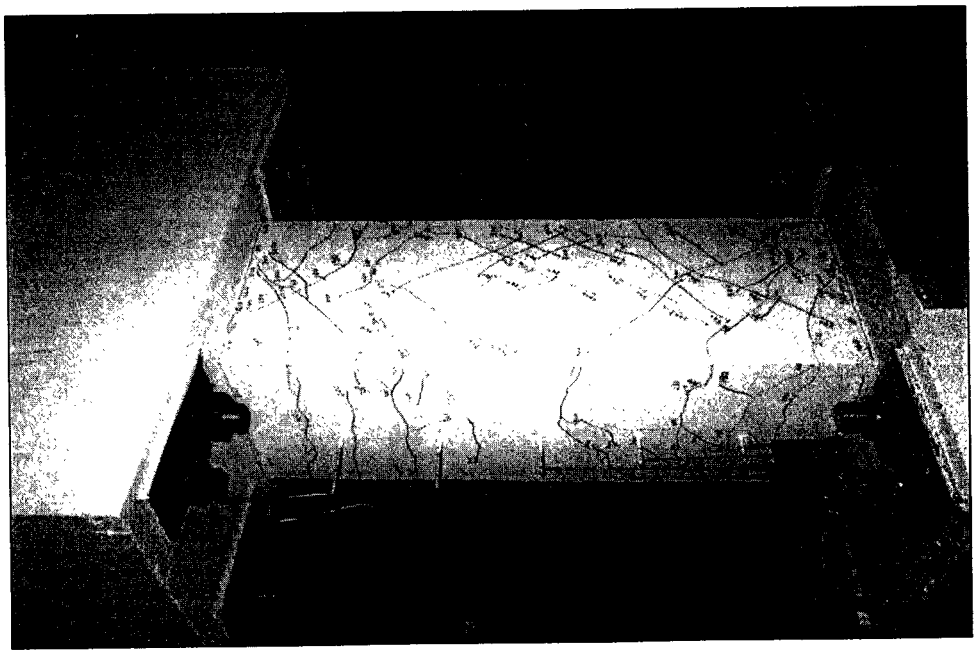

(a) after $1\Delta_y$ (second cycle)

Figure 6.3 Crack pattern for specimen SC1 (Continued)

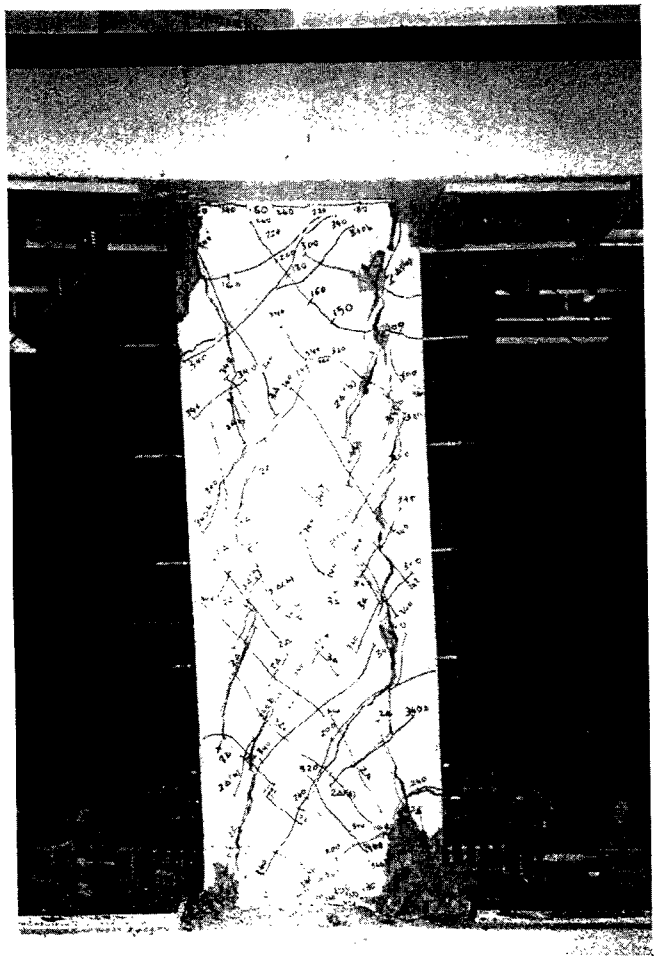

(c) after $3\Delta_y$ (first cycle)

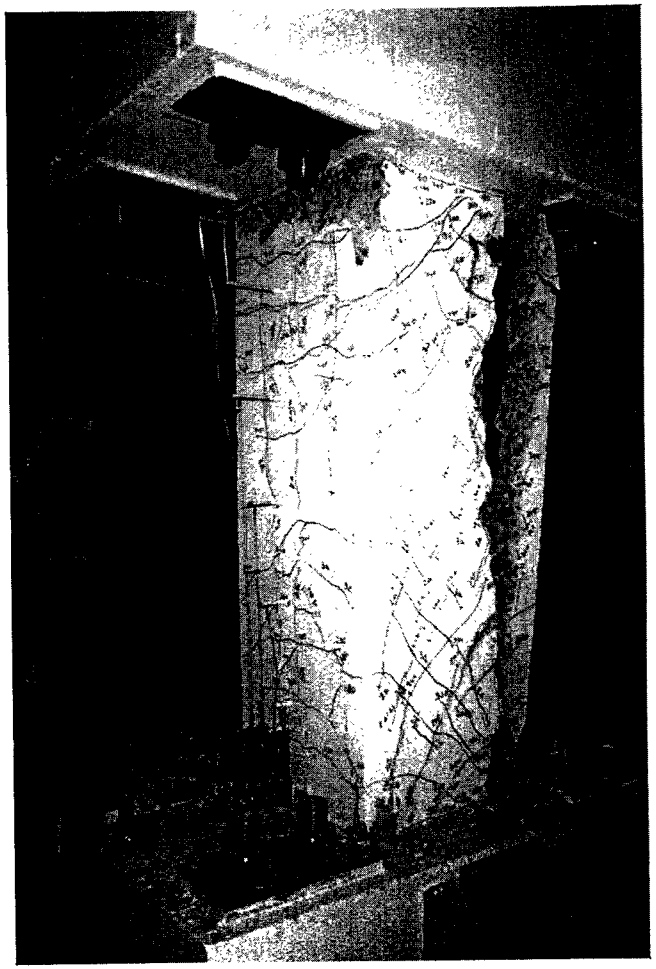

(d) after $3\Delta_y$ (second cycle)

Figure 6.3 Crack pattern for specimen SC1 (Continued)

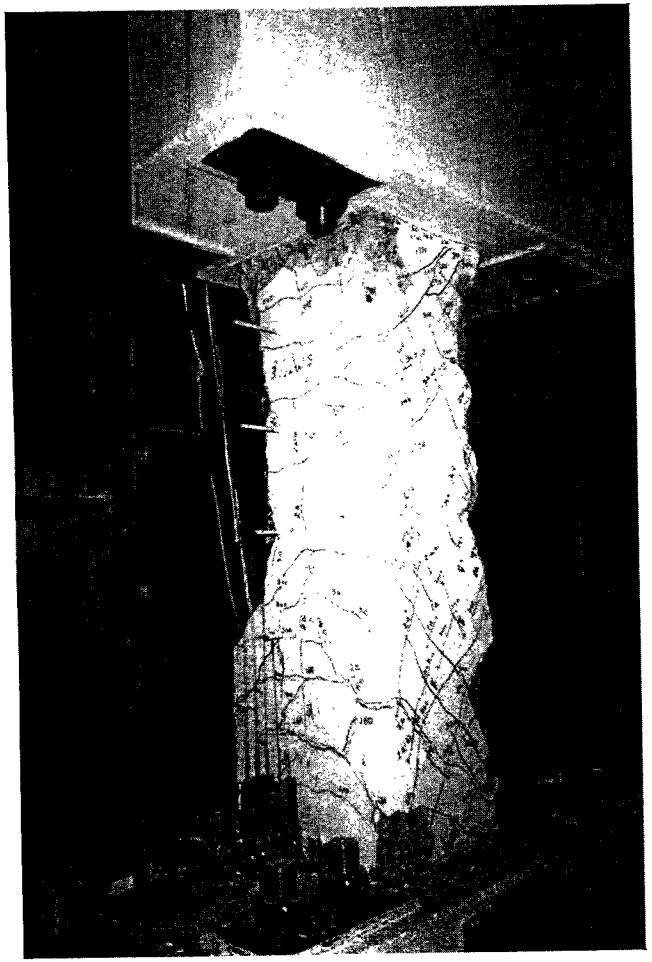

(e) Failure (north-east view)

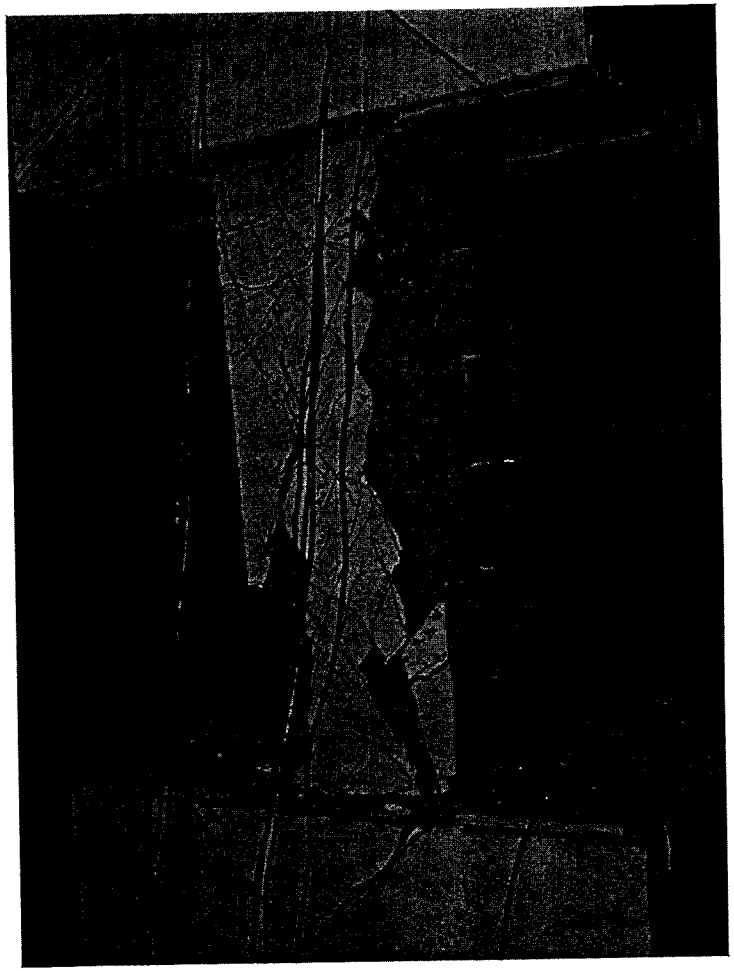

(f) Failure (south-east view)

Figure 6.3 Crack pattern for specimen SC1 (Continued)

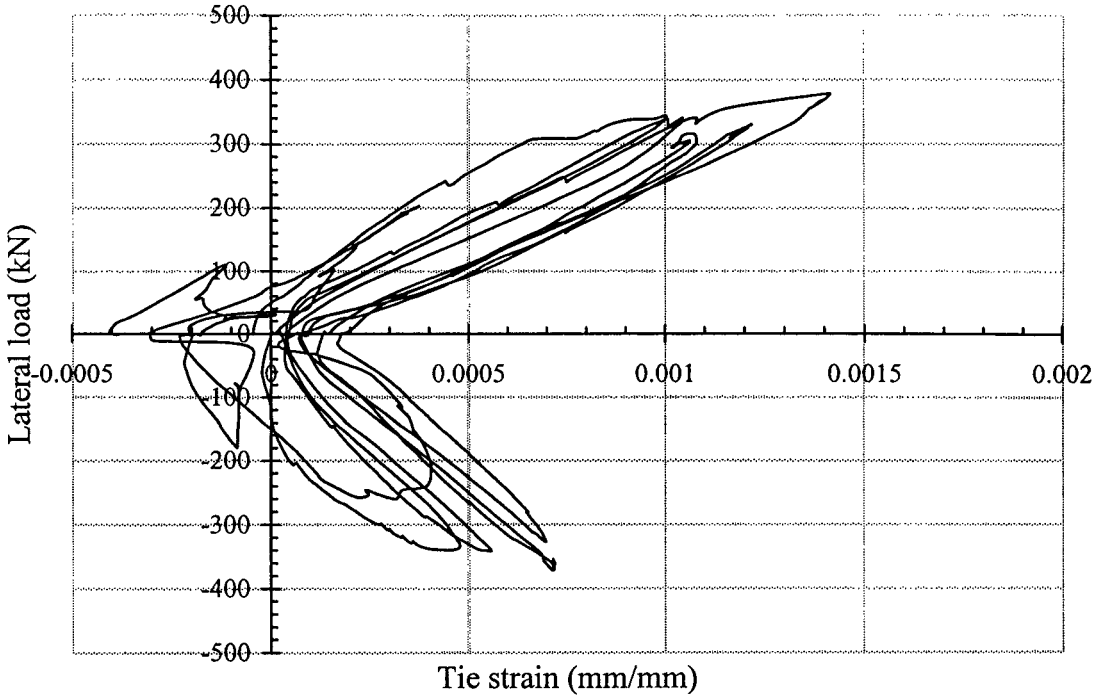

Figure 6.4 Measured strain in tie at one-sixth of the column height

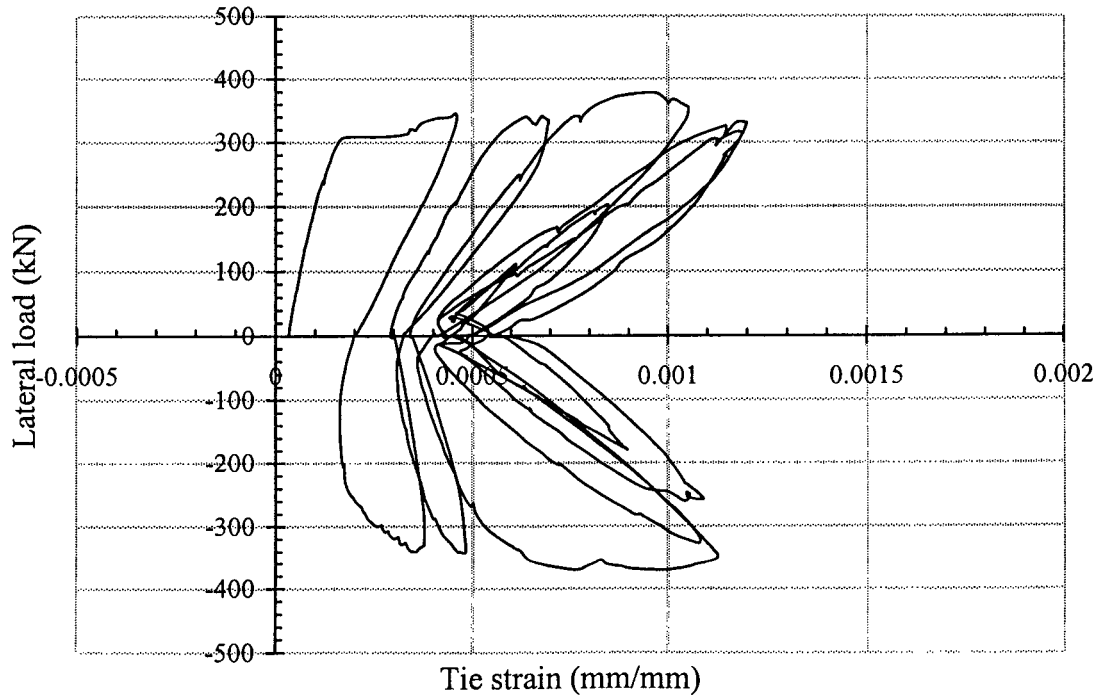

Figure 6.5 Measured strain in tie at mid column height

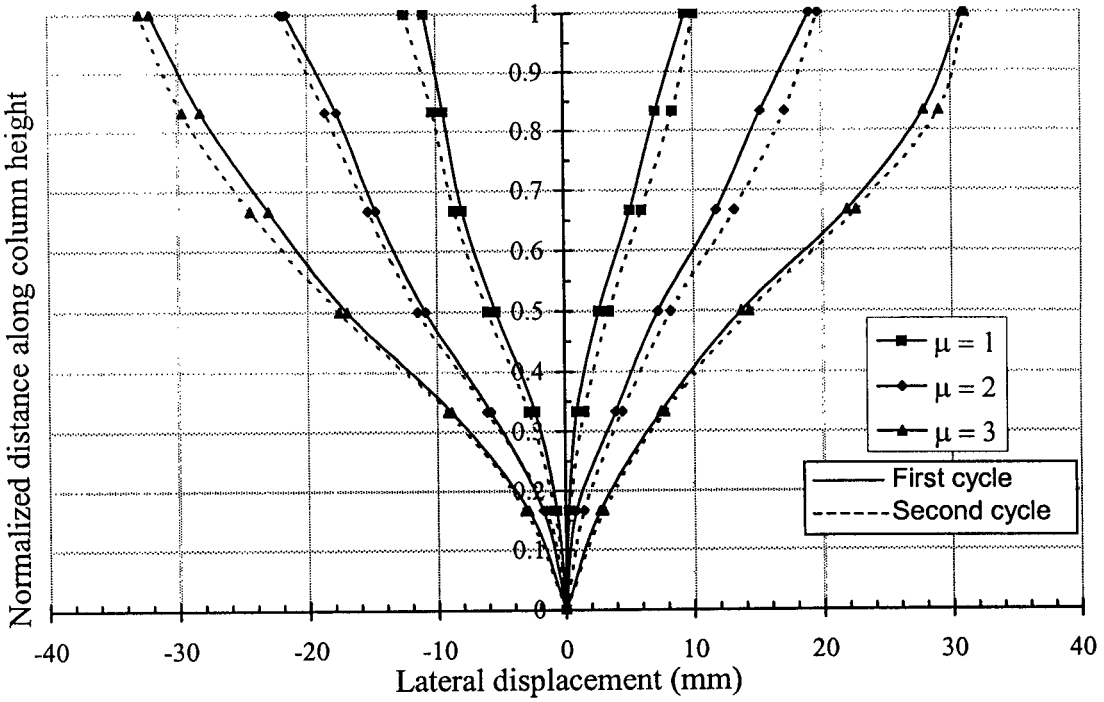

Figure 6.6 Lateral displacement distribution along the column height

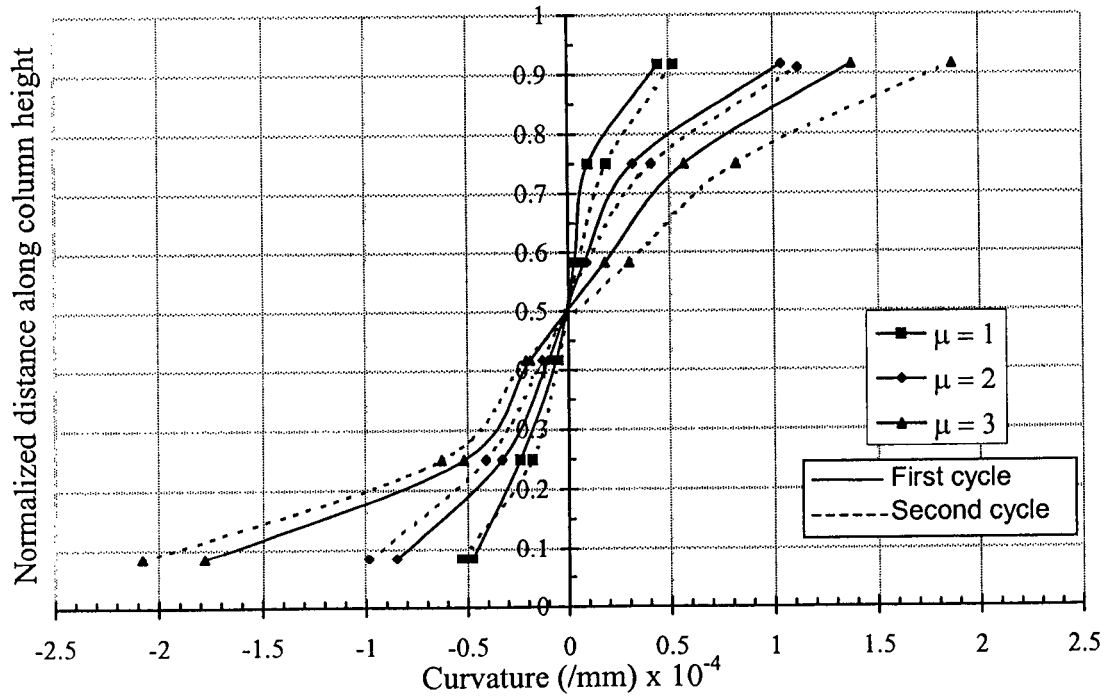

Figure 6.7 Change of curvature along the column height

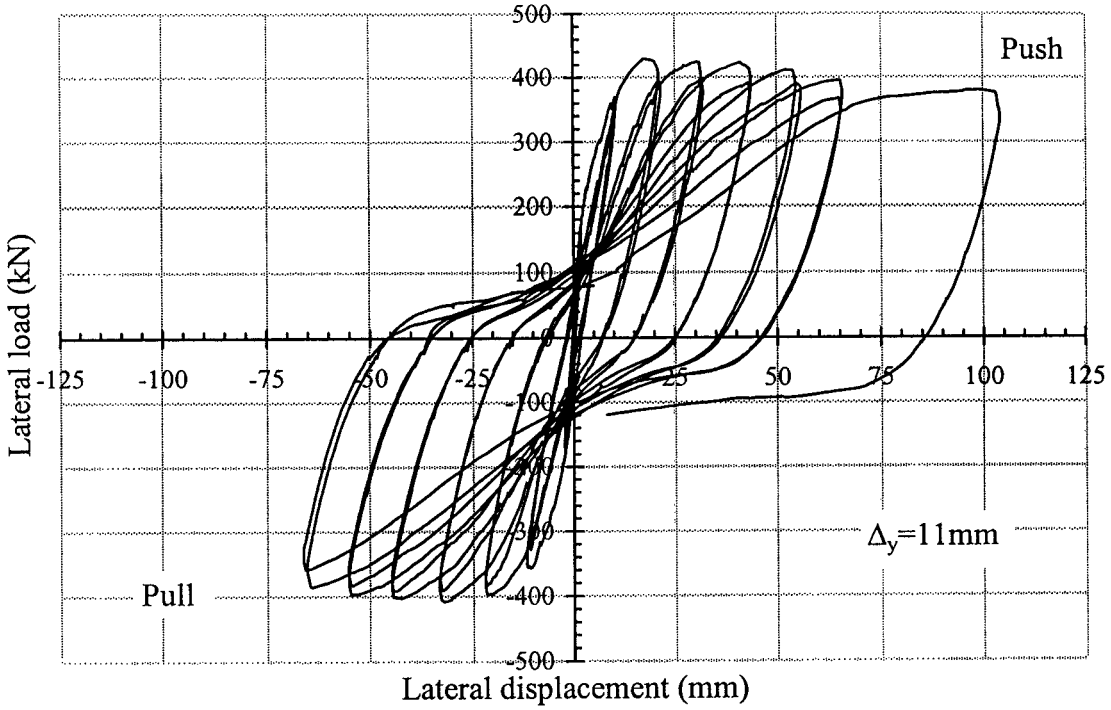

Figure 6.8 Lateral force-displacement relationship for specimen SC2

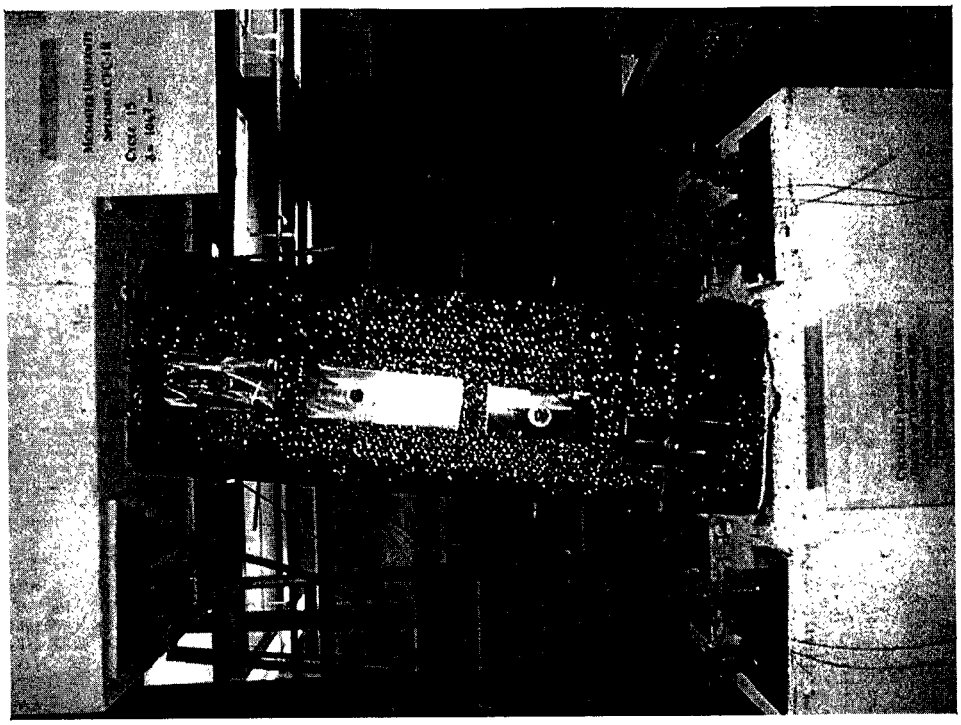

(b)

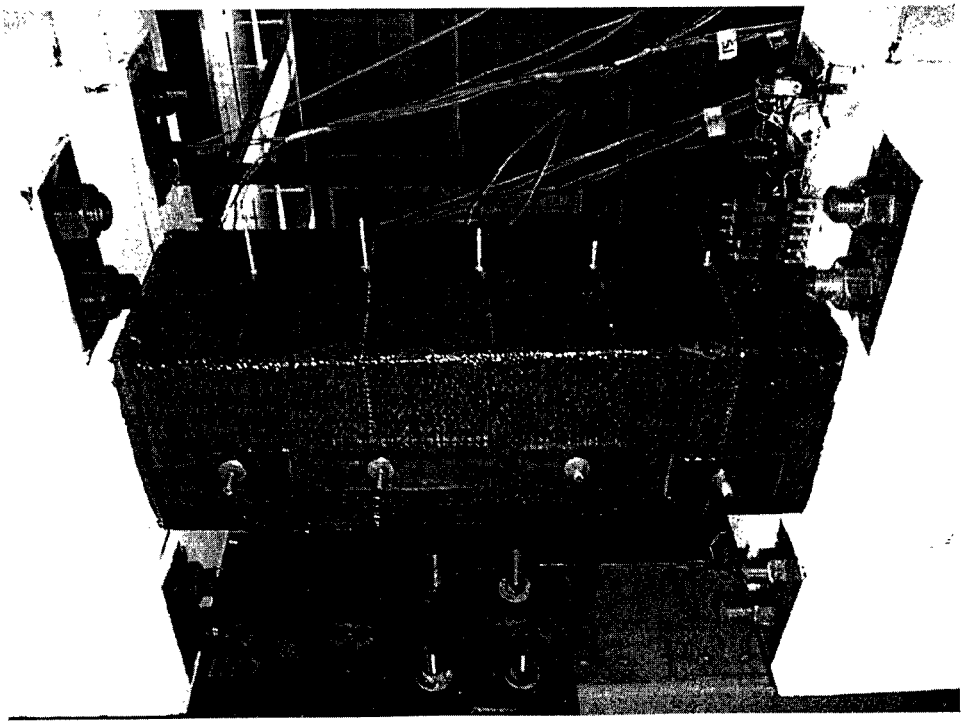

(a)

Figure 6.9 Specimen SC2: (a) Before test; (b) At maximum lateral displacement (Continued)

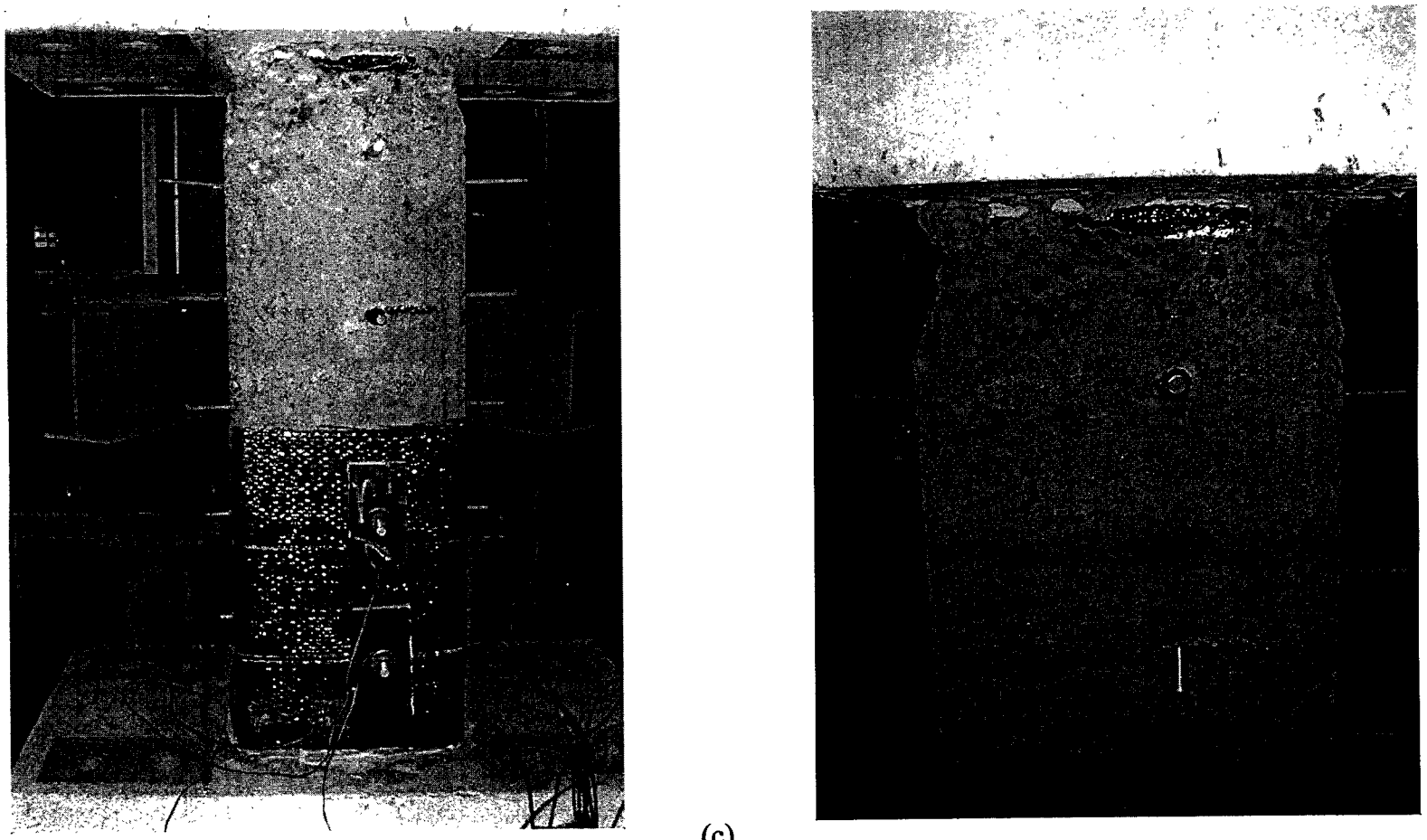

(c)

Figure 6.9 Specimen SC2: (c) After removing the CFRP

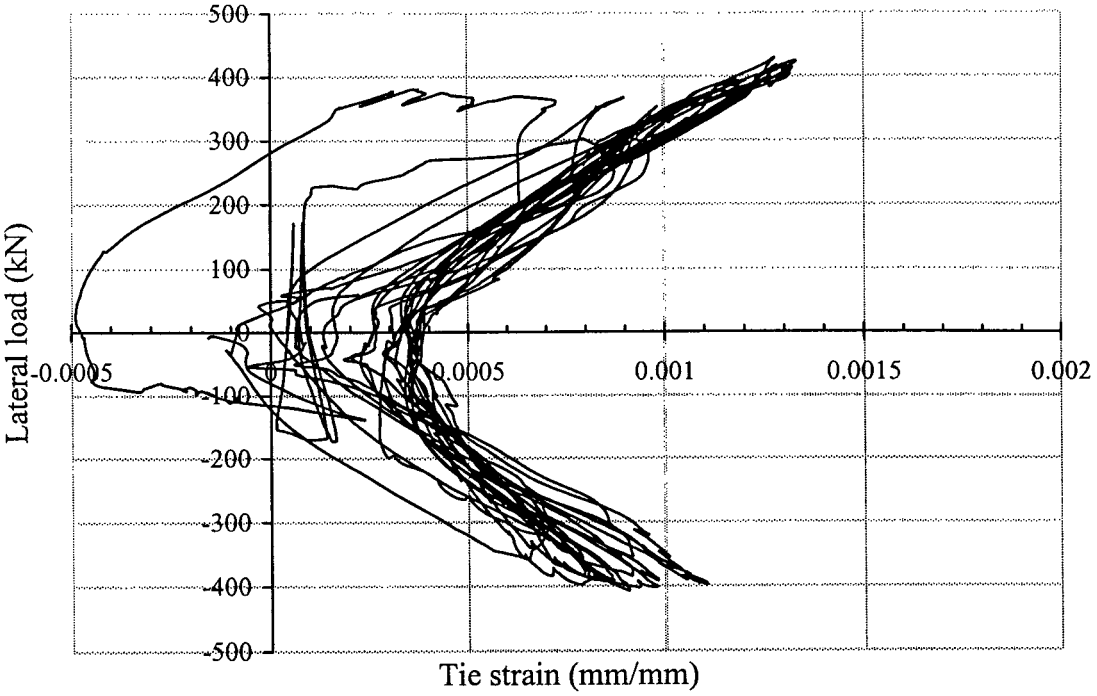

Figure 6.10 Measured strain in tie at one-sixth of the column height

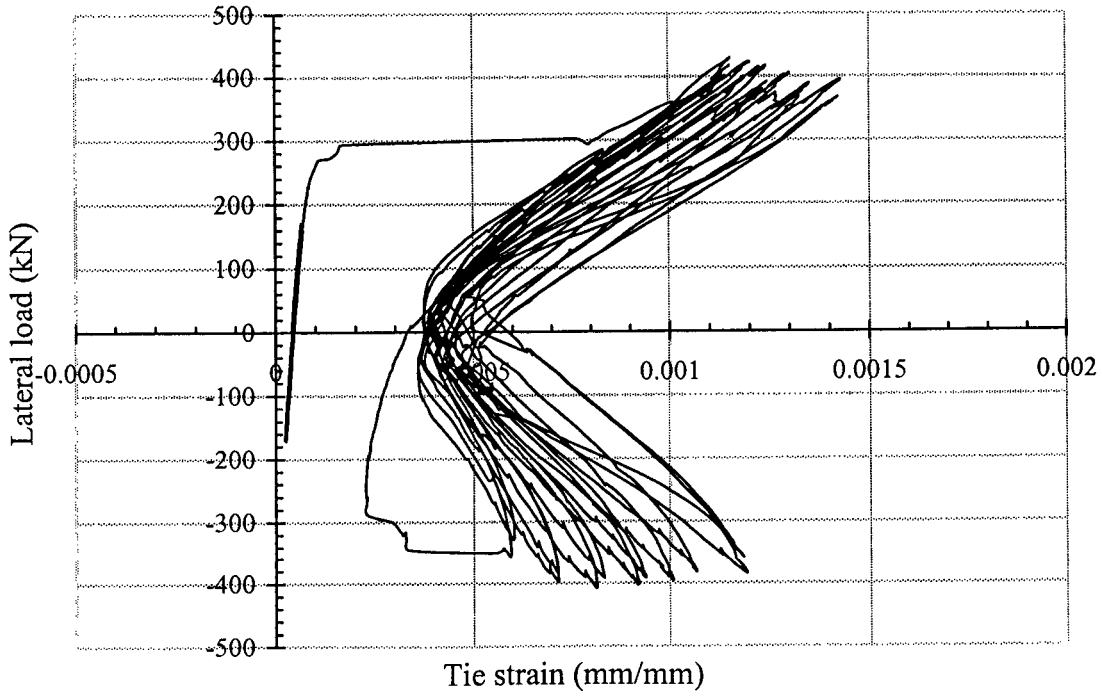

Figure 6.11 Measured strain in tie at mid column height

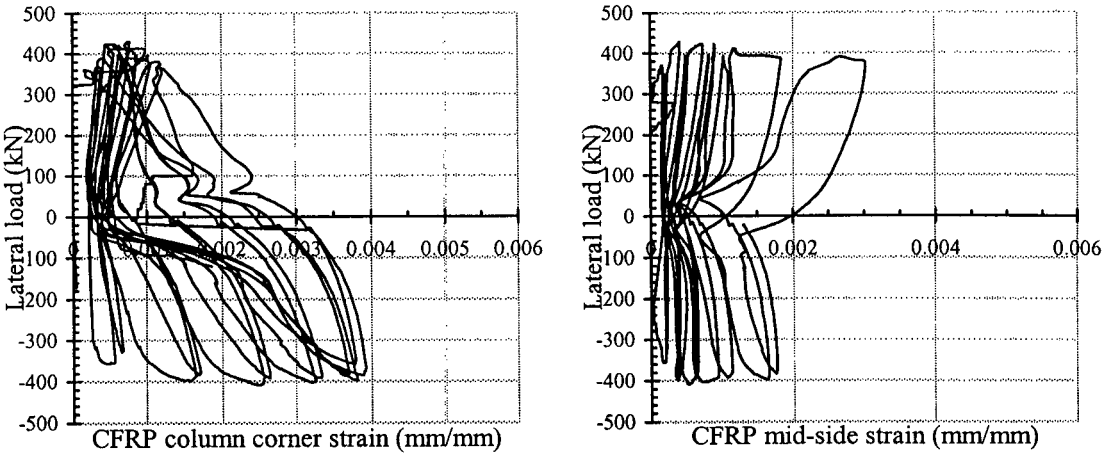

Figure 6.12 CFRP strain - lateral load relationship (top end of column)

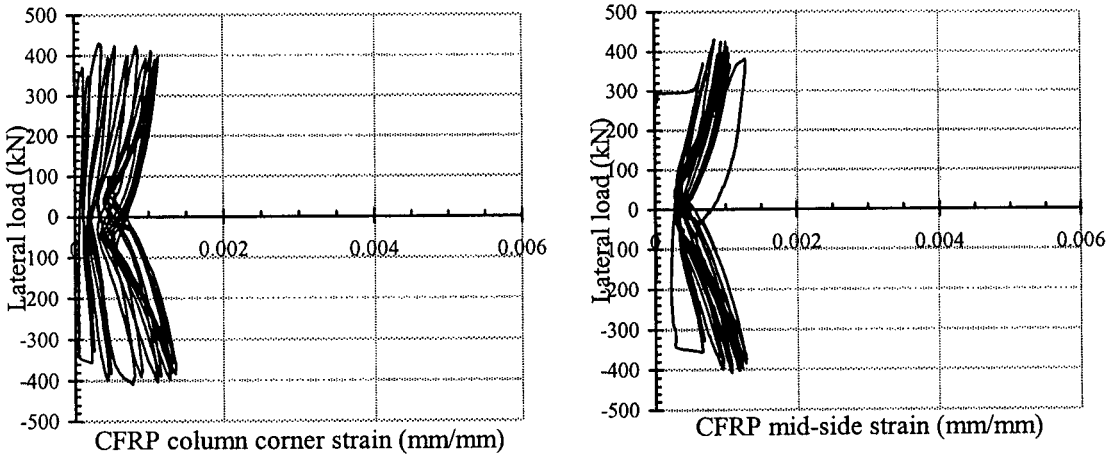

Figure 6.13 CFRP strain - lateral load relationship (mid-height of column)

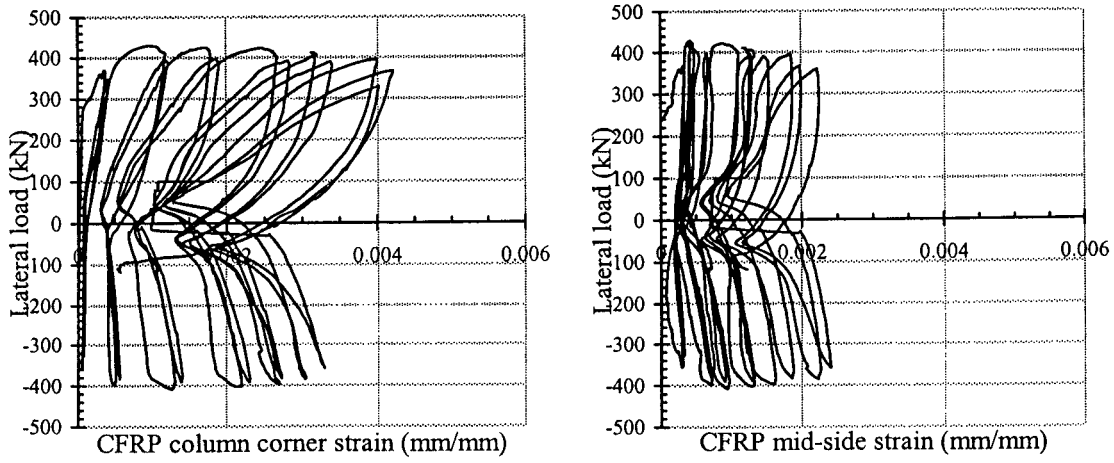

Figure 6.14 CFRP strain - lateral load relationship (bottom end of column)

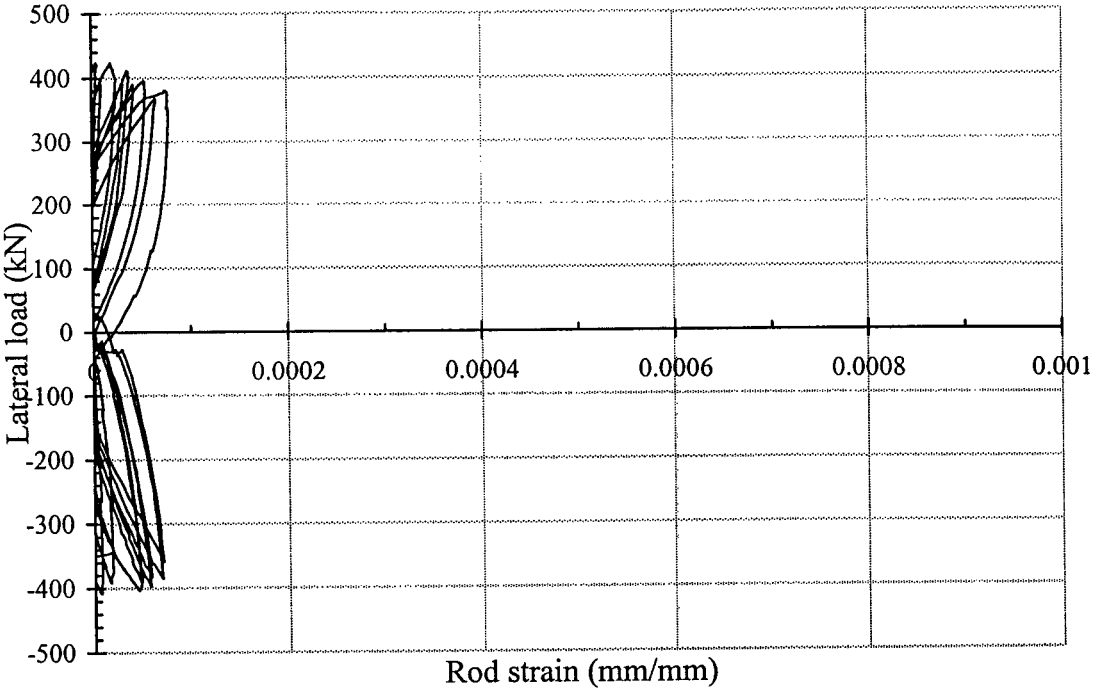

Figure 6.15 Measured strain in the tie rod near mid column height

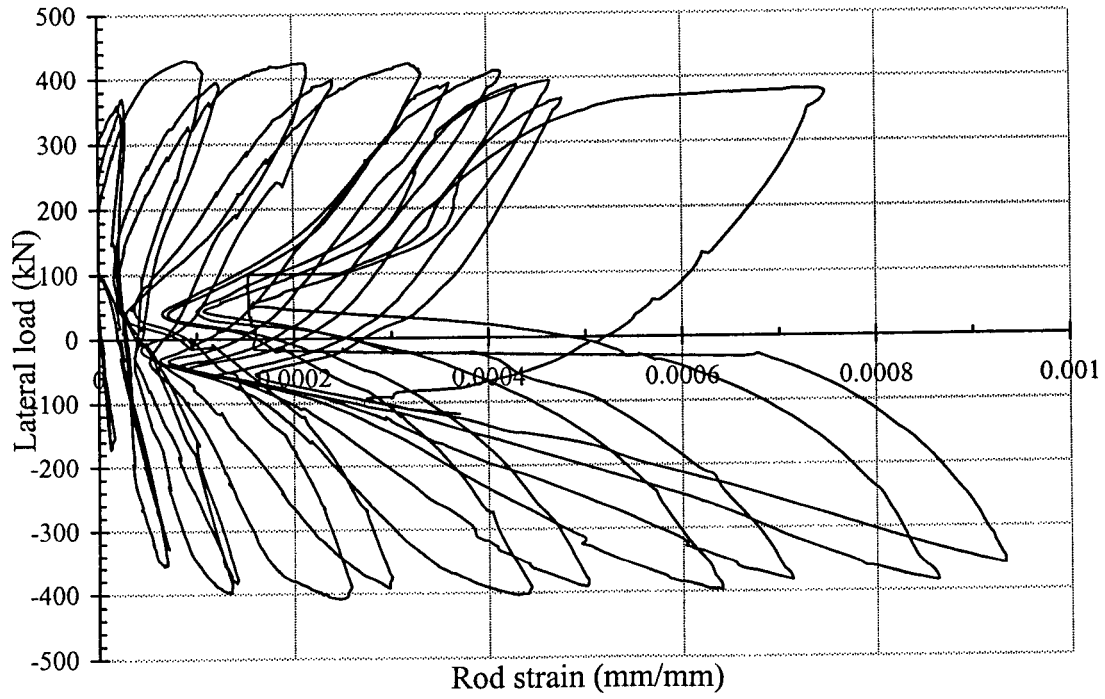

Figure 6.16 Measured strain in the tie rod near column bottom

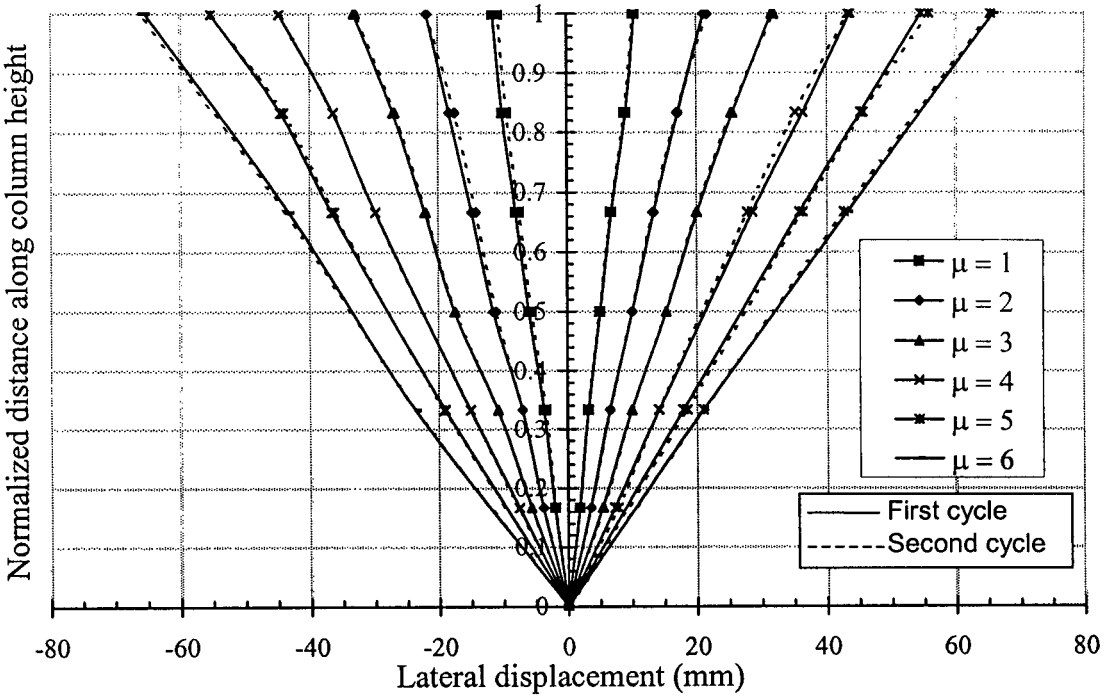

Figure 6.17 Lateral displacement distribution along the column height

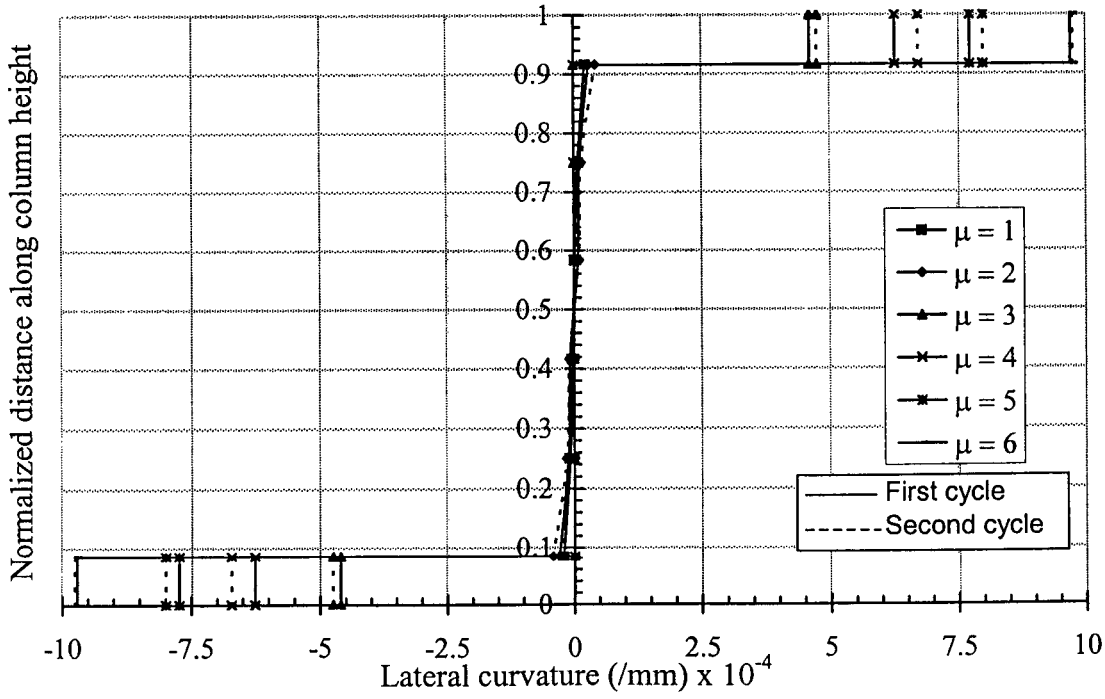

Figure 6.18 Change of curvature along the column height

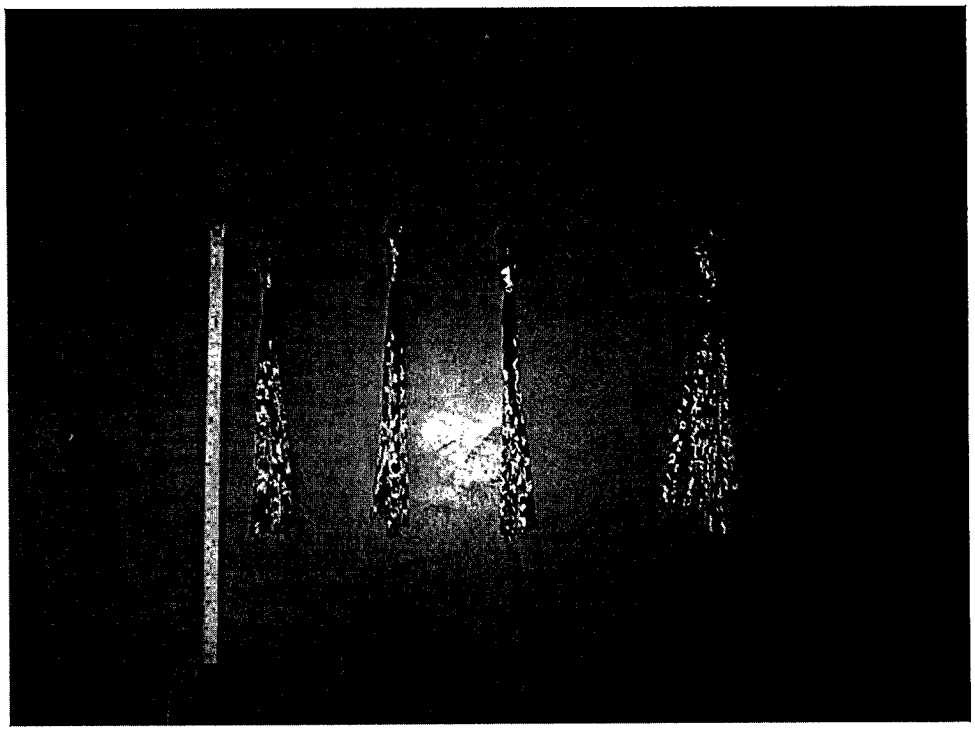

Figure 6.19 CFRP anchors

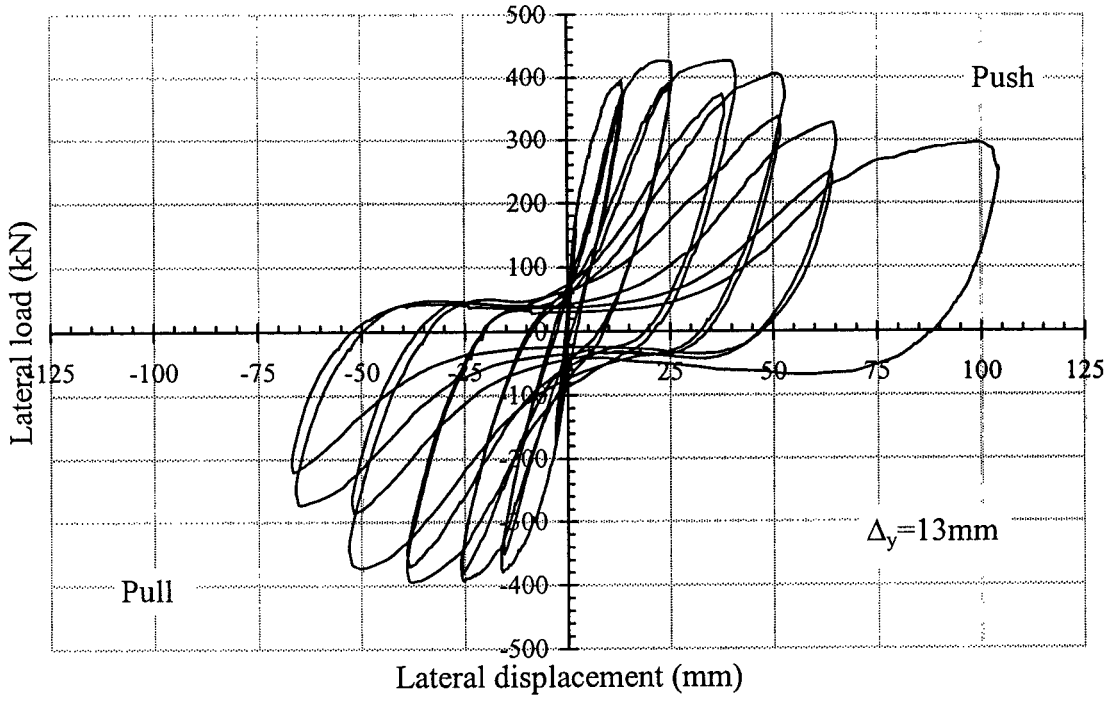

Figure 6.20 Lateral force-displacement relationship for specimen SC3

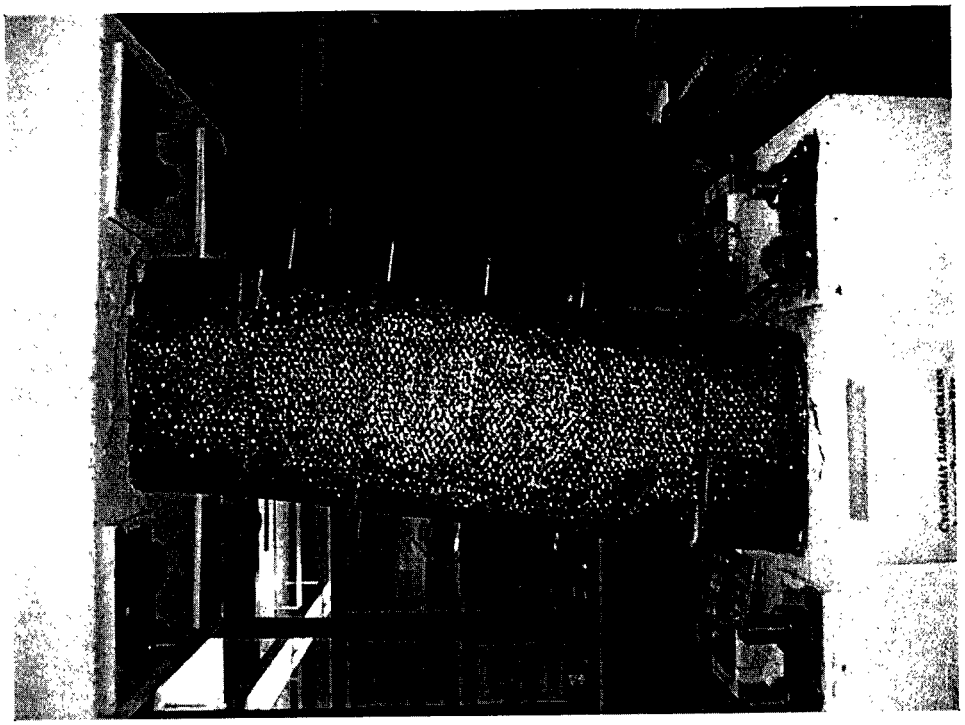

(b)

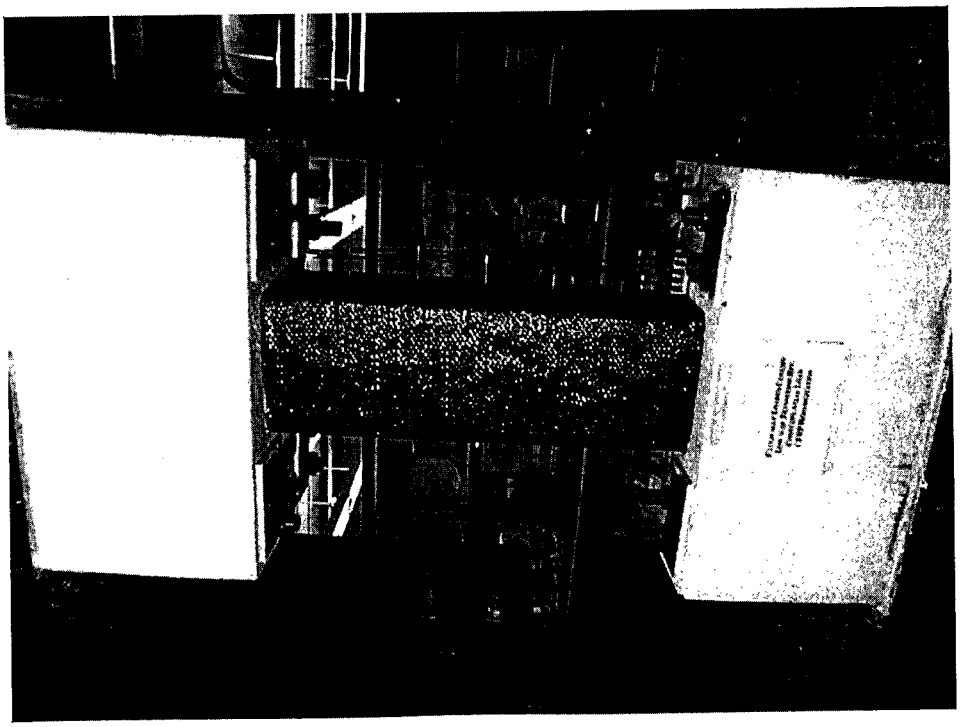

(a)

Figure 6.21 Specimen SC3: (a) Before test; (b) At maximum lateral displacement

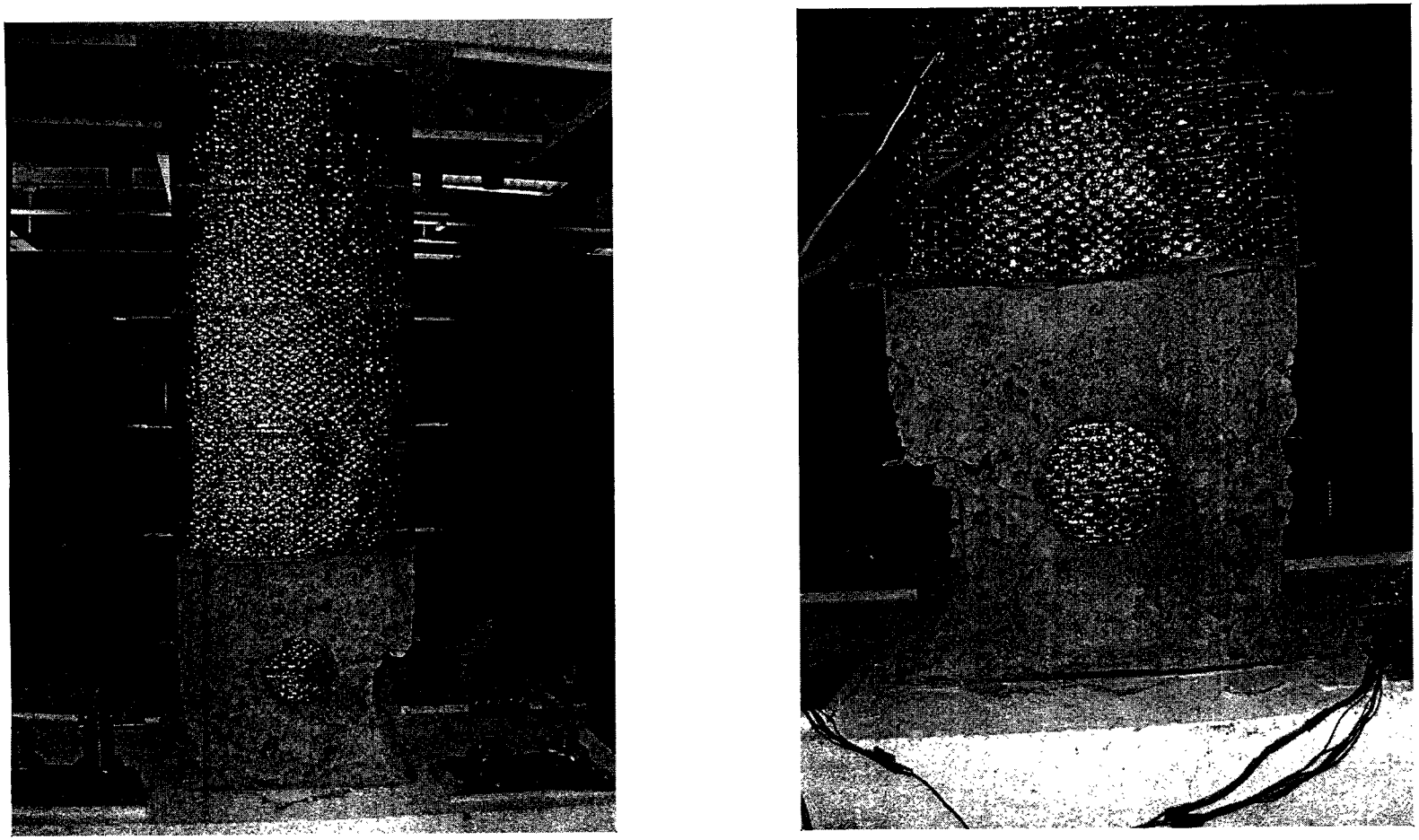

Figure 6.22 Specimen SC3: Plastic hinge location after removing the CFRP

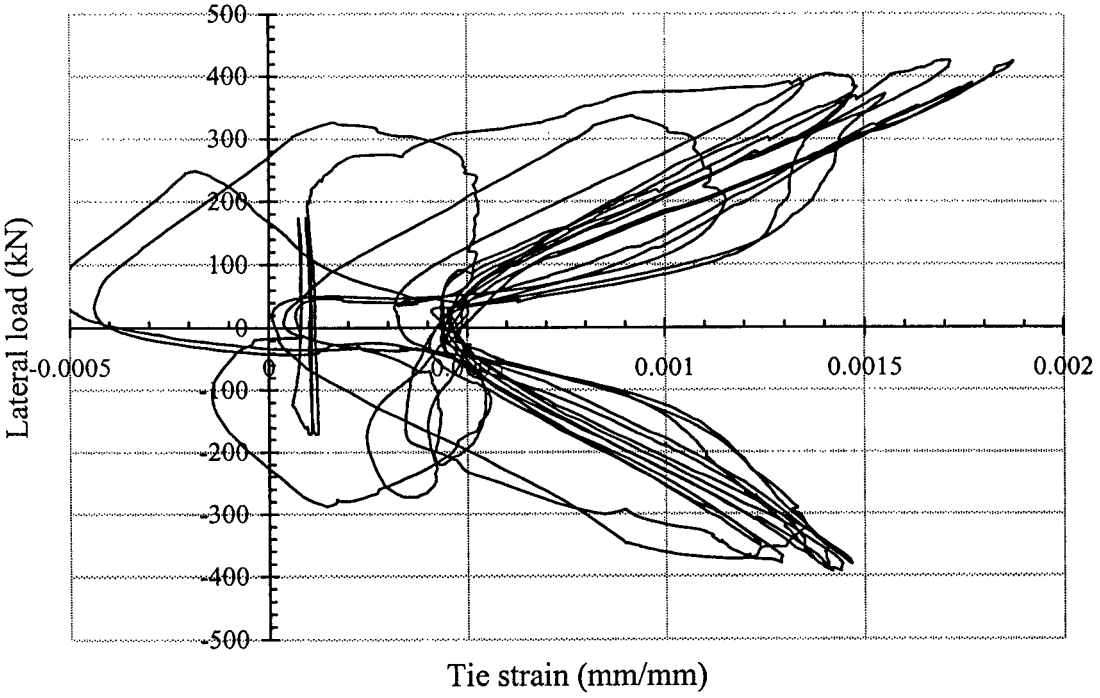

Figure 6.23 Measured strain in tie at one-sixth of the column height

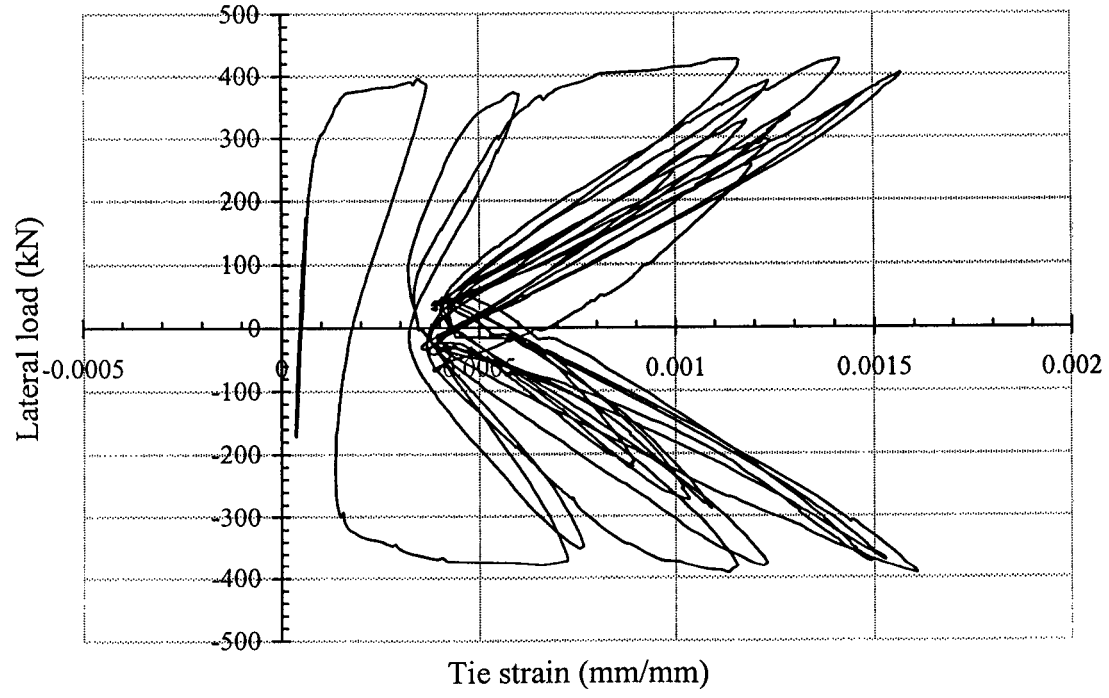

Figure 6.24 Measured strain in tie at mid column height

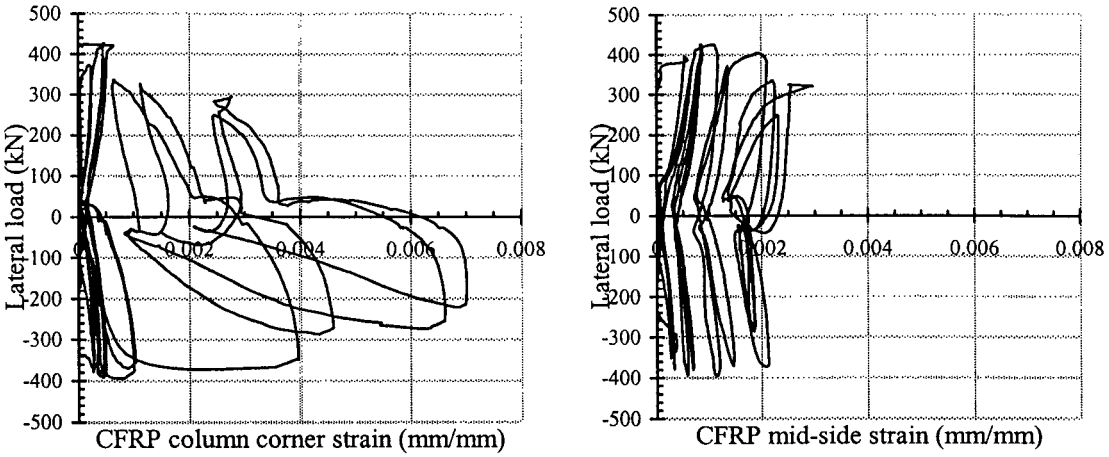

Figure 6.25 CFRP strain - lateral load relationship (top end of column)

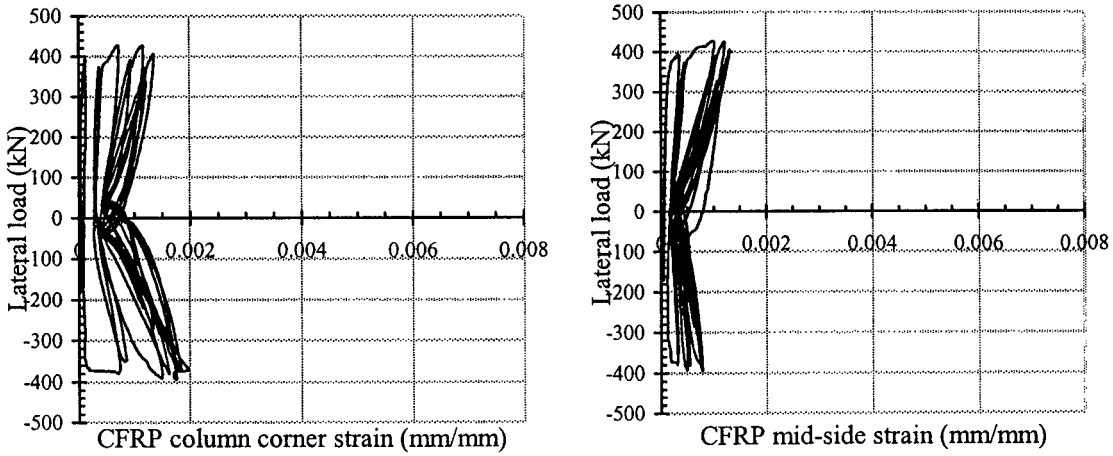

Figure 6.26 CFRP strain - lateral load relationship (mid-height of column)

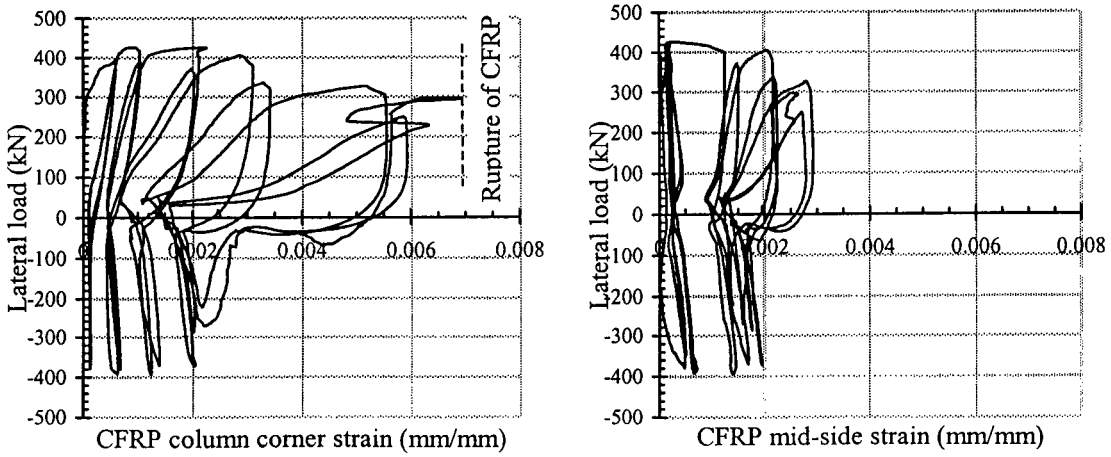

Figure 6.27 CFRP strain - lateral load relationship (bottom end of column)

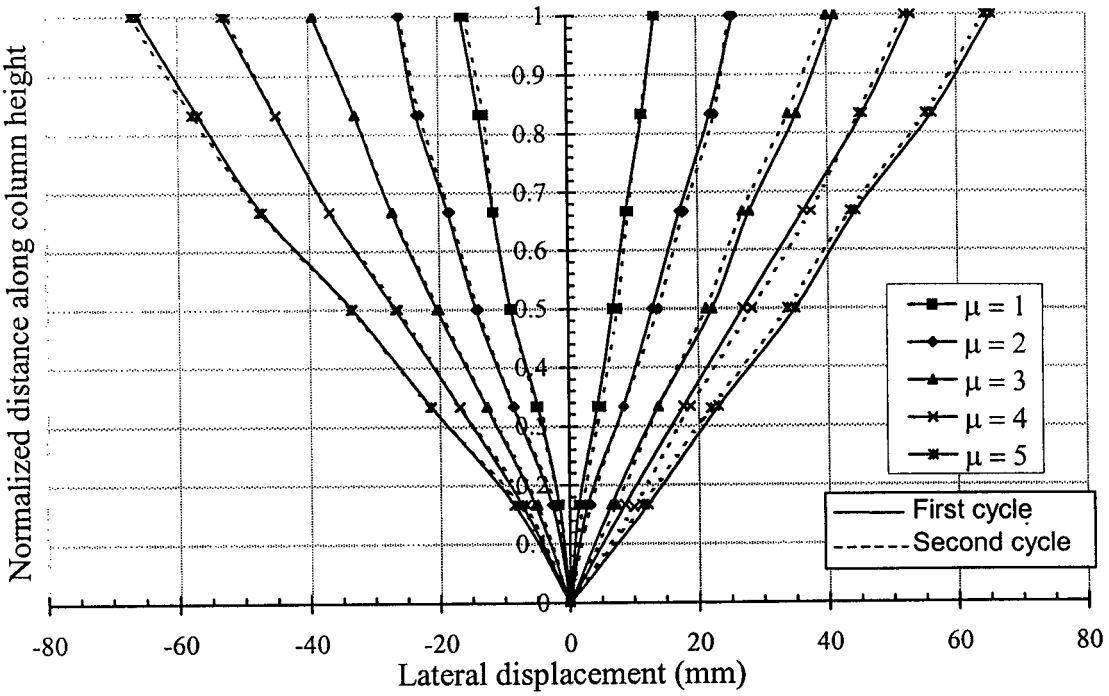

Figure 6.28 Lateral displacement distribution along the column height

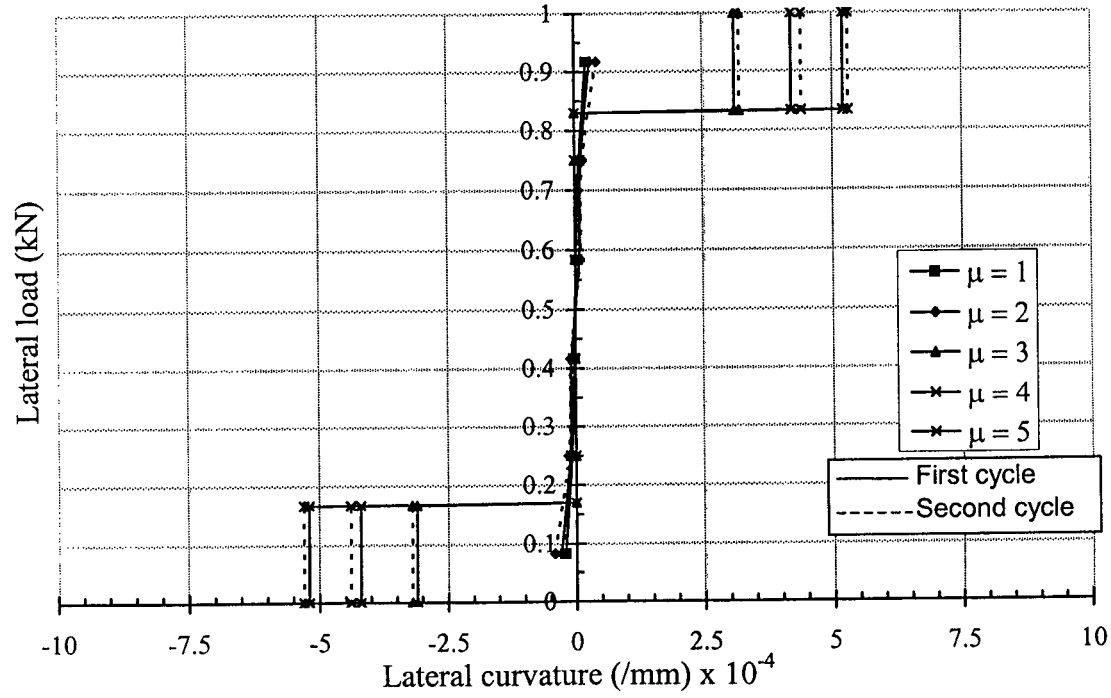

Figure 6.29 Curvature distribution along the column height

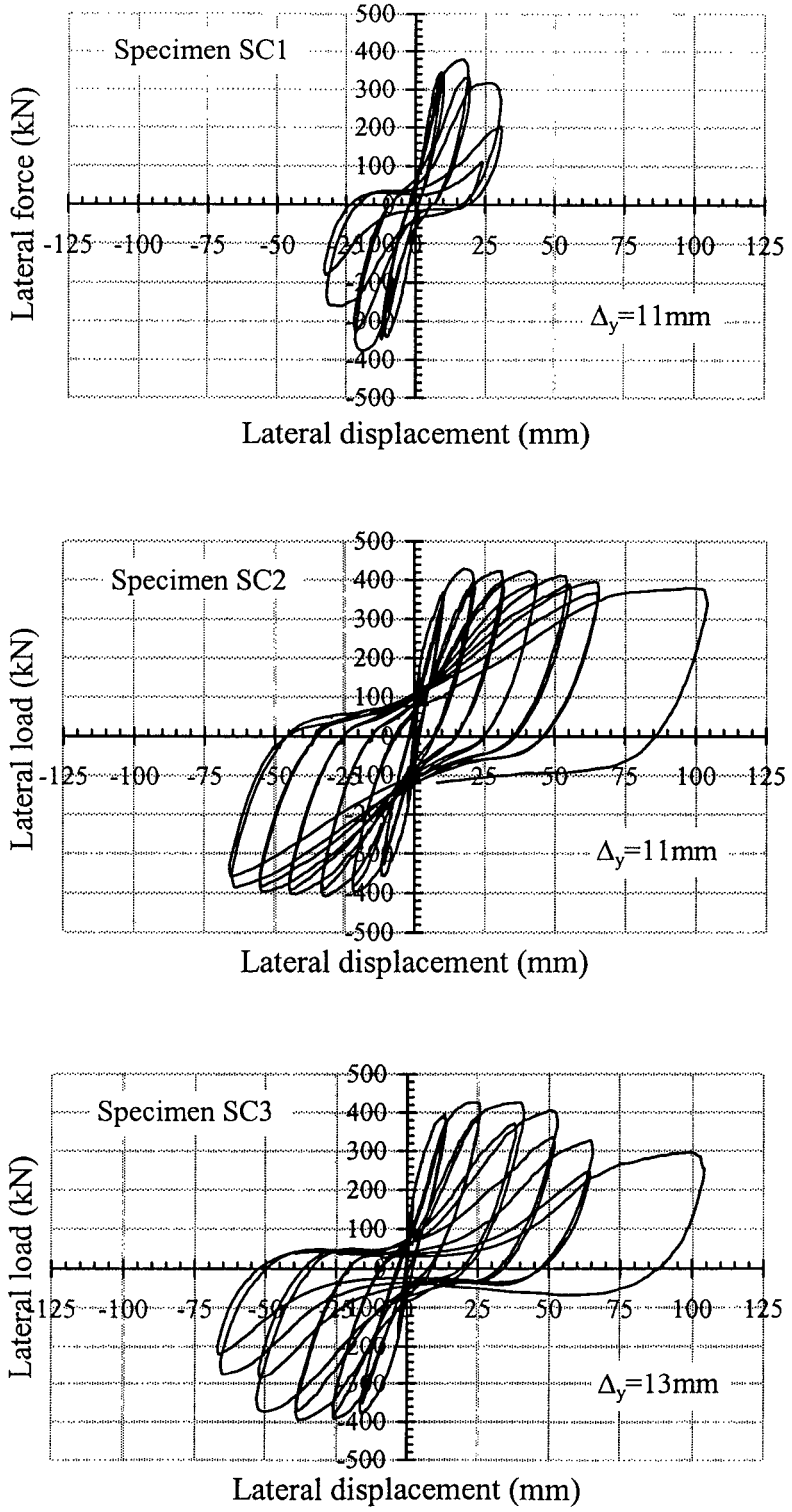

Figure 6.30 Comparison between the lateral force-displacement relationship for the three specimens

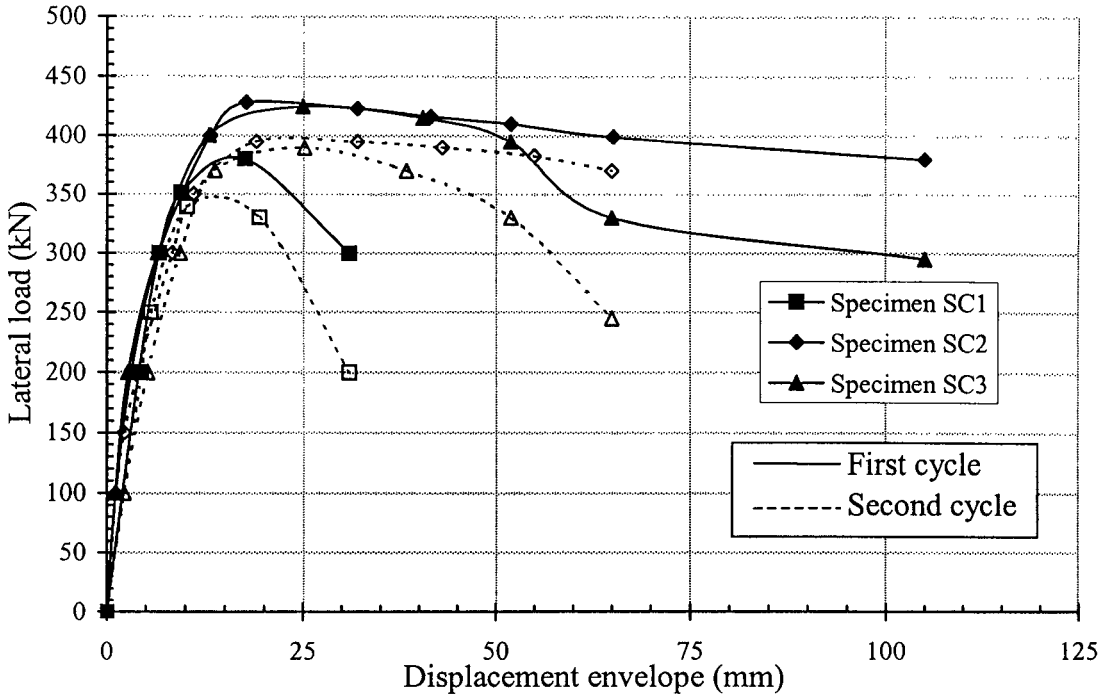

Figure 6.31 Lateral load capacity of the three specimens

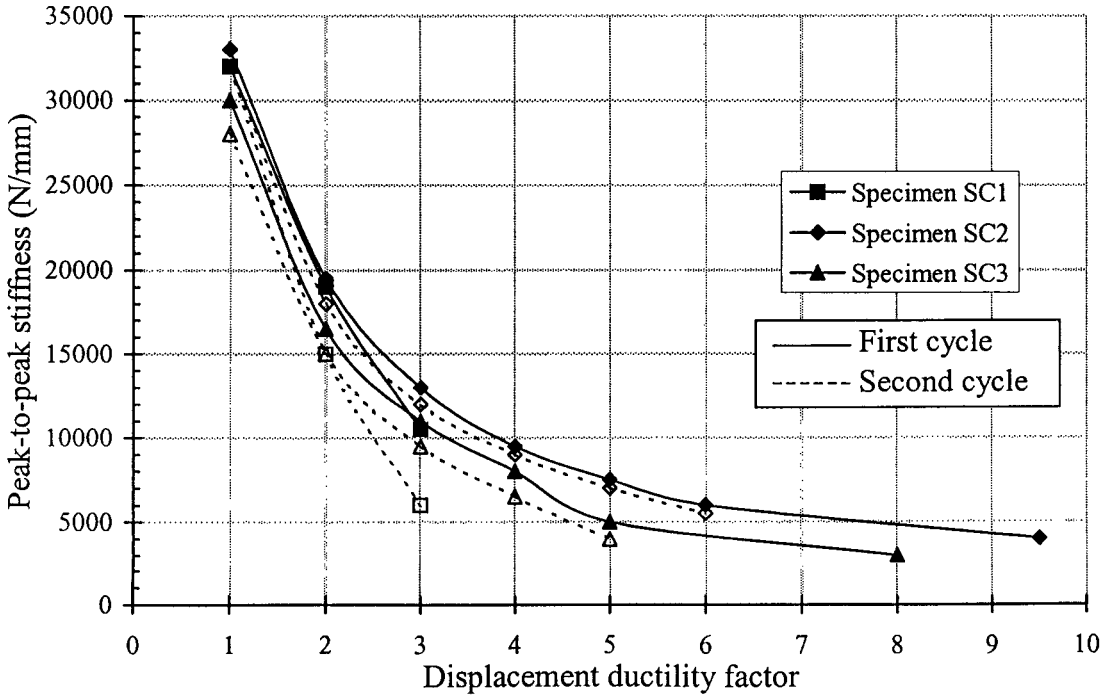

Figure 6.32 Peak-to-peak stiffness - displacement ductility factor relationship

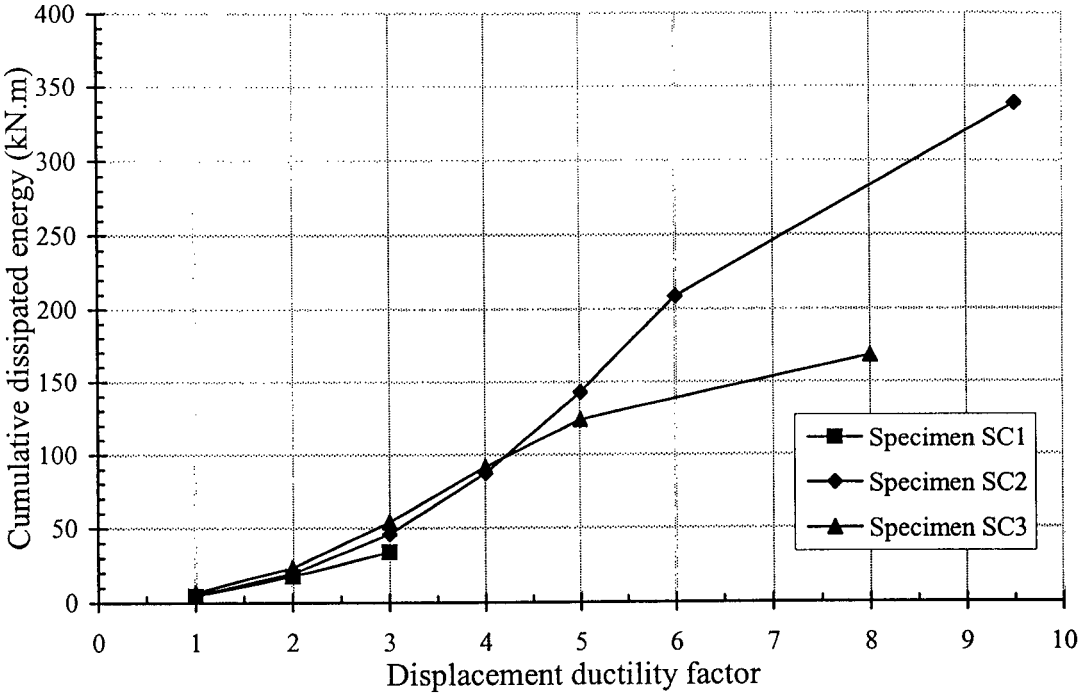

Figure 6.33 Cumulative dissipated energy - displacement ductility factor relationship

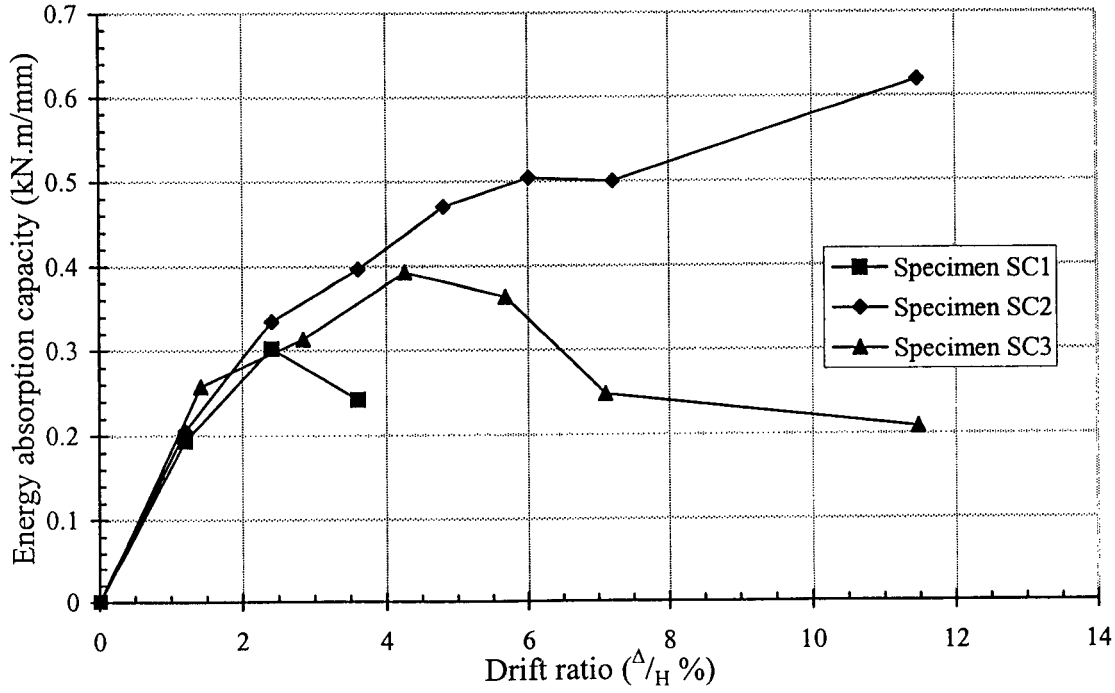

Figure 6.34 Energy absorption capacity - lateral displacement relationship

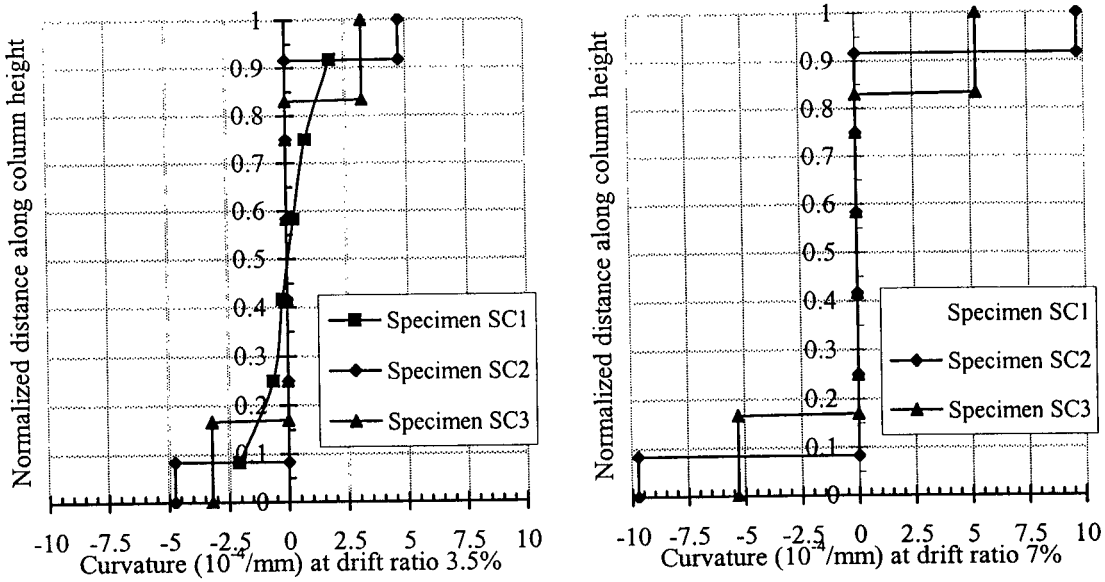

Figure 6.35 Curvature distribution along the column height at drift ratios 3.5% and 7%

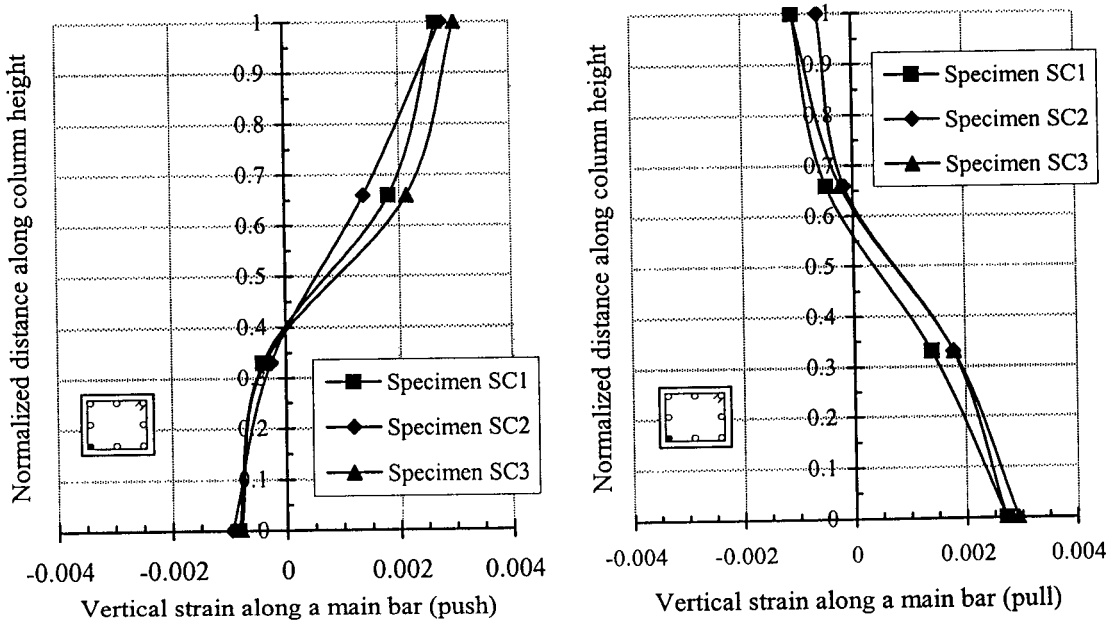

Figure 6.36 Strain distribution along a main rebar at yield

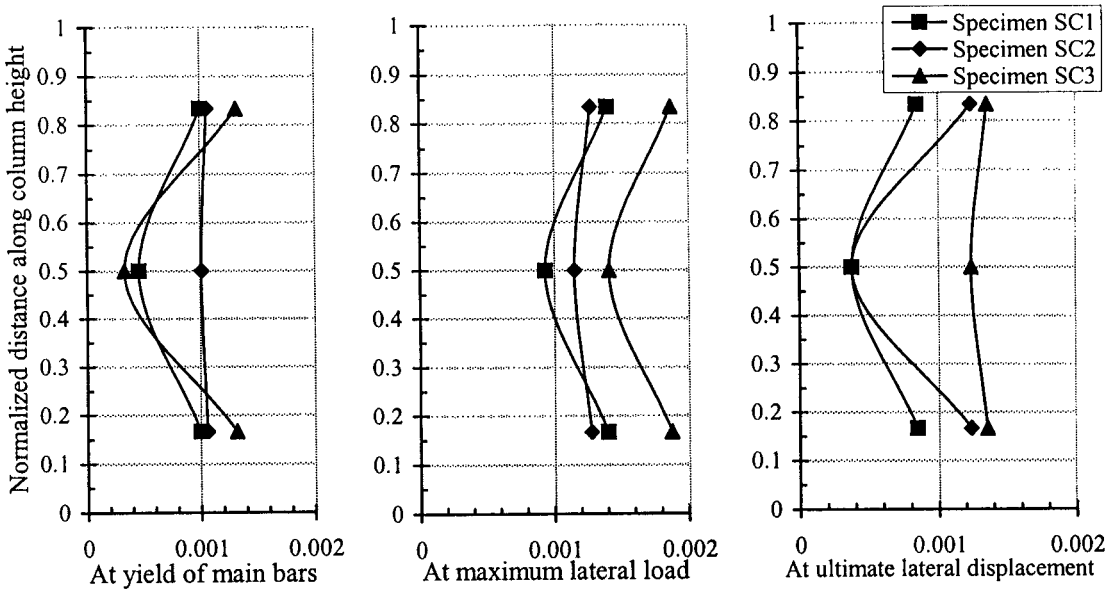

Figure 6.37 Tie strain distribution along the column height

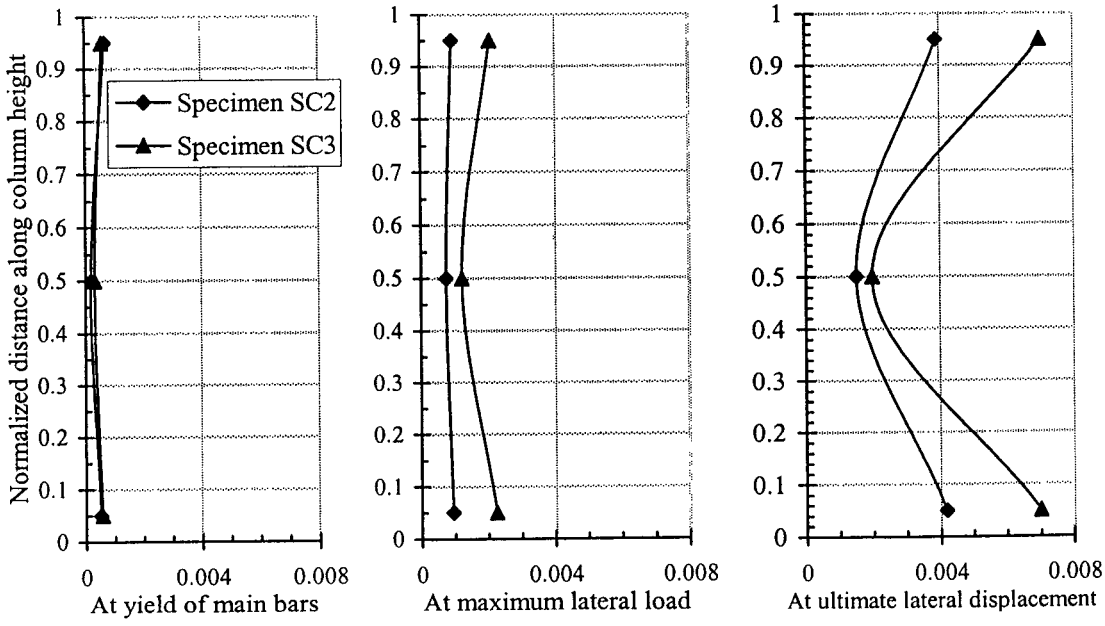

Figure 6.38 Transverse CFRP strain distribution along the column height

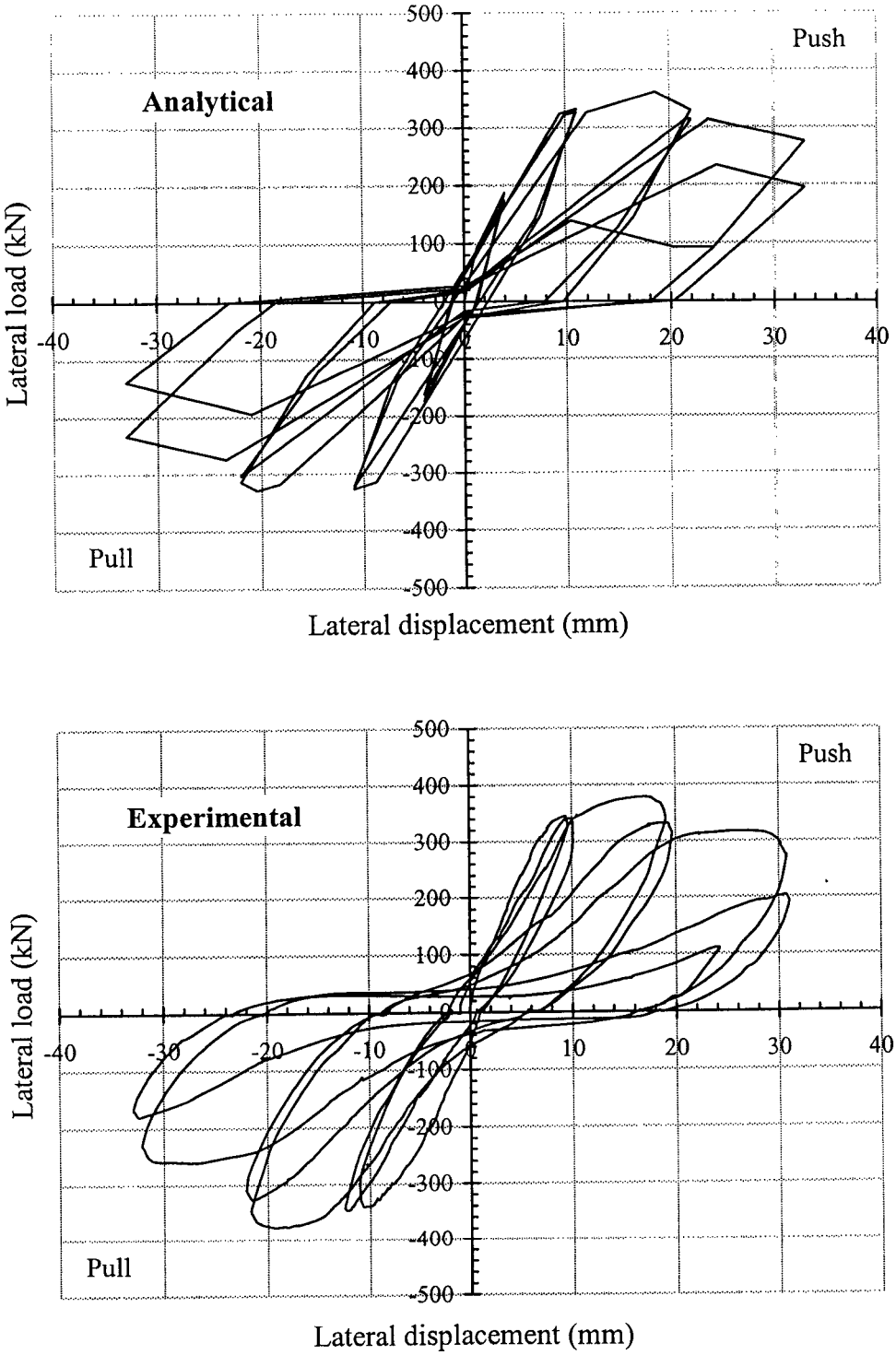

Figure 6.39 Comparison between analytical and experimental lateral force-displacement relationship for specimen SC1

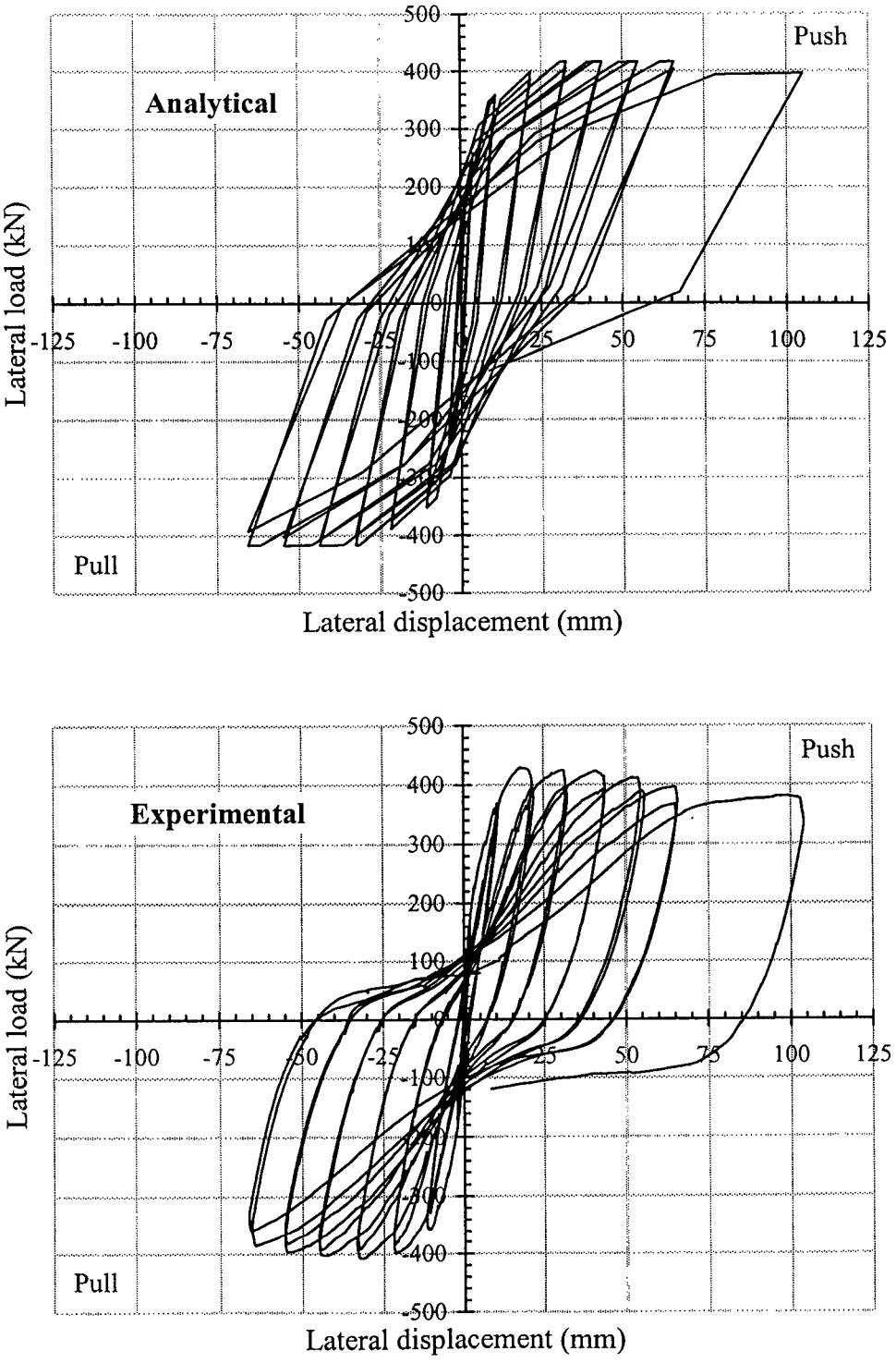

Figure 6.40 Comparison between analytical and experimental lateral force-displacement relationship for specimen SC2

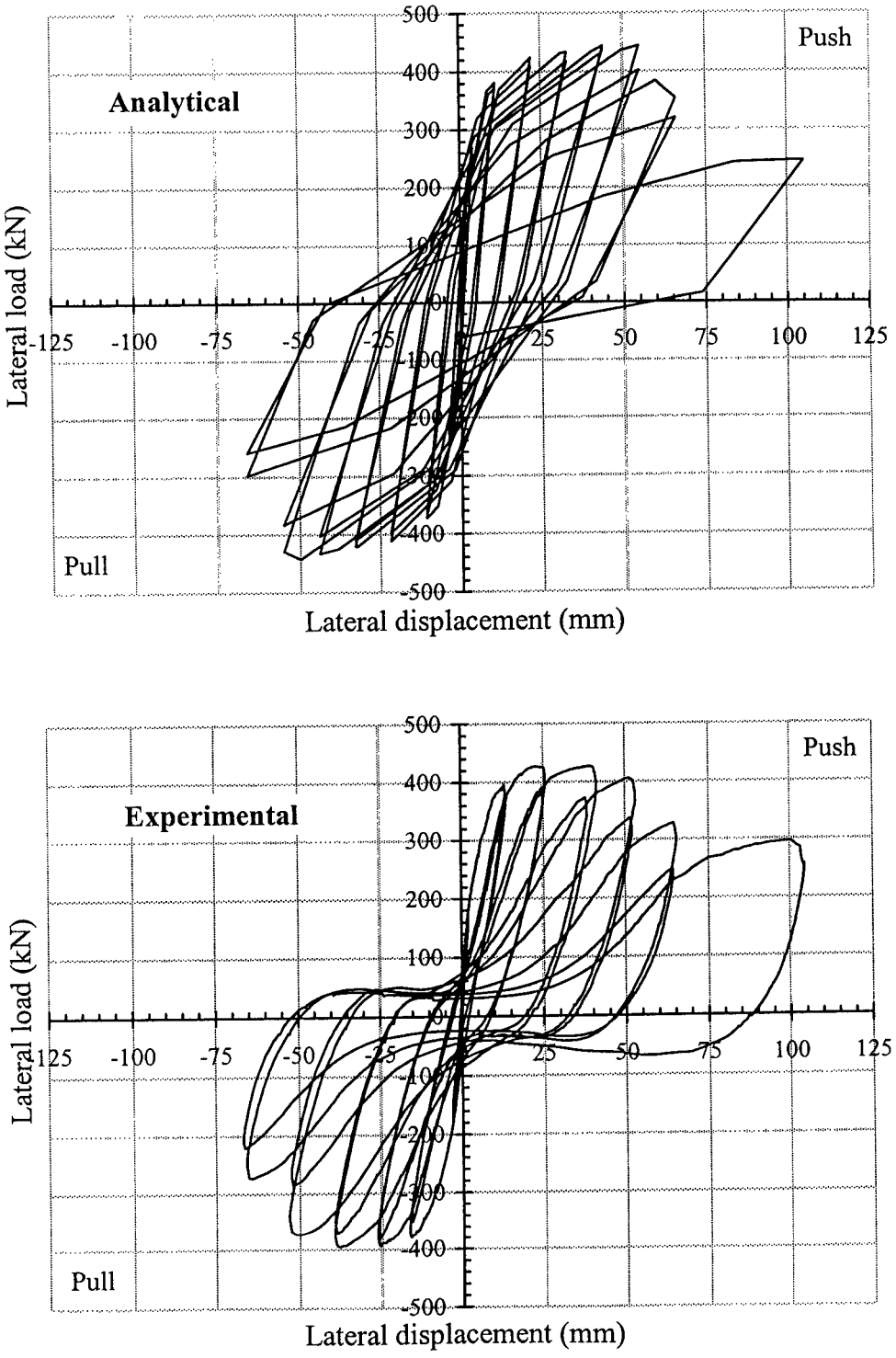

Figure 6.41 Comparison between analytical and experimental lateral force-displacement relationship for specimen SC3

CHAPTER 7

CONCLUSIONS AND RECOMMENDATIONS

7.1 SUMMARY

The principal objectives of this study are to analytically and experimentally evaluate the non-linear behaviour of non-ductile reinforced concrete columns under cyclic deformations.

The analytical phase of the study included the development of a 3D beam-column element based on the lumped plasticity modeling. The model represents flexural response by a quadrilinear force-deformation relationship, and shear response by strength and stiffness degrading relationship. The model takes into account the effect of axial load variation on lateral deformation and its interaction with biaxial moments and shear.

An analytical procedure to obtain the moment-rotation and force-deflection relationships for reinforced concrete columns, which are needed as input data for the 3D element, was developed. This procedure uses the basic mechanical and geometrical properties of the element. It takes into consideration the effect of bond-slip of tensile bars, buckling of compression bars as well as flexure and shear deformations. This procedure was verified using available experimental data. The comparison showed good agreement. A parametric study to evaluate the effect of variation in section and material properties was also conducted.

The performance of the proposed 3D model and the analytical procedure were assessed by comparing the model's predicted response versus experimental results. An analytical study on the effect of several variable axial load paths on the response of cyclically loaded RC column was conducted.

The experimental phase of the study included testing three reinforced concrete short columns under cyclic lateral loads and constant axial load. The first specimen represents columns designed according to current code (CSA A23.3-94). The second specimen was identical to the first one but rehabilitated using anchored carbon fibre reinforced polymers (CFRP). The third specimen represents a non-ductile short column designed according to pre-1970 codes and rehabilitated using anchored CFRP wraps. Two different anchoring techniques to prevent debonding between the CFRP wraps and the column were used in the two rehabilitated specimens; namely, by using through steel rods and fibre anchors.

7.2 CONCLUSIONS

The following conclusions were reached from results of the analytical and experimental research:

1. A 3D model based on the lumped plasticity was developed. The model accounts for uniaxial and biaxial flexure and shear behaviours, as well as the variation of axial load. The model was validated using available experimental results in the literature by several independent researchers and showed sufficient accuracy in predicting the columns response and failure mechanism.

2. An analytical procedure to evaluate the moment-rotation backbone relationship for RC members was introduced and tested. This method takes into account the effect of bond-slip of tensile bars, buckling of compression bars as well as flexure and shear deformations. The methodology is found to be rational and capable of estimating the deformation components of RC columns with a reasonable accuracy.
3. A complete response analysis for RC columns should include the variation in axial force component. The level and type of applied varying axial path as well as its phase shift with respect to the applied lateral displacement path will affect the hysteretic response of RC columns and its energy dissipation capacity.
4. A short RC column designed according to the current code (CSA A23.3-94) failed in shear with a non-ductile behaviour when subjected to lateral cyclic displacements.
5. Rehabilitating a short RC column that contains high percentage of transverse reinforcement (designed according to current code) using anchored CFRP jacket significantly improves its displacement ductility and energy dissipation capacity.
6. Rehabilitating a short RC column that contains low percentage of transverse reinforcement (designed according to pre-1970 codes) using anchored CFRP jacket improves its displacement ductility and energy dissipation capacity.
7. Both anchoring techniques used in the current experimental investigation; i.e. through steel rods and fibre anchors, are effective in eliminating the concrete bulging at the column sides.

8. Rehabilitating RC columns using CFRP jackets provides both confinement to the concrete and additional shear resistance mechanism. The contribution of the CFRP jacket to the total shear strength of a RC column increases with the decrease of the lateral reinforcement content.

Finally, it should be mentioned that the presented results are based on a limited number of analyses and tests. To establish general conclusions on the spatial behaviour of non-ductile reinforced concrete columns, a more comprehensive study is needed.

7.3 RECOMMENDATIONS FOR FUTURE RESEARCH

The following recommendations may be considered in future research involving spatial modeling and rehabilitation of non-ductile RC columns:

1. The developed element needs to be implemented in a global nonlinear frame analysis program.
2. The developed 3D element may be extended to model the effect of rehabilitating reinforced concrete elements using fibre reinforced polymers (FRP) wraps.
3. The 3D element may be extended to model the non-ductile behaviour of brick and masonry columns and walls.
4. The effect of variation of axial load on rehabilitated non-ductile RC columns needs to be investigated experimentally.
5. The effect of diagonal and multi-directional lateral loading on rehabilitated non-ductile RC columns needs to be investigated experimentally.

APPENDIX A

ANCHORAGE SLIP SOLUTION STRATEGY

The following describes the solution strategy adopted to obtain the stress-strain relationship of embedded bar subjected to monotonic pull and taking bond slip into consideration:

A.1 Before bar slip (figure 3.5a): $(l_e + l_{pl}) < l_{bar}$

- By applying a tension force to the bar at the pull side end, then:

$$l_e = \frac{f_s d_b}{4 q_e} \tag{A.1}$$

$$q_e = \frac{f_y d_b}{4 l_d} \tag{A.2}$$

$$l_d = \frac{440 \ A_b}{3 d_b \sqrt{f_c'}} \frac{f_y}{400} \geq 300 \ mm \qquad \text{(MPa units)} \tag{A.3}$$

where: q_e = The average bond stress proposed by ACI (1985);
l_d = Development length (mm);
A_b = Tensile bar area (mm^2); and
d_b = Tensile bar diameter (mm).

$$l_{pl} = \frac{(f_s - f_y) d_b}{4 q_f} \tag{A.4}$$

$$q_f = (5.5 - 0.07 \frac{S_L}{H_L}) \sqrt{\frac{f_c'}{27.6}} \ MPa \tag{A.5}$$

where: q_f = The frictional bond stress proposed by Pochanart and Harmon (1989);

S_L = The clear spacing of lugs; and

H_L = The clear height of lugs.

q_f can be simplified to be $q_f = 5\sqrt{\frac{f_c'}{27.6}}\ MPa$ for most practical applications.

A.2 After bar slip (figure 3.5b): $(l_e' + l_{pl}) = l_{bar}$

- By increasing the tension force applied to the bar, then:

$$l_e' = l_{bar} - l_{pl}$$

$q = \frac{f_y d_b}{4l_e'}$ obtain δ_{slip} (from the local bond stress-slip relationship, figure 3.4)

until $\delta_{slip} = \delta_1$

- Apply incremental δ_{slip} at cut off end (from δ_1 to δ_2):

$$q = q_1 = q_2$$

$$\therefore\ l_e' = \frac{f_y d_b}{4q_1}$$

- Apply incremental δ_{slip} at cut off end (from δ_2 to δ_3):

$$\therefore\ q < q_1$$

$$l_e' = \frac{f_y d_b}{4q}$$

$$l_{pl} = l_{bar} - l_e'$$

APPENDIX B

DESIGN OF SHORT COLUMN

This section contains the design steps for a short R.C. column according to CSA A23.3-94. The column has cross section of 305x305 mm and is reinforced by 8 # 20 mm bars and is subjected to compressive axial load equal to 500 kN.

B.1 Transverse reinforcement spacing (Clause 21.4.4.3):

Transverse reinforcement shall be spaced at distances not exceeding:

a) One-quarter of the minimum member dimension = t/4 = 305/4 = 76.25 mm

b) 100 mm

c) 6 times the diameter of the smallest longitudinal bar; i.e. 6×19.5=117 mm

∴ The maximum tie spacing = 76.25 mm

B.2 Transverse reinforcement content (Clause 21.4.4.2):

Transverse reinforcement, specified as follows, shall be provided unless a larger amount is required by clause 21.7:

The total cross sectional area of rectangular hoop reinforcement shall no be less than the larger of the amounts given by equations 21-3 and 21-4 as follows:

$$A_{sh} = 0.3sh_c \frac{f_c'}{f_{yh}}\left(\frac{A_g}{A_{ch}} - 1\right) \qquad \text{(B.1) CSA A23.3 21-3}$$

$$A_{sh} = 0.09sh_c \frac{f_c'}{f_{yh}} \qquad \text{(B.2) CSA A23.3 21-4}$$

where s is the tie spacing;

h_c is the length of tie;

f_c' is the concrete compressive strength;

f_{yh} is the yielding stress of the column;

A_s is the gross area of the column; and

A_{ch} is the core area bounded by the ties.

Equation B.1: $$A_{sh} = 0.3\times65\times254\times\frac{39}{430}\left(\frac{305\times305}{254\times254}-1\right)=198.5\ \ mm^2$$

Equation B.2: $$A_{sh} = 0.09\times65\times254\times\frac{39}{430}=134.8\ \ mm^2$$

$\therefore A_{sh} = 198.5\ mm^2$ use #10 bars closed ties

B.3 Check shear capacity (Clause 21.7.3):

Members subjected to seismic shear shall be designed such that: $V_r \geq V_f$.

Where V_r is the resisting shear force, while V_f is the factored design shear force.

1-The factored design shear force:

For a double flexure fixed-fixed column: $M = Vh/2$. Thus $V = 2M/h$. Where h is the column height.

$$\therefore V_f = \frac{2M_f}{h} = \frac{2\times140kN.m}{0.9144m} = 306\ \ kN$$

2-The resisting shear force:

$$V_r = V_c + V_s \leq \left(V_c + 0.8\lambda\Phi_c\sqrt{f_c'}bd\right) \qquad \text{(B.3)}$$

Where $V_c = 0.1\lambda\Phi_c\sqrt{f_c'}bd = 0.1\times1.0\times0.6\times\sqrt{39}\times305\times260 = 30\ \ kN$

And $$V_s = \frac{\Phi_s A_v f_{yh} d}{s} = \frac{0.85\times200\times430\times260}{65} = 295\ \ kN$$

$\therefore V_r = 30 + 295 = 325$ kN

Thus $V_r \geq V_f$.

APPENDIX C

3D ELEMENT COMPUTER PROGRAM

This appendix includes the solution algorithm and listing of the main program subroutines for the beam-column 3D element computer program explained in Chapter 2.

C.1 SOLUTION ALGORITHM

Figure C.1 shows the flow chart of the 3D element. Each subroutine includes a brief description of its function.

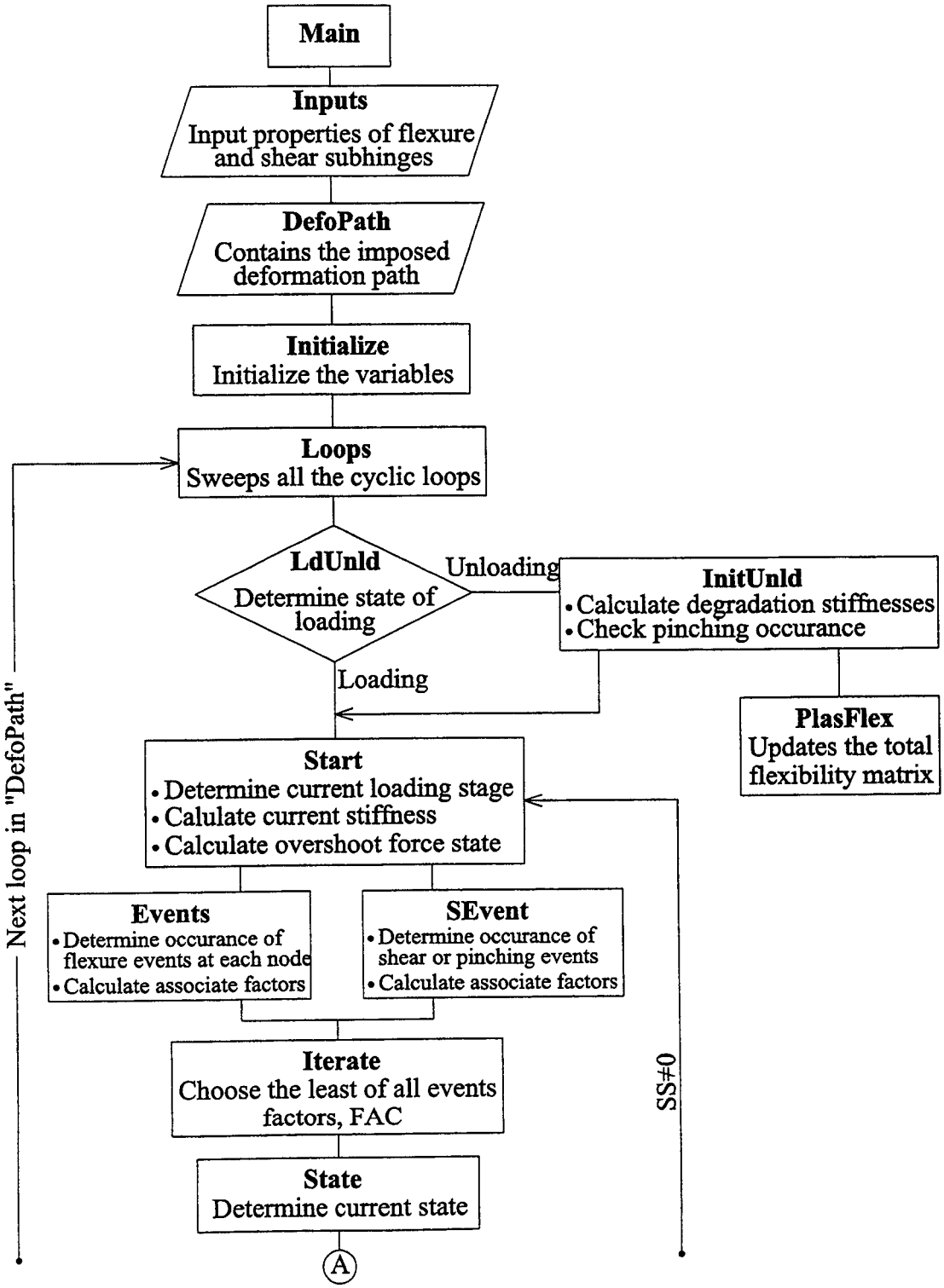

Figure C.1 3D Model flow chart (continued)

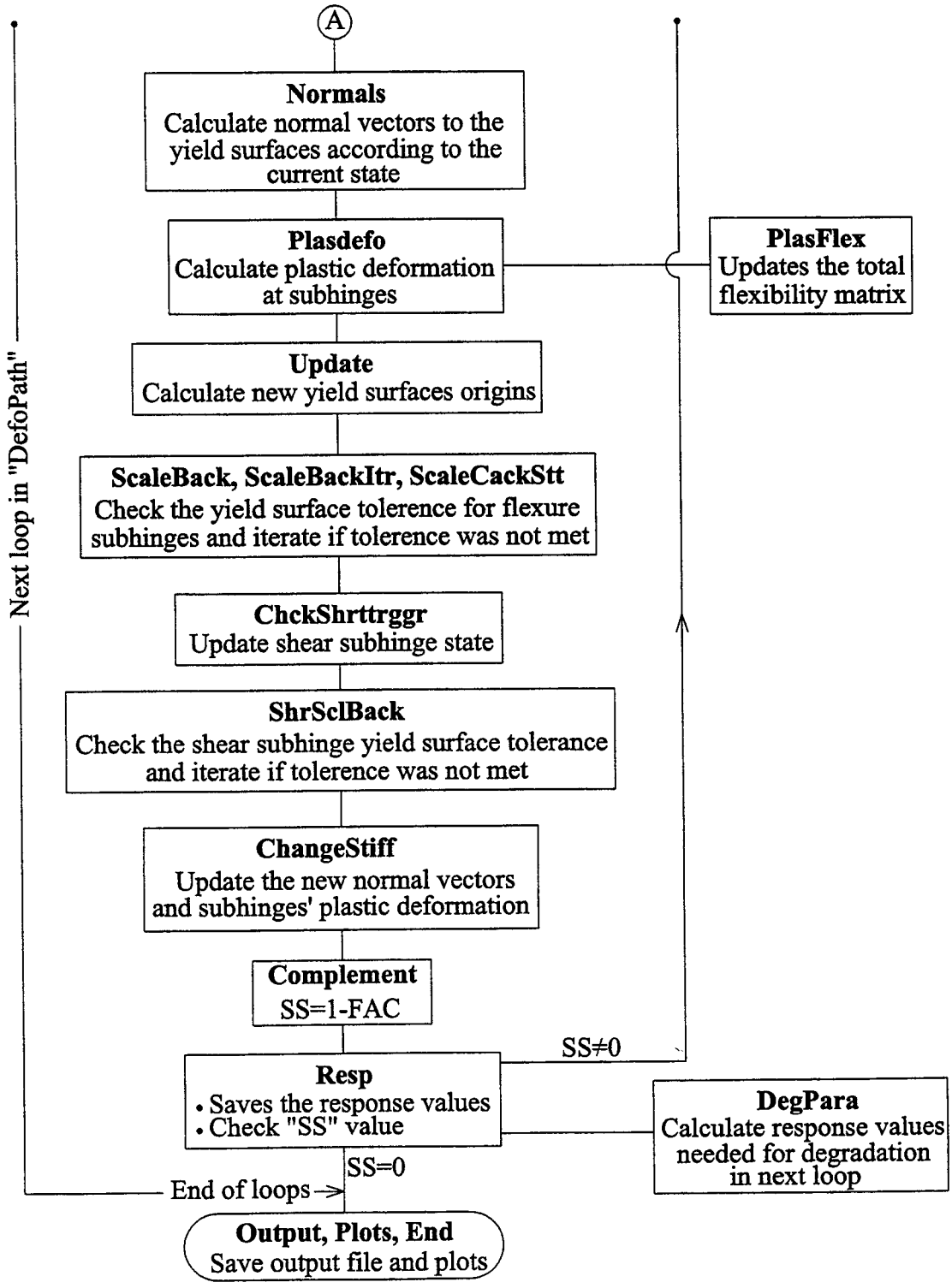

Figure C.1 3D Model flow chart (continue)

C.2 LISTING OF THE PROGRAM

The listing of the beam-column 3D element computer program is presented. A sample input file (in **Inputs**) and imposed deformation path (in **DefoPath**) for the test conducted by Takizawa and Aoyama (1976) are included:

Main

```
clear
delete 3DElement.out;
run_time=cputime;
Inputs
Initialize
Loops
Plots
run_time=cputime-run_time
```

Inputs (Sample of test conducted by Takizawa and Aoyama (1976))

```
Fl=60;                  %Full Length of the element
Lfac=1.0;               %1.0 for Cantilever & 0.5 for fixed-fixed
% Case of Moment-rotationrelationship (Beam with end moments)
Fleff=Lfac*Fl;
% Case of Force-deflection relationship
Fleff=1.0;
%Hinge Bending properties about Local y-axis
Muy1i=1.5; Muy2i=3.25; Muy3i=4.8;KMy1i=22.7; KMy2i=10.7; KMy3i=6.7;     KMy4i=0.05;
Muy1j=1.5; Muy2j=3.25; Muy3j=4.8; KMy1j=22.7;KMy2j=10.7; KMy3j=6.7; KMy4j=0.05;
%Hinge Bending properties about Local z-axis
Muz1i=1.5; Muz2i=3.25; Muz3i=4.8; KMz1i=22.7; KMz2i=10.7; KMz3i=6.7; KMz4i=0.05;
Muz1j=1.5; Muz2j=3.25; Muz3j=4.8; KMz1j=22.7;KMz2j=10.7; KMz3j=6.7; KMz4j=0.05;
```

```
%Hinge Bending properties about Local x-axis "torsional Moment"
Mux1i=50; Mux2i=50; Mux3i=50;KMx1i=103; KMx2i=102; KMx3i=101; KMx4i=1;
Mux1j=50; Mux2j=50; Mux3j=50;KMx1j=103; KMx2j=102; KMx3j=101; KMx4j=1;
%Hinge Axial properties
Fu1i=50; Fu2i=50; Fu3i=50;KF1i=103; KF2i=102; KF3i=101; KF4i=1;
Fu1j=50; Fu2j=50; Fu3j=50;KF1j=103; KF2j=102; KF3j=101; KF4j=1;
% Elastic beam stiffnesses
KMye11=KMy1i; KMye12=KMy1i ; KMye22=KMy1i;
KMze11=KMz1i; KMze12=KMz1i ; KMze22=KMz1i;
KMxe1=KMx1i;  KFe1=KF1i;
% Elastic beam shear stiffnesses
G=6*KMye11;Aye=1e10;Aze=1e10;L=Fleff;
Kvy=-0.5;  Kvz=-0.5; % decreasing Kvy or Kvz increases the decending slope
%Shear Capacity
Vyf=100;Vzf=100;
% Allowable tolerence in the yield surfaces
Tol=0.01;TolShr=0.01;
err=1e-12;      % allowable numerical error, range between 1e-14 to 1e-10
%Values of the initial origin of the yield surfaces 'phi'
alpha1i=[0;0;0;30]; alpha2i=[0;0;0;30]; alpha3i=[0;0;0;30];
alpha1j=[0;0;0;30]; alpha2j=[0;0;0;30]; alpha3j=[0;0;0;30];
% Input the Torque and Axial loads
Torque=0; Axial=16;
%Stiffness Degradation coefficients
DegFacy=0.10; DegFacz=0.10;
DegFacsy=0.05; DegFacsz=0.05;
PnchngDeg=0.05;
```

DefoPath (Sample of test conducted by Takizawa and Aoyama (1976) Path No. 4)

```
  %Dr(,)=[dispxi;dispyi;dispzi;rotxi;rotyi;rotzi;dispxj;dispyj;dispzj;rotxj;rotyj;rotzj];
Dr(:,1)=[00.000;00.000;00.000;00.00;00.00;00.00;00.000;+0.900;+0.000;00.00;00.00;00.00];vartor(1)=0; varax(1)=+00;
```

```
Dr(:,2)=[00.000;00.000;00.000;00.00;00.00;00.00;00.000;+0.100;+0.950;00.00;00.00;00.00];vartor(2)=0; varax(2)=+00;
Dr(:,3)=[00.000;00.000;00.000;00.00;00.00;00.00;00.000;-1.900;+0.250;00.00;00.00;00.00];vartor(3)=0; varax(3)=+00;
Dr(:,4)=[00.000;00.000;00.000;00.00;00.00;00.00;00.000;-0.300;-2.100;00.00;00.00;00.00];vartor(4)=0; varax(4)=+00;
Dr(:,5)=[00.000;00.000;00.000;00.00;00.00;00.00;00.000;+2.100;-0.300;00.00;00.00;00.00];vartor(5)=0; varax(5)=+00;
Dr(:,6)=[00.000;00.000;00.000;00.00;00.00;00.00;00.000;+0.300;+2.250;00.00;00.00;00.00];vartor(6)=0; varax(6)=+00;
Dr(:,7)=[00.000;00.000;00.000;00.00;00.00;00.00;00.000;-2.100;+0.250;00.00;00.00;00.00];vartor(7)=0; varax(7)=+00;
Dr(:,8)=[00.000;00.000;00.000;00.00;00.00;00.00;00.000;-0.300;-2.200;00.00;00.00;00.00];vartor(8)=0; varax(8)=+00;
Dr(:,9)=[00.000;00.000;00.000;00.00;00.00;00.00;00.000;+2.100;-0.800;00.00;00.00;00.00];vartor(9)=0; varax(9)=+00;
Dr(:,10)=[00.000;00.000;00.000;00.00;00.00;00.00;00.000;+0.300;+1.800;00.00;00.00;00.00];vartor(10)=0; varax(10)=+00;
Dr(:,11)=[00.000;00.000;00.000;00.00;00.00;00.00;00.000;+0.800;+0.100;00.00;00.00;00.00];vartor(11)=0; varax(11)=+00;
Dr(:,12)=[00.000;00.000;00.000;00.00;00.00;00.00;00.000;+0.200;+1.800;00.00;00.00;00.00];vartor(12)=0; varax(12)=+00;
Dr(:,13)=[00.000;00.000;00.000;00.00;00.00;00.00;00.000;-4.400;+0.500;00.00;00.00;00.00];vartor(13)=0; varax(13)=+00;
Dr(:,14)=[00.000;00.000;00.000;00.00;00.00;00.00;00.000;-0.600;-4.500;00.00;00.00;00.00];vartor(14)=0; varax(14)=+00;
Dr(:,15)=[00.000;00.000;00.000;00.00;00.00;00.00;00.000;+4.900;-0.600;00.00;00.00;00.00];vartor(15)=0; varax(15)=+00;
```

Loops

```
% This subroutine will contain the whole segmented loops
DefoPath; cycles=ad*Dr; nloop=size(cycles,2);
for loop=1:nloop
  Dv=cycles(:,loop); Dvartor=vartor(loop);Dvarax=varax(loop);
  Deflyi=[Deflyi Deflyi(loop)+cycles(1,loop)];Deflzi=[Deflzi Deflzi(loop)+cycles(3,loop)];
  Deflyj=[Deflyj Deflyj(loop)+cycles(2,loop)];Deflzj=[Deflzj Deflzj(loop)+cycles(4,loop)];
  Torsplot=[Torsplot Torsplot(loop)+vartor(loop)];Axialplot=[Axialplot Axialplot(loop)+varax(loop)];
  statusiold=statusi; statusjold=statusj; iprev=iold;iold=i+1;
  D1posold=max(D1posold,D1pos);D2posold=max(D2posold,D2pos);D3posold=max(D3posold,D3pos);
  D4posold=max(D4posold,D4pos);D5posold=max(D5posold,D5pos);D6posold=max(D6posold,D6pos);
  D1negold=max(D1negold,D1neg);D2negold=max(D2negold,D2neg);D3negold=max(D3negold,D3neg);
  D4negold=max(D4negold,D4neg);D5negold=max(D5negold,D5neg);D6negold=max(D6negold,D6neg);
  stagesold=stages;highactsold=highacts;MinShr=0;phism=0; loop
  ilp=0; LdUnld; Start
end
```

LdUnld

```
% Check status for end i
if highacti==0 & stagei==0 & loop>1
  n0i1x1=cycles(1,loop)*cycles(1,loop-1)+cycles(3,loop)*cycles(3,loop-1);
  if n0i1x1>=0; statusi=1;
    if loop>2; status=statusi*statusiold; end
  else statusi=-1;
    if loop>2; statusi=statusi*statusiold; end
    message=sprintf(' Note... Unloading in joint i, in the elastic range; Loop No. %d and statusi is %d', loop,statusi)
    InitUnldi; PlasFlex; stagei=0;stages=0;highacts=0;
  end
end
if highacti==1 & stagei==1 & loop>1
  n1i6x1=[n1i(1);0;n1i(2);0;n1i(3);n1i(4)]; FKelasDeg=inv(inv(FKelas)+FLple1i+FLple1j);
  if n1i6x1'*FKelasDeg*cycles(:,loop) >= 0; statusi=1;
    if loop>2; statusi=statusi*statusiold; end
  else statusi=-1;
    if loop>2; statusi=statusi*statusiold; end
     message=sprintf(' Note... Unloading in joint i, n1i'*DS1i is negative; Loop No. %d and statusi is %d', loop,statusi)
    InitUnldi; PlasFlex; stagei=0;stages=0;highacts=0;
  end
end
if highacti==2 & stagei==2 & loop>1;
n2i6x1=[n2i(1);0;n2i(2);0;n2i(3);n2i(4)];FKelasDeg=inv(inv(FKelas)+FLple1i+FLple2i+FLple1j+FLple2j);
  if n2i6x1'*FKelasDeg*cycles(:,loop) >= 0; statusi=1;
    if loop>2; statusi=statusi*statusiold; end
  else statusi=-1;
    if loop>2; statusi=statusi*statusiold; end
     message=sprintf(' Note... Unloading in joint i, n2i'*DS2i is negative; Loop No. %d and statusi is %d', loop,statusi)
    InitUnldi; PlasFlex; stagei=0;stages=0;highacts=0;
```

```
  end
end
if highacti==3 & stagei==3 & loop>1
n3i6x1=[n3i(1);0;n3i(2);0;n3i(3);n3i(4)];FKelasDeg=inv(inv(FKelas)+FLple1i+FLple2i+FLple3i+FLple1j+FLple2j+FLple3j);
  if n3i6x1'*FKelasDeg*cycles(:,loop) >= 0; statusi=1;
    if loop>2; statusi=statusi*statusiold; end
  else statusi=-1;
    if loop>2; statusi=statusi*statusiold; end
    message=sprintf(' Note... Unloading in joint i, n3i'*DS3i is negative; Loop No. %d and statusi is %d', loop,statusi)
    InitUnldi; PlasFlex; stagei=0;stages=0;highacts=0;
  end
end
% Check status for end j
(similar to end i)
```

InitUnldi

```
degFlag1i=0;degFlag2i=0;degFlag3i=0; D1max=v(1);D3max=v(3); dD1maxold=dD1max;dD3maxold=dD3max;
if loop>1
  D1pos=max(v1loop(iprev:iold,loop-1));D1neg=min(v1loop(iprev:iold,loop-1));dD1max=D1pos-D1neg;
  D3pos=max(v3loop(iprev:iold,loop-1));D3neg=min(v3loop(iprev:iold,loop-1));dD3max=D3pos-D3neg;
  D5pos=max(v5loop(iprev:iold,loop-1));D5neg=min(v5loop(iprev:iold,loop-1));
  D6pos=max(v6loop(iprev:iold,loop-1));D6neg=min(v6loop(iprev:iold,loop-1));
  D1posabs=max(v1);D1negabs=min(v1);dD1maxabs=D1posabs-D1negabs;
  D3posabs=max(v3);D3negabs=min(v3);dD3maxabs=D3posabs-D3negabs;
  D5posabs=max(v5);D5negabs=min(v5);dD5maxabs=D5posabs-D5negabs;
  D6posabs=max(v6);D6negabs=min(v6);dD6maxabs=D6posabs-D6negabs;
  S1pos=max(S1(find(v1==max(v1))));S1neg=min(S1(find(v1==min(v1))));dS1max=S1pos-S1neg;
  S3pos=max(S3(find(v3==max(v3))));S3neg=min(S3(find(v3==min(v3))));dS3max=S3pos-S3neg;
  S5pos=max(S5(find(v5==max(v5))));S5neg=min(S5(find(v5==min(v5))));
  S6pos=max(S6(find(v6==max(v6))));S6neg=min(S6(find(v6==min(v6))));
end
```

```
if highacti==0
  dcryi=0;dyldyi=0;dultyi=0; dyld_dcryi=0;dult_dyldyi=0;dmax_dultyi=0;
  dcrzi=0;dyldzi=0;dultzi=0; dyld_dcrzi=0;dult_dyldzi=0;dmax_dultzi=0;
elseif highacti==1
  dyldyi=0;dultyi=0; dyld_dcryi=abs(abs(dD1max)-dcryi);dult_dyldyi=0;dmax_dultyi=0;
  dyldzi=0;dultzi=0; dyld_dcrzi=abs(abs(dD3max)-dcrzi);dult_dyldzi=0;dmax_dultzi=0;
elseif highacti==2
  dultyi=0; dyld_dcryi=dyldyi-dcryi;dult_dyldyi=abs(abs(dD1max)-dyldyi);dmax_dultyi=0;
  dultzi=0; dyld_dcrzi=dyldzi-dcrzi;dult_dyldzi=abs(abs(dD3max)-dyldzi);dmax_dultzi=0;
elseif highacti==3;
  dyld_dcryi=dyldyi-dcryi;dult_dyldyi=dultyi-dyldyi;dmax_dultyi=abs(abs(dD1max)-dultyi);
  dyld_dcrzi=dyldzi-dcrzi;dult_dyldzi=dultzi-dyldzi;dmax_dultzi=abs(abs(dD3max)-dultzi);
end
dcryiold=dcryi;dyldyiold=dyldyi;dultyiold=dultyi; sumdefoyi=dyld_dcryi+dult_dyldyi+dmax_dultyi;
dcrziold=dcrzi;dyldziold=dyldzi;dultziold=dultzi; sumdefozi=dyld_dcrzi+dult_dyldzi+dmax_dultzi;
if highacti>0
  if dS1max~=0 & sumdefoyi~=0
    FLple1in(1,1)=DegFacy*(dyld_dcryi/sumdefoyi)*(dD1maxabs/dS1max) ;
    FLple2in(1,1)=DegFacy*(dult_dyldyi/sumdefoyi)*(dD1maxabs/dS1max) ;
    FLple3in(1,1)=DegFacy*(dmax_dultyi/sumdefoyi)*(dD1maxabs/dS1max) ;
  else FLple1in(1,1)=0;FLple2in(1,1)=0;FLple3in(1,1)=0;
  end
  if dS3max~=0 & sumdefozi~=0
    FLple1in(3,3)=DegFacz*(dyld_dcrzi/sumdefozi)*(dD3maxabs/dS3max);
    FLple2in(3,3)=DegFacz*(dult_dyldzi/sumdefozi)*(dD3maxabs/dS3max);
    FLple3in(3,3)=DegFacz*(dmax_dultzi/sumdefozi)*(dD3maxabs/dS3max);
  else FLple1in(3,3)=0;FLple2in(3,3)=0;FLple3in(3,3)=0;
  end
  FLple1in(6,6)=0; FLple2in(6,6)=0; FLple3in(6,6)=0;
elseif highacti==0
  FLple1in(6,6)=0;FLple2in(6,6)=0;FLple3in(6,6)=0;
```

```
end
FLple1i=FLple1i+FLple1in; FLple2i=FLple2i+FLple2in; FLple3i=FLple3i+FLple3in;
highacti=0;stagei=0; phi1i=0;phi2i=0;phi3i=0; n1i=[0;0;0;0];n2i=[0;0;0;0];n3i=[0;0;0;0];
DS1i=[0;0;0;0];DS2i=[0;0;0;0];DS3i=[0;0;0;0]; KEVTi=0; KEVTs=0;highacts=0;stages=0;iv=0;is=0;
FLpls=[0;0;0;0;0;0]*[0 0 0 0 0 0]; FLplsp=[0;0;0;0;0;0]*[0 0 0 0 0 0];
Pnchngstateold=Pnchngstate;Pnchngevntold=Pnchngevnt;Pnchngstate=0;Pnchngevnt=0;
if stagesold==1
  if dD1max~=0; if dS1max~=0;SFelas(1,1)=DegFacsy*(dD1maxabs/dS1max);end; end
  if dD3max~=0; if dS3max~=0;SFelas(3,3)=DegFacsz*(dD3maxabs/dS3max);end; end
end
ip=0;
```

PlasFlex

```
% Calculation of the flexure flexibility of each subhinge, for end i
if highacti==0; FLpli=FLple1i;
elseif highacti==1; g1i=n1i/sqrt(n1i'*Ksplp1i*n1i); u1i=[g1i(1);0;g1i(2);0;g1i(3);g1i(4)]; FLplp1i=u1i*u1i';
  FLpli=FLplp1i+FLple1i+FLple2i;
elseif highacti==2; g1i=n1i/sqrt(n1i'*Ksplp1i*n1i); u1i=[g1i(1);0;g1i(2);0;g1i(3);g1i(4)]; FLplp1i=u1i*u1i';
  g2i=n2i/sqrt(n2i'*Ksplp2i*n2i); u2i=[g2i(1);0;g2i(2);0;g2i(3);g2i(4)]; FLplp2i=u2i*u2i';
  FLpli=FLplp1i+FLplp2i+FLple1i+FLple2i+FLple3i;
elseif highacti==3; g1i=n1i/sqrt(n1i'*Ksplp1i*n1i); u1i=[g1i(1);0;g1i(2);0;g1i(3);g1i(4)]; FLplp1i=u1i*u1i';
  g2i=n2i/sqrt(n2i'*Ksplp2i*n2i); u2i=[g2i(1);0;g2i(2);0;g2i(3);g2i(4)]; FLplp2i=u2i*u2i';
  g3i=n3i/sqrt(n3i'*Ksplp3i*n3i); u3i=[g3i(1);0;g3i(2);0;g3i(3);g3i(4)]; FLplp3i=u3i*u3i';
  FLpli=FLplp1i+FLplp2i+FLplp3i+FLple1i+FLple2i+FLple3i;%new
end
% Calculation of the flexure flexibility of each subhinge, for end j
(similar to end i)
% Calculation of the shear flexibility:
if stages==1
  FLpls=1/L*[     1/Kvy          (1-Lfac)/Kvy     0          0      0 0;
             (1-Lfac)/Kvy        1/Kvy            0          0      0 0;
```

```
                0          0          1/Kvz   (1-Lfac)/Kvz    0   0;
                0          0    (1-Lfac)/Kvz      1/Kvz       0  0;
                0          0          0          0          0  0;
                0          0          0          0          0  0];
else FLpls=[0;0;0;0;0;0]*[0 0 0 0 0 0];
end
if Pnchngstate==1
  if dD1max~=0;FLplsp(1,1)=SFelas(1,1)/PnchngDeg;end; if dD2max~=0;FLplsp(2,2)=SFelas(2,2)/PnchngDeg;end
  if dD3max~=0;FLplsp(3,3)=SFelas(3,3)/PnchngDeg;end; if dD4max~=0;FLplsp(4,4)=SFelas(4,4)/PnchngDeg;end
else FLplsp=[0;0;0;0;0;0]*[0 0 0 0 0 0];
end
if Pnchngstateold==1
  if dD1max~=0;FLplse(1,1)=SFelas(1,1)/DegFacse;end; if dD2max~=0;FLplse(2,2)=SFelas(2,2)/DegFacse;end
  if dD3max~=0;FLplse(3,3)=SFelas(3,3)/DegFacse;end; if dD4max~=0;FLplse(4,4)=SFelas(4,4)/DegFacse;end
else FLplse=[0;0;0;0;0;0]*[0 0 0 0 0 0];
end
if Pnchngstate==0 & Pnchngstateold==1 & ip==0
  ip=1;  FLpli=FLpli/(DegFacsep);  FLplj=FLplj/(DegFacsep);
end
% Total plastic flexibility of all subhimges at both ends
FLpl=FLpli+FLplj+FLplsp+FLpls+FLplse;
```

Start

```
i=i+1; Flag=0; Ratio=1;Ratioindex=0;RATIOi=1;RATIOj=1;RATIO=1;
Scale=1;r=[1 1];rr=[1 1];sr=[1 1];FACMi=1;FACMj=1;FACs=1;srm=[1 1];FACsm=1;
Jumpi=0;FactoriJmp1=0;FactoriJmp2=0;FactoriJmp3=0; Jumpj=0;FactorjJmp1=0;FactorjJmp2=0;FactorjJmp3=0;
stageiold=stagei;stagejold=stagej; highactiold=highacti;highactjold=highactj;
Faczerosi=1;Faczerosj=1;Faczeros=1;Faczerov=1; Faczerosimat=[1 1 1 1];Faczerosjmat=[1 1 1 1];Faczerovmat=[1 1 1 1];
if ilp==1;Pnchngstateold=Pnchngstate;end
Shiold=Shi; Shjold=Shj; Sold=S;
alpha1iold=alpha1i;alpha2iold=alpha2i;alpha3iold=alpha3i; alpha1jold=alpha1j;alpha2jold=alpha2j;alpha3jold=alpha3j;
```

```
Dvold=Dv;vold=v;volds=vold; Dvartorold=Dvartor;Dvaraxold=Dvarax;
% Determination of the new stages for end i (case of iterartion)
if stagei==0 & highacti==1; stagei=1; end
if stagei==1 & highacti==2; stagei=2; end
if stagei==2 & highacti==3; stagei=3; end
% Determination of the new stages for end j (case of iterartion)
(similar to end i)
% Determination of the new stages for the shear hinge
if highacts==1; stages=1; end
if stages==1 & KEVTsm==1; MinShr=1; end
if Pnchngevnt==1; Pnchngstate=1;
elseif Pnchngevnt==0; Pnchngstate=0;
end
if iv==1 & volds(1)>=-err & volds(1)<=err; volds(1)=0;Pnchngevnt=0;Pnchngstate=0;Faczeros=1;Faczerov=1;iv=0;
  message=sprintf('... Shear pinshing ended at i = %d', i-1);
end
if iv==2 & volds(2)>=-err & volds(2)<=err; volds(2)=0;Pnchngevnt=0;Pnchngstate=0;Faczeros=1;Faczerov=1;iv=0;
  message=sprintf('... Shear pinshing ended at i = %d', i-1);
end
if iv==3 & volds(3)>=-err & volds(3)<=err; volds(3)=0;Pnchngevnt=0;Pnchngstate=0;Faczeros=1;Faczerov=1;iv=0;
  message=sprintf('... Shear pinshing ended at i = %d', i-1);
end
if iv==4 & volds(4)>=-err & volds(4)<=err; volds(4)=0;Pnchngevnt=0;Pnchngstate=0;Faczeros=1;Faczerov=1;iv=0;
  message=sprintf('... Shear pinshing ended at i = %d', i-1);
end
Stiff
if MinShr==0; FL=FK^-1;
elseif MinShr==1; FL=[1e8;1e8;1e8;1e8;1e8;1e8]*[1e8 1e8 1e8 1e8 1e8 1e8];
end
DS=FK*Dv;
bi=[1 0 0 0 0 0; 0 0 1 0 0 0; 0 0 0 0 1 0; 0 0 0 0 0 1]; bj=[0 1 0 0 0 0; 0 0 0 1 0 0; 0 0 0 0 1 0; 0 0 0 0 0 1];
```

```
DShi=bi*DS; DShj=bj*DS;    Vyprev=Vy; Vzprev=Vz; Pprev=P;    Shi=Shi+DShi; Shj=Shj+DShj;
DShi(3)=Dvartor;DShi(4)=Dvarax; DShj(3)=Dvartor;DShj(4)=Dvarax;
Shi(3)=Shi(3)+DShi(3);Shi(4)=Shi(4)+DShi(4); Shj(3)=Shj(3)+DShj(3);Shj(4)=Shj(4)+DShj(4);
Vy=(Shi(1)+Shj(1))/L*Lfac;dVy=(DShi(1)+DShj(1))/L*Lfac; Vz=(Shi(2)+Shj(2))/L*Lfac;dVz=(DShi(2)+DShj(2))/L*Lfac;
dP=Dvarax;P=Shiold(4)+dP;
if stages==1 & KEVTsm==0
  phis=(Vy/(Vfac*Vyf))^2+(Vz/(Vfac*Vzf))^2+((P-Pav)/Pult)^2;
  Vfac=sqrt(( ((Vyprev+dVy)/Vyf)^2+((Vzprev+dVz)/Vzf)^2 )/(1-((Pprev+dP-Pav)/Pult)^2));
else Vfac=1; KEVTs=0;is=0;
end
Shis=Shi;Shjs=Shj;Shiolds=Shiold;Shjolds=Shjold;Ss=S;
if stages==0 & MinShr==0
  Events
  SEvent
  Iterate
elseif stages==1 | MinShr==1
  if stages==1
    phism=(Vy/Vym)^2+(Vz/Vzm)^2+((P-Pav)/Pult)^2;
    if phism>(1+err); KEVTsm=0;FACsm=1;FACM=1;
    elseif phism>(1-err) & phism<(1+err); KEVTsm=1;FACsm=1;FACM=1;
    elseif phism<(1-err); KEVTsm=1;FactorSm;FACM=FACsm;KEVTsm=1;MinShr=1;
    end
  end
  if highacti==1;alpha1i=alpha1iold+(Shi-Shiold);end
  if highacti==2;alpha1i=alpha1iold+(Shi-Shiold);alpha2i=alpha2iold+(Shi-Shiold);end
  if highacti==3;alpha1i=alpha1iold+(Shi-Shiold);alpha2i=alpha2iold+(Shi-Shiold);alpha3i=alpha3iold+(Shi-Shiold);end
  if highactj==1;alpha1j=alpha1jold+(Shj-Shjold);end
  if highactj==2;alpha1j=alpha1jold+(Shj-Shjold);alpha2j=alpha2jold+(Shj-Shjold);end
  if highactj==3;alpha1j=alpha1jold+(Shj-Shjold);alpha2j=alpha2jold+(Shj-Shjold);alpha3j=alpha3jold+(Shj-Shjold);end
  Complement
end
```

Stiff

```
Plasflex
FK=((FKelas)^-1+SFelas+FLpl)^-1;
if MinShr==1
  FK=[0;0;0;0;0;0]*[0 0 0 0 0 0];
end
if det(FK)<0
  message='error....negative stiffness';
end
```

Events

```
% Determination of occurance of events in end i
if stagei==0
  Checkphi1i
  if phi1i>(1+err)
    highacti=1;KEVTi=1;Factori; Checkphi2i
    if phi2i>(1+err)
      FactoriJmp1=FACMi;highacti=2;Factori;Jumpi=1; Checkphi3i
      if phi3i>(1+err); FactoriJmp2=FACMi;highacti=3;Factori;Jumpi=2;
      elseif phi3i>=(1-err) & phi3i<=(1+err); highacti=3;FactoriJmp2=FACMi;Jumpi=2;
      elseif phi3i<=(1-err); highacti=2;
      end
    elseif phi2i>=(1-err) & phi2i<=(1+err)
      highacti=2;FactoriJmp1=FACMi;Jumpi=1; Checkphi3i
      if phi3i>(1+err); FactoriJmp1=FACMi;FactoriJmp2=FACMi;highacti=3;Factori;Jumpi=2;
      elseif phi3i>=(1-err) & phi3i<=(1+err); highacti=3;FactoriJmp2=FACMi;Jumpi=2;
      elseif phi3i<(1-err); highacti=2;
      end
    elseif phi2i<(1-err)
      highacti=1; Checkphi3i
```

```
    if phi3i>(1+err)
      phi2i=1;FactoriJmp1=FACMi;highacti=2;FactoriJmp;FactoriJmp2=FACMiJmp;highacti=3;Factori;Jumpi=2;
    elseif phi3i>=(1-err) & phi3i<=(1+err)
      phi2i=1;FactoriJmp1=FACMi;highacti=2;FactoriJmp;FactoriJmp2=FACMiJmp;highacti=3;Jumpi=2;
    elseif phi3i<(1-err); highacti=1;phi3i=0;
    end
  end
elseif phi1i>=(1-err) & phi1i<=(1+err)
  FACMi=1;highacti=1;KEVTi=1; Checkphi2i
  if phi2i>(1+err)
    FactoriJmp1=FACMi;highacti=2;Factori;Jumpi=1; Checkphi3i
    if phi3i>(1+err); FactoriJmp2=FACMi;highacti=3;Factori;Jumpi=2;
    elseif phi3i>=(1-err) & phi3i<=(1+err); highacti=3;FactoriJmp2=FACMi;Jumpi=2;
    elseif phi3i<(1-err); highacti=2;
    end
  elseif phi2i>=(1-err) & phi2i<=(1+err)
    highacti=2;FactoriJmp1=FACMi;Jumpi=1; Checkphi3i
    if phi3i>(1+err); FactoriJmp1=FACMi;FactoriJmp2=FACMi;highacti=3;Factori;Jumpi=2;
    elseif phi3i>=(1-err) & phi3i<=(1+err); highacti=3;FactoriJmp2=FACMi;Jumpi=2;
    elseif phi3i<(1-err); highacti=2;
    end
  elseif phi2i<(1-err)
    highacti=1; Checkphi3i
    if phi3i>(1+err); FactoriJmp1=FACMi;highacti=2;FactoriJmp;FactoriJmp2=FACMiJmp;highacti=3;Factori;Jumpi=2;
    elseif phi3i>=(1-err)&Phi3i<=(1+err)
      FactoriJmp1=FACMi;highacti=2;FactoriJmp;FactoriJmp2=FACMiJmp;highacti=3;Jumpi=2;
    elseif phi3i<(1-err); highacti=1;phi3i=0;
    end
  end
elseif phi1i<(1-err)
  highacti=0;KEVTi=0;FACMi=1; Checkphi2i
```

```
    if phi2i>(1+err)
      highacti=1;FactoriJmp;FactoriJmp1=FACMiJmp;highacti=2;Factori;Jumpi=1; Checkphi3i
      if phi3i>(1+err); FactoriJmp2=FACMi;highacti=3;Factori;Jumpi=2;
      elseif phi3i>=(1-err) & phi3i<=(1+err); highacti=3;FactoriJmp2=FACMi;Jumpi=2;
      elseif phi3i<(1-err); highacti=2;
      end
    elseif phi2i>=(1-err) & phi2i<=(1+err)
      highacti=1;FactoriJmp;FactoriJmp1=FACMiJmp;highacti=2;FACMi=1;Jumpi=1; Checkphi3i
      if phi3i>(1+err); FactoriJmp2=FACMi;highacti=3;Factori;Jumpi=2;
      elseif phi3i>=(1-err) & phi3i<=(1+err); highacti=3;FactoriJmp2=FACMi;Jumpi=2;
      elseif phi3i<(1-err); highacti=2;
      end
    elseif phi2i<(1-err); highacti=0; Checkphi3i
      if phi3i>(1+err)
highacti=1;FactoriJmp;FactoriJmp1=FACMiJmp;highacti=2;FactoriJmp;FactoriJmp2=FACMiJmp;highacti=3;Factori;Jumpi=2;
      elseif phi3i>=(1-err) & phi3i<=(1+err)
highacti=1;FactoriJmp;FactoriJmp1=FACMiJmp;highacti=2;FactoriJmp;FactoriJmp2=FACMiJmp;highacti=3;FACMi=1;Jumpi=2;
      elseif phi3i<(1-err); highacti=0;
      end
    end
  end
end
if stagei==1
  ratio1i=(Shi(1)-alpha2i(1))/Muy2i; ratio2i=(Shi(2)-alpha2i(2))/Muz2i;
  ratio3i=(Shi(3)-alpha2i(3))/Mux2i; ratio4i=(Shi(4)-alpha2i(4))/Fu2i;
  phi2i=ratio1i^2 + ratio2i^2 + ratio3i^2 + ratio4i^2;
  if phi2i>(1+err); highacti=2;KEVTi=1;Factori; Checkphi3i
    if phi3i>(1+err); FactoriJmp3=FACMi;highacti=3;Factori;Jumpi=3;
    elseif phi3i>=(1-err) & phi3i<=(1+err); FactoriJmp3=FACMi;highacti=3;Jumpi=3;
    elseif phi3i<(1-err); highacti=2;
    end
```

```
  elseif phi2i>=(1-err) & phi2i<=(1+err)
    highacti=2;KEVTi=1;FACMi=1; Checkphi3i
    if phi3i>(1+err); FactoriJmp3=FACMi;highacti=3;Factori;Jumpi=3;
    elseif phi3i>=(1-err) & phi3i<=(1+err); FactoriJmp3=FACMi;highacti=3;FACMi=1;Jumpi=3;
    elseif phi3i<(1-err); highacti=2;
    end
  elseif phi2i<(1-err); highacti=1;KEVTi=0;FACMi=1;
    if phi3i>(1+err); highacti=2;FactoriJmp;FactoriJmp3=FACMiJmp;highacti=3;Factori;Jumpi=3;
    elseif phi3i>=(1-err) & phi3i<=(1+err)
      highacti=2;FactoriJmp;FactoriJmp3=FACMiJmp;highacti=3;FACMi=1;Jumpi=3;
    elseif phi3i<(1-err); highacti=1;
    end
  end
end
if stagei==2
  ratio1i=(Shi(1)-alpha3i(1))/Muy3i; ratio2i=(Shi(2)-alpha3i(2))/Muz3i;
  ratio3i=(Shi(3)-alpha3i(3))/Mux3i; ratio4i=(Shi(4)-alpha3i(4))/Fu3i;
  phi3i=ratio1i^2 + ratio2i^2 + ratio3i^2 + ratio4i^2;
  if phi3i>(1+err); highacti=3;KEVTi=1;Factori
  elseif phi3i>=(1-err) & phi3i<=(1+err); highacti=3;KEVTi=1;FACMi=1;
  elseif phi3i<(1-err); highacti=2;KEVTi=0;FACMi=1;
  end
end
if stagei==3
  FACMi=1; KEVTi=0;
end
% Determinations of occurance of events in end j
(similar to end i)

% SEvent
if highacts==0 & stages==0
```

```
  phis=(Vy/(Vfac*Vyf))^2+(Vz/(Vfac*Vzf))^2+((P-Pav)/Pult)^2;
    if phis>(1+err); KEVTs=1;FactorS
    elseif phis>(1-err) & phis<(1+err); KEVTs=1;FACs=1;
    elseif phis<(1-err); KEVTs=0;FACs=1;
    end
end
Shis=Shi;Shjs=Shj;Shiolds=Shiold;Shjolds=Shjold;Ss=S;
if Shrtrggr==1 & loop>1
    % Event of zero Moment and Shear:
  if Pnchngevnt==0;
    if dD1max~=0 & cycles(1,loop)~=0
      if sign(Shis(1))~=sign(Shiolds(1)) & DShi(1)~=0;Faczerosimat(1)=-Shiolds(1)/DShi(1);is=1;end
    end
    if dD3max~=0 & cycles(3,loop)~=0
      if sign(Shis(2))~=sign(Shiolds(2)) & DShi(2)~=0;Faczerosimat(2)=-Shiolds(2)/DShi(2);is=3;end
    end
    if Faczerosimat(1)==0;Faczerosimat(1)=2;end; if Faczerosimat(2)==0;Faczerosimat(2)=2;end
    if dD2max~=0 & cycles(2,loop)~=0
      if sign(Shjs(1))~=sign(Shjolds(1)) & DShj(1)~=0;Faczerosjmat(1)=-Shjolds(1)/DShj(1);is=2;end
    end
    if dD4max~=0 & cycles(4,loop)~=0
      if sign(Shjs(2))~=sign(Shjolds(2)) & DShj(2)~=0;Faczerosjmat(2)=-Shjolds(2)/DShj(2);is=4;end
    end
    if Faczerosjmat(1)==0;Faczersojmat(1)=2;end; if Faczerosjmat(2)==0;Faczersojmat(2)=2;end
        Faczeros=min([Faczerosimat,Faczerosjmat]);
  end
    % Event of zero deformation:
    if Pnchngevnt==1;
        if sign(volds(1))~=sign(vs(1)+Dv(1)) & Dv(1)~=0;Faczerovmat(1)=-volds(1)/Dv(1);iv=1;end
        if sign(volds(2))~=sign(vs(2)+Dv(2)) & Dv(2)~=0;Faczerovmat(2)=-volds(2)/Dv(2);iv=2;end
        if sign(volds(3))~=sign(vs(3)+Dv(3)) & Dv(3)~=0;Faczerovmat(3)=-volds(3)/Dv(3);iv=3;end
```

```
        if sign(volds(4))~=sign(vs(4)+Dv(4)) & Dv(4)~=0;Faczerovmat(4)=-volds(4)/Dv(4);iv=4;end
        if Faczerovmat(1)==0;Faczerovmat(1)=2;end; if Faczerovmat(2)==0;Faczerovmat(2)=2;end
        if Faczerovmat(3)==0;Faczerovmat(3)=2;end; if Faczerovmat(4)==0;Faczerovmat(4)=2;end
        Faczerov=min(Faczerovmat);
  end
end
```

FactorS

```
Vy=Vy-dVy; Vz=Vz-dVz; P=P-dP;
    coeff(1)=(dVy/Vyf)^2+(dVz/Vzf)^2+(dP/Pult)^2;
    coeff(2)=2*Vy*dVy/Vyf^2 + 2*Vz*dVz/Vzf^2+2*dP*(P-Pav)/Pult^2;
    coeff(3)=(Vy/Vyf)^2+(Vz/Vzf)^2+((P-Pav)/Pult)^2-1;
    sr=roots(coeff);
  if (coeff(2)^2-4*coeff(1)*coeff(3))<0
   messageerr='error...imagenary value for sr, shear subhinge'
    i
  end
  if sign(max(sr))>sign(min(sr)); FACs=max(sr); end
  if sign(max(sr))==sign(min(sr)) & sign(max(sr))>0
    if min(sr)>0 & min(sr)<(0+err) & max(sr)<(1+err); FACs=max(sr); else FACs=max(sr); end
  end
  if sign(max(sr))<0 & max(sr)>=(0-err) & max(sr)<=0
    FACs=max(sr); alpha1i=alpha1i-FACs*DShi; alpha2i=alpha2i-FACs*DShi; alpha3i=alpha3i-FACs*DShi; FACs=0;
  elseif sign(max(sr))<0 & max(sr)<(0-err); FACs=max(sr);
  end

  if sign(max(sr))<0 & max(sr)<(0-err)
    FACs=max(sr);
    messageerr=sprintf('... note: a slight movement was made with the percentage %0.5g at iteration %d', FACMi,i)
  end
  if FACs > (1+err)
```

```
    messageerr='error...factor of shear subhinge is >1'
    FACs
    FACs-1
    i
  end
```

Iterate

```
FACM=min([FACMi,FACMj,FACs,Faczeros,Faczerov]);%,FACsm]);
if FACM==FACs & FACs<1
  KEVTs=1;highacts=1;
  if sti==0; sti=sti+1;Shrtrggr=1;end
elseif FACM==Faczeros & Faczeros<1; Pnchngevnt=1;
elseif FACM==Faczerov & Faczerov<1; Pnchngevnt=0;
elseif FACM==min(FACMi,FACMj) & min(FACMi,FACMj)<1; KEVTs=0;highacts=0;
elseif FACM==1; KEVTi=0;KEVTj=0;KEVTs=0;
end
Shi=Shi-DShi+FACM*DShi; Shj=Shj-DShj+FACM*DShj;
Vy=(Shi(1)+Shj(1))/L*Lfac; Vz=(Shi(2)+Shj(2))/L*Lfac; P=Shi(4);
phis=(Vy/Vyf)^2+(Vz/Vzf)^2+((P-Pav)/Pult)^2;
if phis>(1-err) & phis<(1+err); phis=1; end
State
```

State

```
if stages==0
% Check the state of joint i
  if highacti==1
    phi1i=((Shi(1)-alpha1i(1))/Muy1i)^2 + ((Shi(2)-alpha1i(2))/Muz1i)^2 + ((Shi(3)-alpha1i(3))/Mux1i)^2 + ((Shi(4)-
alpha1i(4))/Fu1i)^2;
    if phi1i<(1-err); highacti=0;KEVTi=0;stagei=0;
    elseif phi1i>(1+err); highacti=1;KEVTi=1;stagei=1;
    elseif phi1i>=(1-err) & phi1i<=(1+err); highacti=1;KEVTi=1;stagei=0;phi1i=1;
```

```
    end
  elseif highacti==2
    phi2i=((Shi(1)-alpha2i(1))/Muy2i)^2 + ((Shi(2)-alpha2i(2))/Muz2i)^2 + ((Shi(3)-alpha2i(3))/Mux2i)^2 + ((Shi(4)-
alpha2i(4))/Fu2i)^2;
    if phi2i<(1-err); highacti=1;KEVTi=0;stagei=1;
    elseif phi2i>(1+err); highacti=2;KEVTi=1;stagei=2;
    elseif phi2i>=(1-err) & phi2i<=(1+err); highacti=2;KEVTi=1;stagei=1;phi1i=1;phi2i=1;
    end
  elseif highacti==3
    phi3i=((Shi(1)-alpha3i(1))/Muy3i)^2 + ((Shi(2)-alpha3i(2))/Muz3i)^2 + ((Shi(3)-alpha3i(3))/Mux3i)^2 + ((Shi(4)-
alpha3i(4))/Fu3i)^2;
    if phi3i<(1-err); highacti=2;KEVTi=0;stagei=2;
    elseif phi3i>(1+err); highacti=3;KEVTi=1;stagei=3;
    elseif phi3i>=(1-err) & phi3i<=(1+err); highacti=3;KEVTi=1;stagei=2;phi1i=1;phi2i=1;phi3i=1;
    end
  end
% Check the state of joint j
  (similar to end i)
if Jumpi==0 & Jumpj==0; Normals
else UpdateJump
end
elseif stages==1; Plasdefo; end
```

Normals

```
% Calculation of the normal vector n?i(4x1) at the active subhinges for hinge i
if highacti==1 & n1i==[0;0;0;0]
  phi1idash=[2*(Shi(1)-alpha1i(1))/Muy1i^2; 2*(Shi(2)-alpha1i(2))/Muz1i^2; 0*2*(Shi(3)-alpha1i(3))/Mux1i^2; 0*2*(Shi(4)-
alpha1i(4))/Fu1i^2];
  n1i=phi1idash/sqrt(phi1idash'*phi1idash); n2i=[0;0;0;0]; n3i=[0;0;0;0];
end
if highacti==2 & n2i==[0;0;0;0]
```

```
  phi2idash=[2*(Shi(1)-alpha2i(1))/Muy2i^2; 2*(Shi(2)-alpha2i(2))/Muz2i^2; 0*2*(Shi(3)-alpha2i(3))/Mux2i^2; 0*2*(Shi(4)-
alpha2i(4))/Fu2i^2];
  n2i=phi2idash/sqrt(phi2idash'*phi2idash); n3i=[0;0;0;0]; end
if highacti==3 & n3i==[0;0;0;0]
  phi3idash=[2*(Shi(1)-alpha3i(1))/Muy3i^2; 2*(Shi(2)-alpha3i(2))/Muz3i^2; 0*2*(Shi(3)-alpha3i(3))/Mux3i^2; 0*2*(Shi(4)-
alpha3i(4))/Fu3i^2];
  n3i=phi3idash/sqrt(phi3idash'*phi3idash);
end
% Calculation of the normal vector n?j(4x1) at the active subhinges for hinge j
(similar to end i)
Plasdefo
```

Plasdefo

```
PlasFlex
% Calculation of Dvpl :-
Dvpl = ((diag([1 1 1 1 1 1])+FLpl*FKelas)^-1)*FLpl*FKelas*FACM*Dv; % Till now, no need for this
if Jumpi==0 & Jumpj==0; Update
else UpdateJump
end
```

Update

```
% Calculate new origins for all subhinges, at end i
if stagei==0
  Dalpha1i=[0;0;0;0]; Dalpha2i=[0;0;0;0]; Dalpha3i=[0;0;0;0];
elseif stagei==1
  DS1i=Shi-Shiold; Su12i=diag([Muy2i/Muy1i Muz2i/Muz1i Mux2i/Mux1i Fu2i/Fu1i]);
  dummy=(Su12i-diag([1 1 1 1]))*(Shi-[0;0;Torque;Axial])-(Su12i*alpha1i-alpha2i);
  Dalpha1i=dummy*phi1idash'*DS1i/(phi1idash'*dummy); Dalpha1i(3)=Shi(3)-Shiold(3);Dalpha1i(4)=Shi(4)-Shiold(4);
  Dalpha2i=[0;0;0;0]; Dalpha3i=[0;0;0;0];
elseif stagei==2
  DS2i=Shi-Shiold; Su23i=diag([Muy3i/Muy2i Muz3i/Muz2i Mux3i/Mux2i Fu3i/Fu2i]);
```

```
  dummy=(Su23i-diag([1 1 1 1]))*(Shi-[0;0;Torque;Axial])-(Su23i*alpha2i-alpha3i);
  Dalpha2i=dummy*phi2idash'*DS2i/(phi2idash'*dummy); Dalpha2i(3)=Shi(3)-Shiold(3);Dalpha2i(4)=Shi(4)-Shiold(4);
  Dalpha1i=Dalpha2i; Dalpha3i=[0;0;0;0];
elseif stagei==3
  DS3i=Shi-Shiold; dummy=(Shi-[0;0;Torque;Axial])-alpha3i;
  Dalpha3i=dummy*phi3idash'*DS3i/(phi3idash'*dummy); Dalpha3i(3)=Shi(3)-Shiold(3);Dalpha3i(4)=Shi(4)-Shiold(4);
  Dalpha2i=Dalpha3i; Dalpha1i=Dalpha3i;
end
% Calculate new origins for all subhinges, at end j
(similar to end i)
% Updating the yield surfaces origins
alpha1i=alpha1i+Dalpha1i; alpha2i=alpha2i+Dalpha2i; alpha3i=alpha3i+Dalpha3i;
alpha1j=alpha1j+Dalpha1j; alpha2j=alpha2j+Dalpha2j; alpha3j=alpha3j+Dalpha3j;
% Updating the total plastic deformation vpl
vpl = vpl + Dvpl;
ScaleBacki
ScaleBackj
ScaleBackItr
ScaleBackStt
Vy=(Shi(1)+Shj(1))/L*Lfac; Vz=(Shi(2)+Shj(2))/L*Lfac; P=Shi(4);
if RATIO ~= 1
  phis=(Vy/(Vfac*Vyf))^2+(Vz/(Vfac*Vzf))^2+((P-Pav)/Pult)^2;
  if phis>(1+err); KEVTs=1;highacts=1; message=sprintf('... Shear failure at i = %d', i)
    if sti==0; sti=sti+1;Shrtrggr=1; end
  elseif phis>(1-err) & phis<(1+err); KEVTs=1;highacts=1;stages=0; message=sprintf('... Shear failure at i = %d', i)
    if sti==0; sti=sti+1;Shrtrggr=1; end
  elseif phis<(1-err); KEVTs=0;highacts=0;stages=0; FLpls=[0;0;0;0;0;0]*[0 0 0 0 0 0];
    if sti==1; sti=0;Shrtrggr=0;
    end
  end
  ChckShrtrggr
```

```
end
if Vfac>(1+err); Vfac=1; phis=(Vy/Vyf)^2+(Vz/Vzf)^2+((P-Pav)/Pult)^2; ShrSclBck; end
ChangeStiff
Complement
```

ScaleBacki

```
% Check the Yield Surface Tolerance for end i
if highacti==1
  phi1i=((Shi(1)-alpha1i(1))/Muy1i)^2 + ((Shi(2)-alpha1i(2))/Muz1i)^2 + ((Shi(3)-alpha1i(3))/Mux1i)^2 + ((Shi(4)-
alpha1i(4))/Fu1i)^2;
  if phi1i>=(1-err) & phi1i<=(1+err);  rr(1)=1;rr(2)=1;Scale=1;Ratio=1;RATIOi=1;phi1i=1; end
  if phi1i <(1-Tol-err); highacti=1; RatioTol=-Tol;
    az=FACM*DShi(1)-Dalpha1i(1);bz=Shiold(1)-alpha1iold(1);cz=FACM*DShi(2)-Dalpha1i(2);ez=Shiold(2)-alpha1iold(2);
    fz=FACM*DShi(3)-Dalpha1i(3);gz=Shiold(3)-alpha1iold(3);hz=FACM*DShi(4)-Dalpha1i(4);iz=Shiold(4)-alpha1iold(4);
    k=Muy1i;l=Muz1i;m=Mux1i;n=Fu1i; RatioSc; RATIOi=Ratio;
  end
  if phi1i >(1+Tol+err); highacti=1; RatioTol=Tol;
    az=FACM*DShi(1)-Dalpha1i(1);bz=Shiold(1)-alpha1iold(1);cz=FACM*DShi(2)-Dalpha1i(2);ez=Shiold(2)-alpha1iold(2);
    fz=FACM*DShi(3)-Dalpha1i(3);gz=Shiold(3)-alpha1iold(3);hz=FACM*DShi(4)-Dalpha1i(4);iz=Shiold(4)-alpha1iold(4);
    k=Muy1i;l=Muz1i;m=Mux1i;n=Fu1i; RatioSc; RATIOi=Ratio;
 end
end
if highacti==2
  phi2i=((Shi(1)-alpha2i(1))/Muy2i)^2 + ((Shi(2)-alpha2i(2))/Muz2i)^2 + ((Shi(3)-alpha2i(3))/Mux2i)^2 + ((Shi(4)-
alpha2i(4))/Fu2i)^2;
  if phi2i>=(1-err)&phi2i<=(1+err);rr(1)=1;rr(2)=1;Scale=1;Ratio=1;RATIOi=1;phi2i=1;alpha1i=alpha1iold+(Shi-Shiold);end
  if phi2i <(1-Tol-err); highacti=2; RatioTol=-Tol;
    az=FACM*DShi(1)-Dalpha2i(1);bz=Shiold(1)-alpha2iold(1);cz=FACM*DShi(2)-Dalpha2i(2);ez=Shiold(2)-alpha2iold(2);
    fz=FACM*DShi(3)-Dalpha2i(3);gz=Shiold(3)-alpha2iold(3);hz=FACM*DShi(4)-Dalpha2i(4);iz=Shiold(4)-alpha2iold(4);
    k=Muy2i;l=Muz2i;m=Mux2i;n=Fu2i; RatioSc; RATIOi=Ratio;
  end
```

```
  if phi2i >(1+Tol+err); highacti=2; RatioTol=Tol;
    az=FACM*DShi(1)-Dalpha2i(1);bz=Shiold(1)-alpha2iold(1);cz=FACM*DShi(2)-Dalpha2i(2);ez=Shiold(2)-alpha2iold(2);
    fz=FACM*DShi(3)-Dalpha2i(3);gz=Shiold(3)-alpha2iold(3);hz=FACM*DShi(4)-Dalpha2i(4);iz=Shiold(4)-alpha2iold(4);
    k=Muy2i;l=Muz2i;m=Mux2i;n=Fu2i; RatioSc; RATIOi=Ratio;
  end
end
if highacti==3
  phi3i=((Shi(1)-alpha3i(1))/Muy3i)^2 + ((Shi(2)-alpha3i(2))/Muz3i)^2 + ((Shi(3)-alphâ3i(3))/Mux3i)^2 + ((Shi(4)-
alpha3i(4))/Fu3i)^2;
  if phi3i>=(1-err) & phi3i<=(1+err); rr(1)=1;rr(2)=1;Scale=1;Ratio=1;RATIOi=1;phi3i=1;
    alpha1i=alpha1iold+(Shi-Shiold); alpha2i=alpha2iold+(Shi-Shiold);
  end
  if phi3i <(1-Tol-err); highacti=3; RatioTol=-Tol;
    az=FACM*DShi(1)-Dalpha3i(1);bz=Shiold(1)-alpha3iold(1);cz=FACM*DShi(2)-Dalpha3i(2);ez=Shiold(2)-alpha3iold(2);
    fz=FACM*DShi(3)-Dalpha3i(3);gz=Shiold(3)-alpha3iold(3);hz=FACM*DShi(4)-Dalpha3i(4);iz=Shiold(4)-alpha3iold(4);
    k=Muy3i;l=Muz3i;m=Mux3i;n=Fu3i; RatioSc; RATIOi=Ratio;
  end
  if phi3i >(1+Tol+err); highacti=3; RatioTol=Tol;
    az=FACM*DShi(1)-Dalpha3i(1);bz=Shiold(1)-alpha3iold(1);cz=FACM*DShi(2)-Dalpha3i(2);ez=Shiold(2)-alpha3iold(2);
    fz=FACM*DShi(3)-Dalpha3i(3);gz=Shiold(3)-alpha3iold(3);hz=FACM*DShi(4)-Dalpha3i(4);iz=Shiold(4)-alpha3iold(4);
    k=Muy3i;l=Muz3i;m=Mux3i;n=Fu3i; RatioSc; RATIOi=Ratio;
  end
end
```

ScaleBackItr

```
RATIO = min(RATIOi,RATIOj);
Shi=Shiold+RATIO*(Shi-Shiold);
Shj=Shjold+RATIO*(Shj-Shjold);
```

ScaleBackStt

```
% Check the Yield Surface Tolerance for end i
```

```
if highacti==1
  alpha1i=alpha1iold+RATIO*Dalpha1i;
  phi1i=((Shi(1)-alpha1i(1))/Muy1i)^2 + ((Shi(2)-alpha1i(2))/Muz1i)^2 + ((Shi(3)-alpha1i(3))/Mux1i)^2 + ((Shi(4)-
alpha1i(4))/Fu1i)^2;
  if phi1i>=(1-Tol-err) & phi1i<(1-err); highacti=1; RatioTol=0;
    az=Shi(1)-alpha1i(1);bz=az;cz=Shi(2)-alpha1i(2);ez=cz; fz=0;gz=Shi(3)-alpha1i(3);hz=0;iz=Shi(4)-alpha1i(4);
    k=Muy1i;l=Muz1i;m=Mux1i;n=Fu1i; RatioSc; Scale=Ratio;
    Shi(1)=Shi(1)+Scale*(Shi(1)-alpha1i(1)); Shi(2)=Shi(2)+Scale*(Shi(2)-alpha1i(2));
  end
  if phi1i>(1+err) & phi1i<=(1+Tol+err); highacti=1; RatioTol=0;
    az=Shi(1)-alpha1i(1);bz=0;cz=Shi(2)-alpha1i(2);ez=0; fz=0;gz=Shi(3)-alpha1i(3);hz=0;iz=Shi(4)-alpha1i(4);
    k=Muy1i;l=Muz1i;m=Mux1i;n=Fu1i; RatioSc; Scale=Ratio;
    Shi(1)=alpha1i(1)+Scale*(Shi(1)-alpha1i(1)); Shi(2)=alpha1i(2)+Scale*(Shi(2)-alpha1i(2));
  end
  phi1i=((Shi(1)-alpha1i(1))/Muy1i)^2 + ((Shi(2)-alpha1i(2))/Muz1i)^2 + ((Shi(3)-alpha1i(3))/Mux1i)^2 + ((Shi(4)-
alpha1i(4))/Fu1i)^2;
  if phi1i>=(1-err) & phi1i<=(1+err); phi1i=1;
  else message=sprintf('...note: a slight error1= %0.5g at iteration %d',phi1i-1,i)
  end
  phi2i=((Shi(1)-alpha2i(1))/Muy2i)^2 + ((Shi(2)-alpha2i(2))/Muz2i)^2 + ((Shi(3)-alpha2i(3))/Mux2i)^2 + ((Shi(4)-
alpha2i(4))/Fu2i)^2;
  if phi2i>=(1-err) & phi2i<=(1+err); highacti=2;phi2i=1;
  else highacti=1; n2i=[0;0;0;0];
  end
end
if highacti==2 ; alpha2i=alpha2iold+RATIO*Dalpha2i;
  phi2i=((Shi(1)-alpha2i(1))/Muy2i)^2 + ((Shi(2)-alpha2i(2))/Muz2i)^2 + ((Shi(3)-alpha2i(3))/Mux2i)^2 + ((Shi(4)-
alpha2i(4))/Fu2i)^2;
  if phi2i>=(1-Tol-err) & phi2i<(1-err); highacti=2;  RatioTol=0;
    az=Shi(1)-alpha2i(1);bz=az;cz=Shi(2)-alpha2i(2);ez=cz; fz=0;gz=Shi(3)-alpha2i(3);hz=0;iz=Shi(4)-alpha2i(4);
    k=Muy2i;l=Muz2i;m=Mux2i;n=Fu2i; RatioSc; Scale=Ratio;
```

```
    Shi(1)=Shi(1)+Scale*(Shi(1)-alpha2i(1)); Shi(2)=Shi(2)+Scale*(Shi(2)-alpha2i(2));
  end
  if phi2i>(1+err) & phi2i<=(1+Tol+err); highacti=2; RatioTol=0;
    az=Shi(1)-alpha2i(1);bz=0;cz=Shi(2)-alpha2i(2);ez=0; fz=0;gz=Shi(3)-alpha2i(3);hz=0;iz=Shi(4)-alpha2i(4);
    k=Muy2i;l=Muz2i;m=Mux2i;n=Fu2i; RatioSc; Scale=Ratio;
    Shi(1)=alpha2i(1)+Scale*(Shi(1)-alpha2i(1)); Shi(2)=alpha2i(2)+Scale*(Shi(2)-alpha2i(2));
  end
  alpha1i=alpha1iold+(Shi-Shiold);
  phi1i=((Shi(1)-alpha1i(1))/Muy1i)^2 + ((Shi(2)-alpha1i(2))/Muz1i)^2 + ((Shi(3)-alpha1i(3))/Mux1i)^2 + ((Shi(4)-
alpha1i(4))/Fu1i)^2;
  if phi1i>=(1-err) & phi1i<=(1+err); phi1i=1;
  else message=sprintf('...note: a slight error1= %0.5g at iteration %d',phi1i-1,i)
  end
  phi2i=((Shi(1)-alpha2i(1))/Muy2i)^2 + ((Shi(2)-alpha2i(2))/Muz2i)^2 + ((Shi(3)-alpha2i(3))/Mux2i)^2 + ((Shi(4)-
alpha2i(4))/Fu2i)^2;
  if phi2i>=(1-err) & phi2i<=(1+err); phi2i=1;
  else message=sprintf('...note: a slight error2= %0.5g at iteration %d',phi2i-1,i)
  end
  phi3i=((Shi(1)-alpha3i(1))/Muy3i)^2 + ((Shi(2)-alpha3i(2))/Muz3i)^2 + ((Shi(3)-alpha3i(3))/Mux3i)^2 + ((Shi(4)-
alpha3i(4))/Fu3i)^2;
  if phi3i>=(1-err) & phi3i<=(1+err); highacti=3;phi3i=1;
  else highacti=2; n3i=[0;0;0;0];
  end
end
if highacti==3; alpha3i=alpha3iold+RATIO*Dalpha3i;
  phi3i=((Shi(1)-alpha3i(1))/Muy3i)^2 + ((Shi(2)-alpha3i(2))/Muz3i)^2 + ((Shi(3)-alpha3i(3))/Mux3i)^2 + ((Shi(4)-
alpha3i(4))/Fu3i)^2;
  if phi3i>=(1-Tol-err) & phi3i<(1-err); highacti=3; RatioTol=0;
    az=Shi(1)-alpha3i(1);bz=az;cz=Shi(2)-alpha3i(2);ez=cz; fz=0;gz=Shi(3)-alpha3i(3);hz=0;iz=Shi(4)-alpha3i(4);
    k=Muy3i;l=Muz3i;m=Mux3i;n=Fu3i; RatioSc; Scale=Ratio;
    Shi(1)=Shi(1)+Scale*(Shi(1)-alpha3i(1)); Shi(2)=Shi(2)+Scale*(Shi(2)-alpha3i(2));
```

```
  end
  if phi3i>(1+err) & phi3i<=(1+Tol+err); highacti=3; RatioTol=0;
    az=Shi(1)-alpha3i(1);bz=0;cz=Shi(2)-alpha3i(2);ez=0; fz=0;gz=Shi(3)-alpha3i(3);hz=0;iz=Shi(4)-alpha3i(4);
    k=Muy3i;l=Muz3i;m=Mux3i;n=Fu3i; RatioSc; Scale=Ratio;
    Shi(1)=alpha3i(1)+Scale*(Shi(1)-alpha3i(1)); Shi(2)=alpha3i(2)+Scale*(Shi(2)-alpha3i(2));
  end
  alpha1i=alpha1iold+(Shi-Shiold);
  phi1i=((Shi(1)-alpha1i(1))/Muy1i)^2 + ((Shi(2)-alpha1i(2))/Muz1i)^2 + ((Shi(3)-alpha1i(3))/Mux1i)^2 + ((Shi(4)-
alpha1i(4))/Fu1i)^2;
  if phi1i>=(1-err) & phi1i<=(1+err); phi1i=1;
  else message=sprintf('...note: a slight error1= %0.5g at iteration %d',phi1i-1,i)
  end
  alpha2i=alpha2iold+(Shi-Shiold);
  phi2i=((Shi(1)-alpha2i(1))/Muy2i)^2 + ((Shi(2)-alpha2i(2))/Muz2i)^2 + ((Shi(3)-alpha2i(3))/Mux2i)^2 + ((Shi(4)-
alpha2i(4))/Fu2i)^2;
  if phi2i>=(1-err) & phi2i<=(1+err); phi2i=1;
  else message=sprintf('...note: a slight error2= %0.5g at iteration %d',phi2i-1,i)
  end
  phi3i=((Shi(1)-alpha3i(1))/Muy3i)^2 + ((Shi(2)-alpha3i(2))/Muz3i)^2 + ((Shi(3)-alpha3i(3))/Mux3i)^2 + ((Shi(4)-
alpha3i(4))/Fu3i)^2;
  if phi3i>=(1-err) & phi3i<=(1+err); phi3i=1;
  else message=sprintf('...note: a slight error3= %0.5g at iteration %d',phi3i-1,i)
  end
end
% Check the Yield Surface Tolerance for end j
```
(similar to end i)

ChckShrtrggr

```
Shis=Shi;Shjs=Shj;Shiolds=Shiold;Shjolds=Shjold;Ss=S;
if Shrtrggr==1 & loop>1
    % Event of zero Moment and Shear:
```

```
 if Pnchngevnt==1;
   if dD1max~=0 & is==1; if sign(Shis(1))==sign(Shiolds(1));Pnchngevnt=0;end;  end
   if dD3max~=0 & is==3; if sign(Shis(2))==sign(Shiolds(2));Pnchngevnt=0;end;  end
   if dD2max~=0 & is==2; if sign(Shjs(1))==sign(Shjolds(1));Pnchngevnt=0;end;  end
   if dD4max~=0 & is==4; if sign(Shjs(2))==sign(Shjolds(2));Pnchngevnt=0;end; end
 end
   % Event of zero deformation:
   if Pnchngevnt==0;
   if sign(volds(1))==sign(vs(1)+FACM*RATIO*Dv(1)) & iv==1;Pnchngevnt=1;end ;
       if sign(volds(2))==sign(vs(2)+FACM*RATIO*Dv(2)) & iv==2;Pnchngevnt=1;end
       if sign(volds(3))==sign(vs(3)+FACM*RATIO*Dv(3)) & iv==3;Pnchngevnt=1;end
       if sign(volds(4))==sign(vs(4)+FACM*RATIO*Dv(4)) & iv==4;Pnchngevnt=1;end
 end
end
```

ShrSclBck

```
iShrSclBck=i
if phis>(1+TolShr); ShearScale
  Vy=Vyprev+ScaleShr*dVy; Vz=Vzprev+ScaleShr*dVz; P=Pprev+ScaleShr*dP;
  FACM=ScaleShr*FACM; phis=(Vy/Vyf)^2+(Vz/Vzf)^2+((P-Pav)/Pult)^2;
end
if phis>1 & phis<=(1+TolShr+err); ScaleShr=sqrt(1/phis)
  Vy=ScaleShr*Vy; Vz=ScaleShr*Vz; P=Pav+ScaleShr*(P-Pav);
  ShiShrSc=Shi;ShjShrSc=Shj;
  Shi(1)=0.5*(Vy*L/Lfac);Shj(1)=0.5*(Vy*L/Lfac); Shi(2)=0.5*(Vz*L/Lfac);Shj(2)=0.5*(Vz*L/Lfac);
  Shi(4)=P;Shj(4)=P;
  alpha1i=alpha1i+(Shi-ShiShrSc);  alpha2i=alpha2i+(Shi-ShiShrSc); alpha3i=alpha3i+(Shi-ShiShrSc);
  alpha1j=alpha1j+(Shj-ShjShrSc);  alpha2j=alpha2j+(Shj-ShjShrSc); alpha3j=alpha3j+(Shj-ShjShrSc);
end
phis=(Vy/Vyf)^2+(Vz/Vzf)^2+((P-Pav)/Pult)^2
if phis>(1-err) & phis<(1+err); phis=1;end
```

ChangeStiff

```
% This subroutine is called from ScaleBack.m, in case of iteration needed. It is a combination of Normals.m & Plasdefo.m
% Calculation of the normal vector n?i(4x1) at the active subhinges for hinge i
if highacti==1
  phi1idash=[2*(Shi(1)-alpha1i(1))/Muy1i^2; 2*(Shi(2)-alpha1i(2))/Muz1i^2; 0*2*(Shi(3)-alpha1i(3))/Mux1i^2; 0*2*(Shi(4)-
alpha1i(4))/Fu1i^2]; n1i=phi1idash/sqrt(phi1idash'*phi1idash); n2i=[0;0;0;0]; n3i=[0;0;0;0];
elseif highacti==2
  phi1idash=[2*(Shi(1)-alpha1i(1))/Muy1i^2; 2*(Shi(2)-alpha1i(2))/Muz1i^2; 0*2*(Shi(3)-alpha1i(3))/Mux1i^2; 0*2*(Shi(4)-
alpha1i(4))/Fu1i^2]; n1i=phi1idash/sqrt(phi1idash'*phi1idash);
  phi2idash=[2*(Shi(1)-alpha2i(1))/Muy2i^2; 2*(Shi(2)-alpha2i(2))/Muz2i^2; 0*2*(Shi(3)-alpha2i(3))/Mux2i^2; 0*2*(Shi(4)-
alpha2i(4))/Fu2i^2]; n2i=phi2idash/sqrt(phi2idash'*phi2idash); n3i=[0;0;0;0];
elseif highacti==3
  phi1idash=[2*(Shi(1)-alpha1i(1))/Muy1i^2; 2*(Shi(2)-alpha1i(2))/Muz1i^2; 0*2*(Shi(3)-alpha1i(3))/Mux1i^2; 0*2*(Shi(4)-
alpha1i(4))/Fu1i^2]; n1i=phi1idash/sqrt(phi1idash'*phi1idash);
  phi2idash=[2*(Shi(1)-alpha2i(1))/Muy2i^2; 2*(Shi(2)-alpha2i(2))/Muz2i^2; 0*2*(Shi(3)-alpha2i(3))/Mux2i^2; 0*2*(Shi(4)-
alpha2i(4))/Fu2i^2]; n2i=phi2idash/sqrt(phi2idash'*phi2idash);
  phi3idash=[2*(Shi(1)-alpha3i(1))/Muy3i^2; 2*(Shi(2)-alpha3i(2))/Muz3i^2; 0*2*(Shi(3)-alpha3i(3))/Mux3i^2; 0*2*(Shi(4)-
alpha3i(4))/Fu3i^2]; n3i=phi3idash/sqrt(phi3idash'*phi3idash);
end
% Calculation of the normal vector n?j(4x1) at the active subhinges for hinge j
(similar to end i)
PlasFlex
% Calculation of Dvpl :-
Dvpl = ((diag([1 1 1 1 1 1])+FLpl*FKelas)^-1)*FLpl*FKelas*FACM*Dv;
```

Complement

```
% Calculation of the complement of the displacement Dv
SSS=1-FACM*RATIO; Deltav=FACM*RATIO*Dv; Dv=SSS*Dv; Dvartor=SSS*Dvartor;Dvarax=SSS*Dvarax;
if highacts==1 & Vfac<1 & MinShr==0; Vyf=FACM*RATIO*Vfac*Vyf; Vzf=FACM*RATIO*Vfac*Vzf;
elseif highacts==1 & MinShr==1; Vyf=Vym; Vzf=Vzm;
```

```
end
if SSS ~= 0; Resp; Start
elseif SSS==0; Resp
end
```

Resp

```
S=[Shi(1); Shj(1); Shi(2); Shj(2); 0.5*(Shi(3)+Shj(3)); 0.5*(Shi(4)+Shj(4))];
Vy=(S(1)+S(2))/L*Lfac; Vz=(S(3)+S(4))/L*Lfac; P=S(6);
Shis=Shi;Shjs=Shj;Ss=S;
for counter=1:4
  if Shis(counter)>=-err & Shis(counter)<=err; Shis(counter)=0;end;
  if Shjs(counter)>=-err & Shjs(counter)<=err; Shjs(counter)=0;end
  if Ss(counter)>=-err & Ss(counter)<=err; Ss(counter)=0;end
  if Pnchngstate==1 & Scale~=1
  if Shis(counter)>=-Tol & Shis(counter)<=Tol; Shis(counter)=0;end
  if Shjs(counter)>=-Tol & Shjs(counter)<=Tol; Shjs(counter)=0;end
  if Ss(counter)>=-Tol & Ss(counter)<=Tol; Ss(counter)=0;end
  end
end
R=ad'*S; v=v+Deltav; vs=v;
if Pnchngevnt==1 & Pnchngstate==1
  if vs(1)>=-err & vs(1)<=+err & Dvold(1)~=0;iv=1;end; if vs(2)>=-err & vs(2)<=+err & Dvold(2)~=0;iv=2;end
  if vs(3)>=-err & vs(3)<=+err & Dvold(3)~=0;iv=3;end; if vs(4)>=-err & vs(4)<=+err & Dvold(4)~=0;iv=4;end
end
v1=[v1 v(1)]; v2=[v2 v(2)]; v3=[v3 v(3)]; v4=[v4 v(4)]; v5=[v5 v(5)]; v6=[v6 v(6)];
S1=[S1 S(1)]; S2=[S2 S(2)]; S3=[S3 S(3)]; S4=[S4 S(4)]; S5=[S5 S(5)]; S6=[S6 S(6)];
DegPara
v1loop(iold:i,loop)=v1(iold:i)';v1loop(i+1,loop)=v1(i+1); v2loop(iold:i,loop)=v2(iold:i)';v2loop(i+1,loop)=v2(i+1);
v3loop(iold:i,loop)=v3(iold:i)';v3loop(i+1,loop)=v3(i+1); v4loop(iold:i,loop)=v4(iold:i)';v4loop(i+1,loop)=v4(i+1);
v5loop(iold:i,loop)=v5(iold:i)';v5loop(i+1,loop)=v5(i+1); v6loop(iold:i,loop)=v6(iold:i)';v6loop(i+1,loop)=v6(i+1);
if sti==1 & Shrtrggr==1; message=sprintf('... Shear Trigger = 1 at i = %d', i)
```

```
  sti=sti+1;
end
if Pnchngstateold==0 & Pnchngstate==1; message=sprintf('... Shear pinshing started at i = %d', i)
elseif Pnchngstateold==1 & Pnchngstate==0; message=sprintf('... Shear pinshing ended at i = %d', i)
end
ilp=1;
if Lfac==0.5
  if abs(Shi(1)-Shj(1))<=err | abs(Shi(2)-Shj(2))<=err |abs(Shi(3)-Shj(3))<=err | abs(Shi(4)-Shj(4))<=err; Shj=Shi;end
  if abs(alpha1i(1)-alpha1j(1))<=err | abs(alpha1i(2)-alpha1j(2))<=err | abs(alpha1i(3)-alpha1j(3))<=err | abs(alpha1i(4)-
  alpha1j(4))<=err; alpha1j=alpha1i; end
  if abs(alpha2i(1)-alpha2j(1))<=err | abs(alpha2i(2)-alpha2j(2))<=err | abs(alpha2i(3)-alpha2j(3))<=err | abs(alpha2i(4)-
  alpha2j(4))<=err; alpha2j=alpha2i; end
  if abs(alpha3i(1)-alpha3j(1))<=err | abs(alpha3i(2)-alpha3j(2))<=err | abs(alpha3i(3)-alpha3j(3))<=err | abs(alpha3i(4)-
  alpha3j(4))<=err; alpha3j=alpha3i; end
end
```

Outputs

DegPara

```
% For joint i
if degFlag1i==0 & highactiold==0 & highacti==1; dcryi=abs(v(1)-D1max); dcrzi=abs(v(3)-D3max); degFlag1i=1; end
if degFlag2i==0 & highactiold==1 & highacti==2; dyldyi=abs(v(1)-D1max); dyldzi=abs(v(3)-D3max); degFlag2i=1; end
if degFlag3i==0 & highactiold==2 & highacti==3; dultyi=abs(v(1)-D1max);  dultzi=abs(v(3)-D3max);  degFlag3i=1; end
if degFlag1i==0 & highactiold==0 & highacti==2; dcryi=abs(v(1)-D1max); dcrzi=abs(v(3)-D3max); dyldyi=abs(v(1)-
D1max); dyldzi=abs(v(3)-D3max); degFlag1i=1; degFlag2i=1; end
if degFlag1i==0 & highactiold==0 & highacti==3; dcryi=abs(v(1)-D1max); dcrzi=abs(v(3)-D3max); dyldyi=abs(v(1)-
D1max); dyldzi=abs(v(3)-D3max); dultyi=abs(v(1)-D1max); dultzi=abs(v(3)-D3max); degFlag1i=1; degFlag2i=1;
degFlag3i=1; end
if degFlag2i==0 & highactiold==1 & highacti==3; dyldyi=abs(v(1)-D1max); dyldzi=abs(v(3)-D3max); dultyi=abs(v(1)-
D1max); dultzi=abs(v(3)-D3max); degFlag2i=1; degFlag3i=1; end
% For joint j
```

(similar to end i)

APPENDIX D

SHEAR STRENGTH AND CONFINEMENT MODEL FOR ANCHORED CFRP WRAPS

Wrapping RC columns with CFRP sheets provides both confinement to the concrete and additional shear resistance mechanism. The column's total shear resistance can be written as the sum of various components as:

$$V_n = V_c + V_s + V_p + V_{FRP} \tag{D.1}$$

where V_n = nominal shear strength;

V_c = shear strength from concrete mechanism;

V_s = shear strength from steel mechanism;

V_p = shear strength from axial force mechanism; and

V_{FRP} = shear strength from the CFRP mechanism.

In order to calculate the confinement effectiveness for rectangular concrete sections confined by rectangular ties in addition to anchored CFRP wraps, an approach analogous to Mander et al. (1988) model was adopted.

Figure D.1 shows the effectively confined core for sections with rectangular hoop reinforcement and external anchored FRP wraps. In this figure, arching action is assumed to occur vertically between levels of transverse hoop bars and horizontally between levels of longitudinal bars. Thus, the effectively confined area of concrete at hoop level will be the total area enclosed by the CFRP wraps less the areas of the parabolas containing the ineffectively confined concrete.

The ineffective area for one parabola is $(w_i')^2/6$ where w_i' is the ith clear distance between adjacent longitudinal bars. Thus, the total plan area of ineffectively confined concrete at the level of the ties when there are n longitudinal bars is

$$A_i = \sum_{i=1}^{n} \frac{(w_i)^2}{6} \tag{D.2}$$

Considering the influence of the ineffective areas in the elevation, the area of effectively confined concrete core at midway between levels of transverse ties reinforcement and FRP anchors is

$$A_e = (bd - A_i)\left(1 - \frac{s_x}{2b}\right)\left(1 - \frac{s_y}{2d}\right) \tag{D.3}$$

where s_x and s_y are the least of transverse hoop reinforcement and FRP anchors spacing in x and y directions, respectively.

The confinement effectiveness coefficient, K_e, for rectangular ties similar to that defined by Mander et al. (1988) is used

Where $K_e = \dfrac{A_e}{A_{cc}}$ and $A_{cc} = A_c(1 - \rho_{cc})$

Such that A_e = area of effectively confined concrete core;

A_c = area of concrete section enclosed by the CFRP wraps; and

ρ_{cc} = ratio of area of longitudinal reinforcement to area of concrete section.

Therefore $$K_e = \frac{A_e/bd}{\left(1 - \dfrac{A_s}{bd}\right)} \tag{D.4}$$

where A_s = total area of longitudinal reinforcement.

In case of fibre wrapped RC columns, lateral confinement is provided by two different materials, transverse steel ties and anchored CFRP. Moreover, it is possible for rectangular reinforced concrete members to have different quantities of transverse confining steel in the x and y directions. An equivalent transformed confinement content in both directions can be estimated as:

$$\rho_x = \frac{A_{sx}}{sd_c} + \frac{t_{fx}}{d} \cdot \frac{f_{yf}}{f_{yh}} \tag{D.5a}$$

and

$$\rho_y = \frac{A_{sy}}{sb_c} + \frac{t_{fy}}{b} \cdot \frac{f_{yf}}{f_{yh}} \tag{D.5b}$$

where A_{sx} and A_{sy} = the total area of transverse bars running in the x and y directions, respectively (see figure D.1);

t_{fx} and t_{fy} = CFRP design thickness in x and y directions, respectively;

f_{yf} = design tensile strength of CFRP; and

f_{yh} = yield strength of transverse reinforcement.

Therefore, the total lateral confining stress on the concrete (total transformed confinement content multiplied by transverse steel yield strength) is given in the x and y directions as:

$$f_{lx} = \rho_x f_{yh} \tag{D.6a}$$

$$f_{ly} = \rho_y f_{yh} \tag{D.6b}$$

In order to allow for the fact that $A_e < A_{cc}$, it is considered that the effective lateral confining pressure in x and y directions are:

$$f'_{lx} = K_e f_{lx} \tag{D.7a}$$

$$f'_{ly} = K_e f_{ly} \tag{D.7b}$$

To determine the confined concrete compressive strength f'_{cc}, a simplified constitutive model, which is based on the "five-parameter" multi-axial failure surface described by William and Wranke (1975) and used by Mander et al. (1988), was adopted. Figure D.2 shows the confined strength ratio determination from the two lateral confining stresses of rectangular sections.

Therefore $f'_{cc} = K'_{cc} f'_{co}$ (D.8)

Where K'_{cc} = confined strength ratio from figure D.2; and

f'_{co} = unconfined concrete compressive strength.

Now, the shear strength from the concrete mechanism V_c, can be calculated as follows:

$$V_c = K_c \sqrt{f'_{cc}} A_e \qquad \text{MPa} \tag{D.9}$$

Where K_c is the displacement ductility-concrete shear resistance reduction factor such that: $K_c = 0.3 - 0.08\left(\frac{f'_{cc}}{f'_{co}}\right)(\mu - 1) \geq 0.05$ (D.10)

where μ is the displacement ductility factor.

K_c is introduced to account for the reduced shear capacity from concrete mechanism when increasing the displacement ductility level. This concept was first introduced and verified by Priestley at al. (1991). The current formulation assumes that the rate of the reduction in concrete shear strength is directly proportional to the confinement strength ratio K'_{cc} as shown in figure D.3.

The shear strength from steel mechanism V_s in x and y directions is equal to:

$$V_{sx} = \frac{A_{sx} f_{yh} d_c}{s} \tag{D.11a}$$

$$V_{sy} = \frac{A_{sy} f_{yh} b_c}{s} \tag{D.11b}$$

The steel mechanism contribution to the shear strength is stipulated that the tie spacing is less than the column's depth.

The shear strength from axial force mechanism V_p in x and y directions can be calculated as follows:

$$V_{px} = K_p \frac{P b/2}{H} \tag{D.12a}$$

$$V_{py} = K_p \frac{P d/2}{H} \tag{D.12b}$$

where P is the axial force on the column;

H is the column height; and

K_p is a displacement ductility-axial force shear resistance reduction factor such that: $K_p = 1 - 0.25(\mu - 1) \geq 0$ (D.13)

Figure D.4 shows the compression strut in a fixed-fixed column where the strut is assumed to be the hypotenuse of a triangle with the column height is one side and half the section depth is the other side of the triangle. The assumption of a compression zone equal to half the column depth at the critical section was also adopted by Watanabe and Ichinose (1991). K_p was introduced to account for the reduced contribution from the

axial force mechanism when increasing the displacement ductility levels which results in the reduction of the inclination –thus the contribution– of the compression strut.

Note that V_p should be taken by half the aforementioned values for a cantilever column.

The shear strength from FRP mechanism V_{FRP} in x and y directions can be calculated as follows:

$$V_{FRPx} = 2t_{fx} f_{yf} b \tag{D.14a}$$

$$V_{FRPy} = 2t_{fy} f_{yf} d \tag{D.14b}$$

Taking t_f and f_{yf} as provided by the supplier may ignore the reduction in the tensile capacity of FRP wraps due to the resin impregnation. Thus, it is recommended to use the results of tensile coupon test. In this case, $t_{fx} f_{yf}$ will be equal to the force per unit width of a coupon test with the same number of fibre layers that was used to wrap the specimen.

Figure D.5 along with Table D.1 contain the parameters and values used to calculate the confinement effectiveness for the three tested specimens using the aforementioned methodology. Table 6.1 shows the calculated and measured yield and ultimate lateral load for the three specimens.

Table D.1 Parameters used to calculate the confinement effectiveness for the three tested specimens

Specimen	A_i	A_e	K_e	$\rho_x=\rho_y$	$f_{lx}=f_{ly}$	$f'_{lx}=f'_{ly}$	f'_{co}	$\frac{f'_{lx}}{f'_{co}}=\frac{f'_{ly}}{f'_{co}}$	$\frac{f'_{cc}}{f'_{co}}$	f'_{cc}
	mm^2	mm^2			MPa		MPa			MPa
SC1	15265	41850	0.642	0.0118	4.70	3.01	39	0.077	1.39	54
SC2	15265	64370	0.710	0.0255	10.73	7.62	39	0.195	1.98	77
SC3	15265	20735	0.229	0.0162	6.82	1.56	39	0.04	1.20	47

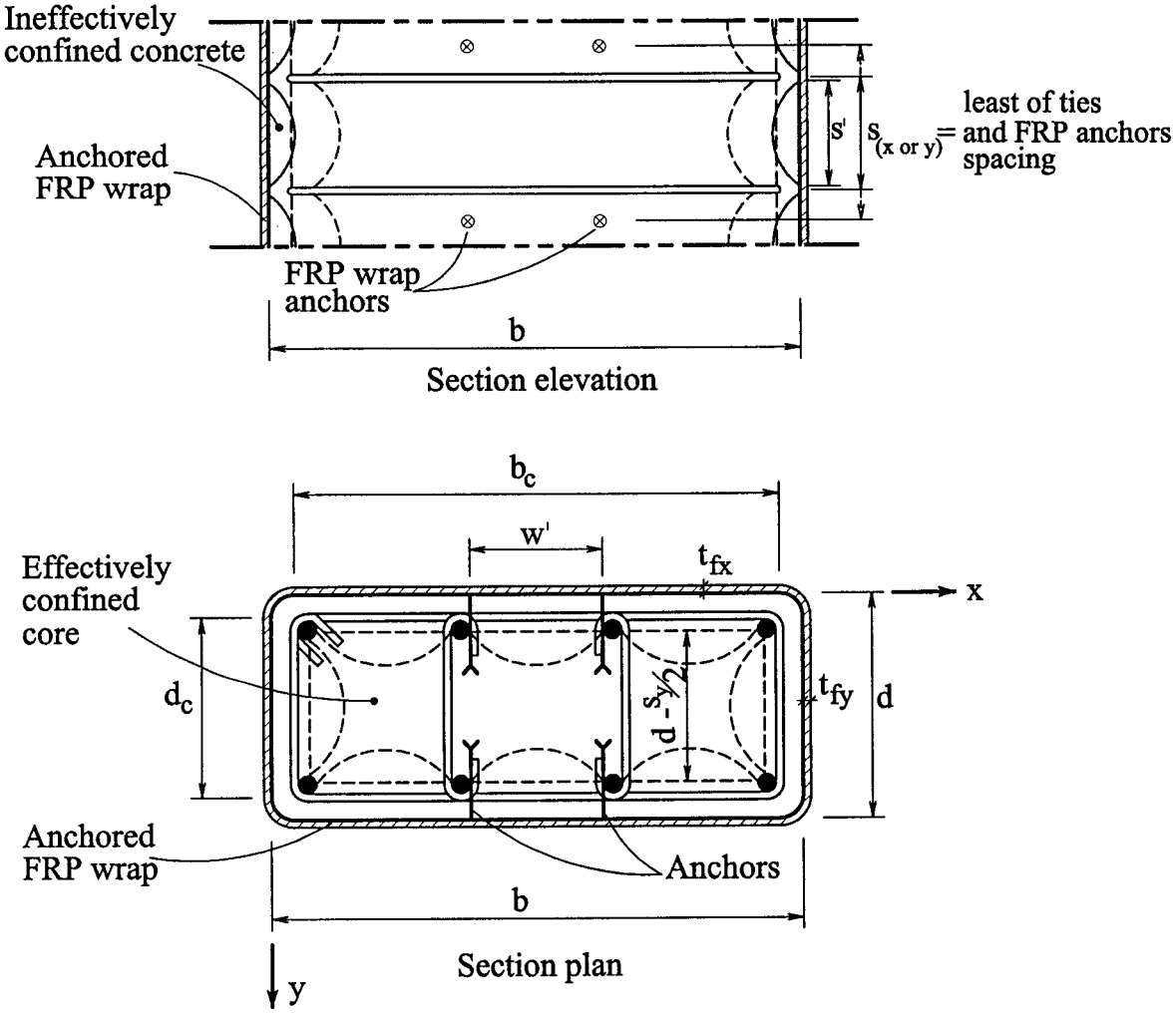

Figure D.1 Effectively confined core for sections with rectangular hoop reinforcement and anchored FRP wraps

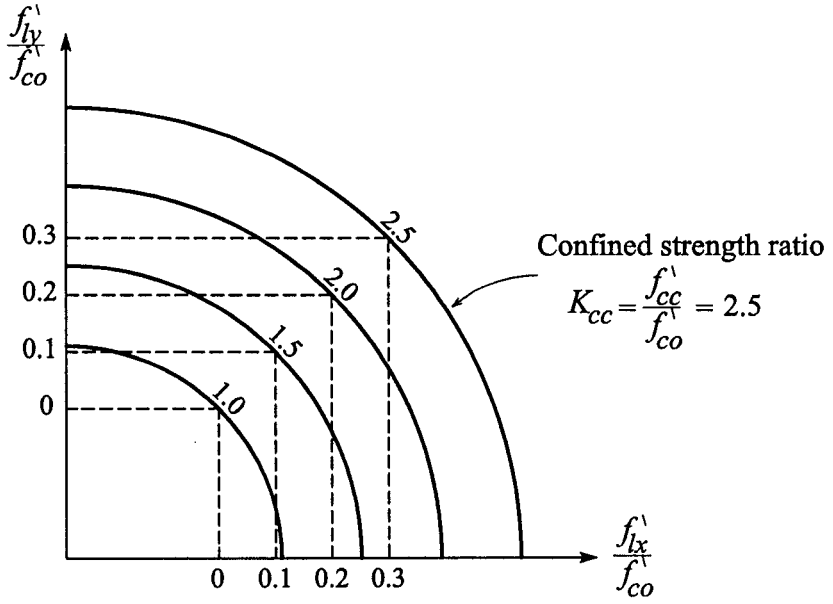

Figure D.2 Confined strength ratio determination from the two lateral confining stresses of rectangular sections

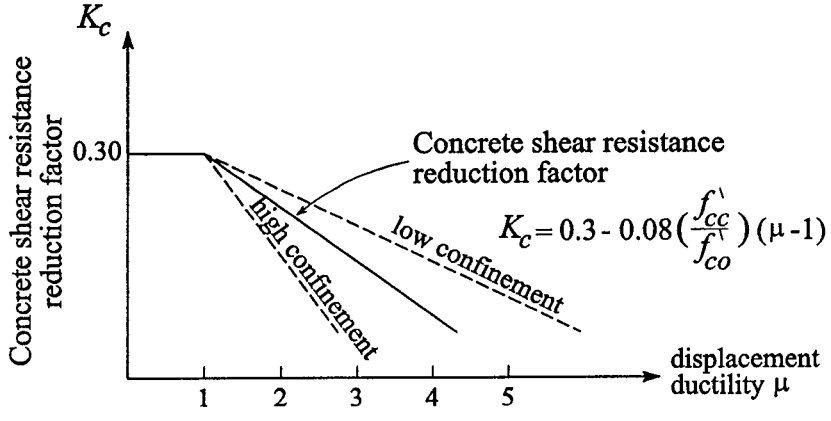

Figure D.3 Reduction of concrete shear resistance with increasing displacmenet ductility μ

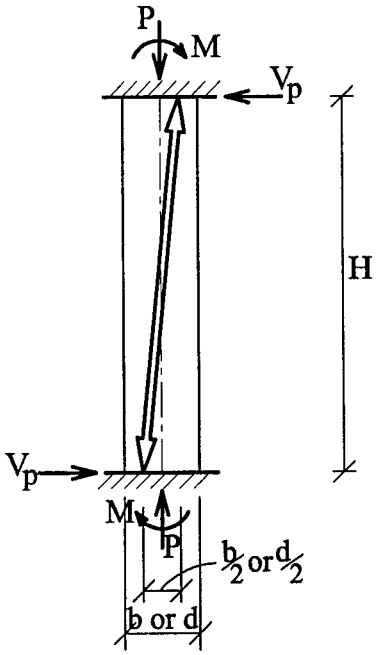

Figure D.4 Shear strength due to axial force mechanism

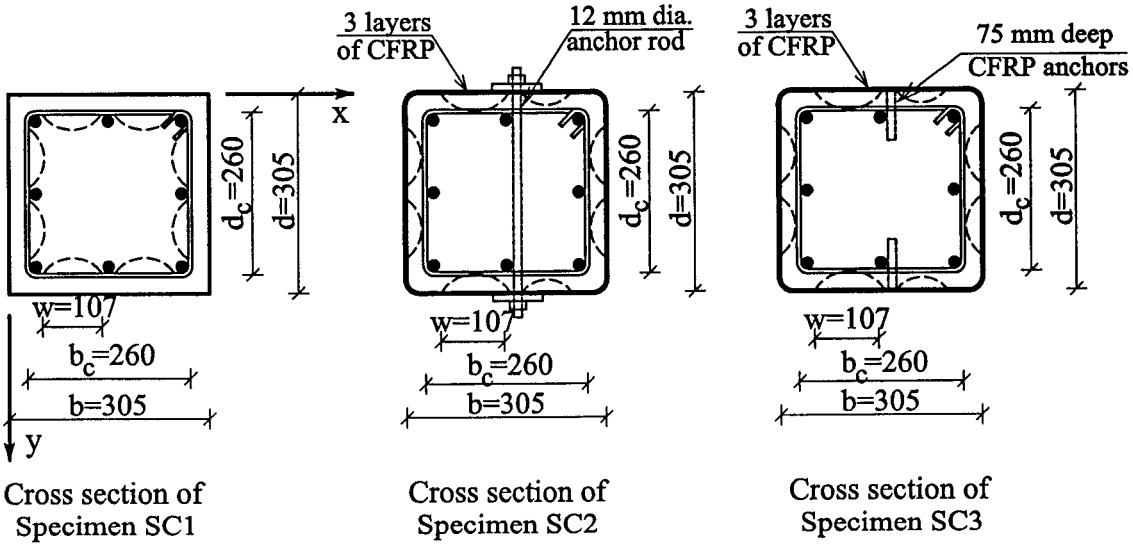

Figure D.5 Effect of anchored CFRP wraps on section confinement at tie loacations

REFERENCES

- Abou-Elfath, H., Ghobarah, A., and Aziz, T.S., 1998, "Seismic Analysis of Non-Ductile Frames," Proceedings, Sixth U.S. National Conference on Earthquake Engineering [CD-ROM], Earthquake Engineering Research Institute, EERI, Oakland, California, 12 pages.

- Abrams, D.P., 1987, "Influence of Axial Force Variations on Flexural Behavior of Reinforced Concrete Columns," ACI Structural Journal, Vol. 84, No.3, May-June, pp. 246-254.

- AIJ, 1988, "Design for Earthquake Resistant Reinforced Concrete Buildings Based on Ultimate Strength Concept," Structural Committee, Architectural Institute of Japan, Tokyo, Japan.

- ACI Manual of Concrete Practice, 1968, American Concrete Institute, Detroit, USA, Part 2, Committee 318.

- ACI Manual of Concrete Practice, 1985, American Concrete Institute, Detroit, USA, Part 3, Committee 408-1R-79.

- Alsiwat, J.M., and Saatcioglu, M., 1992, "Reinforced Anchorage Slip Under Monotonic Loading," Journal of Structural Engineering, ASCE, Vol. 118, pp. 2421-2438.

- Aschheim, M., 2000, "Towards Improved Models of Shear Strength Degradation in Reinforced Concrete Members," Structural Engineering and Mechanics, Vol. 9, No. 6, pp. 601-613.

- Baker, A.L.L., 1956, "Ultimate Load Theory Applied to the Design of Reinforced and Prestressed Concrete Frames," Concrete Publications ltd., London, 91 pages.

- Bayrak, O., and Sheikh, S.A., 2001, "Plastic Hinge Analysis," Journal of Structural Engineering, Vol. 127, No. 9, pp. 1092-1100.

- Bousias, N.S., Verzelletti, G., Fardis, M.N., and Gutierrez, E., 1995, "Load-Path Effects in Column Biaxial Bending with Axial Force," Journal of Engineering Mechanics, Vol. 121, No. 5, pp. 596-605.

- Chen, P.F. and Powell, G.H., 1982, "Generalized Plastic Hinge Concepts for 3D Beam-Column Elements," EERC Report No. 82-20, Earthquake Engineering Research Center, University of California, Berkeley, California.

- Ciampi, V., Eligehausen, R., Bertero, V.V., and Popov, E.P., 1982, "Analytical Model for Concrete Anchorage of Reinforcing Bar Under Generalized Excitation," Report No. EERC 82/23, University of California, Berkeley, California.

- Corley, W.G., 1966, "Rotational Capacity of Reinforced Concrete Beams," Journal of Structural Division, ASCE, Vol. 92, No. ST10, pp. 121-146.

- CSA A23.3-94, 1994, "Design of Concrete Structures", Canadian Standards Association, Rexdale, Ontario, Canada, 209 pages.

- Drucker, D.C., and Palgen, L., 1981, "On Stress-Strain Relations Suitable for Cyclic and Other Loading," Journal of Applied Mechanics, ASME, Vol. 48, No. 3, pp. 479-485.

- EERI, Jan., 2002, The Earthquake Engineering Research Institute, Oakland, California, http://www.eeri.org/earthquakes/Reconn/Nazca/Nazca1.html

- Eligehausen, R., Popov, E.P., and Bertero, V.V., 1983, "Local Bond Stress-Slip Relationship of a Deformed Bar Under Generalized Excitation," Report No. 83/23, University of California, Berkeley, California.

- Filippou, F.C., 1985, "A Simple Model for Reinforcing Bar Anchorage Under Cyclic Excitations," Report No. EERC 85/05, University of California, Berkeley, California.

- Filippou, F.C., Popov, E.P., and Bertero, V.V., 1983, "Effect of Bond Deterioration on Hysteretic Behavior of Reinforced Concrete Joints," Report No. EERC 83/19, University of California, Berkeley, California.

- Fischniger, M., Isakovic, T., and Krizaj, S., 1999, "Modeling Inelastic Seismic Response of R.C. Viaducts," Proceedings, Eighth Canadian Conference on Earthquake Engineering, 8CCEE, Vancouver, BC, pp. 689-694.

- Ghee, A.B., Priestley, M.N.J., and Paulay, T., 1989, "Seismic Shear Strength of Circular Reinforced Concrete Columns," ACI Structural Journal, Vol. 86, No. 1, Jan.-Feb., pp. 45-59.

- Ghobarah A., Biddah, A. and Mahgoub, M., 1997, "Seismic Retrofit of RC Columns Using Steel Jackets". European Earthquake Engineering Journal, Vol. 15, pp. 1052-1066.

- Ghusn, G.E., and Saiidi, M., 1986, "A Simple Hysteretic Element for Biaxial Bending of R/C Columns and Implementation in NEABS-86," Report No. CCEER 86-1, University of Nevada, Reno, Nevada.

- Hawkins, N.M., Lin, I., and Ueda, T., 1987, "Anchorage of Reinforcing Bars for Seismic Forces," ACI Structural Journal, Vol. 84, No. 5, pp. 407-418.

- Hidalgo, P. and Clough, R. W., 1974, "Earthquake Simulator Study of a Reinforced Concrete Frame," EERC Report No. 74-13, Earthquake Engineering Research Center, University of California, Berkeley, California.

- Jiang, Y., and Saiidi, M., 1990, "Four-Spring Element for Cyclic Response of R/C Columns," Journal of Structural Engineering, ASCE, Vol. 116, No. 4, pp. 1018-1029.

- Kannan, A. and Powell, G., 1973, "DRAIN-2D: A General Purpose Computer Program for Dynamic Analysis of Inelastic Plane Structures," EERC Report No. 73-22, University of California, Berkeley, California.

- Kent, D.C. and Park, R., 1971, "Flexural Members with Confined Concrete," Journal of the Structural Division, ASCE, Vol. 97, ST7, July, pp. 1969-1990.

- Lai, S.S., Will, G.T., and Otani, S., 1984, "Model for Inelastic Biaxial Bending of Concrete Members," Journal of Structural Engineering, ASCE, Vol. 110, No. 11, pp. 2563-2584.

- Li, K.N., Aoyama, H., and Otani, S., 1988, "Reinforced Concrete Columns Under Varying Axial Load and Bi-Directional Lateral Load Reversals," Proceedings of the 9th World Conference on Earthquake Engineering, Tokyo, Paper No. 5756, volume VIII, pp. 537-542.

- Litton, R.W., 1975, "A Contribution to the Analysis of Concrete Structures under Cyclic Loading," Ph.D. Dissertation, Department of Civil Engineering, University of California, Berkeley, California.

- Maruyama, K., Ramirez, H., and Jirsa, J.O., 1984, "Short Rectangular RC Columns Under Bilateral Load Histories," Journal of Structural Engineering, ASCE, Vol. 110, No. 1, pp. 120-137.

- MATLAB ®, 1997, The Math Works Inc., Massachusetts.

- Mattock, A.H., 1967, Discussion of "Rotational Capacity of Reinforced Concrete Beams," by W.G. Corley, Journal of Structural Division, ASCE, Vol. 93, ST2, pp. 519-522.
- Mau, S.T., and El-Mabsout, M, 1989, "Inelastic Buckling of Reinforced Bars," Journal of Engineering Mechanics, Vol. 115, No. 1, pp. 1-17.
- Mau, S.T., 1990, "Effect of Tie Spacing on Inelastic Buckling of Reinforced Bars," ACI Structural Journal, Vol. 87, No. 6, pp. 671-677.
- Monti, G., and Spacone, E., 2000, "Reinforced Concrete Fiber Beam Element with Bond-Slip," Journal of Structural Engineering, Vol. 126, No. 6, pp. 654-661.
- Master Builders Inc., Feb., 2001, www.Mbrace.com
- Mroz, Z., 1969,"An Attempt to Describe the Behavior of Metals Under Cyclic Loads Using More General Work-hardening Model," Acta Mechanica, Vol. 7, pp. 199-212.
- Mukaddam, M., and Kaski, M.B., 1986, "Reinforced Concrete Joints Under Cyclic Loading," Journal of Structural Engineering, ASCE, Vol. 112, No. 4, pp. 937-954.
- Ngo, D., and Scordelis, A.C., 1967, "Finite Element Analysis of Reinforced Concrete Beams," ACI Structural Journal, Vol. 64, No.3.
- Otani, S. and Sozen, M.A., 1972, "Behaviour of Multi-storey Reinforced Concrete Frames During Earthquakes," Civil Engineering Studies, Structural Research Series No. 392, University of Illinois, Urbana, Illinois.
- Otani, S., Cheung, V. W.-T., and Lai, S. S., 1979, "Behaviour and Analytical Models of Reinforced Concrete Columns Under Biaxial Earthquake Loads," Third Canadian Conference on Earthquake Engineering, Canadian National Committee for Earthquake Engineering, Montreal, Vol. 2, pp. 1141-1167.
- Otani, S., and Cheung, V., 1981, "Behavior of Reinforced Concrete Columns Under - Biaxial Lateral Load Reversals," Report 81-02, Department of Civil Engineering, University of Toronto.

- Park, Y.-J., and Ang A.H.S., 1985, "Mechanistic Seismic Damage Model for Reinforced Concrete," Journal of Structural Engineering, Vol. 111, No. 4, pp. 722-739.
- Park, R., and Paulay, T., 1975, Reinforced Concrete Structures, Jon Wiley and Sons, New York, 769 pages.
- Park, R., Priestley, M.J.N., and Gill, W.D., 1982, "Ductility of Square-Confined Concrete Columns," Journal of Structural Division, ASCE, Vol. 108, No. ST4, pp.929-950.
- Perdomo, M.E., Ramirez, A.R., and Lopez, J.F., 1999, "Simulation od Damage in RC Frames with Variable Axial Force," Earthquake Engineering and structural Dynamics, Vol. 28, pp. 311-328.
- Petrangeli, M., Pinto, P.E., and Ciampi, V., 1999, "Fiber Element for Cyclic Bending and Shear of RC structures. I: Theory," Journal of Engineering Mechanics, Vol. 125, No. 9, pp. 994-1001.
- Petrangeli, M., 1999, "Fiber Element for Cyclic Bending and Shear of RC structures. II: Verification," Journal of Engineering Mechanics, Vol. 125, No. 9, pp. 1002-1009.
- Pochanart, S., and Harmon, T., 1989, "Bond-Slip Model for Generalized Excitation Including Fatigue," ACI Material Journal, Vol. 86, No. 5, pp. 465-474.
- Powell, G.H., and Campbell, S., 1994, "DRIAN-3DX: Element Description and User Guide," SEMM Report No. 94/08. Department of Civil Engineering, University of California, Berkeley, California.
- Priestley, M.N.J., and Park, K., 1987, "Strength and Ductility of Concrete Bridge Columns Under Seismic Loading," ACI Structural Journal, Vol. 84, No. 1, pp. 61-76.
- Priestley, M.J.N., Seible, F., Xiao, Y., and Verma, R., 1992, "Shear Retrofit of Bridge Columns by Steel Jacketing," Proceedings of First Annual Seismic Research Workshop, Caltrans, Department of Transportation, Division of Structures, Sacramento, California, pp. 209-216.
- Priestley, M.J.N., Seible F., Verma, R., and Xiao, Y., 1993, "Seismic Shear Strength of Reinforced Concrete Columns," SSRP-93/06, Department and Applied Mechanics and Engineering Sciences, University of California, San Diego, La Jolla, California, 120 pages.

- Priestley, M.J.N., Verma, R., and Xiao, Y., 1994, "Seismic Shear Strength of Reinforced Concrete Columns," Journal of Structural Engineering, Vol. 120, No. 8, pp. 2310-2329.

- Ramirez, H., and Jirsa, J.O., 1980, "Effect of axial load on shear behaviour of short RC columns under cyclic lateral deformations," PMFSEL Report 80-1, Phil M. Ferguson Structural Engineering Lab., University of Texas, Austin, 162 pages.

- Razvi, S. R., and Saatcioglu, M., 1999, "Analysis and Design of Concrete Columns for Confinement," Journal of Earthquake Spectra, Volume 15, No. 4, pp. 791-811.

- Riahi, A., Powell, G.H., and Mondkar, D.P., 1979, "3D Beam-Column Element (Type 2-Parallel Element Theory) for the ANSR-II Program," EERC Report No. 79-31, Earthquake Engineering Research Center, University of California, Berkeley, California.

- Ricles, J.M., Yang, Y.S., and Priestley, M.J.N, 1998, "Modeling Non-Ductile R/C Columns for Seismic Analysis of Bridges," Journal of Structural Engineering, ASCE, Vol. 124, No. 4, pp. 415-425.

- Russo, G., Zingone, G., and Ramano, F., 1990, "Analytical Solution for Bond-Slip of Reinforcing Bars in RC Joints," Journal of Structural Engineering, ASCE, Vol. 116, No. 2, pp. 336-355.

- Saiidi, M., Lawver, R., and Hart, J., 1986, "User's Manual for ISADAB and SIBA, Computer Programs for Nonlinear Transverse Analysis of Highway Bridges Subjected to Static and Dynamic Lateral Loads," CCEER Report No 86-2, University of Nevada-Reno, Center for Civil Engineering Earthquake Research, Reno, Nevada, 74 pages.

- Saatcioglu, M. and Ozcebe, G., 1987, "Effect of Bar Slip on Hysteretic Behaviour of Concrete Columns," Earthquake Engineering: Fifth Canadian Conference, A.A. Balkima, Rotterdam, pp. 833-839.

- Saatcioglu, M. and Ozcebe, G., 1989, "Response of Reinforced Concrete Columns to Simulated Seismic Loading," ACI Structural Journal, Vol. 86, No. 1, pp. 3-12.

- Saatcioglu, M., Gardner, N.J., and Ghobarah, A., 2001, "1999 Turkey Earthquake: Performance of RC Structures," Concrete International, Vol. 23, No. 3, March, pp. 46-56.

- Saatcioglu, M., Mitchell, D., Tinawi, R., Gardner, N.J., Gillies, A.G., Ghobarah, A., Anderson, D.L., and Lau, D., 2001, "The August 17, 1999 Kocaeli (Turkey) Earthquake: Damage to Structures," Canadian Journal of Civil Engineering, August, Vol. 28, No. 4, pp. 715-737.

- Sawyer, H.A., 1964, "Design of Concrete Frames for Two Failure States," Proceedings of the International Symposium on the Flexural Mechanics of Reinforced Concrete, ASCE-ACI, Miami, pp. 405-431.

- Sheikh, S. A., and Khoury, S. S., 1993, "Confined Concrete Columns with Stub," ACI Structural Journal, Vol. 90, No. 4, pp. 414-431.

- Soroushian, P., Sim, J., and Hsu, J.-W., 1991, "Axial/Flexural Behavior of Reinforced Concrete Sections: Effects of the Design Variable," ACI Structural Journal, Vol. 88, No. 1, pp. 17-21.

- Spacone, E., Filippou, F.C., and Taucer, F.F., 1996, "Fibre beam-Column Model for Nonlinear Analysis of R/C Frames, Part II: Applications," Earthquake Engineering and Structural Dynamics, Vol. 25, No. 7, pp. 727-742.

- Takeda, T., Sozen, M., and Neilson, N., 1970, "Reinforced Concrete Response to Simulated Earthquakes," Journal of Structural Division, ASCE, Vol. 96, No. ST12, pp.2557-2573.

- Takizawa, H. and Aoyama, H., 1976, "Biaxial Effects in Modeling Earthquake Response of R/C Structures," Earthquake Engineering and Structural Dynamics, Vol. 4, pp. 523-552.

- Ueda, T., Lin, I., and Hawkins, N.M., 1986, "Beam Bars Anchorage in Exterior Column-Beam Connections," ACI Structural Journal, Vol. 83, No. 3, pp. 412-422.

- Umehara, H. and Jirsa, J.O., 1984, "Short Rectangular RC Columns Under Bi-Directional Loadings," Journal of Structural Engineering, ASCE, Vol. 110, No. 3, pp. 605-618.

- Vecchio, F. and Collins, M., 1986, "The Modified Compression-Field Theory for Reinforced Concrete Elements Subjected to Shear," ACI Structural Journal, Vol. 83, No. 1, pp. 219-231.

- Verma R., Xiao, Y., Priestley, M.J.N., and Seible, F., 1993, "Seismic retrofit design for shear strength enhancement of squat bridge columns," Proceedings of the Second Annual Seismic Research Workshop, Caltrans, Sacramento, California.

- Viwathanatepa, S., Popov, E.P., and Bertero, V.V., 1979, "Effects of Generalized Loadings on Bond of Reinforcing Bars Embedded in Confined Concrete Blocks," Report No. EERC 79/22, University of California, Berkeley, California.

- Watanabe, F., and Ichinose, T., 1991, "Strength and Ductility Design of RC Members Subjected to Combined Bending and Shear," Proceedings of the Workshop on Concrete Shear in Earthquake, University of Houston, Houston, Texas, pp. 429-438.

- Wong Y.L., Paulay, T., and Priestly, M.J.N., 1990, "Squat Circular Bridge Piers Under Multi-Directional Seismic Attack," Report 90-4, Department of Civil Engineering, University of Canterbury, New Zealand.

- Woodward, K. and Jirsa, J.O., 1984, "Influence of Reinforcement on RC Short Column Lateral Resistance," Journal of Structural Engineering, ASCE, Vol. 110, No. 1, pp. 90-104.

- Xiao, Y., and Martirossyan, A., 1998, "Seismic Performance of High-Strength Concrete Columns," Journal of Structural Engineering, Vol. 124, No. 3, pp. 241-251.

- Yalcin, C., and Saatcioglu, M., 2000, "Inelastic Analysis of Reinforced Concrete columns," Computers & Structures, Vol. 77, No. 5, pp. 539-555.

- Zayas, V.A., Mahin, S.A., and Popov, E.P., 1980, "Cyclic Inelastic Behaviour of Steel Offshore Structures," EERC Report No. 80-28, Earthquake Engineering Research Center, University of California, Berkeley, California.

- Zeigler, H., 1959, "A Modification of Prager's Hardening Rule," Quarterly of Applied Math., Vol. 17, 55 pages.

- Zeris, C.A., and Mahin, S.A., 1991, "Behavior of reinforced concrete structures subjected to biaxial excitation," Journal of Structural Engineering, ASCE, Vol. 117, No. 9, pp. 2640-2656.